U.S. Department of Transportation

Urban Mass Transportation Administration

UMTA-MA-06-0025-83-10
DOT-TSC-UMTA-83-31

Stability and Curving Performance of Conventional and Advanced Rail Transit Vehicles

D. N. Wormley
J. K. Hedrick
M. L. Nagurka

Massachusetts Institute of Technology
Department of Mechanical Engineering
Cambridge MA 02139

January 1984
Final Report

This document is available to the public through the National Technical Information Service, Springfield, Virginia 22161.

UMTA Technical Assistance Program

Technical Report Documentation Page

1. Report No.
UMTA-MA-06-0025-83-10

2. Government Accession No.

3. Recipient's Catalog No.

4. Title and Subtitle
STABILITY AND CURVING PERFORMANCE OF CONVENTIONAL AND ADVANCED RAIL TRANSIT VEHICLES

5. Report Date
January 1984

6. Performing Organization Code
DTS-76

7. Author(s)
D.N. Wormley, J.K. Hedrick, M.L. Nagurka

8. Performing Organization Report No.
DOT-TSC-UMTA-83-31

9. Performing Organization Name and Address
Massachusetts Institute of Technology*
Department of Mechanical Engineering
Cambridge, Massachusetts 02139

10. Work Unit No. (TRAIS)
UM377/R3691

11. Contract or Grant No.
DTRS 57-80C-00152

12. Sponsoring Agency Name and Address
U.S. Department of Transportation
Urban Mass Transportation Administration
Office of Technical Assistance
Washington DC 20590

13. Type of Report and Period Covered
Final Report
Jan. 1981 - Nov. 1982

14. Sponsoring Agency Code
URT-11

15. Supplementary Notes
*Under Contract to: U.S. Department of Transportation
Research and Special Programs Administration
Transportation Systems Center
Cambridge MA 02142

16. Abstract
Analytical studies are presented which compare the curving performance and speed capability of conventional rail transit trucks with self steering (cross-braced) and forced steering (linkages between carbody and wheelsets) radial trucks. Truck curving performance is measured in terms of the work performed by the wheel/rail friction forces in the contact zone during curve negotiation. The contact work is used as an indication of wheel and rail wear rates as well as the additional power required to negotiate curves. Truck speed capability is expressed in terms of the maximum operating speed before lateral instability or hunting occurs.

The studies are based upon a generalized computational model which is capable of representing conventional and innovative trucks that are currently being considered for implementation. The stability analysis utilizes a linear model while the curving analysis includes the essential nonlinearities associated with wheel/rail profile geometry, wheel/rail friction force saturation and suspension stiffnesses. In addition, the curving analysis includes an accurate description of two-point wheel/rail contact which can occur with common wheel profiles during flanging.

Results of the study indicate that for curves greater than 5°, forced steering trucks can offer substantial performance improvements in comparison to well designed conventional trucks in terms of work performed during curve negotiation. Also comparison of a new AAR 1/20 wheel profile with a modified Heumann (single point contact) profile indicates that the latter profile can offer substantial performance improvements in terms of reduced work during curve negotiation.

17. Key Words
Rail Vehicles
Rail Trucks
Radial Trucks
Forced Steering Trucks

18. Distribution Statement
DOCUMENT IS AVAILABLE TO THE PUBLIC THROUGH THE NATIONAL TECHNICAL INFORMATION SERVICE, SPRINGFIELD, VIRGINIA 22161

19. Security Classif. (of this report)	20. Security Classif. (of this page)	21. No. of Pages	22. Price
Unclassified	Unclassified	348	

Form DOT F 1700.7 (8-72) Reproduction of completed page authorized

METRIC CONVERSION FACTORS

Approximate Conversions to Metric Measures

Symbol	When You Know	Multiply by	To Find	Symbol
		LENGTH		
in	inches	*2.5	centimeters	cm
ft	feet	30	centimeters	cm
yd	yards	0.9	meters	m
mi	miles	1.6	kilometers	km
		AREA		
in^2	square inches	6.5	square centimeters	cm^2
ft^2	square feet	0.09	square meters	m^2
yd^2	square yards	0.8	square meters	m^2
mi^2	square miles	2.6	square kilometers	km^2
	acres	0.4	hectares	ha
		MASS (weight)		
oz	ounces	28	grams	g
lb	pounds	0.45	kilograms	kg
	short tons (2000 lb)	0.9	tonnes	t
		VOLUME		
tsp	teaspoons	5	milliliters	ml
Tbsp	tablespoons	15	milliliters	ml
fl oz	fluid ounces	30	milliliters	ml
c	cups	0.24	liters	l
pt	pints	0.47	liters	l
qt	quarts	0.95	liters	l
gal	gallons	3.8	liters	l
ft^3	cubic feet	0.03	cubic meters	m^3
yd^3	cubic yards	0.76	cubic meters	m^3
		TEMPERATURE (exact)		
°F	Fahrenheit temperature	5/9 (after subtracting 32)	Celsius temperature	°C

*1 in = 2.54 (exactly). For other exact conversions and more detailed tables, see NBS Misc. Publ. 286, Units of Weights and Measures, Price $2.25, SD Catalog No. C13.10:286.

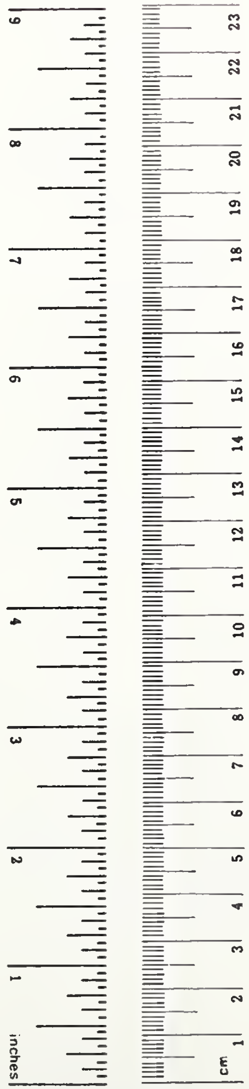

Approximate Conversions from Metric Measures

Symbol	When You Know	Multiply by	To Find	Symbol
		LENGTH		
mm	millimeters	0.04	inches	in
cm	centimeters	0.4	inches	in
m	meters	3.3	feet	ft
m	meters	1.1	yards	yd
km	kilometers	0.6	miles	mi
		AREA		
cm^2	square centimeters	0.16	square inches	in^2
m^2	square meters	1.2	square yards	yd^2
km^2	square kilometers	0.4	square miles	mi^2
ha	hectares (10,000 m^2)	2.5	acres	
		MASS (weight)		
g	grams	0.035	ounces	oz
kg	kilograms	2.2	pounds	lb
t	tonnes (1000 kg)	1.1	short tons	
		VOLUME		
ml	milliliters	0.03	fluid ounces	fl oz
l	liters	2.1	pints	pt
l	liters	1.06	quarts	qt
l	liters	0.26	gallons	gal
m^3	cubic meters	35	cubic feet	ft^3
m^3	cubic meters	1.3	cubic yards	yd^3
		TEMPERATURE (exact)		
°C	Celsius temperature	9/5 (then add 32)	Fahrenheit temperature	°F

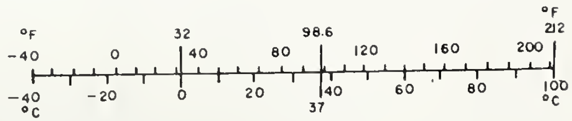

PREFACE

In support of the Office of Rail and Construction Technology of the Urban Mass Transportation Administration (UMTA), the Transportation Systems Center is conducting analytical and experimental studies to relate transit truck design characteristics to wheel rail forces and wheel rail wear ratio. The results of these studies are expected to provide rail transit systems with options for reducing the wheel-rail wear rates while maintaining or improving equipment performance.

In the past decade, there have been significant efforts toward developing steerable truck configurations employing direct connections between axles and supplemental linkages connecting the axles to the carbody. These new configurations aid in steering while maintaining the speed capability of the truck design. Under contracts DOT-TSC-1739 and DOT-TSC-1740 with the Budd Company and with the Urban Transportation Development Corporation, design studies have been conducted for the retrofit of existing trucks to linkage-steered configurations.

Under an earlier contract with the U.S. Department of Transportation, Office of University Research (DOT-03-70052), the Department of Mechanical Engineering of Massachusetts Institute of Technology had conducted studies of the performance limits of conventional and self-steering trucks for intercity passenger application.

This study used curve negotiation criteria in which both flange contact and wheel slip were prevented. Such a study is unrealistic for the sharp curves typical of transit application.

The study described in this document extends the previous analyses to include regions of significant flange contact for sharper curve radii. Also considered is the performance achievable with forced steering mechanizations employing truck to carbody linkages.

The work was performed under contract to the Transportation Systems Center in support of the Urban Mass Transportation Administration. The authors would like to thank Dr. Herbert Weinstock for many productive discussions on the work in progress and his careful review and comments on this report.

TABLE OF CONTENTS

LIST OF FIGURES

Figure		Page

Figure		Page

Figure		Page

Figure		Page

LIST OF TABLES

Table | Page

LIST OF SYMBOLS

a	half of track gage
a_e	longitudinal semi-axis of contact patch ellipse
a_{11}	wheelset roll coefficient
A_r	area of contact
b	half of wheelbase
b_e	lateral semi-axis of contact patch ellipse
B	proportionality constant
$\underline{\bar{C}}_{fs}$	damping matrix contribution from the interaxle connections
C_{px}	primary longitudinal damping (4 per truck)
C_{py}	primary lateral damping (4 per truck)
$\underline{\bar{C}}_r$	damping matrix from the wheel/rail interaction
$\underline{\bar{C}}_s$	suspension damping matrix
C_{sy}	secondary lateral damping (2 per truck)
C_{sz}	secondary vertical damping (2 per truck)
d_c	critical plastic displacement
d_p	half of the spacing of primary longitudinal springs
d_s	half of the spacing of secondary longitudinal springs
f_{ij_N}	nominal creep coefficients
f_{11}	lateral creep coefficient
f_{12}	lateral/spin creep coefficient
f_{22}	spin creep coefficient
f_{33}	longitudinal creep coefficient
F_{buff}	lateral buff load
$\underline{F}_c$	creep force vector (with components F_{CPX}, F_{CPY}, and M_{CP} in longitudinal, lateral, and normal contact patch directions, respectively)

F_{CPX}, F_{CPY} creep force in longitudinal, lateral contact patch direction

F'_{CPX}, F'_{CPY} unlimited creep force in longitudinal, lateral contact patch direction

F_{CXi} longitudinal track frame component of creep force at ith contact patch; i = L (left), R (right) for single-point; i = LT (left tread), LF (left flange), R (right) for two-point

F_{CYi} lateral track frame component of creep force at i-th contact patch; i = L (left), R (right) for single-point; i = LT (left tread), LF (left flange), R (right) for two-point

F_{CZi} vertical track frame component of creep force at i-th contact patch; i = L (left), R (right) for single-point; i = LT (left tread), LF (left flange), R (right) for two-point

F_{cr} net lateral force on the wheelset due to creepages

F_f lateral flange force

$\underline{F}_{fs}$ vector of generalized force due to the steering linkages

$\underline{F}'_{fs}$ vector of damper forces due to interaxle dampings

F_g lateral gravitational stiffness force

F_j lateral force on the wheelset due to gyroscopic effect

F_{lat} wheelset lateral force (in lateral track frame direction) provided by suspension and body (cant deficiency) forces

F_{Ni} normal force at i-th contact patch; i = L (left), R (right) for single-point; i = LT (left tread), LF (left flange), R (right) for two-point

F_{NYi} lateral track frame component of normal force at i-th contact patch; i = L (left), R (right) for single-point; i = LT (left tread), LF (left flange), R (right) for two-point

F_{NZi} vertical track frame component of normal force at i-th contact patch; i = L (left), R (right) for single-point; i = LT (left tread), LF (left flange), R (right) for two-point

F_{rail_L}, F_{rail_R} lateral rail reaction force at left, right rail

F'_R unlimited resultant creep force

F_s suspension force

F_{sec} lateral force applied at secondary

F_t longitudinal thrust or drawbar force (in longitudinal track frame direction

F_{YL}, F_{YR} net force in lateral track frame direction at left, right wheel (sum of lateral components of creep and normal forces)
Note: For lateral equilibrium: $F_{YL} + F_{YR} + F_{lat} = 0$

F_{YLF},F_{YLT} net force in lateral track frame direction at flange, tread contact patch of left wheel (sum of lateral components of creep and normal forces)

F_{ZLF},F_{ZLT} net force in vertical track frame direction at flange, tread contact patch of left wheel (sum of vertical components of creep and normal forces)
Note: For two-point contact: $F_{ZLF} + F_{ZLT} - V_L = 0$

G track curvature steering gain

$G_{c\ell}$ steering gain to follow the track centerline

$G_{pr\ell}$ steering gain to follow the pure rolling line

h_c vertical distance from rail plane to coupler

h_{cs} vertical distance from secondary suspension to carbody cg

h_{ts} vertical distance from truck cg to secondary suspension

h_{tp} vertical distance from primary suspension to truck cg

h_1 thickness of wear particles

H cant deficiency steering gain

I_{cx} roll moment of inertia of carbody

I_{cy} pitch moment of inertia of carbody

I_{cz} yaw moment of inertia of carbody

I_{tx} roll moment of inertia of truck frame

I_{ty} pitch moment of inertia of truck frame

I_{tz} yaw moment of inertia of truck frame

I_{wx} roll moment of inertia of wheelset

I_{wy} pitch moment of inertia of wheelset

I_{wz} yaw moment of inertia of wheelset

$\underline{\bar{I}}$	identity matrix
j	imaginary number ($\sqrt{-1}$)
k_b	total bending stiffness of a truck
k_{b2}	interaxle bending stiffness
k_{px}	primary longitudinal stiffness (4 per truck)
k_{py}	primary lateral stiffness (4 per truck)
k_{pz}	primary vertical stiffness (4 per truck)
k_r	effective lateral rail stiffness
k_s	total shear stiffness of a truck
k_{sy}	secondary lateral stiffness (2 per truck)
k_{sz}	secondary vertical stiffness (2 per truck)
k_{s2}	interaxle shear stiffness
$k_{s\psi}$	secondary yaw stiffness (1 per truck)
$\underline{\bar{K}}_{fs}$	stiffness matrix contribution from the steering linkages
$\underline{\bar{K}}_r$	stiffness matrix from wheel/rail interaction
$\underline{\bar{K}}_s$	suspension stiffness matrix
ℓ_s	half of truck center pin spacing
M_c	mass of carbody
M_{CP}	creep moment normal to contact patch
M_{CYi}	lateral track frame component of creep moment at i-th contact patch; i = L (left), R (right) for single-point; i = LT (left tread), LF (left flange), R (right) for two-point
M_{CZi}	vertical track frame component of creep moment at i-th contact patch; i = L (left), R (right) for single-point; i = LT (left tread), LF (left flange), R (right) for two-point
M_t	mass of truck frame
M_w	mass of wheelset
M_{yaw}	wheelset yaw moment (in vertical wheelset frame direction) provided by suspension forces

$\underline{\underline{M}}$	inertia matrix
N	normal load (same as F_{Ni})
N_N	Nominal normal load
P_{in}, P_{out}	input, output power
r_i	rolling radius measured from wheelset spin axis to i-th contact patch; i = L (left), R (right) for single-point, i = LT (left tread), LF (left flange), R (right) for two-point
r_o	rolling radius for centered wheelset; nominal rolling radius
R	curve radius, often expressed in degree curve, D, where $D = 2[\sin^{-1}(\frac{50}{R})] \simeq \frac{5730}{R}$ deg with R in ft.
S	sliding distance
T_B	secondary yaw breakaway torque
T_{cr}	net yaw moment from creepages
T_d	wheelset drive/brake torque
T_g	yaw moment due to gravitational stiffness force
T_j	yaw moment contribution from gyroscopic effect
T_s	net yaw moment on wheelset due to primary suspension elements
V	vehicle speed
V_{cr}	critical speed of the vehicle
V_L, V_R	external vertical load acting on left, right wheel (in negative vertical track frame direction) provided by body and suspension forces
W_V	total vehicle weight
W'_V	wear volume
W_1	contact patch work per distance traveled (in force units) $W_1 = \underline{F}_c \cdot \underline{\xi}$
W_2	contact patch work per distance traveled (W_1) divided by contact patch area
x	longitudinal coordinate
y	lateral coordinate

y_{fc} flange clearance

y_{rail_L}, y_{rail_R} lateral displacement of left, right rail

z vertical coordinate

$\dot{\beta}$ spin perturbation rate (from pure rolling angular speed)

δ_i contact angle at i-th contact patch; i = L (left), R (right) for single-point; i = LT (left tread), LF (left flange), R (right) for two-point

δ_o centered wheelset contact angle

Δ contact angle difference coefficient

Δx_i longitudinal displacement of i-th contact patch from vertically below wheelset axis

Δy track curvature steering offset

$\Delta\psi$ cant deficiency steering offset

ε creep force saturation constant

λ wheel conicity

λ_i i^{th} eigenvalue of a system

μ coefficient of friction

μ_f coefficient of flange friction

ξ_i damping ratio of the i^{th} eigenvalue

ξ_R resultant creepage

ξ_{spi} spin creepage in normal contact patch direction at i-th contact patch

ξ_{xi} longitudinal creepage at i-th contact patch

ξ_{yi} lateral creepage at i-th contact patch

$\underset{\sim}{\xi}$ creepage vector (with components ξ_{xi}, ξ_{yi}, and ξ_{spi} in longitudinal, lateral, and normal contact patch directions, respectively)

ρ wheelset spin speed per forward speed (or, wheelset pitch per distance traveled)

$$\rho = \frac{\Omega}{V} = \frac{1}{r_o} + \frac{\dot{\beta}}{V}$$

σ_i	real part of the i^{th} eigenvalue
ϕ_d	cant deficiency (lateral unbalance load) $\phi_d = \frac{V^2}{Rg} - \phi_{SE}$
ϕ_{SE}	track superelevation (or bank) angle
ϕ_w	wheelset roll angle with respect to track plane
ψ	yaw angle
ψ_w	wheelset angle of attack, or yaw angle with respect to radial alignment
ω	frequency, rad/sec
ω_i	imaginary part of the i^{th} eigenvalue
ω_{ni}	natural frequency of the i^{th} eigenvalue, rad/sec
Ω	wheelset spin speed

EXECUTIVE SUMMARY

Analytical studies are presented which compare the curving and stability performance of conventional rail transit trucks with recently introduced innovative trucks such as self-steering (cross bracing between wheelsets) and forced steering (linkages between the carbody and wheelsets) radial trucks. Truck curving performance is measured by calculating the work performed by the wheel/rail friction forces in the contact patches per unit distance traveled. The contact area work is used as an indicator of the wheel and rail wear rate as well as a measure of the additional power required to pull the truck through the curve. Truck speed capability is measured by calculating the maximum forward speed the vehicle can operate at before undamped lateral oscillation or hunting occurs. This maximum speed is called the critical speed in this report; in general, the operating speed of the vehicle is chosen to be a comfortable safety factor below this speed.

Studies have been conducted to determine the influence of truck suspension parameters and wheel profile on the truck speed and curving performance. These studies are summarized in Tables 5.3 and 5.4 in the report.

For conventional trucks the two dominant design parameters influencing stability and curving performance are truck primary longitudinal suspension stiffness and wheel profile. As the longitudinal stiffness is increased, the work index and the critical speed increase until an upper value of stiffness is reached where the critical speed decreases with further increases in stiffness. For typical stiffness ranges of 10^5 lb/ft to 2×10^6 lb/ft per axlebox, critical speeds of 110 mph to 210 mph were computed for the baseline transit vehicle parameters using a standard new AAR wheel profile with a 1/20 tread conicity. The work index for this stiffness range for the vehicle negotiating a 10° curve was 85 ft-lb/ft to 155 ft-lb/ft for the flanging wheel which is generally the lead axle, high rail wheel. For a given speed the additional power required to overcome the resistance per wheel can be computed from the work index. For example, for a forward speed of 50 ft/sec (34 mph) a work index of 155 ft-lb/ft corresponds to 14 horsepower. Typically the flanging wheel has the highest work index by a substantial margin. For the case of the flanging wheel having 155 ft-lb/ft on a 10° curve the work of the other three wheels of the truck increases the total work to 250 ft-lb/ft. The numerical results indicate that truck designs with reduced primary suspension longitudinal stiffnesses have significantly reduced work generated during curving; however, the lower critical speeds associated with this reduction in longitudinal stiffness must be acceptable.

The performance of a single point contact Heumann profile wheel with a 0.2 conicity on the conventional truck has been studied. To achieve the same critical speed as the 1/20 AAR wheel design a higher longitudinal primary suspension stiffness is required for the 0.2 conicity wheel; for example, to achieve a critical speed of 125 mph the Heumann wheel profile requires a stiffness six times that of the lower 1/20 conicity wheel; however at this critical speed the Heumann wheel profile truck design requires 22% less work per unit distance to negotiate a 10° curve than the truck designed for 1/20 conicity wheels. In the range of designs corresponding to critical speeds of 90 to 130 mph, the Heumann wheel profile designs generally have reduced work generated in curving in comparison to the 1/20 conicity wheel profile designs for the same critical speed. It is noted that in the range of practical longitudinal stiffnesses considered, the 0.2 conicity wheel was found to have a maximum design critical speed of 130 mph and if higher critical speeds are desired reduced conicity wheels are required.

For self-steering radial trucks with cross bracing between the wheelsets the interaxle bending and shear stiffness as well as the primary suspension longitudinal stiffness and wheel profile are important design parameters. The best stability/curving performance tradeoff was obtained for designs with a low interaxle bending, high interaxle shear and intermediate primary longitudinal stiffness. For self-steered radial trucks designed with identical critical speeds of 100 mph, the work required in curving is similar for low (0.05) and high (0.2) conicity wheels. For designs with identical critical speeds of 130 mph, the truck designs with a higher conicity wheel requires 20% less work to negotiate a 10° curve than the 0.05 conicity design. The self-steering radial truck designs for both low and high conicity wheels require approximately 12% less work to negotiate a 10° curve than an equivalent 130 mph critical speed conventional truck design for both low and high conicity wheels.

Techniques have been developed and implemented to assess the performance of a wide variety of forced steering truck designs employing linkages between the carbody and truck/wheelset elements. One of the configurations which is appropriate for transit systems and contains the essential design characteristics in terms of stiffnesses and steering gains which are necessary to illustrate forced steering truck performance characteristics has been studied in detail. Thus, while the study results are in general indicative of forced steering truck performance characteristics, specific configurations may have particular curving or stability characteristics which differ from those of the configuration studied. The geometric gain of the forced-steering truck configuration studied has been selected to yield a design which kinematically tracks the same rolling line (in the absence of flanging) for any constant radius curve. For this design principal stability/curving tradeoff design parameters include truck primary suspension longitudinal stiffness, steering link stiffness and wheel profile.

The studies indicate that a combination of low values of primary longitudinal stiffness ranging from 10^3 lb/ft to 7×10^4 lb/ft coupled with high values of steering link stiffness above 10^5 lb/ft provide critical speeds in the range of 90 mph to 130 mph. The practical lower limit on primary suspension stiffness is determined by a combination of factors involving the details of truck propulsion and braking system while the upper limit on steering link stiffness is established by link geometry and material selection.

For forced-steered truck designs with low stiffness the steering linkages can exert a destabilizing yaw moment on the front truck. In extreme design cases, with very low stiffness and conicities, kinematic instability can occur resulting in a critical speed near zero. Studies have shown that for primary lateral stiffnesses greater than 10^5 lb/ft, secondary yaw stiffnesses greater than 10^5 ft-lb/rad*, and for conicities greater than 0.01 that kinematic instabilities will not occur. This range of parameters corresponds to the typical designs considered in this study.

Analytical data comparing the work required to negotiate a 10° curve for designs with a 130 mph critical speed show that the lower primary stiffness (10^3 lb/ft) designs require approximately 50% of the work per unit distance as the higher primary stiffness (7×10^4 lb/ft) designs and show that designs with 0.2 conicity Heumann wheels require approximately 50% of the work per unit distance as the 1/20 conicity wheel truck designs.

Work required during curving for forced steering trucks is significantly lower than for conventional and self-steering radial trucks designed with the same critical speed. For designs using 1/20 conicity wheels with a critical speed of 130 mph, the work required per unit distance to negotiate a 10° curve for a conventional truck design is reduced to 89% for an equivalent

---

*Ref. [27] shows that secondary yaw stiffness is primarily important in the extremely low (< 0.01) conicity case.

self steering radial truck, to 58% for an equivalent forced steering truck design with a primary stiffness of 7×10^4 lb/ft and to 24% for a forced steering design with a primary stiffness of 10^3 lb/ft. For higher conicity 0.2 Heumann wheel profile designs with 130 mph critical speeds, the forced steering trucks require respectively 8% for the high and 3% for the low primary stiffness designs of the work required to negotiate a 10° curve as the equivalent conventional truck. The forced-steering truck designs have the most significant improvements in performance with the higher conicity Heumann wheels and the lower values of primary longitudinal stiffness. The forced steering trucks have the potential to effectively utilize the higher conicity wheel for designs with critical speeds in the range of 90 to 130 mph. If higher critical speeds are desired, then lower conicity wheels (less than 0.2) are required.

A summary comparison of the power required to negotiate a curve for the prototype truck designs illustrates the potential performance improvement of advanced designs. The power associated with negotiation of a 10° curve at 50 ft/sec (34 mph) is summarized in the following table for conventional, self-steered radial, and the two forced radial truck designs with new wheels. The truck suspensions are designed for identical critical speeds of 120 mph. The table illustrates the potential advantages of employing forced-steering to reduce wheel/rail wear and fuel consumption in terms of the dissipated power in the wheel/rail contact patches.

The significant potential for reduction in wheel wear during curving offered by forced-steering truck designs must be assessed in terms of the increased complexity associated with the steering linkages and the practicality of maintaining the high relative stiffness of the forced-steering links. The capability to accommodate braking and propulsion forces with low primary suspension longitudinal stiffnesses must also be provided. For a specific transit authority, the selection of an appropriate truck design depends upon the number and severity of curves which influence the importance of wheel wear, and upon the desired critical speed which is related to maximum operating speed.

	Conventional Design	Self-Steered Radial Design	Forced-Steered Radial	
			Moderate Primary Stiffness	Soft Primary Stiffness
Front Truck Power (HP)	10.7	9.4	7.2	4.1
Rear Truck Power (HP)	10.7	7.6	5.2	2.3
Total Vehicle Power (HP)	21.4	17.0	12.4	6.4

FIGURE 1. COMPARISON OF POWER REQUIREMENTS OF BASELINE TRUCK DESIGNS WITH NEW WHEELS NEGOTIATING 10° CURVES AT 50 FT/SEC (34 mph)

CHAPTER 1

INTRODUCTION

1.1 Background

The service provided in an urban rail transportation system and the associated operating costs are strongly influenced by the state of the rolling stock and the fixed track structure. Maintenance of rolling stock and the track structure are essential to good service and control of operating costs. Components associated with rolling stock including wheels, axles, suspension elements and the carbody plus power and braking equipment suspended from the car as well as rails, switching gear, ties and ballast sustain wear and experience forces directly related to the wheel/rail interaction forces. The control and limitation of these forces can have a significant impact upon urban rail transit system maintenance requirements. These forces are associated directly with vehicle stability or hunting, vehicle curve negotiation capability and vehicle vertical and lateral suspension capability to accomodate track irregularities.

In the last decade an increasing interest in developing vehicles which control these interaction forces to reduce wheel and rail wear and vehicle and track deterioration has developed and led to proposals for:

(1) Conventional suspension trucks employing rubber or mechanical components between the axle and truck frame which have reduced stiffness.

(2) Self steering radial trucks which employ direct links between truck axles to aid in aligning the axles radially in curves.

(3) Forced steering trucks which employ direct links between carbody-truck-axle elements to force the axles into radial alignment on curves.

These developments have been motivated primarily by the desire to reduce wheel and rail wear associated with curve negotiation while maintaining adequate dynamic stability to avoid hunting and adequate suspension capability to accomodate forces developed due to rail irregularities.

The evaluation of various types of conventional, self steering radial and forced steering trucks represents a tradeoff between a potential for performance improvement and increased truck complexity. The selection of an appropriate type of truck for a specific urban system depends strongly on the system route characteristics--particularly, the prevalence and distribution of small radius curves. For example in systems with few small radius curves conventional truck suspensions may provide a good compromise between performance and truck design complexity, while for older systems with many small radius curves, self-steering or forced-steering trucks may prove to provide the best overall performance. To facilitate the evaluation of truck design by urban rail operating authorities, analytical evaluation methods, design data and field test data are required. This study is directed to providing analytical performance data and evaluation methods for conventional and advanced urban rail truck designs.

1.2 Study Objectives and Scope

A principal objective of this study is to develop performance data for evaluating the stability and curving performance of conventional, self-steering radial and forced steering trucks designed for urban rail systems. The analytical basis for the study has been provided by developing a generic truck model which directly reduces to conventional, self-steering radial and forced steering truck designs. Thus, a consistent and common basis is provided for evaluation of the various truck designs.

The model has been incorporated into a linear stability program which allows computation of the truck critical speed at which sustained hunting occurs and computation of the damping ratios associated with truck modes of oscillation.

The model has also been incorporated into a nonlinear steady-state curving program which computes wheelset, truck and carbody angles of attack and wheel/rail as well as suspension forces for negotiation of a constant radius curve at constant speed with a given superelevation. The effects of multiple point wheel/rail contact which occur in flanging conditions for certain wheel/rail geometries are included directly in the computations. An indication of wheel/rail wear has been computed based upon the work performed at the wheel/rail interface.

While the forces predicted with the curving analysis have not been directly compared with experimental data, the basic trends predicted by the model are consistent with the limited experimental data available in the literature.

The influence of truck primary suspension longitudinal stiffness, wheel profile and curve radius reported for tests conducted at WMATA* [1, 2]** on conventional trucks correspond directly with the effects predicted in this study. Specifically, the observations from the WMATA tests that lateral curving forces are reduced as conventional truck primary longitudinal stiffness is reduced, and as single point contact wheel profiles are employed correspond directly with the results described in detail in this study.

An extensive parameter study has been conducted to determine the influence of suspension and wheel profile design parameters on stability and curving performance of conventional, self-steering radial and forced-steering truck

*Washington Metropolitan Area Transit Authority.

**Bracketed number indicates reference list at the end of this report.

designs. These performance studies have provided tradeoff data necessary to identify truck designs for a given critical speed which result in reduced wear for a given radius curve.

As a part of the study a preliminary evaluation has been performed to determine the influence of radial and lateral misalignment in truck lead and trailing axles on curving forces and resultant wear. Axle misalignment, which may result from construction practice or as the truck is operated, may lead to significant increases in work required to negotiate a section of curved or tangent track.

This study has focused on assessment of the linear critical speed and the steady-state curving wear index. These are considered to be prime performance indicators for urban trucks and provide meaningful design information. Additional evaluations of curve entry and exit capability, of dynamic behavior after the onset of hunting, and of the capability to accommodate track irregularities are necessary in a more complete evaluation of truck performance. The development of a nonlinear, dynamic curving model is planned as a subsequent task to the research reported in this document to address these issues.

CHAPTER 2

STUDY METHODOLOGY

This chapter describes the performance criteria and the computational models used to investigate the dynamic performance of conventional and innovative transit trucks.

2.1 Performance Criteria

A primary motivation for considering innovative self and forced steered radial trucks is the potential for reduced wheel/rail wear and forces. Analytic studies [3] have indicated that reduced wear is the result of a more radial orientation of the axles during curve negotiation through self or forced steering. In general, improved curving performance is achieved at the expense of decreased lateral stability. This report establishes the relationship between curve negotiation capability and maximum operating speed capability.

2.1.1 Lateral Stability

Analytical and experimental studies have shown that rail vehicles have a tendency to "hunt" above a speed called the "critical speed". This instability is in general a coupled lateral and yaw motion involving the wheelsets, truck frames and possibly the carbody. Once the onset of hunting begins, nonlinearities such as creep force saturation and flange contact generally limit the amplitude of the oscillation.

In this report, the linear critical speed is selected as the stability performance index. This speed is calculated by computing the eigenvalues of a linear model as a function of the vehicle speed. Since wheel/rail creep forces decrease with increasing speed (for small creepages) as speed increases a limiting speed is reached where one of the modes of the vehicle vibration attains zero damping. The speed at which this occurs is called the linear critical speed. Vehicle designs should achieve a critical speed significantly greater than the vehicle operating speed. While the critical speed serves as a good "single number" indicator of vehicle stability, the performance of a vehicle near, or above, the critical speed is of interest and should be evaluated using a nonlinear vehicle model to assess wheel climb in the region near the critical speed. This type of evaluation for prototype vehicles considered in this study is recommended as a future task.

2.1.2 Curve Negotiation

Several performance indices have been developed to represent the ability of a rail vehicle to negotiate a curve. A number of simultaneous objectives can be identified, such as perfect steering, prevention of derailment, minimum wheel/rail forces, and minimum wheel/rail wear.

Optimal curve negotiation, or perfect steering, is achieved if each wheelset in a vehicle adopts a radial position and displaces laterally so that it rolls without slip around the curve. As such, the wheelset lateral excursion and the wheelset angle of attack or radial misalignment are natural performance indices. The lateral excursion is usually measured from the track centerline or from the pure rolling line. The wheelset angle of attack is the yaw angle of the wheelset with respect to radial alignment. In this report, y_w denotes the wheelset lateral excursion with respect to the track centerline and ψ_w represents the wheelset angle of attack. These displacements are defined in Figure 2.1. An undesirable situation exists when these indices reach large magnitudes.

The derailing tendencies of a vehicle are associated with the ratio of lateral flange force to vertical wheel load. When this ratio exceeds a

PLAN VIEW

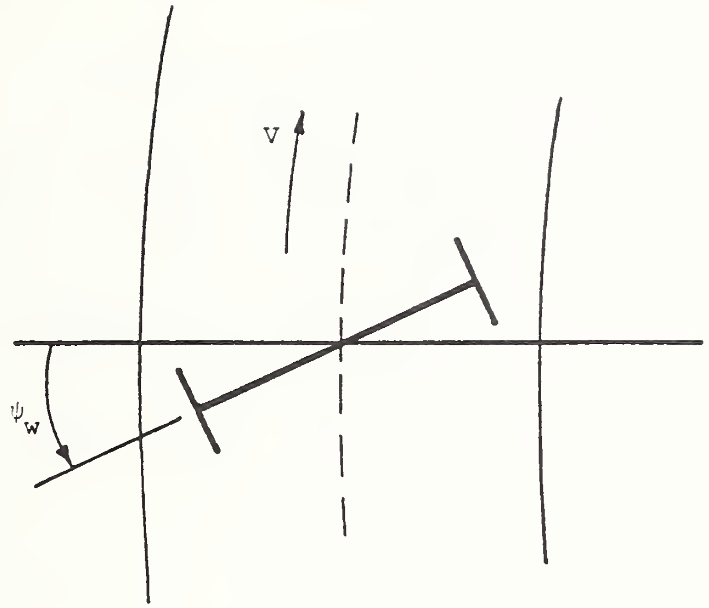

a) Angle of Attack

PLAN VIEW

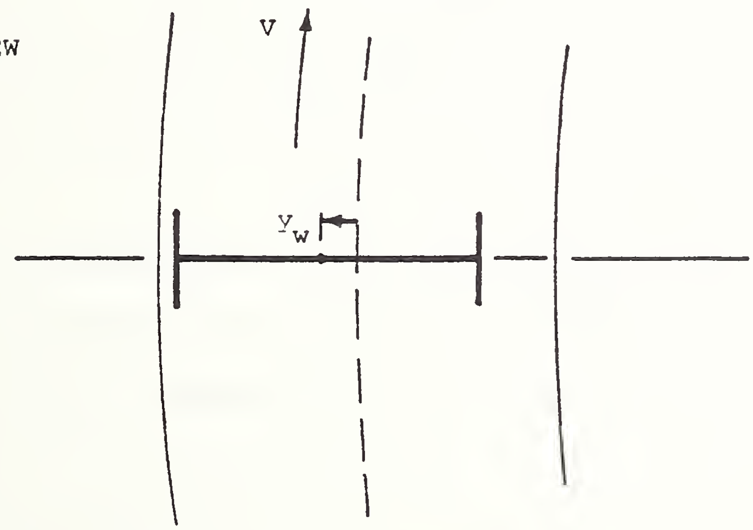

b) Lateral Wheelset Excursion

Figure 2.1 Definition of Angle of Attack and Lateral Wheelset Excursion critical value, a situation conducive to a flange-climbing type derailment occurs [4, 5].

Several wear indices have been proposed to predict wear rates at the wheel/rail interface. Due to the complex nature of modeling wear, these indices are intended to indicate relative levels of wear for use in performance comparisons, rather than to attempt accurate predictions of actual wear levels. A list of proposed wear indices appears in Table 2.1. The wheelset angle of attack, ψ_w, the creepages (or normalized rates of slippage), ξ_i, and the lateral flange force (for a flanging wheel), F_f, are related to the wear rate [6, 7]. The effect of increased ψ_w, ξ_i, and/or F_f is to increase wear at the wheel/rail contact zone.

Heumann proposed using the product of flange force and angle of attack, $F_f\psi_w$ as a wear index [3]. This flange wear index as well as Marcotte's two-point contact flange wear index [3] are related to the energy dissipated through Coulomb friction between the wheel flange and the rail. As a measure of wheel tread and top of rail head wear, Doyle introduced a tread wear index, defined as the product of the vertical wheel load and the resultant total creepage, $V_i\xi_R$ [8].

A wear index designed to be a more complete measure of the work expended at the wheel/rail contact interface has been recommended by British Rail [9]. Their index is the work done in the contact patch, defined as the dot product of the resultant creep force and resultant creep vectors. When summed over all contact patches, this index represents the additional work per unit distance along the track required to pull the vehicle through the curve in steady-state conditions. This index has units of work per distance, or force.

No comprehensive verification of the proposed wear indices has been conducted. Limited tests by British Rail and I.I.T. have shown potentially

Table 2.1 Proposed Wear Indices*

WEAR INDEX		UNITS	SOURCE
ψ_w	Angle of Attack	(rad)	[6, 7]
ξ_i	Creepage	(-)	
F_f	Flange Force	(lb)	
$F_f\psi_w$	Flange Wear Index	(lb)	[3]
$\mu_f F_f$	$\sqrt{(\Delta_z/r_{LT})^2+(\psi_w \tan\delta_{LF})^2}$ Two-point Flange Wear Index	(lb)	[3]
$V_i\xi_R$	Tread Wear Index	(lb)	[8]
$W_1=\underline{F}_c \cdot \underline{\xi}$	Contact Patch Work	(ft-lb/ft)	[9]
$W_2 = \frac{W_1}{\pi a_e b_e}$	Contact Patch Work/Area	(lb/ft^2)	[10]

*Variables in Table 2.1 are defined in the nomenclature.

useful trends [10, 11]. Dry wear laboratory tests by British Rail [12] have suggested that the wear rate can be expressed in terms of creep force, creepage, and Hertzian contact area. Wide-scale experimental validation of wear models needs to be undertaken to identify which indices can be related directly with wear.

In this report, the forces and creepages at the wheel/rail interface are computed so that most of the indices listed in Table 2.1 can be predicted. Typically, flange contact occurs at the leading outer wheel as a vehicle negotiates a curve. Both wheel and track deterioration are due to the significant wear which occurs at the flanging wheel. In particular, it is the leading outer wheel which is responsible for the vast majority of the wear that takes place on the gage face of the high rail and on the wheel flange [13]. In the curving studies, the contact patch work at the flanging wheel (W_1) is used as the curve negotiation performance index.

2.2 Truck Configurations

This section describes the conventional and innovative truck configurations whose performance is investigated. All of the physical configurations discussed in Section 2.2.1 through 2.2.3 represent special cases of the generic model presented in Section 2.2.4.

2.2.1 Conventional Truck

A conventional truck as illustrated in Figure 2.2 has a primary suspension between the axle and truck frame. The primary suspension is typically made up of coiled springs, rubber chevrons or rubber bushings between the bearing adapter and the truck frame. In Figure 2.2 k_{px} is the primary longitudinal stiffness, k_{py} is the primary lateral stiffness, $2d_p$ is the distance between the longitudinal springs and 2b is the truck wheelbase.

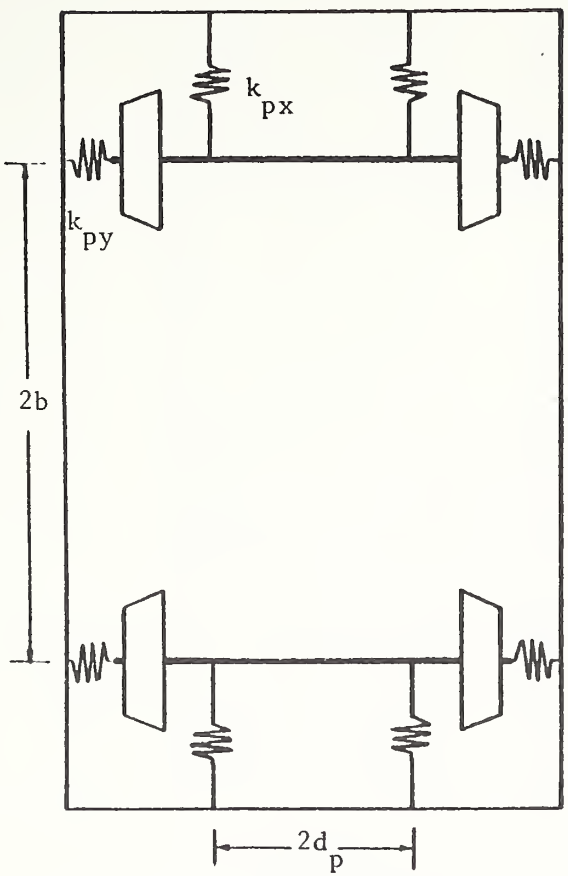

Figure 2.2 Schematic of Conventional Truck

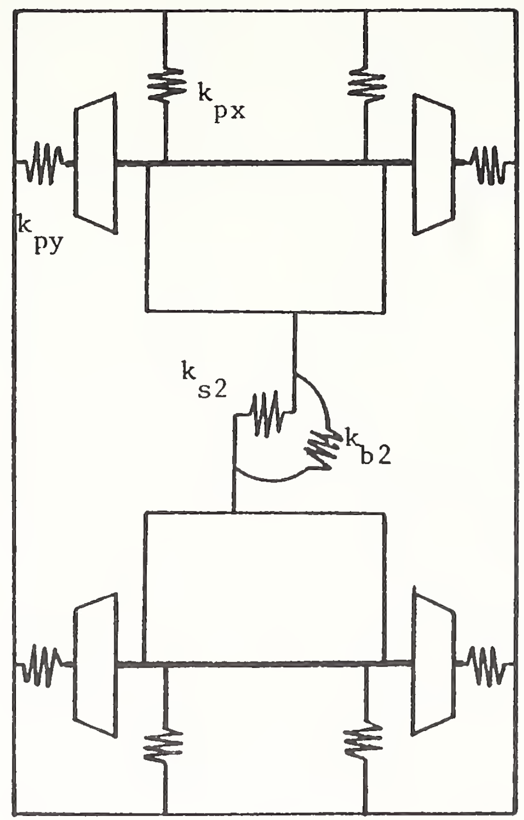

Figure 2.3 Schematic of Self-Steering Radial Truck

2.2.2 Self-Steering Radial Truck

A self-steering radial truck is a conventional truck with an additional direct connection between the two wheelsets by means of passive springs or structural members in shear and bending. A schematic representation of a self steering truck is shown in Figure 2.3. Figure 2.4 illustrates two physical implementations; a cross braced truck is shown in Figure 2.4a and a steering arm truck in Figure 2.4b.

A self steering truck has two additional stiffness parameters which connect the two wheelsets directly as shown in Figure 2.3. These are defined as the direct interaxle bending stiffness, k_{b2}, and the direct interaxle shear stiffness, k_{s2}. The stiffnesses k_{b2} and k_{s2} are sufficient to model any direct elastic connection between the two wheelsets. Most often this connection takes the form of steering arms [14], cross braces [15], or similar linkages. The term self-steering radial truck describes the steering action produced by direct interwheelset connections when the stiffness k_{b2} is low, i.e., a yaw motion of one wheelset causes the other wheelset to yaw in the opposite direction tending to cause the wheelsets to align radially in a curve.

The basic concept of the radial truck is to directly interconnect the wheelsets by means of steering arms with transverse (shear) and bending stiffnesses at their junction. The shear spring can increase the total shear stiffness of the self-steering truck above the value achievable by a conventional truck, thus providing the possibility for better stability and/or curving performance.

Reference [16] points out that the self-steering radial design has two essential differences from the conventional design: 1) forces are transmitted

(a) Cross-Braced

(b) Steering Arm

Figure 2.4 Alternative Self-Steering Truck Configurations.

directly between the wheelsets, and 2) the total truck shear stiffness is not limited as it is in the conventional design. The first property allows the truck frame to be dynamically decoupled from the hunting wheelsets [16]. This results in an increase in critical speed for equivalent truck shear and bending stiffnesses. The second property allows the truck to achieve reduced lateral flange forces and angle-of-attack on curves after flanging has occurred.

The dynamics of a flexible truck are strongly affected by the inter-wheelset forces either through the truck frame as in the case of the conventional truck or through the interconnection elements as in the case of the self steering radial truck. It is convenient to use a generalized set of stiffnesses suggested by Wickens [17]. These are the total truck static shear and bending stiffness, defined in Figure 2.5 as:

Shear Stiffness:

$$k_s = \left. \frac{\text{lateral force on leading wheelset due to lateral displacement of trailing wheelset}}{\text{lateral displacement of trailing wheelset}} \right|_{\Delta\psi = 0}$$

Bending Stiffness:

$$k_b = \left. \frac{\text{yaw moment on leading wheelset due to yaw displacement of trailing wheelset}}{\text{yaw displacement of trailing wheelset}} \right|_{\Delta y = 0}$$

For a free truck (not connected to a carbody) with two wheelsets, the expressions for k_b and k_s are

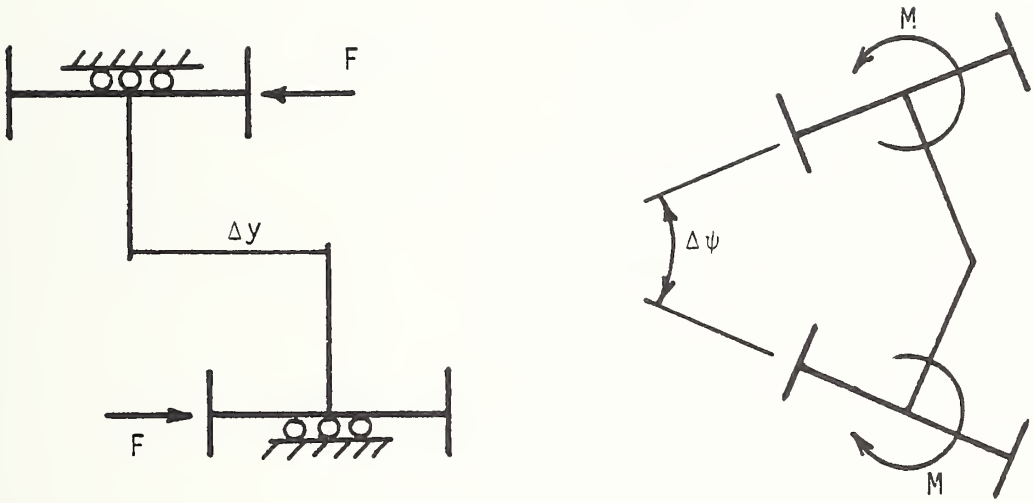

$$k_s = \frac{F}{\Delta y}$$

Shear Stiffness

$$k_b = \frac{M}{\Delta \psi}$$

Bending Stiffness

Figure 2.5 Shear and Bending Stiffness Definitions

Conventional Truck:

$$k_b = d_p^2 \, k_{px} \qquad (2\text{-}1)$$

$$k_s = \frac{d_p^2 \, k_{px} k_{py}}{d_p^2 \, k_{px} + b^2 \, k_{py}} \qquad (2\text{-}2)$$

Self-Steering Radial Truck:

$$k_b = d_p^2 \, k_{px} + k_{b2} \qquad (2\text{-}3)$$

$$k_s = \frac{d_p^2 \, k_{px} k_{py}}{d_p^2 \, k_{px} + b^2 \, k_{py}} + k_{s2} \qquad (2\text{-}4)$$

These stiffnesses are useful in identifying the design region of different types of trucks in the $k_s - k_b$ plane. Equations (2-1) and (2-2) imply that conventional trucks have to satisfy the relation $k_s < \frac{k_b}{b^2}$ in the limit as primary lateral stiffness is increased to infinity. With this limitation conventional truck designs have to lie below the line $k_s = \frac{k_b}{b^2}$ on the $k_s - k_b$ plane, shown in Figure 2.6. The self-steering designs can be anywhere in the $k_s - k_b$ plane by virtue of the interaxle bending and shear stiffnesses.

One drawback of the $k_s - k_b$ plane is that a particular design point in the plane can be obtained with different combinations of primary and inter-axle stiffnesses yielding different stability characteristics. The stability properties are not unique due to differences in the distribution of truck frame mass (i.e., truck frame inertia) which affects the kinematic modes of the truck. Since the location of the truck frame vibrational natural frequencies with respect to the truck kinematic frequency determines the

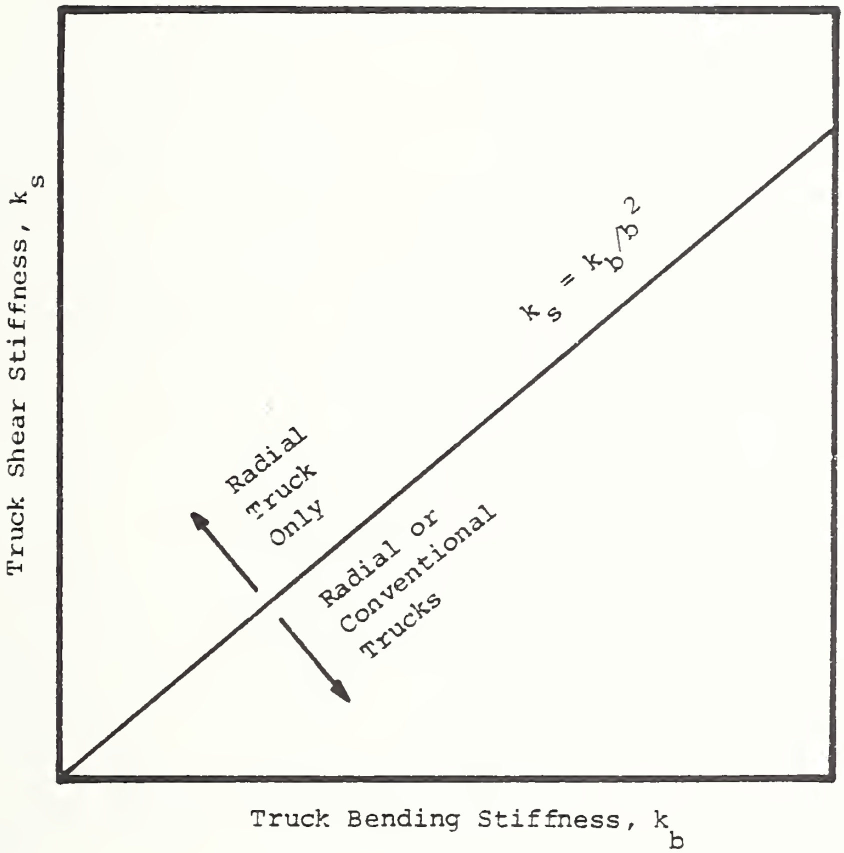

Figure 2.6 Design Region for Conventional and Radial Trucks in the Truck Shear vs. Truck Bending Stiffness Plane.

stability behavior [16], the k_s - k_b designation does not uniquely define the stability characteristics of a truck.

2.2.3 Forced-Steering Radial Truck

A "forced-steering truck" utilizes linkages between the carbody and the truck frame to force the axles into near radial alignment when traversing curves. The essential motivation behind forced steering is to make use of the relative truck/carbody orientation that develops as a vehicle negotiates a curve. In particular, the steady-state yaw angle that develops between the carbody and the truck is related to the curve radius, and linkages between the carbody and the wheelsets can be used to force the wheelsets into a more radial alignment. Similarly the lateral displacement between the carbody and truck is related to cant deficiency, and linkages can be designed to produce forces on the wheelsets as a function of the cant deficiency. Thus what distinguishes a forced-steering truck from the conventional and self-steering radial trucks is the presence of forces on the axles which are a function of the relative yaw and lateral displacement between the carbody and truck.

Several forced-steering truck configurations have been proposed with different linkage arrangements. The schematics of three configurations that have forced-steering action are shown in Figure 2.7. In this study they are designated the S, L and U trucks because configurationally they are similar to the Scales [18], List [14] and UTDC* [19] designs, respectively.

The bending and shear stiffnesses due to forced-steering linkages are equivalent to "effective" truck interaxle bending and shear stiffnesses,

---

*Urban Transportation Development Corporation Ltd., Ontario, Canada

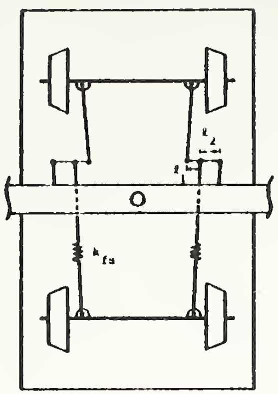

Outboard Axle

Inboard Axle

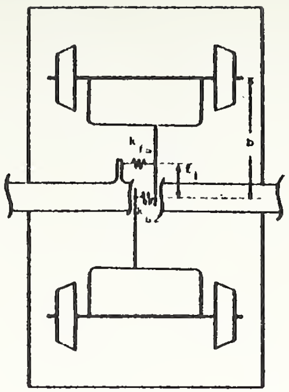

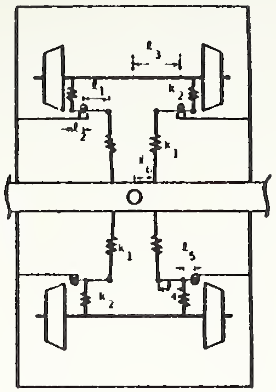

S Prototype

$$\Delta\psi = \pm 2G\left(\frac{\psi_1+\psi_2}{2} - \psi_c\right)$$

$$G = \frac{\ell_1}{\ell_1 + 2\ell_2}$$

$$k_{b2} = \frac{1}{2} d^2 k_{fs}\left(1 + \frac{\ell_2}{\ell_1 + \ell_2}\right)^2$$

(a)

L Prototype

$$\Delta\psi = \pm 2G\left(\frac{y_1-y_2}{2b} - \psi_c\right)$$

$$+2\left(\frac{G+1}{b}\right)\left(\frac{y_1+y_2}{2} - y_T\right)$$

$$G = \frac{\ell_1}{b-\ell_1}$$

$$k_{b2} = \frac{(b-\ell_1)^2 k_{fs} k_{py}}{(4k_{py}+k_{fs})}\ ^*$$

(b)

* Assumes stiff k_{s2} for symmetry.

U Prototype

$$\Delta\psi = \pm 2G(\psi_T - \psi_c)$$

$$G = \frac{\ell_6}{\ell_R \ell_3}$$

$$k_{b3} = \frac{k_1 k_2 \ell_3^2 \ell_R^2}{(\ell_R^2 k_1 + k_2)}$$

$$\ell_R = \begin{cases} \dfrac{\ell_1}{\ell_2} & \text{(Outboard Axle)} \\ \dfrac{\ell_4+\ell_5}{\ell_5} & \text{(Inboard Axle)} \end{cases}$$

(c)

Note: The primary suspension system is not shown in the diagram.

Figure 2.7 Schematic Diagram of Three Forced-Steering Truck Prototypes with Curvature Steering Action.

respectively. Typically, the L type truck has a high value of effective interaxle shear stiffness while the U type truck has zero interaxle shear stiffness. The S truck has properties similar to the three piece freight truck because of the high interaxle bending stiffness but relatively low interaxle shear stiffness. Expressions for the steering gain and effective interaxle bending stiffness in terms of linkage stiffness for each prototype are shown in Figure 2.7 with detailed derivations included in Appendix A.

The actuation of the forced-steering linkages can be represented as a geometric offset in series with a linkage bending and/or shear stiffness. The geometric offsets Δy and $\Delta\psi$ as well as the linkage stiffnesses are shown schematically in Figure 2.8. The forced-steering forces and moments are:

$$\Delta F = k_{s2}\,\Delta y \tag{2-5}$$

$$\Delta M = k_{b2}\,\Delta\psi \tag{2-6}$$

The geometric offsets Δy and $\Delta\psi$ are controlled by the linkage design and can differ in alternative truck designs. In general, though, they are related to the relative lateral and yaw displacements between the truck and carbody, i.e.,

$$\Delta y = 2H(y_T - y_c) \tag{2-7}$$

$$\Delta\psi = \pm 2G(\psi_T - \psi_c) \tag{2-8}$$

The plus and minus sign in equation (2-8) indicates that a counter-clockwise moment acts on the front truck and a clockwise moment acts on the rear truck.* It has been shown in [20] that ΔF can be utilized to control cant deficiency loads while ΔM can be utilized to compensate for track curvature effects. Thus H is called the cant deficiency steering gain and G is called the curvature steering gain.

---

*These directions are shown in Figure 4.10 for secondary yaw moment.

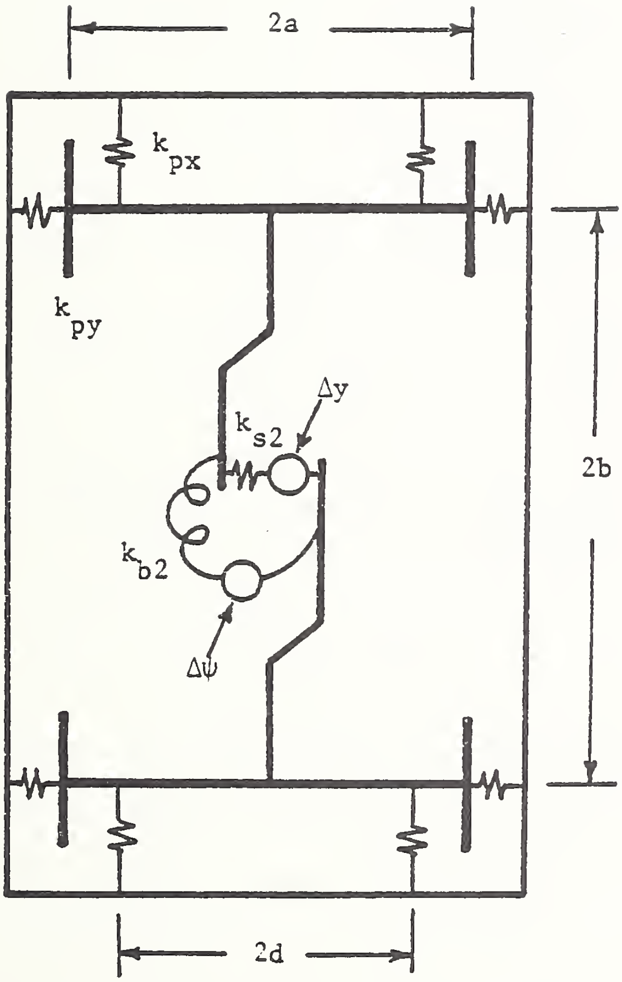

Figure 2.8 Forced-Steering Schematic

The curvature steering gain G and cant deficiency steering gain H in the steering laws are kinematically related to the physical dimensions of the steering linkages, while the interaxle bending stiffness k_{b2} is related to the stiffness of the linkages. Figure 2.9 illustrates a possible forced steering configuration that utilizes a cant deficiency steering law.

The curving performance of a forced-steered truck is a function of the steering gain, G. The numerical value of the gain (and hence the linkage dimensions) can be designed such that kinematically (i.e., with the assumption of rigid steering linkages and no flange forces) the wheelsets track the pure rolling line,* the track centerline or any line parallel to the track centerline. Theoretically, the gain which makes the wheelsets track the pure rolling line - the pure rolling line gain $G_{pr\ell}$ - provides perfect radial (i.e., neutral) steering of the wheelsets, whereas the gain to track the centerline - the centerline gain $G_{c\ell}$ - results in oversteering.

The steering gain which results in both wheelsets tracking the pure rolling line is derived in [21] to be:**

$$G_{pr\ell} = \frac{b}{\ell_s} \tag{2-9}$$

where ℓ_s is half the distance between truck centers. The above kinematic result assumes no flange forces, balanced running (no cant deficiency), and small secondary yaw and primary longitudinal stiffnesses. With the same assumptions plus the assumption of stiff interaxle shear stiffness, the steering gain which causes both wheelsets to track the centerline is also

---

*The lateral displacement that produces pure kinematic rolling of a single wheelset.

**The derivation is repeated in Appendix B.

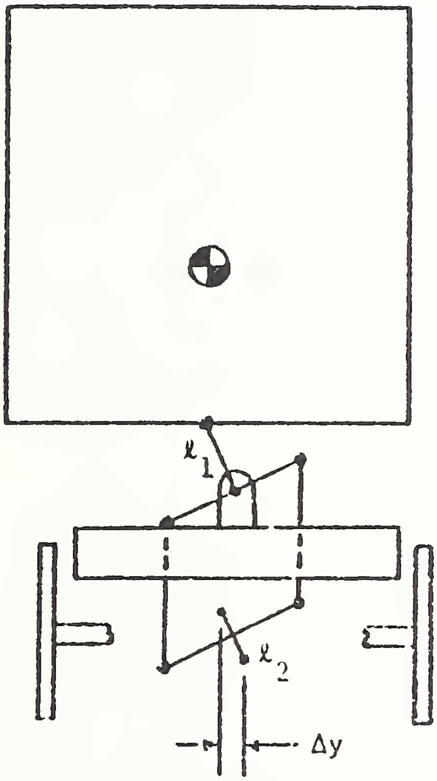

$$\Delta y = 2H\left(\frac{y_1+y_2}{2} - y_c\right)$$

$$H = \frac{\ell_2}{\ell_1}$$

Figure 2.9 Schematic Diagram of a Forced-Steering Truck Model with Cant Deficiency Steering Action derived in [21] to be:*

$$G_{c\ell} = \frac{b}{\ell_s} \left(1 + \frac{f_{33}}{f_{11}} \frac{a^2}{b^2}\right), \qquad (2\text{-}10)$$

and the cant deficiency gain for equal wheelset excursion is:

$$H = \frac{b\, k_{sy}}{2 f_{11}} \qquad (2\text{-}11)$$

In general, the pure rolling line gain is appropriate before flange contact occurs since it correctly aligns the wheelsets radially. However, when flange contact occurs the assumptions implicit in the derivation of the pure rolling line gain are not satisfied and as a result $G_{pr\ell}$ may not align the wheelsets appropriately. Other gains may have relative advantages. The pure rolling line gain is typically used in practice in prototype vehicles [24].

2.2.4 Generic Truck Model

A generic truck model that represents the different forced-steering truck prototypes as well as the conventional and self-steering radial trucks is shown in Figure 2.10. The effect of the linkages between the carbody, the truck and the wheelsets is to generate the geometric offsets $\Delta\psi_1$, $\Delta\psi_2$, Δy_1, and Δy_2, according to the following steering laws:

$$\Delta\psi_1 = \Delta\psi_2 = \pm 2G_1 \left[\frac{\psi_1 + \psi_2}{2} - \psi_c\right] \pm 2G_2 \left[\frac{y_1 - y_2}{2b} - \psi_c\right] + 2G_3 \left[\frac{y_1 + y_2}{2} - y_T\right]$$

$$\pm 2G_4 \left[\psi_T - \psi_c\right] \pm 2G_5 \left[\frac{\psi_1 + \psi_2}{2} - \psi_T\right] \pm 2G_6 \left[\frac{y_1 - y_2}{2b} - \psi_T\right] \qquad (2\text{-}12)$$

---

*f_{33} and f_{11} are the longitudinal and lateral creep coefficients, respectively.

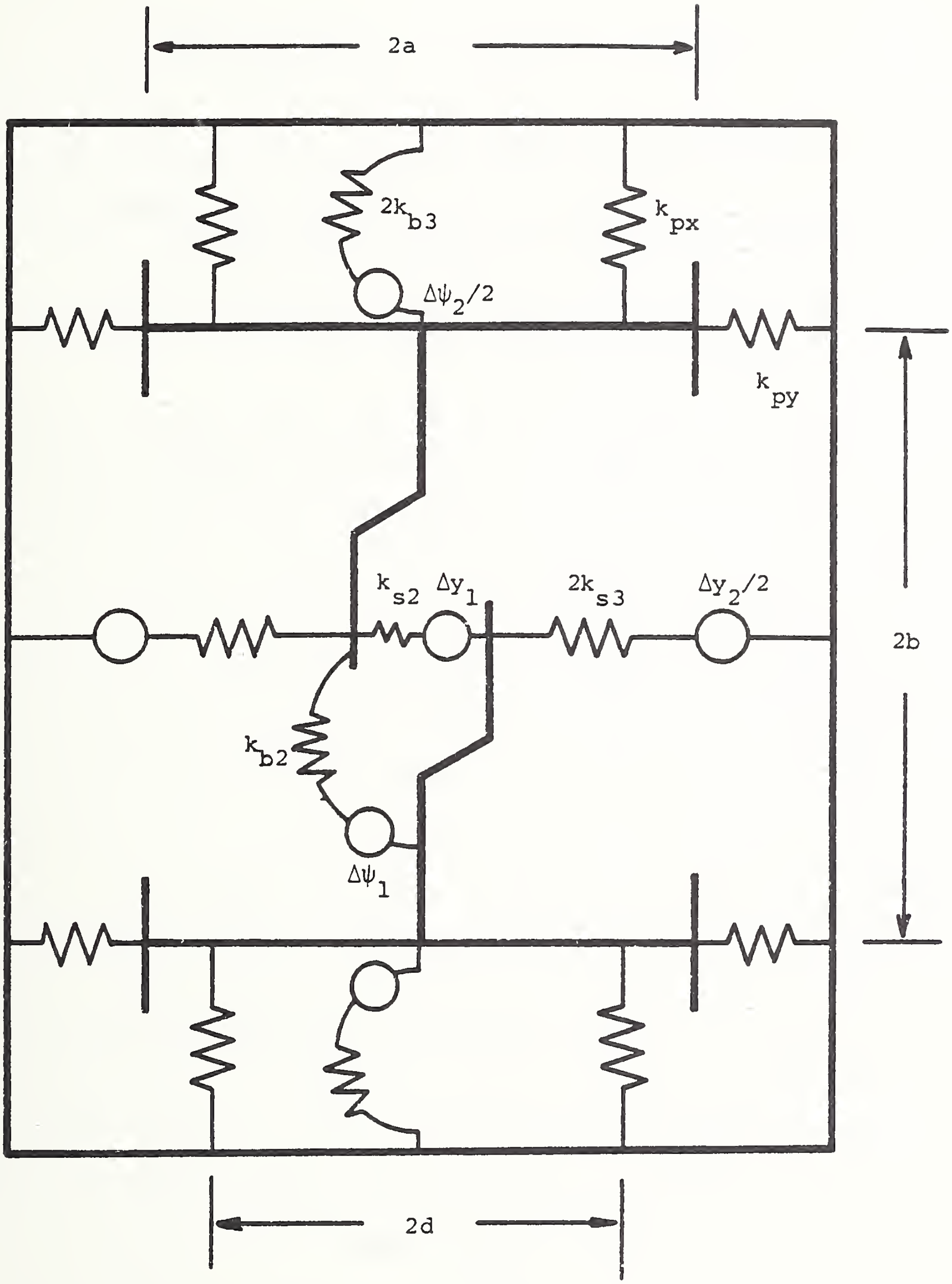

Figure 2.10 Generic Forced-Steering Truck Model

$$\Delta y_1 = \Delta y_2 = 2H_1[\frac{y_1+y_2}{2} - y_c] + 2H_2[y_T - y_c] + 2H_3[\frac{y_1+y_2}{2} - y_T] \quad (2\text{-}13)$$

where the G's and H's are the steering gains.

> y_1, y_2 are the lateral displacements of the leading and trailing wheelsets of the truck, respectively.
>
> ψ_1, ψ_2 are the yaw angles of the leading and trailing wheelsets, respectively.

The steering laws are relatively general. They represent a linear combination of the differences in yaw displacement between the wheelset pair, the truck and the carbody, and the differences in the lateral displacement between the wheelset pair and the truck to sense track curvature and activate $\Delta\psi_1$ and $\Delta\psi_2$. Similarly, a linear combination of the differences in the lateral displacement between the wheelset pair, the truck and the carbody is used to sense cant deficiency and actuate Δy_1 and Δy_2.

The term forced-steering usually implies direct carbody connections to the wheelsets to steer the wheelsets into radial alignment. For the sake of generality and to represent physically realizable trucks, terms that represent wheelset-truck interconnections have been included in the steering laws. These are the terms with the G_3, G_5 and G_6 gains in equation (2-12), and the term with the H_3 gain in equation (2-13). For most practical parameter values, however, the contributions of these terms to the geometric offset $\Delta\psi$ or Δy are negligible as shown below:

- stiff k_{py} implies $y_T \simeq \frac{y_1+y_2}{2}$ $\longrightarrow$ $2G_3(\frac{y_1+y_2}{2} - y_T)$ is negligible

  $\longrightarrow$ $2H_3(\frac{y_1+y_2}{2} - y_T)$ is negligible
- stiff k_{px} implies $\psi_T \simeq \frac{\psi_1+\psi_2}{2}$ $\longrightarrow$ $2G_5(\frac{\psi_1+\psi_2}{2} - \psi_T)$ is negligible

- stiff k_{py} also implies $\psi_T \simeq \frac{y_1-y_2}{2b} \longrightarrow 2G_6(\frac{y_1-y_2}{2b} - \psi_T)$ is negligible

The offsets $\Delta\psi_1$ and $\Delta\psi_2$ are positive in the direction of positive $\psi_1-\psi_2$; Δy_1 and Δy_2 are positive in the direction of positive $b(\psi_1+\psi_2)-(y_1-y_2)$. The differences in yaw displacement between the wheelset pair, the truck and the carbody have an opposite effect on the rear truck than on the front truck because the two trucks yaw in opposite directions in curves. This action is illustrated by the sign change in equation (2-12). The notation used is such that whenever two signs appear in front of a term, the sign at the top is associated with the front truck and the one at the bottom is for the rear truck. When a term has only one sign, the same expression is used for both trucks.

The generic truck model is reduced to particular truck configurations by assigning appropriate stiffnesses and steering gain values, as given in Table 2.2.

Table 2.2 Generic Truck Simplifications

TRUCK TYPE*	k_{b2}	k_{b3}	k_{s2}	G_1	G_2	G_3	G_4
Conventional	0	0	0	0	0	0	0
Self Steering	k_{b2}	0	k_{s2}	0	0	0	0
S Prototype	k_{b2}	0	0	G	0	0	0
L Prototype	k_{b2}	0	k_{s2}	0	G	$\frac{G+1}{b}$	0
U Prototype	0	k_{b3}	0	0	0	0	G

*For these trucks $G_5, G_6, H_1, H_2, H_3, k_{s3} = 0$.

2.3 Stability Model

In Section 2.1.1 a quantitative stability performance index was defined as the lowest forward speed of the vehicle which yields a vehicle dynamic mode with zero damping. This section discusses two linear models which have been used in the parametric studies. The first is a six degree of freedom truck model which treats the carbody as an inertial reference and the second is a 15 degree of freedom full carbody model.

A complete description as well as a listing of the equations of motion for the 6 DOF model are presented in Appendix C. This model was used to compute most of the stability information presented in this report.

In order to be confident that a single truck model was sufficiently accurate the results were ocassionally compared to a 15 DOF full carbody model. The complete description and equations of motion for this model are presented in Appendix E. In general the 6 DOF model proved sufficiently accurate to justify its use.

2.3.1 Numerical Methods

The condition of lateral instability or hunting has traditionally been described in terms of the forward speed or critical speed at which the damping in the least damped eigenvalues equals zero. The vehicle oscillates at the critical speed and is unstable at higher speeds.

The solution technique for calculating the critical speed consists of selecting a speed, calculating the system eigenvalues at that speed and adjusting the speed appropriately for the next iteration until the damping in the least damped eigenvalue is approximately zero.

To calculate the system eigenvalues, the six or 15 second order differential equations of motion (corresponding to the 6 or 15 DOF models.

respectively) are written in matrix form as:

$$\underline{\bar{M}}\,\ddot{\underline{y}} + [\underline{\bar{C}}_s + \underline{\bar{C}}_r + \underline{\bar{C}}_{fs}]\dot{\underline{y}} + [\underline{\bar{K}}_s + \underline{\bar{K}}_r + \underline{\bar{K}}_{fs}]\underline{y} = 0 \qquad (2\text{-}14)$$

where $\underline{y}$ is a 6x1 or 15x1 vector of position degrees of freedom

$\underline{\bar{M}}$ is the inertia matrix

$\underline{\bar{K}}_s$ and $\underline{\bar{C}}_s$ are the suspension stiffness and damping matrices, respectively

$\underline{\bar{K}}_r$ and $\underline{\bar{C}}_r$ are the stiffness and damping matrices resulting from the wheel/rail interaction

($\underline{\bar{K}}_s$, $\underline{\bar{C}}_s$, $\underline{\bar{K}}_r$ and $\underline{\bar{C}}_r$ all correspond to a conventional rail vehicle).

$\underline{\bar{K}}_{fs}$ and $\underline{\bar{C}}_{fs}$ are the stiffness and damping matrices, respectively, due to the interaxle and forced steering linkages.

Two computer programs have been developed for this study; program GEN6 calculates the critical speed of the 6 DOF generic truck model and program GEN15 of the 15 DOF full vehicle model. These programs also calculate the eigenvectors to determine the modes of motion at a certain speed.

2.4 Steady-State Curving Model

As discussed in Section 2.1.2 the primary curving performance index used in this report is the work done at the flanging wheel.

Appendix F presents the equilibrium equations for a single wheelset negotiating a constant radius curve while Appendix H shows the development of the full vehicle steady-state curving equations. The model is fully nonlinear and includes:

- single or two point wheel/rail contact
- nonlinear wheel/rail geometry including large contact angles
- nonlinear primary and secondary suspension characteristics
- laterally flexible rails

* nonlinear wheel/rail friction characteristics

Figure 2.11 is a flow chart of the steady-state curving program SSCURV. The nonlinear algebraic equations are solved by subroutine SROOTS which has proved to be a very robust equation solver. The details of SROOTS are given in Appendix H. Subroutine WHLST1 solves for wheelset equilibrium assuming single-point contact at both wheels, while subroutine WHLST2 solves for wheelset equilibrium under the assumption that the flanging wheel is in two-point tread-flange contact and the inner wheel is in single-point tread contact. The program computes:

* wheel/rail forces
* axle angles of attack
* wheel and axle L/V ratios
* work done at all wheel/rail contact points

2.5 Baseline Rail and Vehicle Parameters

The analytic models described in this chapter are generally capable of representing vehicles with arbitrary wheelset-truck-carbody interconnections. As a result, the models can be used to study conventional, self-steered, and forced-steered radial truck designs. The reduction of the generic truck model to conventional, self-steered, and three proposed forced-steered truck configurations is shown in Table 2.2. The forced-steered truck studies in this report are based primarily on the "L" design. This design was selected as one which has potential for application to transit systems and has the inherent features in terms of capability to parametrically establish values of overall shear and bending stiffnesses and the steering gains which are the most important design parameters for forced-steered truck curving performance. The detailed study parametric results are illustrative of forced-steered truck

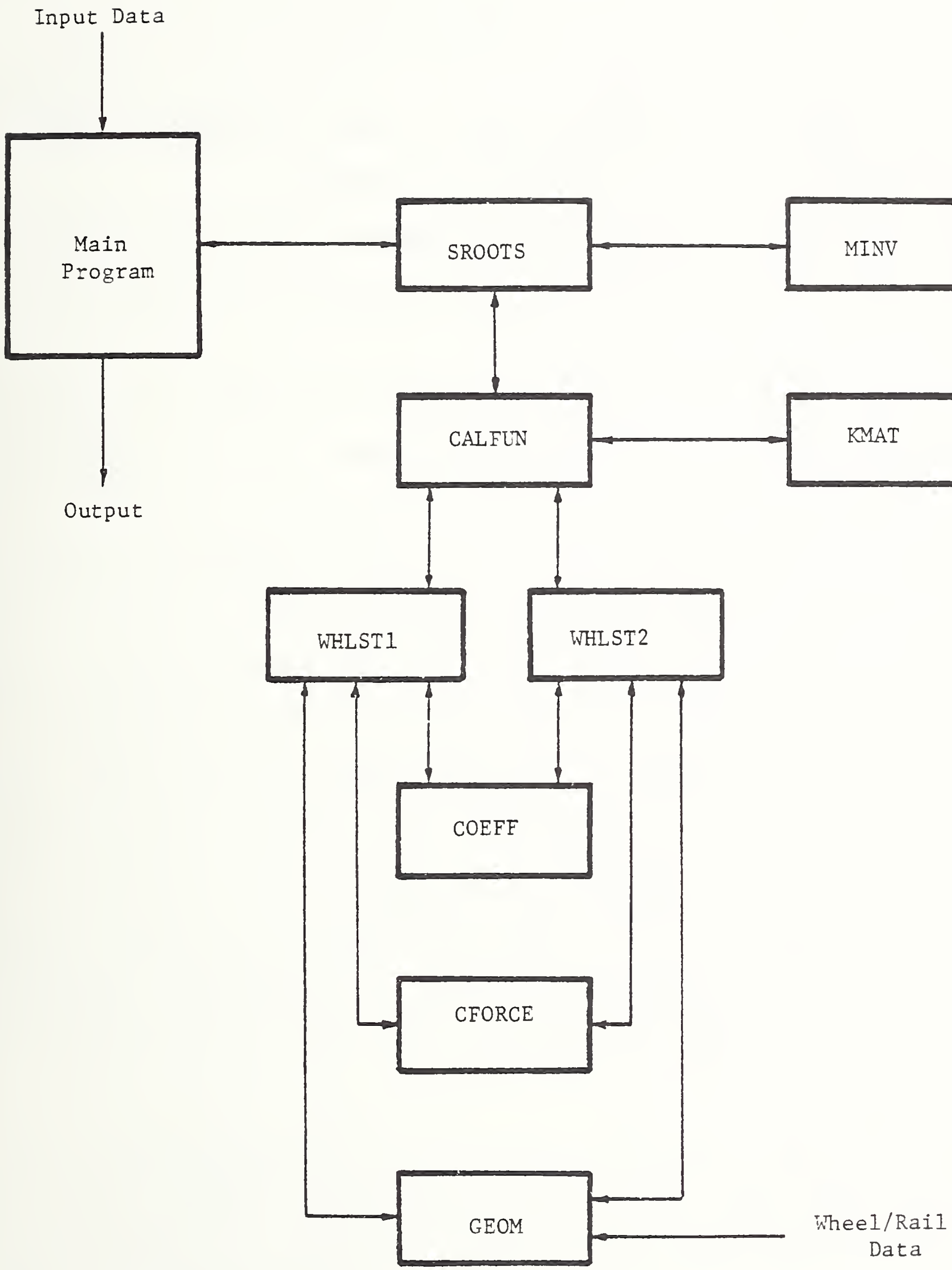

Figure 2.11 Steady-State Curving Program SSCURV Flow Chart

design performance in general. However, there may be relative performance (and detailed design) benefits of specific configurations of forced-steered truck designs not studied in this report. Detailed studies of alternate configurations represent an area of future research.

The baseline rail/vehicle parameters used in this study are listed in Table 2.3. They were selected to represent typical conventional and steered urban transit vehicles.

Two wheel/rail profiles were selected for this study: a new wheel and a Heumann wheel both on worn rail of standard gage. These were identified as representative two-point contact and single-point contact profiles, respectively, as described below. Both profiles, obtained from tables in [22], were smoothed and modified to account for a centered rolling radius of 14.0 in. Geometric constraint functions for these two symmetric profiles are described and shown in Appendix F (Section F.1.2). The new wheel represents a new AAR wheel with 1/20 tread taper and a steep flange. As discussed in Appendix F, single-point contact occurs in the tread region, but due to the steep flange of this profile, two points of contact occur when the wheelset lateral excursion equals the flange clearance. The Heumann wheel profile was designed with the intention of maintaining single-point contact for all wheelset excursions to obtain a profile that would maintain its shape as it wears [23].

Linear creep coefficients typical of the tread and flange of the two wheel profiles were calculated using Hertzian contact theory. Rail and wheel radii of curvature were obtained from [22]. Flange creep coefficients are

Table 2.3 Baseline Rail/Vehicle Parameters

WHEEL RAIL INTERACTION PARAMETERS

WHEEL/RAIL	NEW WHEEL	HEUMANN WHEEL
f_{11T} [lb]*	1.09E6**	1.01E6
f_{12T} [ft-lb]	8615.	9620.
f_{22T} [ft^2-lb]	82.	14.
f_{33T} [lb]	1.18E6	9.805E6
f_{11F} [lb]	7.34E5	5.755E5
f_{12F} [ft-lb]	6820.	4735.
f_{22F} [ft^2-lb]	2.	1.
f_{33F} [lb]	6.71E5	5.26E5
a_{11}	0.05	0.17
δ_o	0.05	0.195
Δ	0.0	4.4
λ	0.05	0.20
μ	0.30	0.30

GEOMETRY PARAMETERS

r_o	[ft]	1.167	h_{ts}	[ft]	1.48
a	[ft]	2.32	h_{tp}	[ft]	0.52
b	[ft]	3.75	h_c	[ft]	2.375
d_p	[ft]	1.92	ℓs	[ft]	23.75
h_{cs}	[ft]	2.90	d_s	[ft]	3.71

*Creep coefficients are half-Kalker values with a nominal contact patch normal load of 15,000 lb.

**E represents to the power of 10, e.g., 1.0E6 = 1.0×10^6

Table 2.3 Baseline Rail/Vehicle Parameters (Cont'd)

COMPONENT MASSES AND MOMENTS OF INERTIA

WHEELSET	CONVENTIONAL TRUCK	RADIAL TRUCKS
M_w [slug]	126.	151.
I_{wx} [slug-ft^2]	399.	494.
I_{wy} [slug-ft^2]	28.	28.
I_{wz} [slug-ft^2]	547.	946.
TRUCK		
M_t [slug]	146.	146.
I_{tx} [slug-ft^2]	1166.	1166.
I_{ty} [slug-ft^2]	668.	668.
I_{tz} [slug-ft^2]	1251.	1251.

CARBODY (unloaded)

M_c [slug]	1560.
I_{cx} [slug-ft^2]	4.40E4
I_{cy} [slug-ft^2]	8.96E5
I_{cz} [slug-ft^2]	8.96E5

VEHICLE WEIGHT	CONVENTIONAL	RADIAL
W_v [lb]* (Unloaded)	75,800	79,000
W_v [lb]** (loaded)	95,800	99,000

---

* $W_{v\ \text{unloaded}}$ = 2 trucks with wheelsets + carbody.

** $W_{v\ \text{loaded}}$ = 2 trucks with wheelset + carbody + passengers .

Table 2.3 Baseline Rail/Vehicle Parameters (Cont'd)

STIFFNESSES AND DAMPING

PRIMARY SUSPENSION

	New Wheel		Heumann Wheel	
	Conventional	Radial	Conventional	Radial
k_{px} [lb/ft]	1.35E5	1.20E5	6.50 E5	5.00E5
C_{px} [lb-sec/ft]	574.	756.	2760.	3150.

k_{py} [lb/ft]	7.50E5	k_{pz} [lb/ft]	1.0E6
C_{py} [lb-sec/ft]	620.	C_{pz} [lb-sec/ft]	600.

INTERWHEELSET STIFFNESSES

	Conventional	Radial
k_{b2} [ft-lb/rad]	0.0	1.0E3
k_{s2} [lb/ft]	0.0	1.0E6

SECONDARY SUSPENSION

k_{sy} [lb/ft]	19,500	k_{sz} [lb/ft]	20,400
C_{sy} [lb-sec/ft]	1420.	C_{sz} [lb-sec/ft]	1630.
$k_{s\psi}$ [ft-lb/rad]	2.6E6		
$C_{s\psi}$ [ft-lb-sec/rad]	0.0	T_B [ft-lb]	7500.

FORCED-STEERING PARAMETERS

G_{prl} = 0.1579 $\quad$ H = 0.0

less than tread coefficients* (by about 30% for longitudinal and lateral coefficients). This decrease in flange creep coefficients is expected since the contact patch area decreases in the flange, and its effect outweighs the opposite effect of increased ellipticity.

Linear profile coefficients were computed by linearization of the profile functions about the centered wheelset position. The nominal conicity in the tread of the Heumann wheel profile is 0.20, compared with a conicity of 0.05 for the new wheel profile.

The vehicle dimensions and weights are representative of urban transit trucks. Specifically, the geometry, masses and inertias are based on those reported for the existing and modified PATCO** Pioneer III trucks [24]. The mass and inertia parameters reflect the fact that in yaw and roll the contribution of the traction motor must be included. In addition, for radial trucks the contribution of the steering arms is added. The mass and roll and pitch inertias of the truck include the side frames, braking equipment, and bolster. The bolster does not influence the truck yaw inertia.

The primary, secondary, and interaxle suspensions are typical of urban truck designs. The primary longitudinal stiffnesses were chosen so that all baseline vehicles have the same stability characteristics, i.e., a critical speed of 120 mph. The interaxle bending stiffness is quite low for the self steered radial truck (k_{b2} = 1.0E3 ft-lb/rad), whereas it is quite high for forced-steered trucks as a result of the stiffnesses of the carbody to wheelset linkages to achieve improved curving performance. This is discussed

---

*The contact patch ellipse (a/b) ratio for the flange patch is limited to 10. This agrees with calculations by British Rail which show that the (a/b) ratio rarely exceeds 10 [9].

**Port Authority Transit Corporation.

in more depth in Chapter 4.

The baseline track curvature steering gain used in the performance studies of the forced-steered truck designs is the pure rolling line gain, $G_{pr\ell}$. The pure rolling line gain is the wheelbase divided by the truck centerpin spacing, according to equation (2-9). A limited study of alternate track curvature steering gains was conducted and the results, presented in Chapter 4, suggest that $G_{pr\ell}$ results in slight understeering of the wheelsets during flanging. This implies that gains slightly larger than $G_{pr\ell}$ may be appropriate during flanging. However, the selection of an optimal track curvature steering gain represents an area of future research. Thus, for the forced-steering studies in this report, the track curvature steering gain is $G_{pr\ell}$. The cant deficiency steering gain, H, is set to zero in the forced-steered studies since the curvature effects are in general much more important.

CHAPTER 3

STABILITY OF CONVENTIONAL, SELF-STEERED AND FORCED-STEERED RADIAL TRUCKS

3.1 Introduction

The speed capability of railway vehicles is limited by (self-excited) motions in the lateral plane commonly referred to as hunting. The speed at which hunting occurs is called the critical speed, and for safety reasons a well-designed vehicle will have a critical speed much higher than the maximum operating speed. Significant study has been devoted to determining the critical speed of conventional and self-steered radial trucks [16, 17, 25]. The development of forced-steered concepts which are directed to improving curving performance introduces additional dynamic effects due to steering links in a vehicle [20], and requires detailed evaluation.

In this chapter the stability properties of the following four truck designs each with new and Heumann wheels are discussed: a conventional truck, a self-steered radial truck (SSR), and two (L-type) forced-steered radial trucks, one (FSR I) with low primary longitudinal stiffness ($k_{px} = 7.0 \times 10^4$ lb/ft) and the second (FSR II) with very low primary longitudinal stiffness ($k_{px} = 1.0 \times 10^3$ lb/ft). As discussed in Section 2.3, a six degree of freedom (DOF) truck model and a 15 DOF vehicle model are available to compute the stability characteristics in terms of critical speed. The 6 DOF model, incorporated in program GEN6, assumes that the front or rear truck is attached to a constant forward moving reference frame through the secondary suspension system. The degrees of freedom associated with the model are the lateral and yaw displacements of the truck frame and the two wheelsets. The model used in program GEN15 is that of a full vehicle consisting of two trucks and a carbody. The carbody degrees of freedom are the lateral, yaw and roll displacements while the degrees of freedom of the two trucks are the same as those in program GEN6. The forced-steering linkages introduce a destabilizing moment on the front truck and stabilizing moment on the rear one, and thus the front truck is less stable than the rear one. For a conventional and self-steered radial truck, the stability of the front truck is the same as that of the rear one. Critical speeds, calculated with programs GEN6 and GEN15, are compared in Table 3.1. The critical speed of the front truck gives an accurate prediction of the vehicle critical speed. This is true except for cases when the carbody mode is important. With the conventional and self-steered trucks, this occurs when the truck kinematic frequency approximately equals the carbody natural frequencies of about 1 Hz, resulting in carbody hunting. The speed at which this happens is usually below 50 mph and occurs only for short periods of time when the vehicle speeds up or slows down. The carbody hunting problem can usually be solved by increasing the secondary lateral damping [26].

Table 3.1 Comparison of Critical Speed of Baseline Conventional and Self-Steered Radial Truck Designs with New Wheels as Calculated with Programs GEN6 and GEN15

Baseline Truck Design*	Critical Speed (mph)	
	Front truck (GEN6)	Vehicle (GEN15)
Conventional ($k_{px} = 1.35 \times 10^5$ lb/ft)	120.8	120.3
Self Steered Radial ($k_{px} = 1.20 \times 10^5$ lb/ft, $k_{b2} = 1.0 \times 10^3$ ft-lb/rad, $k_{s2} = 1.0 \times 10^6$ lb/ft)	120.1	120.3

*With new wheels.

Besides carbody hunting mentioned above, additional carbody modes can occur with forced-steered trucks due to the introduction of steering linkages between the wheelsets and carbody. Figure 3.1 shows a comparison of the critical speed of a forced-steered radial truck (FSR I) with new wheels as a function of effective interaxle bending stiffness, k_{b2}, calculated with programs GEN6 and GEN15. The critical speeds for the 6 DOF front truck and the 15 DOF vehicle models are in agreement up to a high value of k_{b2} at which the critical speed for the full vehicle model decreases suddenly. It was found that the lowest unstable mode (the mode that occurs at the lowest speed) is the one corresponding to the carbody lateral motion [27]. This instability does not occur with a conventional or a self-steered radial truck. It is caused by the wheelset-carbody linkages of a forced-steered truck and can be eliminated by increasing the secondary lateral damping. This mode occurs particularly at low values of creep coefficients and conicity, and is explored in more detail later in Section 3.4.

Unless otherwise specified, all the results of the parametric studies have been performed with program GEN6 for the front truck. Periodic checks were performed with program GEN15 when the carbody mode plays an important role.

The parametric study includes the variation of the truck critical speed as influenced by the primary suspension stiffnesses, secondary yaw stiffness, creep coefficients, and conicity. The effect of the interaxle stiffnesses on the critical speed of the self-steered and forced-steered trucks is also investigated. Finally, the phenomenon of kinematic instability associated with the forced-steered truck is addressed.

The secondary lateral stiffness and damping are usually determined from

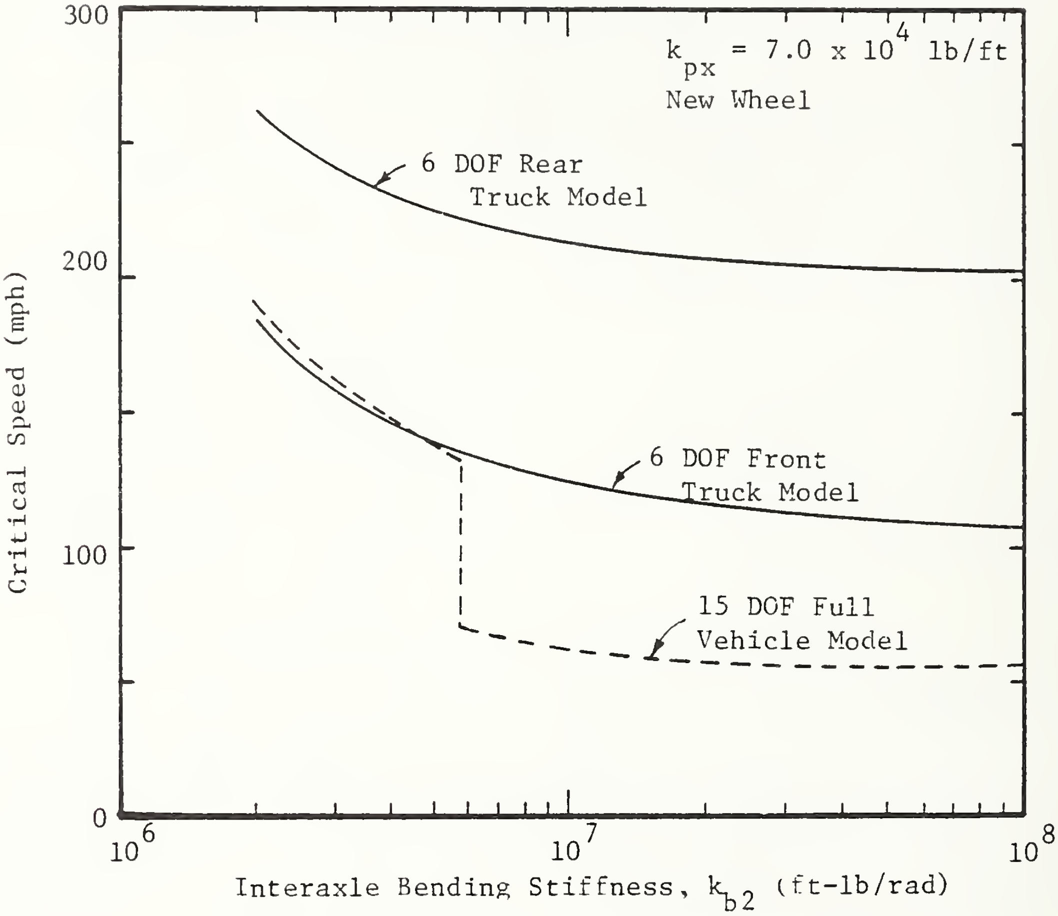

Figure 3.1 Critical Speed as a Function of Interaxle Bending Stiffness for a Forced-Steered Radial Truck with New Wheels Calculated Using 6 and 15 DOF Models

ride quality considerations to yield carbody natural frequencies of about 1 Hz and a damping ratio of about 0.2, and hence are not varied in the study. To avoid unrealistically high damping ratios when a stiffness is decreased, the ratio of the damping to the corresponding stiffness is held constant as the stiffness is varied.

3.2 Stability of Conventional Trucks

The effects of primary suspension stiffnesses, secondary yaw stiffness, creep coefficients and conicity on the critical speed of a conventional truck have been evaluated using the 6 DOF model.

The critical speed of a conventional truck having new and Heumann wheels as a function of primary longitudinal stiffness is shown in Figure 3.2. The stability behavior is similar for trucks with new and Heumann wheels. At all stiffnesses, the critical speed of a truck with new wheels is higher due to the small conicity (λ = 0.05 for new wheels vs. λ = 0.20 for Heumann wheels). For trucks with either wheels, the critical speed increases as the primary longitudinal stiffness, k_{px}, is increased, reaches a maximum and then decreases as k_{px} is increased further. Since the wheelsets of a conventional truck are stabilized by the primary suspension, a low value of k_{px} decouples the wheelset yaw motions from the truck motion. The resulting loosely restrained wheelset yaw motions are referred to as individual wheelset modes [26]. As the primary longitudinal stiffness k_{px} is increased, the coupling between the wheelset and truck yaw motions increases. Coupling to

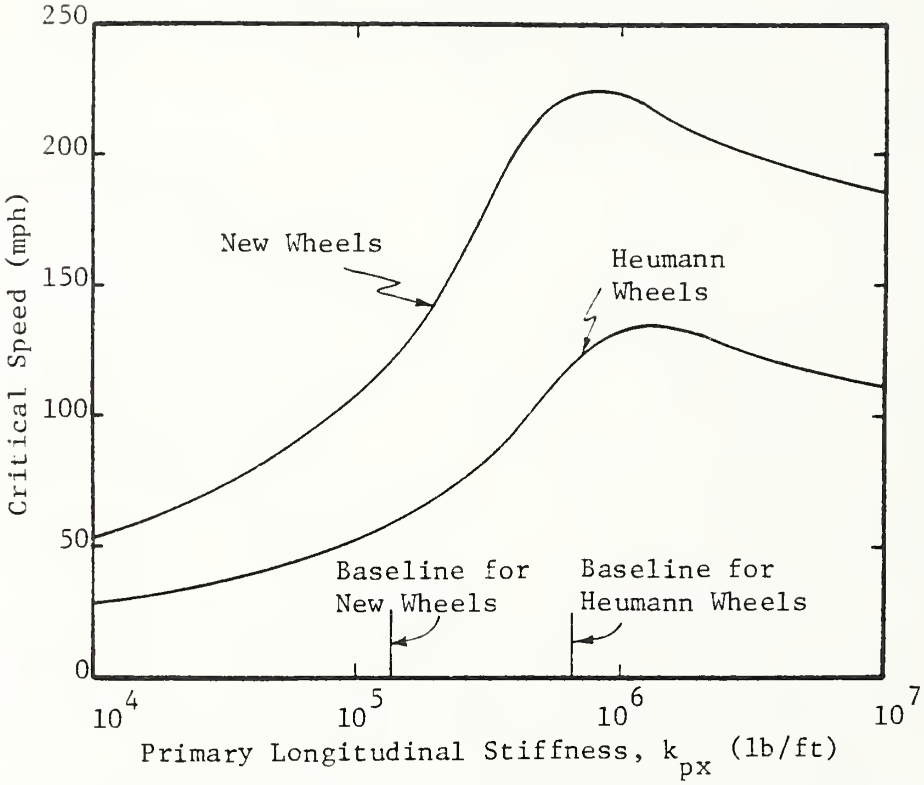

Figure 3.2 Effect of Primary Longitudinal Stiffness on the Critical Speed of a Conventional Truck with New and Heumann Wheels.

the truck frame introduces a destabilizing effect from the increased effective mass and a stabilizing effect from the connection to the inertial carbody through the secondary suspension system. At the value of k_{px} for which the critical speed reaches a maximum, the motion of the two wheelsets are out of phase relative to the truck frame as indicated by the eigenvector corresponding to the least damped eigenvalue. Consequently a yaw motion of one wheelset is stabilized by the truck frame, which in turn is stabilized by the inertial carbody and the other wheelset. At very high values of k_{px}, the yaw of the wheelsets is strongly coupled to the yaw of the truck frame. The wheelsets and the truck frame yaw as a rigid body, stabilized by the inertial carbody through the secondary yaw stiffness.

Suspension elements in a truck will change their properties with time and wear due to general deterioration. These changes may lower the critical speed. In order to allow for a significant reduction in critical speed and still maintain a laterally stable vehicle above the maximum operating speed, vehicle suspension design should be based on a high critical speed. For this reason, in this report baseline suspension parameters are selected such that the trucks have critical speeds of 120 mph. As marked in Figure 3.2, the primary longitudinal stiffness of a baseline conventional truck with new wheels is $k_{px} = 1.35 \times 10^5$ lb/ft and the stiffness of a baseline conventional truck with Heumann wheels is $k_{px} = 6.50 \times 10^5$ lb/ft. The truck with Heumann wheels requires a stiffer primary longitudinal stiffness to achieve the same critical speed as that of a truck with new wheels due to the effect of the higher conicity Heumann wheel. The primary longitudinal stiffnesses of the baseline conventional trucks are within the range of typical stiffnesses: 1.0×10^5 lb/ft $< k_{px} < 2.0 \times 10^6$ lb/ft. For instance, the primary spring of UTDC's existing CTA 2400 rapid transit truck has a primary longitudinal stiffness of 2.0×10^5 lb/ft [19]. The standard WMATA car/ Rockwell truck has a moderately stiff longitudinal stiffness of 3.0×10^5 lb/ft [2]. The Budd Pioneer III truck is very stiff with a primary longitudinal stiffness of 3.5×10^6 lb/ft [28].

The effect of primary lateral stiffness, k_{py}, on the critical speed of a conventional truck with new wheels is shown in Figure 3.3. For soft k_{py}, the wheelsets are relatively free to move laterally with respect to the truck frame, resulting in an individual wheelset mode in the lateral direction. As k_{py} is increased, the wheelset lateral motions start to affect the truck frame. Lateral motion of the two wheelsets in the same direction influences the truck to move laterally in that direction, while a lateral motion of both wheelsets in opposite directions causes the truck to yaw. However, the truck motions are restrained by the secondary suspension system which is connected to the carbody. As a result the critical speed increases as k_{py} is increased. At high values of k_{py} the critical speed reaches an asymptote because the wheelsets are rigidly connected to the truck frame in the lateral direction, and stabilization is provided indirectly by the secondary suspension. A high value of primary lateral stiffness is chosen for the baseline trucks, $k_{py} = 7.5 \times 10^5$ lb/ft, and is typical of current transit truck designs.

Figure 3.4 shows the effect of secondary yaw stiffness, $k_{s\psi}$, on the critical speed. Below a value of 10^5 ft-lb/rad the secondary yaw stiffness does not affect the critical speed. In this range the wheelsets are stabilized by the truck frame through the primary suspension system. As secondary yaw stiffness, $k_{s\psi}$, is increased above 10^5 ft-lb/rad, stabilization

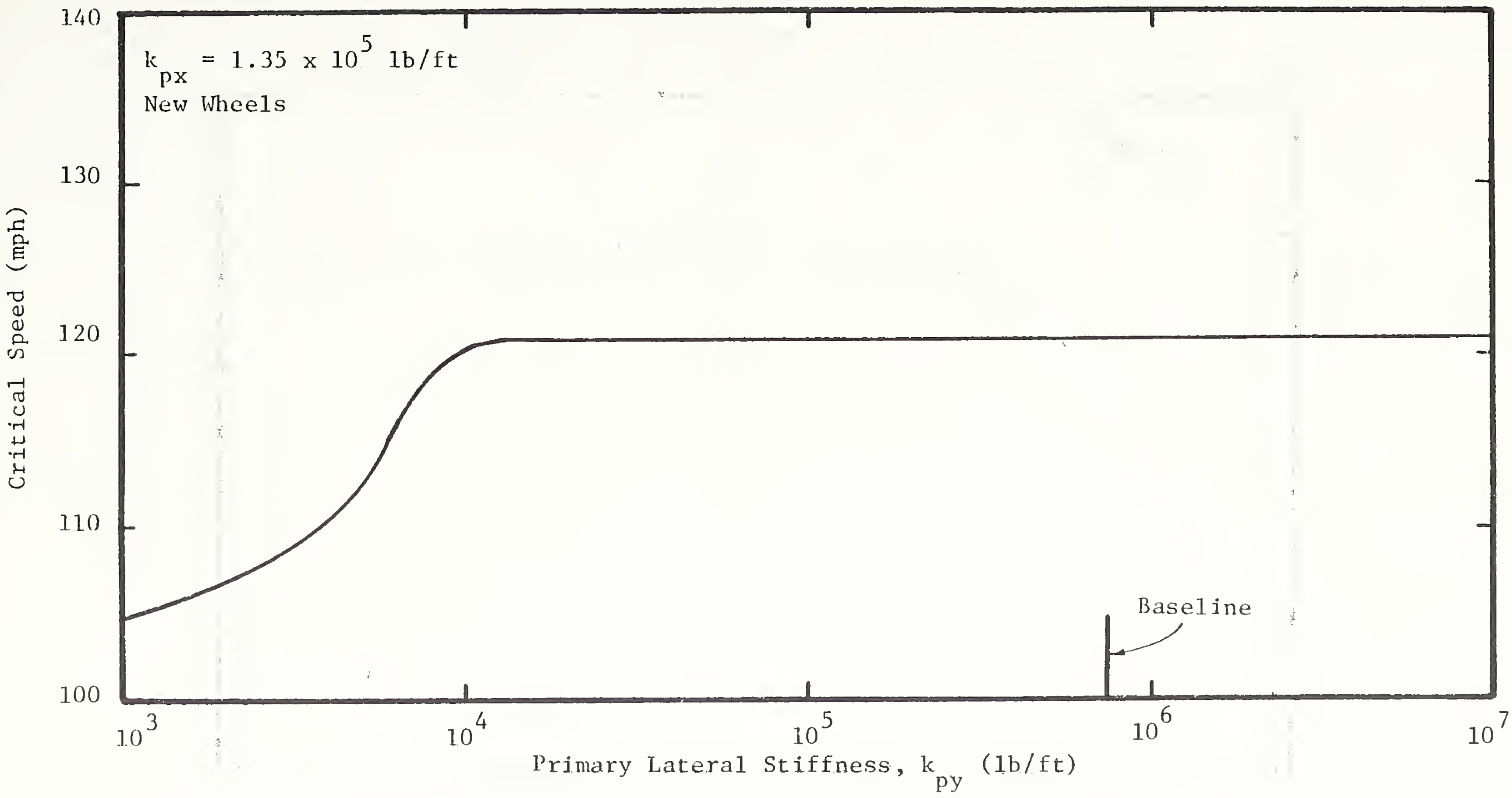

Figure 3.3 Effect of Primary Lateral Stiffness on the Critical Speed of a Conventional Truck with New Wheels.

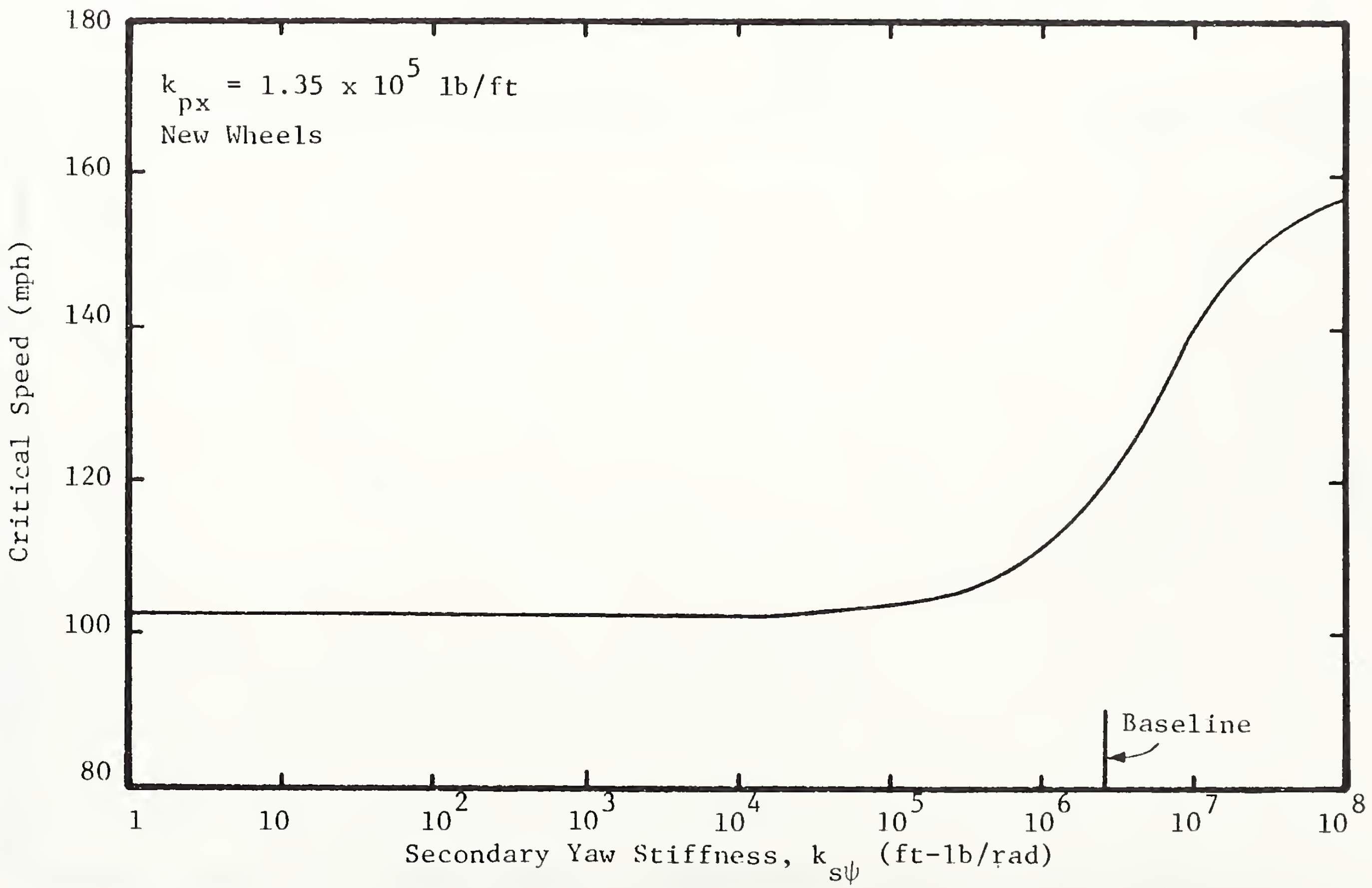

Figure 3.4 Effect of Secondary Yaw Stiffness on the Critical Speed of a Conventional Truck with New Wheels.

of the truck frame by the carbody is significant and results in an increase in the critical speed. In this study, the secondary yaw stiffness is $k_{s\psi} = 2.6 \times 10^6$ ft-lb/rad.

The combined effect of creep coefficients and conicity on the critical speed of a conventional truck with $k_{px} = 1.35 \times 10^5$ lb/ft is plotted in Figure 3.5. Reducing creep coefficients or conicity increases the critical speed. Lowering creep coefficients or conicity reduces the centering moment (which steers the wheelset back to the track centerline once it is displaced) generated by the longitudinal creep forces. Hence the wheelset steering action is also reduced and an increase in the critical speed occurs. In this study, half Kalker creep coefficients are used. Kalker's theoretical linear creep coefficients are typically reduced by 50% to account for field experience in which reduced values are attributed to the effects of rail contamination and other field conditions.

3.3 Stability of Self-Steered Radial Trucks

The stability and curving performance of a self-steered radial (SSR) truck is determined primarily by the primary longitudinal stiffness, k_{px}, and the interaxle bending stiffness, k_{b2}. The effect of these parameters on the critical speed of a self-steered radial truck is analyzed with the 6 DOF model. The variation of the critical speed as a function of the primary lateral stiffness, secondary yaw stiffness, creep coefficients, conicity, and the interaxle shear stiffness is also examined.

The critical speed of a SSR truck having new and Heumann wheels as a function of the primary longitudinal stiffness, k_{px}, is shown in Figure 3.6. The effect of k_{px} on the critical speed of a truck with new or Heumann wheels is similar to that observed for the conventional truck. At low values of k_{px}

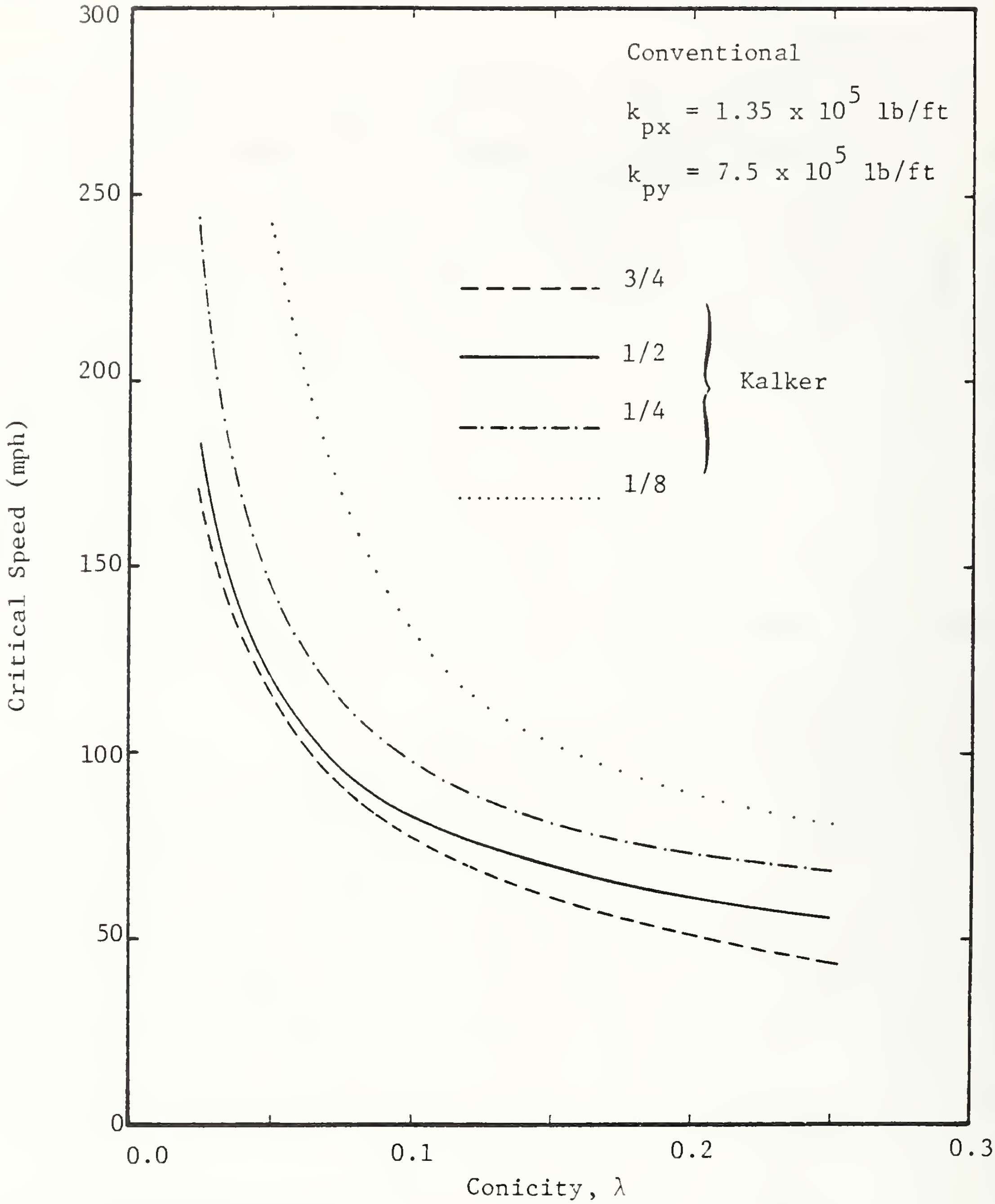

Figure 3.5 Effect of Conicity and Creep Coefficients on the Critical Speed of a Conventional Truck ("Soft" Primary Suspension)

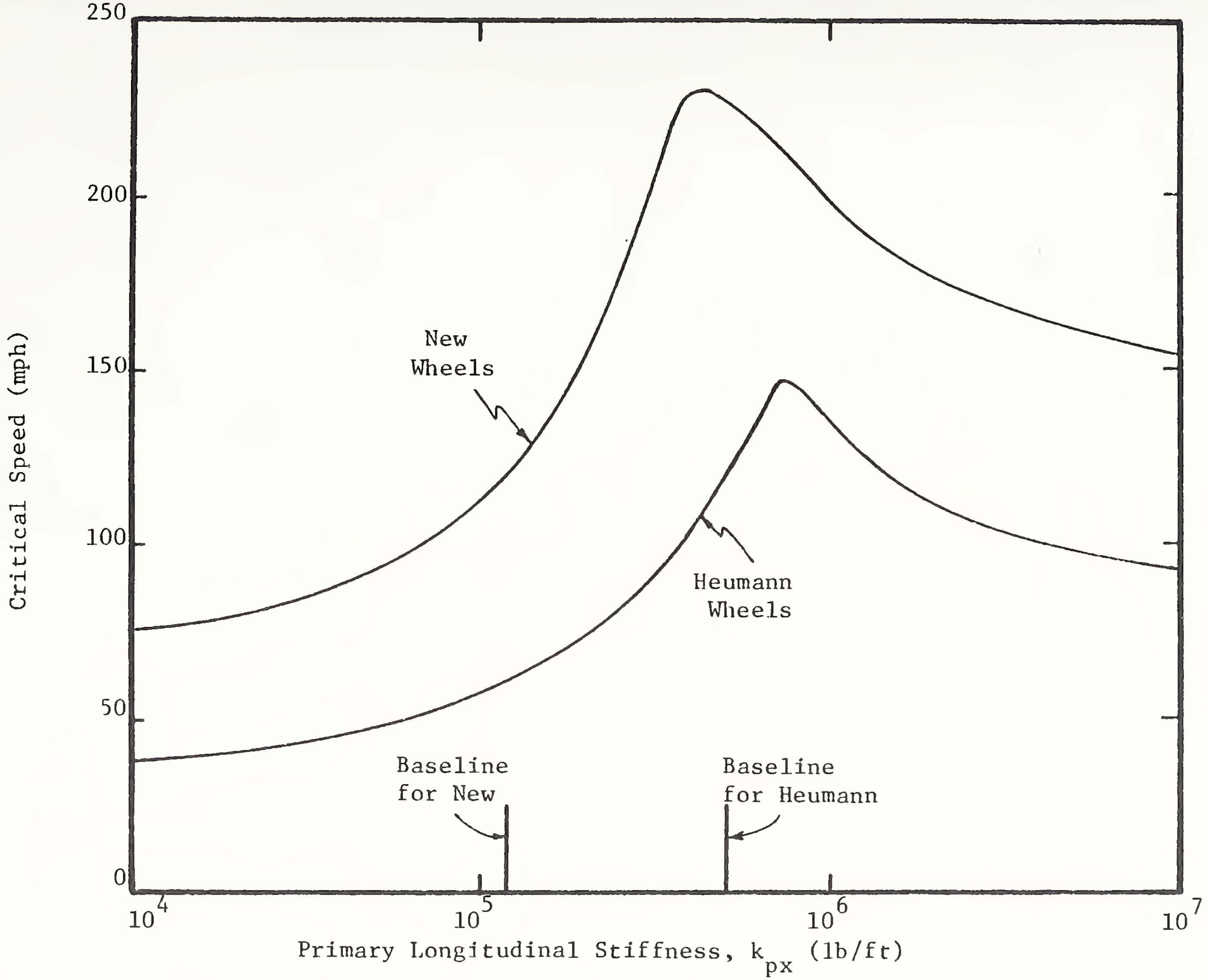

Figure 3.6 Effect of Primary Longitudinal Stiffness on The Critical Speed of a Self-Steered Radial Truck with New and Heumann Wheels.

the wheelset yaw motions are almost decoupled from the truck yaw. The interaxle stiffness provides direct communication between the two wheelsets, resulting in a higher critical speed than that of a conventional truck having the same primary suspension stiffnesses. As k_{px} is increased the critical speed increases until a maximum value is reached. In this region the stabilizing effect from the secondary suspension, as a result of the coupling between the wheelsets and the truck frame, overcomes the destabilizing effect of increased mass. Increasing k_{px} beyond this value results in a decrease in the critical speed as a rigid configuration of the wheelsets and the truck frame in the yaw direction is approached. At very high values of k_{px}, the interaxle stiffnesses further degrade the stability by locking the wheelsets into a more rigid configuration in the lateral as well as yaw directions, resulting in a lower critical speed than that of a conventional truck.

The results shown in Figure 3.6 are for SSR trucks with new and Heumann wheels. These trucks are obtained by adding interwheelset connections to conventional vehicles which result in an increase in the truck critical speed. This increase is due to: (1) decoupling of the truck frame mass from the wheelsets, which reduces the effective mass involved in the hunting motion, and (2) the added stiffness (and slight increase in mass) from the interwheelset links. Baseline self-steered trucks are chosen such that their critical speeds are 120 mph, comparable with the critical speeds of the baseline conventional trucks. This is accomplished by reducing the primary longitudinal stiffness, k_{px} (which, as will be shown in Chapter 4, will improve curving performance). From Figure 3.6 the k_{px} of a baseline SSR truck with new wheels is reduced to 1.20×10^5 lb/ft; for a baseline SSR truck with Heumann wheels, the stiffness is lowered to 5.00×10^5 lb/ft. A baseline critical speed of 120 mph for the SSR truck is consistent with the critical speeds reported for self-steered articulated and cross-anchor trucks [8].

The effect of primary lateral stiffness, k_{py}, on the critical speed of a SSR truck with new wheels is shown in Figure 3.7. At a low value of k_{py}, the wheelset lateral motions are almost decoupled from the truck motion but they are coupled to each other through the interaxle shear stiffness. The critical speed increases as k_{py} is increased. Further increases in k_{py} result in coupled lateral motions of the wheelsets and truck. Stabilization is provided by the secondary suspension system at high values of k_{py}.

Variations of the critical speed of the self-steered truck with the secondary yaw stiffness, as shown in Figure 3.8, and with creep coefficients and conicity, as shown in Figure 3.9, are very similar to those of a conventional truck. The baseline value of secondary yaw stiffness is $k_{s\psi} = 2.6 \times 10^6$ ft-lb/rad.

Figure 3.10 shows the effect of the interaxle shear stiffness, k_{s2}, on the critical speed of a self-steered radial truck with new wheels. At low values of k_{s2}, the wheelsets can sustain the yaw motions represented by the in-phase $(\psi_1 + \psi_2)$ and the out-of-phase $(\psi_1 - \psi_2)$ coordinates. The in-phase $(\psi_1 + \psi_2)$ mode imposes a net yaw moment on the truck frame while the out-of-phase $(\psi_1 - \psi_2)$ motion does not. The interaxle shear stiffness affects the critical speed only at values high enough to suppress the in-phase $(\psi_1 + \psi_2)$ yaw mode, which tends to excite the truck frame motion, and allows interaction between the two wheelsets in the lateral direction. The effect is an increase in the critical speed. For stiffer values of k_{s2} the critical speed remains constant. The baseline value of interaxle shear stiffness, $k_{s2} = 1.0 \times 10^6$ lb/ft, is high enough to take advantage of the increased critical speed due

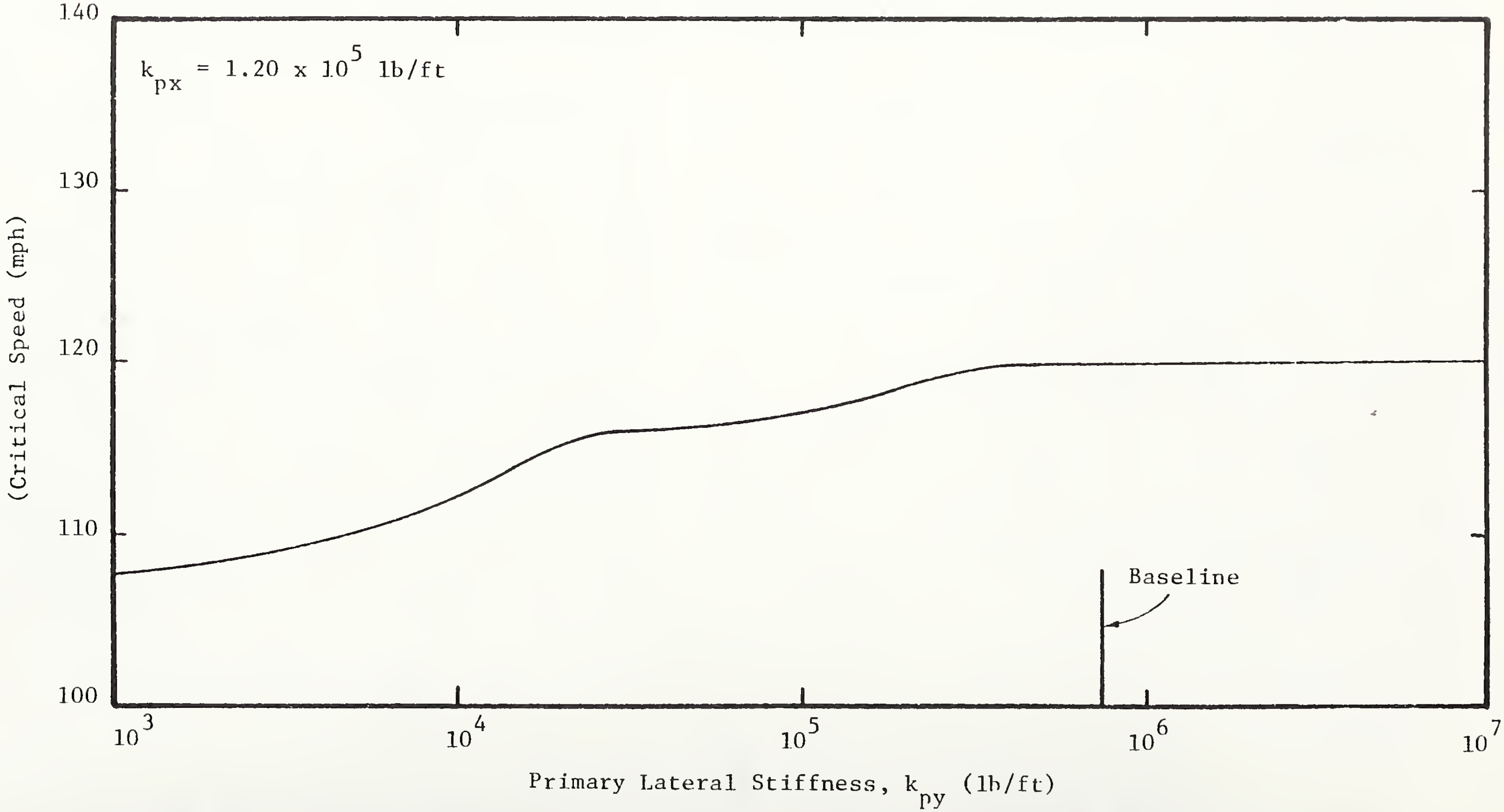

Figure 3.7 Effect of Primary Lateral Stiffness on the Critical Speed of a Self-Steered Radial Truck with New Wheels.

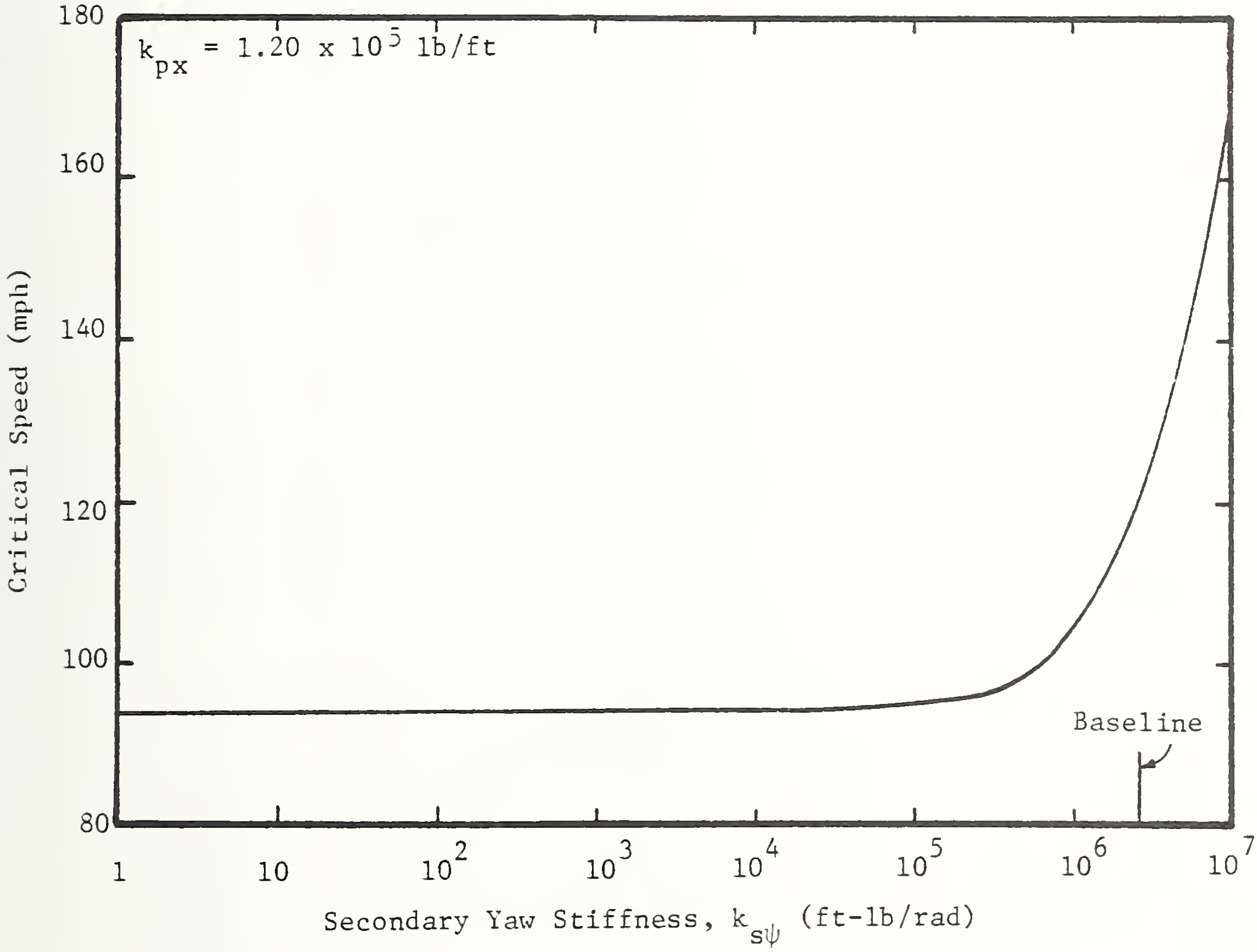

Figure 3.8 Effect of Secondary Yaw Stiffness on the Critical Speed of a Self-Steered Radial Truck with New Wheels

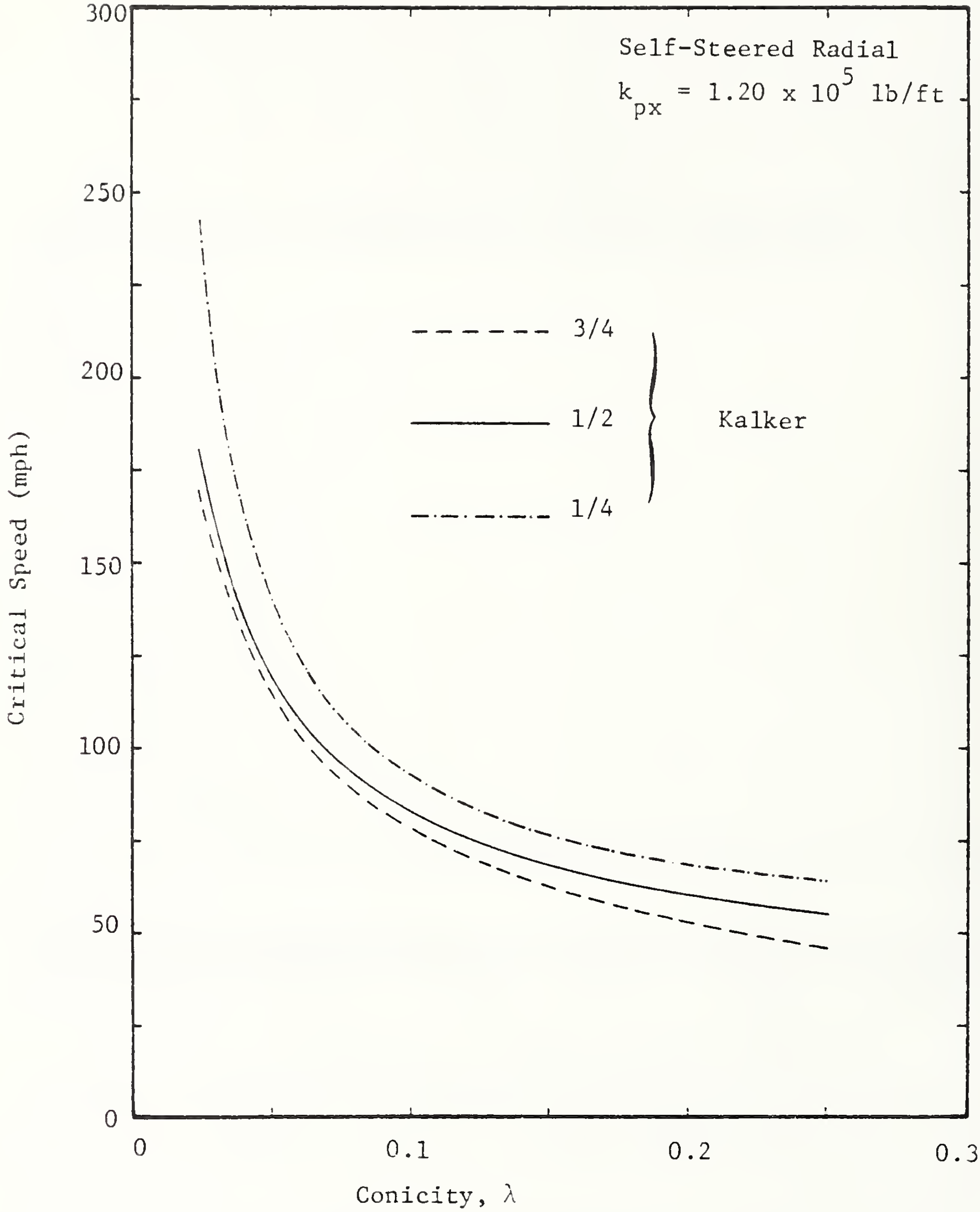

Figure 3.9 Effect of Conicity and Creep Coefficients on the Critical Speed of a Self-Steered Radial Truck with AAR Standard Wheel Profiles

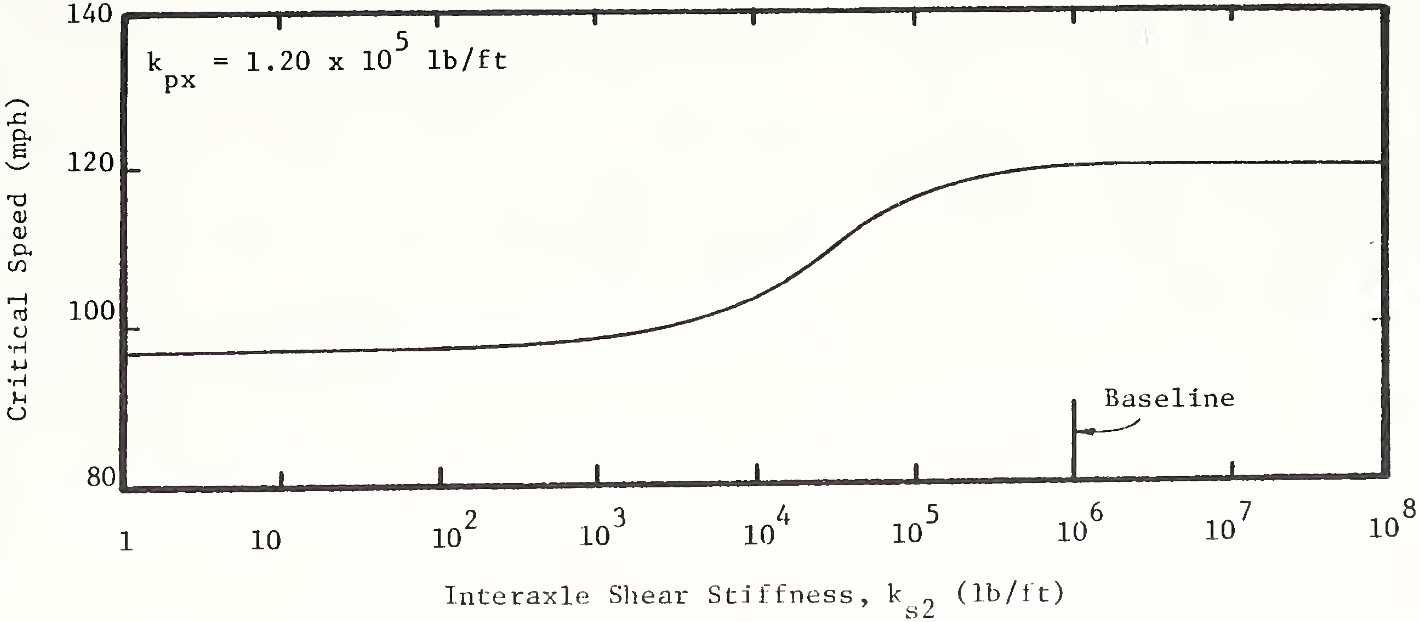

Figure 3.10 Effect of Interaxle Shear Stiffness on the Critical Speed of a Self-Steered Radial Truck with New Wheels

to the interaction of the wheelsets laterally.

The influence of the interaxle bending stiffness, k_{b2}, on the critical speed of a self-steered radial truck with new wheels is shown in Figure 3.11. At low values of k_{b2}, the bending stiffness of the wheelsets is provided entirely from the primary longitudinal stiffness, k_{px}. The constant value of k_{px} is responsible for the constant critical speed. A low value of interaxle bending stiffness, $k_{b2} = 1.0 \times 10^3$ ft-lb/rad, is selected as baseline. Increasing k_{b2} improves stability as more communication between the two wheelsets in the yaw direction is achieved. However, above a specific value an increase in k_{b2} decreases the critical speed as the two wheelsets are locked by the interaxle stiffnesses as a rigid body which is stabilized by the primary suspension only. This effect occurs at high values of k_{b2}.

3.4 Stability of Forced-Steered Radial Trucks

Vehicles with forced-steered radial trucks utilize passive wheelset-carbody linkages to sense track curvature and/or cant deficiency and adjust their wheelsets into radial positions accordingly. The stability performance of these vehicles is influenced by the primary, secondary, and effective interaxle suspension stiffnesses (due to forced-steered linkages) and the wheel/rail profile geometry in terms of nominal conicity. In these studies, the critical speed of an L-type forced-steered truck as a function of suspension stiffnesses, creep coefficients, and conicity is established. The steering action gains of the generic truck model for the wheelsets to kinematically* track the pure rolling line in curves are: $G_1 = 0$, $G_2 = 0.1579$, $G_3 = 0.3088$, $G_4 = G_5 = G_6 = 0$. All cant deficiency steering gains are

*Assuming rigid steering linkages and no flange forces.

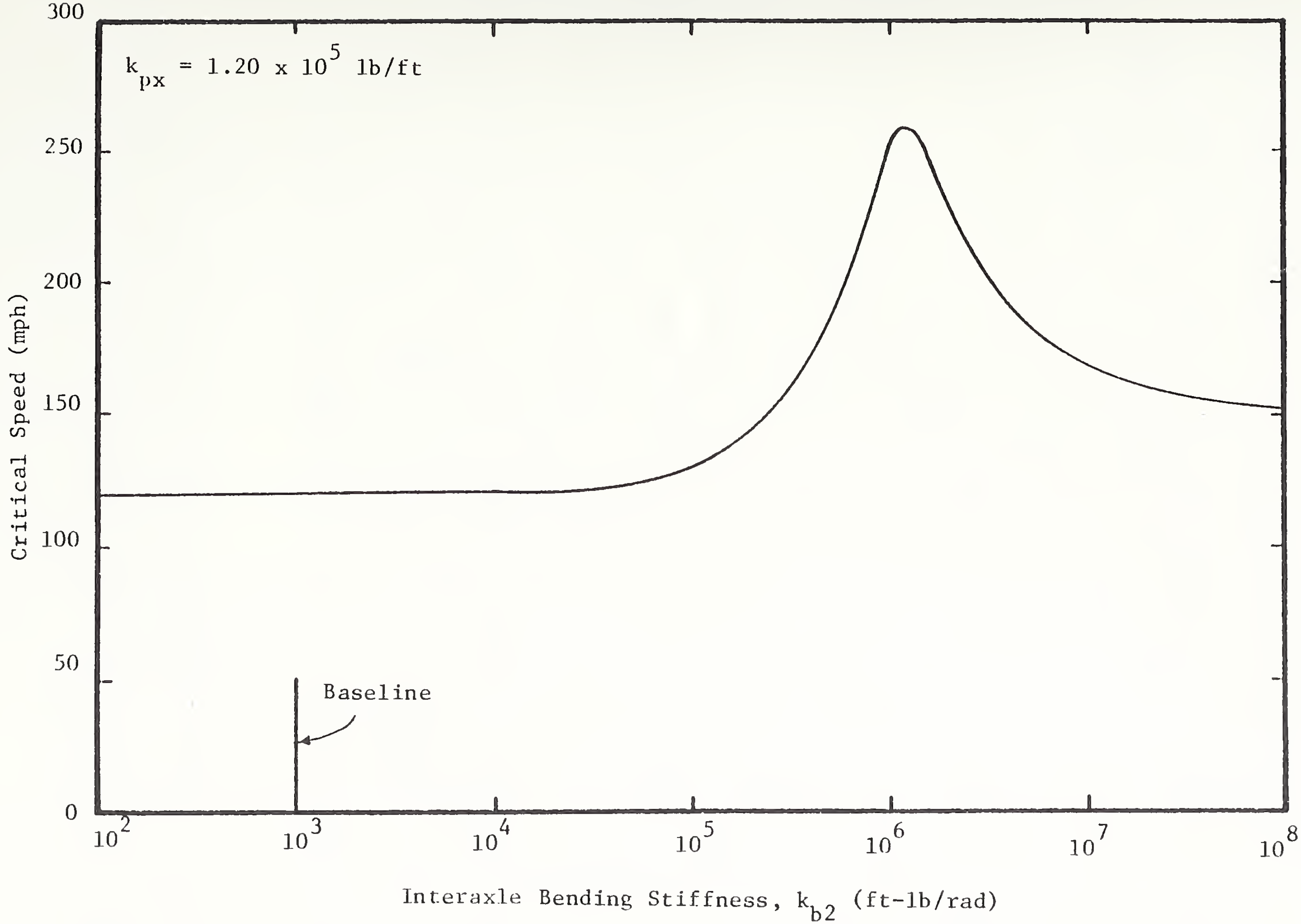

Figure 3.11 Effect of Interaxle Bending Stiffness on the Critical Speed of a Self-Steered Radial Truck with New Wheels.

zero ($H_1 = H_2 = H_3 = 0$).

The stability properties of a forced-steered truck are not unique since different combinations of primary longitudinal stiffness, k_{px}, and effective interaxle bending stiffness, k_{b2}, can yield the same critical speed. For this reason, two forced-steered truck designs are studied. Both designs represent trucks with low values of k_{px}, which is advantageous for curving performance as discussed in Chapter 4; the interwheelset and wheelset-carbody linkages provide the requisite stiffness for stability. The two designs are (1) FSR I with $k_{px} = 7.0 \times 10^4$ lb/ft, and (2) FSR II with $k_{px} = 1.0 \times 10^3$ lb/ft. The soft primary suspensions of these designs are not representative of current transit trucks. However, they have been selected to study the advantages of reduced k_{px} on the stability (and curving) behavior of forced steered trucks. A primary spring has been designed for UTDC with a very soft longitudinal stiffness of $k_{px} = 5.0 \times 10^4$ lb/ft [19]. The spring, consisting of an assembly of rubber shear pads, is for potential use on the CTA 2400 rapid transit trucks. Future experimental studies may be required to determine the practical lower limit which can be reached by softening k_{px}.

The critical speed as a function of the interaxle bending stiffness, k_{b2}, of the two forced-steered radial trucks, FSR I and FSR II, with new wheels is shown in Figure 3.12 and with Heumann wheels in Figure 3.13.* In

*The critical speeds of Figures 3.12 and 3.13 were calculated using the 6 DOF truck model. The results using a 15 DOF vehicle model have a decrease in critical speed at a high value of k_{b2}, as shown in Figure 3.1. However, this drop in critical speed occurs for values of the bending stiffness k_{b2} outside the design parameter region of primary interest.

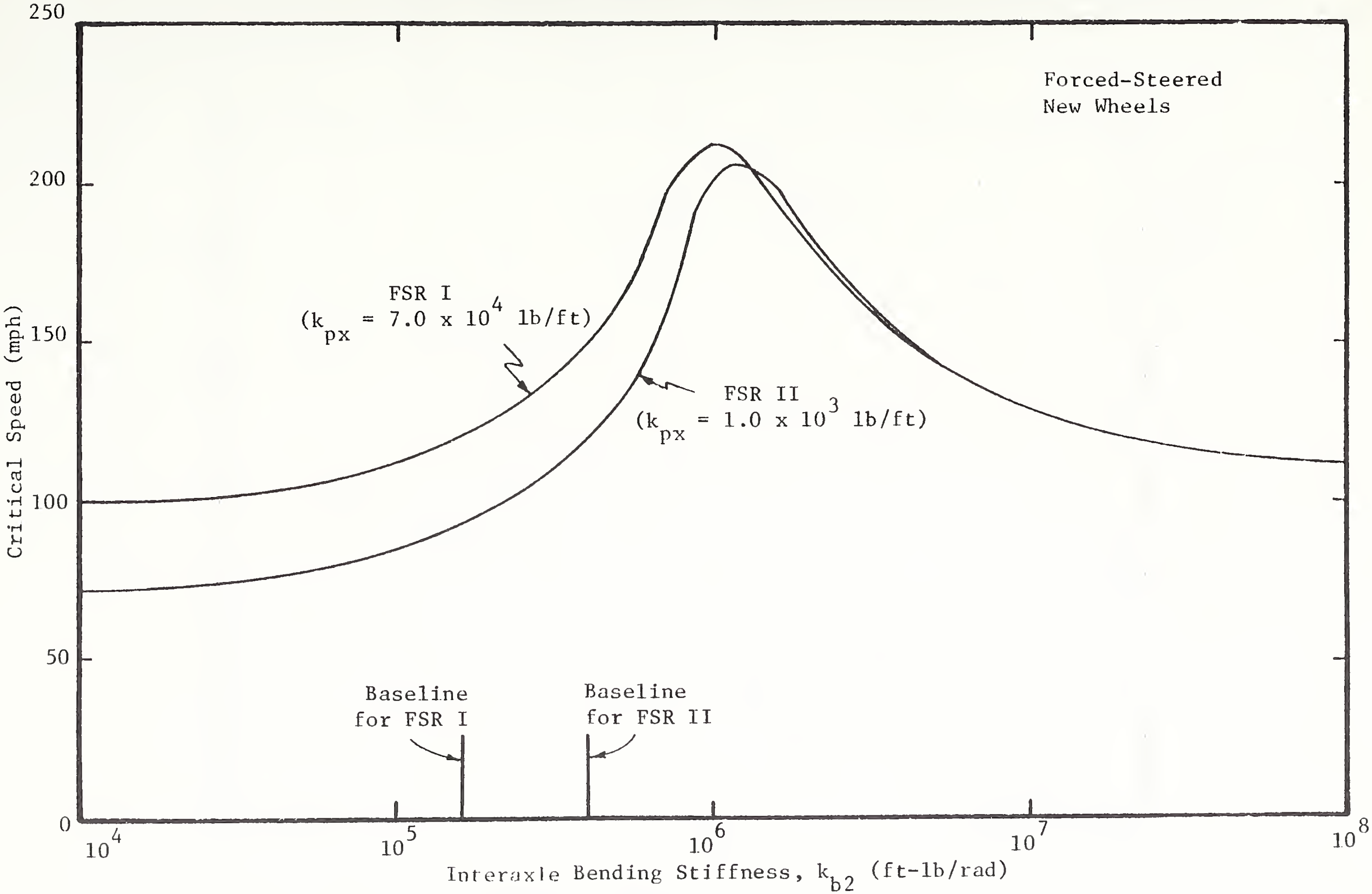

Figure 3.12 Effect of Interaxle Bending Stiffness on the Critical Speed of Forced-Steered Radial Trucks, FSR I and FSR II, with New Wheels

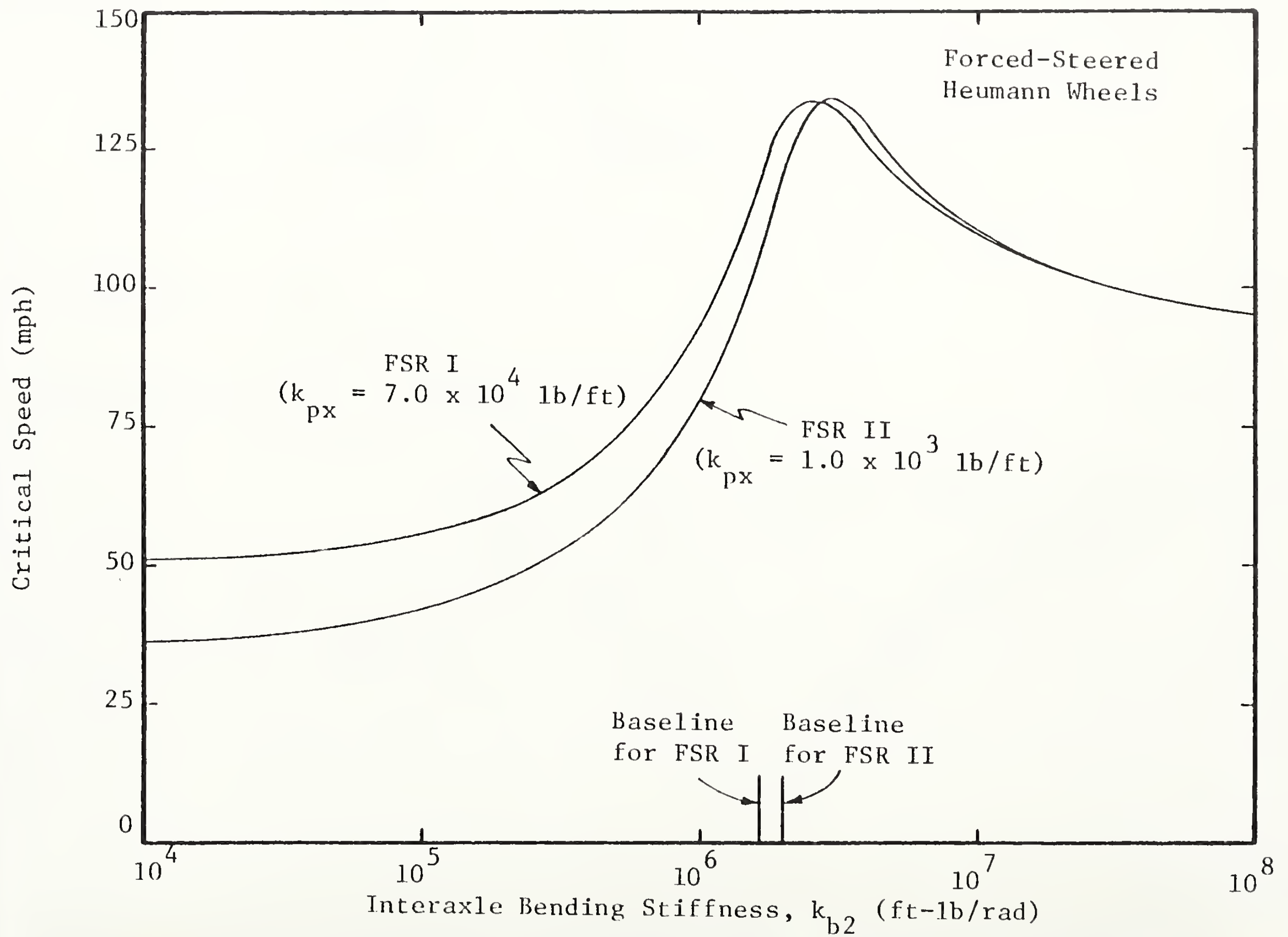

Figure 3.13 Effect of Interaxle Bending Stiffness on the Critical Speed of Forced-Steered Radial Trucks, FSR I and FSR II, with Heumann Wheels.

all cases the effect of k_{b2} on the critical speed is similar. At low values of k_{b2}, the bending stiffness of the primary longitudinal suspension is mainly responsible for the stiffness which governs the stability. Thus, the design with stiffer k_{px}, FSR I, has a higher critical speed for soft k_{b2}. The critical speed increases with increasing k_{b2} as more communication between the wheelsets is achieved through k_{b2}. At high values of k_{b2}, the inter-axle stiffness locks the wheelsets as a rigid body, which results in a decrease in the critical speed. For very stiff k_{b2}, the critical speeds of the two designs, FSR I and FSR II, become the same. As before, the critical speeds of the trucks with new wheels are higher than those of trucks with Heumann wheels at the same stiffnesses due to the stabilizing influence of the lower conicity new wheel. The values of k_{b2} corresponding to baseline forced-steered radial trucks having 120 mph critical speeds are marked in Figures 3.12 and 3.13, and are summarized in Table 3.2.

Table 3.2 Interaxle Bending Stiffnesses for Baseline Forced-Steered Radial Truck Designs with Different Wheel/Rail Profiles All Having Critical Speeds of 120 Mph

k_{b2} (ft-lb/rad) / Profile	FSR I $k_{px} = 7.0 \times 10^4$ lb/ft $k_{s2} = 1.0 \times 10^6$ lb/ft	FSR II $k_{px} = 1.0 \times 10^3$ lb/ft $k_{s2} = 1.0 \times 10^6$ lb/ft
New Wheel	1.68×10^5	4.10×10^5
Heumann Wheel	1.66×10^6	2.00×10^6

Figure 3.14 shows the effect of primary longitudinal stiffness, k_{px}, on the critical speed of the forced-steered radial truck FSR I with new wheels. The result is similar to that obtained for the critical speed of the SSR truck with new wheels shown in Figure 3.6. However, for soft k_{px} higher critical speeds are achieved due to the high value of the interaxle shear stiffness, k_{s2}, of the forced-steered truck ($k_{s2} = 1.0 \times 10^6$ lb/ft). This prevents the wheelsets' in-phase ($\psi_1 + \psi_2$) yaw mode and tends to excite the truck yaw motion. The only possible yaw mode is the out-of-phase ($\psi_1 - \psi_2$) which requires displacement of the interaxle bending stiffness, k_{b2}. Thus, the wheelset pair is partially stabilized by the carbody through k_{b2}. (More complete stabilization via k_{b2} is achieved with a stiffer interaxle bending stiffness. Here, for FSR I, only an intermediate value of k_{b2} is used: $k_{b2} = 1.68 \times 10^5$ ft-lb/rad). The truck frame yaw motion is also stabilized by the carbody through the secondary yaw stiffness. As a result, at low values of k_{px} although the wheelset yaw motions are not coupled directly to the truck yaw, both are stabilized by the carbody. As the primary stiffness, k_{px}, is increased, the wheelset yaw motions couple with the truck yaw resulting in an elastically coupled wheelset mode and increased critical speed. At very high values of k_{px}, the truck and wheelsets move in a rigid truck mode.

Figure 3.15 shows the influence of primary lateral stiffness, k_{py}, on the critical speed of a forced-steered radial truck, FSR I, with new wheels. At low values of k_{py} (less than about 10^4 lb/ft) the critical speed approaches zero. This is caused by the secondary steering action (G_3 steering gain effect) which becomes significant at low values of k_{py}. Due to the stiff k_{s2}, the motion of the wheelsets is coupled in the lateral direction. As k_{py} is increased, the wheelset modes become more elastically coupled (through the

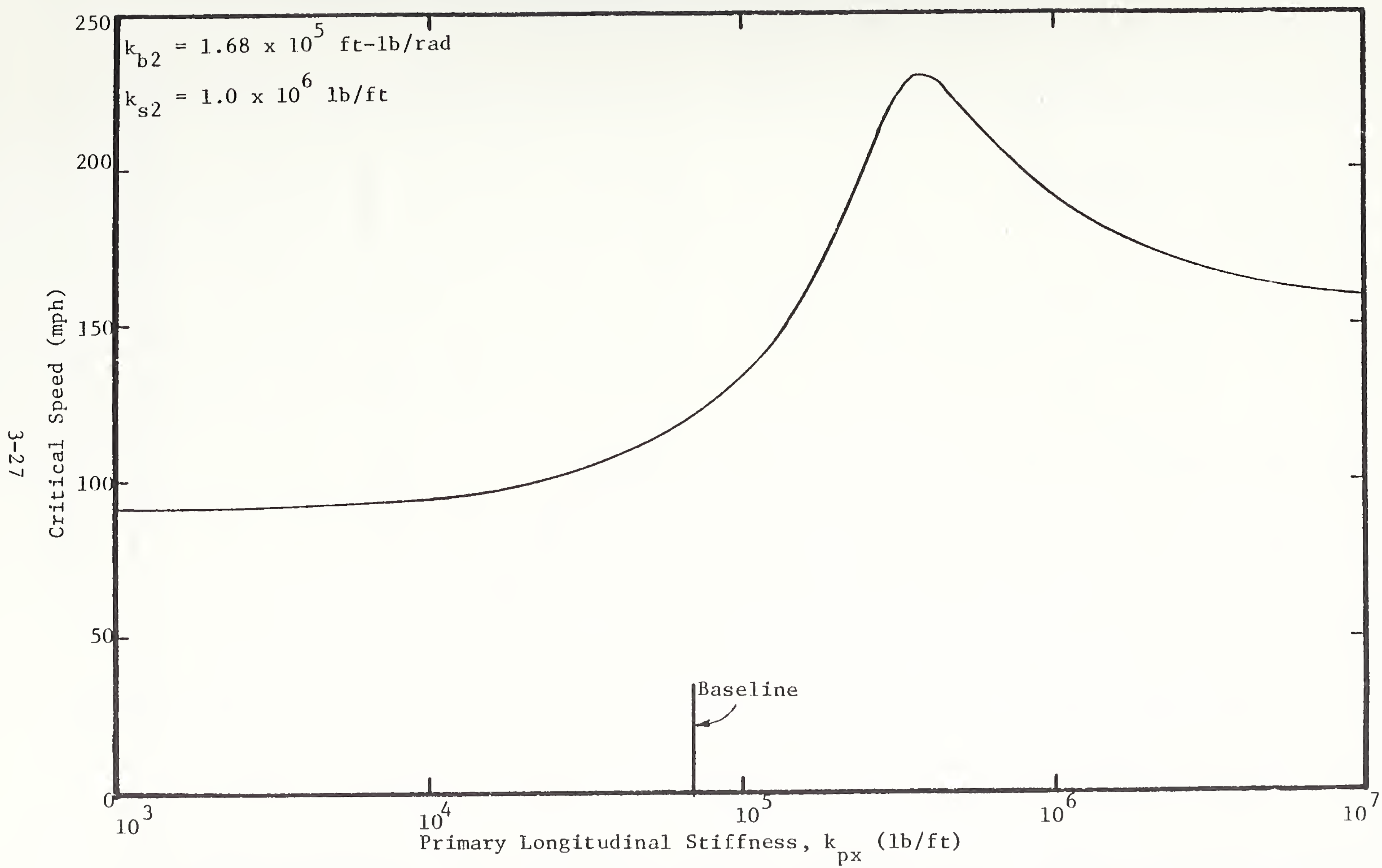

Figure 3.14 Effect of Primary Longitudinal Stiffness on the Critical Speed of a Forced-Steered Radial Truck, FSR I, with New Wheels

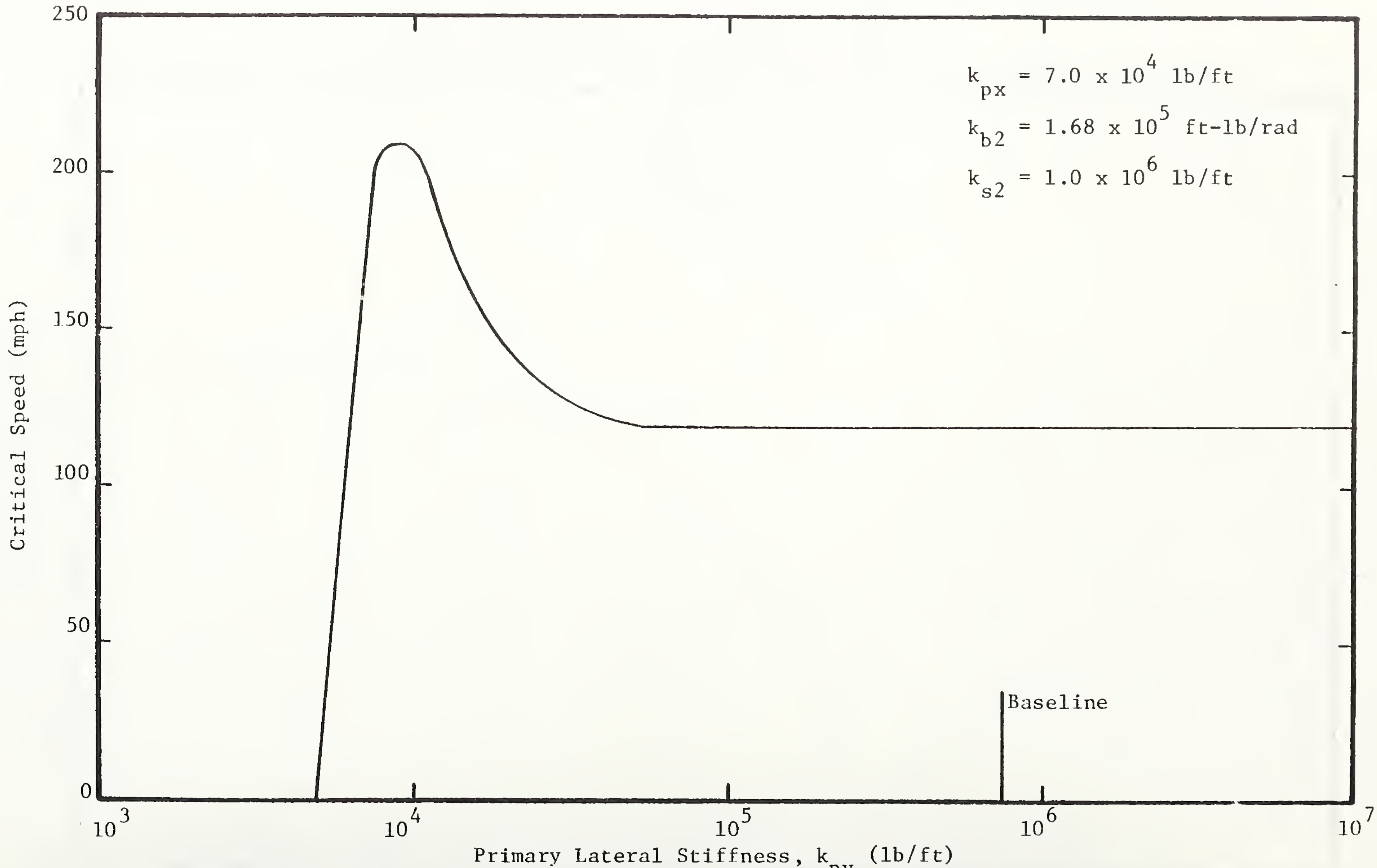

Figure 3.15 Effect of Primary Lateral Stiffness on the Critical Speed of a Forced-Steered Radial Truck, FSR I, with New Wheels

truck frame) and eventually a rigid truck mode is achieved. The secondary suspension system and coupling due to forced-steering from the carbody provide stabilization.

The effect of secondary yaw stiffness, $k_{s\psi}$, on the critical speed of a forced-steered radial truck, FSR I, shown in Figure 3.16 is similar to that of a conventional truck shown in Figure 3.4. For values of $k_{s\psi}$ below 10^5 ft-lb/rad, the critical speed is insensitive to changes in $k_{s\psi}$. The wheelsets are coupled directly through the interaxle stiffnesses and indirectly through the truck frame (elastically coupled wheelset mode). A high value of $k_{s\psi}$ limits the truck yaw displacement and communication between the two wheelsets is achieved primarily through the interaxle stiffnesses. Stabilization of the truck frame by the carbody is significant and the critical speed increases.

Figure 3.17 shows the effect of the interaxle shear stiffness, k_{s2}, on the critical speed of a forced-steered radial truck, FSR I, with new wheels. The behavior is very similar to that exhibited by the SSR truck (Figure 3.10). High values of k_{s2} increase the critical speed due to the interaction of the two wheelsets in the lateral direction, as explained before.

Steering linkages introduce a destabilizing moment on the leading truck of a forced-steered vehicle [20]. This destabilizing moment is proportional to the steering gain and steering linkage stiffness. It is expected that this destabilizing moment at some point cancels the centering moment, which is proportional to G and k_{b2} and inversely proportional to creep coefficients and conicity. Studies using the 15 DOF model have been performed to determine the effects of conicity and creep on the critical speed of a forced steered radial truck, FSR I. The results for conicities larger than 0.025 are

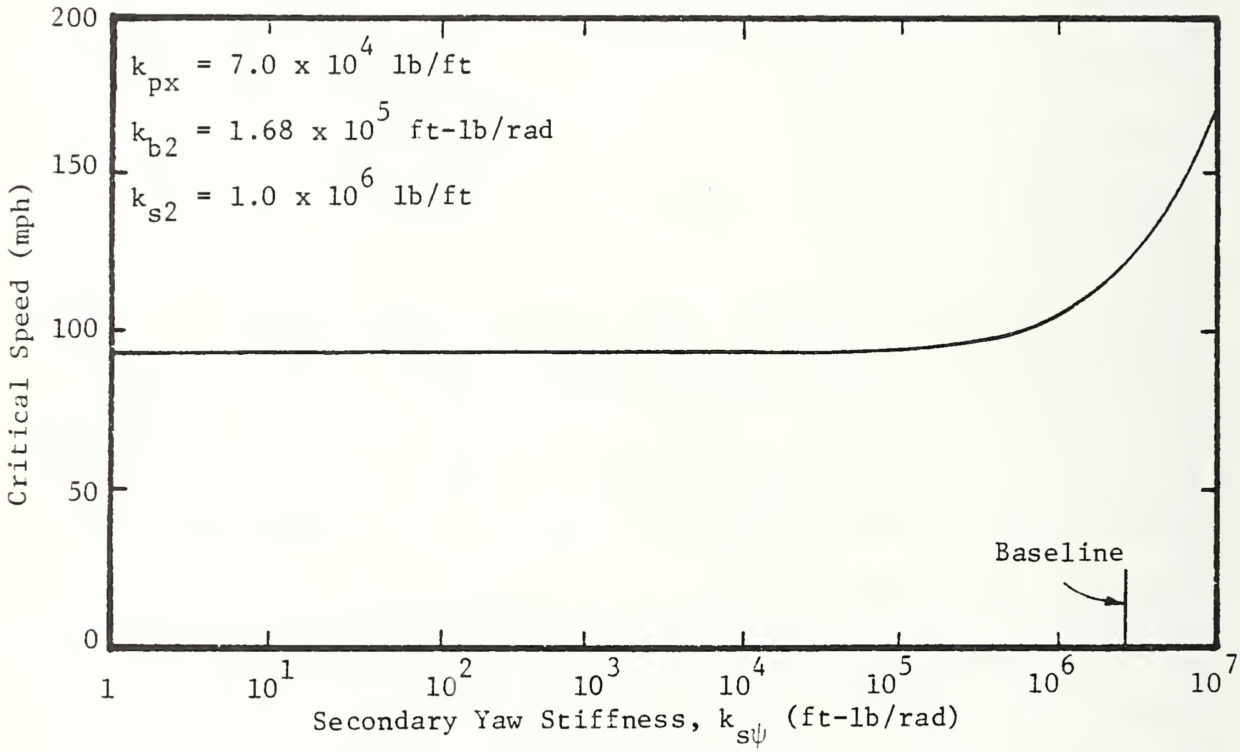

Figure 3.16 Effect of Secondary Yaw Stiffness on the Critical Speed of a Forced-Steered Radial Truck, FSR I, with New Wheels

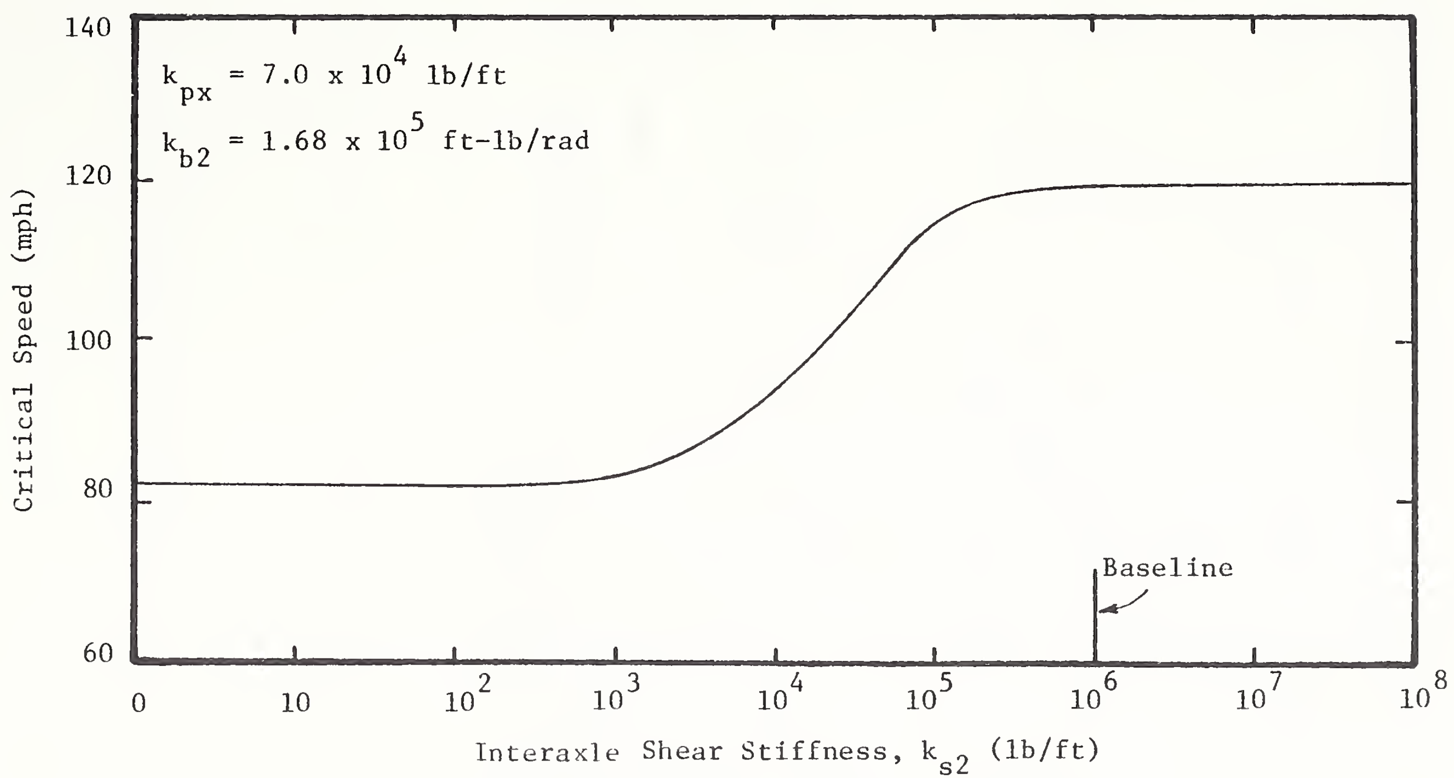

Figure 3.17 Effect of Interaxle Shear Stiffness on the Critical Speed of a Forced-Steered Radial Truck, FSR I, with New Wheels

plotted in Figure 3.18. The critical speed increases for decreased conicity and decreased creep coefficients. The results for very low values of conicity are shown in Figure 3.19, with the conicity plotted in a logarithmic scale. It is noted that the carbody mode plays a role for conicity values below 0.025. Figure 3.19 shows that the critical speed approaches zero at a very low value of conicity. The natural modes (eigenvectors) show that at very low values of conicity, corresponding to almost cylindrical wheels, the whole vehicle moves almost as a rigid body at very low frequencies. This occurs because the longitudinal creep forces that provide the stabilizing moment are very small for small values of conicity. The kinematic instability occurs when the stabilizing moment is overcome by the destabilizing moment of the forced-steering linkages on the front truck. Surjana [27] established the importance of employing finite secondary yaw suspension stiffnesses ($k_{s\psi} > 1 \times 10^6$ ft-lb/rad) in forced steered trucks as a means to delay the occurrence of kinematic instability to very low values of conicity (less than 0.01). It can be concluded that kinematic instability does not occur with a forced-steered truck having the baseline suspension stiffnesses, and a wheel conicity of 0.05 or higher.

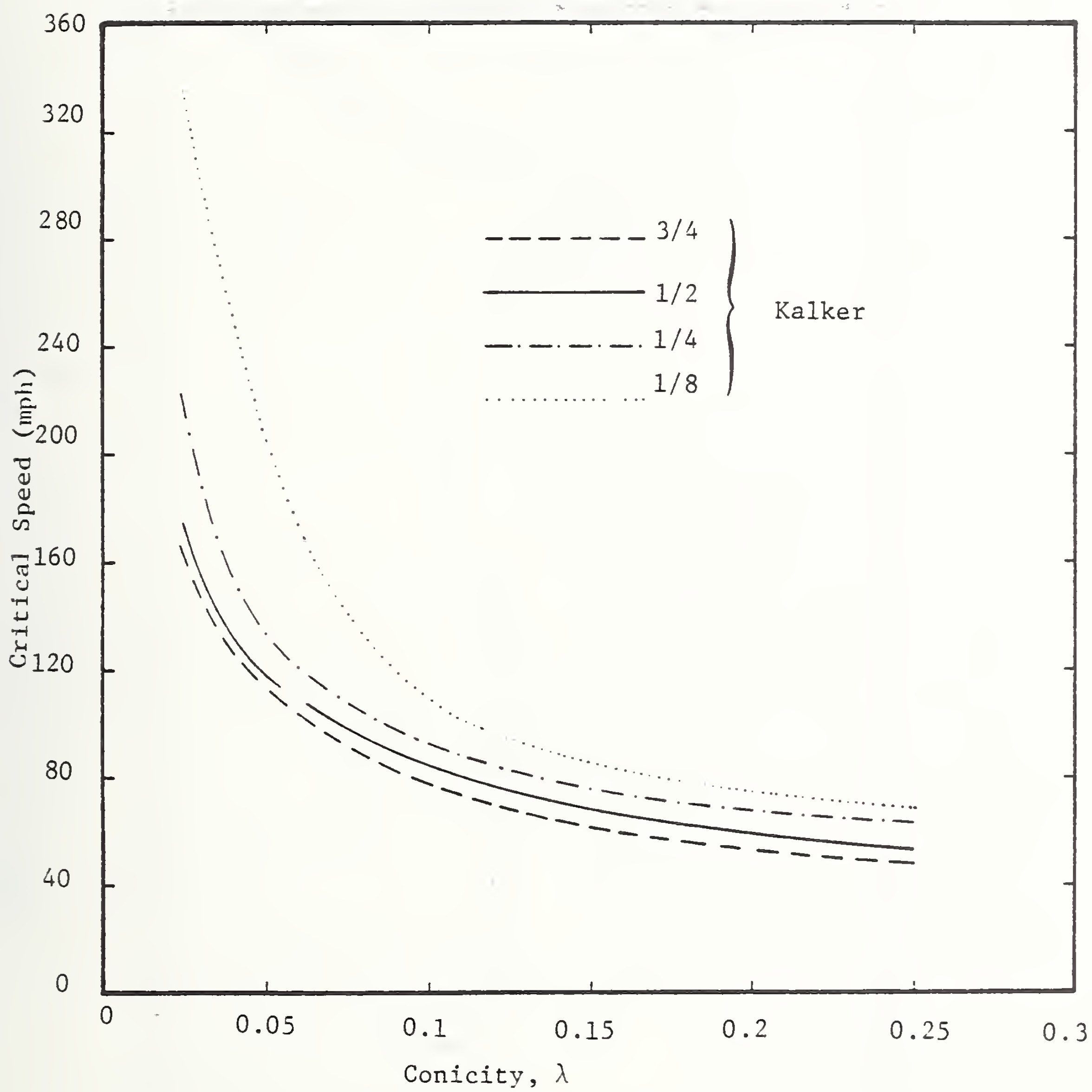

Figure 3.18 Effect of Conicity and Creep Coefficients on the Critical Speed of a Forced-Steered Radial Truck, FSR I, Using 15 DOF Model

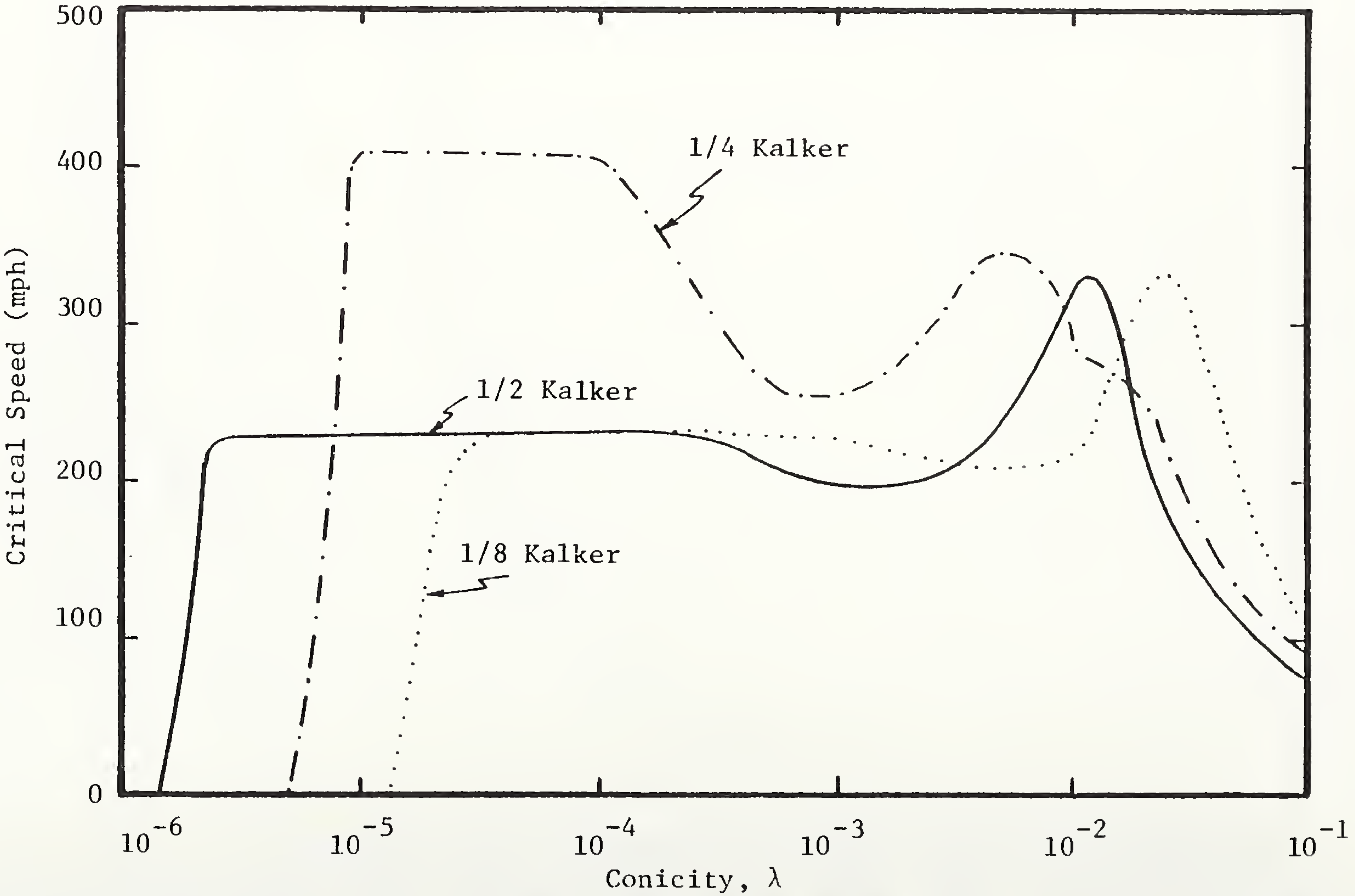

Figure 3.19 Effect of Creep Coefficients on the Critical Speed of a Forced-Steered Radial Truck, FSR I, at Very Low Conicities Using 15 DOF Model.

CHAPTER 4

CURVING PERFORMANCE OF CONVENTIONAL, SELF-STEERED, AND FORCED-STEERED RADIAL TRUCKS

4.1 Introduction

The steady-state curving performance of conventional rail vehicles is influenced strongly by vehicle suspension stiffness elements and wheel/rail profile geometry. As suspension elements between the wheelsets and trucks are stiffened for stability, they prevent radial alignment and induce increased lateral flange forces, especially on tight curves which prevent the wheelsets from developing sufficient rolling radius difference to operate on the pure rolling line. Advanced truck configurations are intended to alleviate these fundamental curving problems while providing adequate stability.

In curved track, the distance which must be traversed along the outer rail is greater than the distance along the inner rail. For a curve of large radius, this difference in distance is small and a wheelset can roll without slip around the curve by displacing outwards slightly. This increases the rolling radius of the outer wheel and decreases the rolling radius of the inner wheel such that the wheel and rail path lengths are identical. This fundamental effect in steady-state curving is known as the lateral shift of the "zero longitudinal creepage" or "pure rolling" line toward the outer rail which occurs with increasing track curvature. When a free wheelset is centered laterally over the pure rolling line and is aligned radially with the curve, the lateral and longitudinal components of creepage (slippage) between the wheel tread and the rail are zero. The wheelset is in steady-state equilibrium since no net forces/moments act on it in the lateral or yaw directions (assuming balanced running and neglecting spin components of creepage).

For shallow curves, the lateral shift of the pure rolling line is less than the available flange clearance and a free wheelset at the pure rolling line can steer itself perfectly around the curve. As the curvature increases, the pure rolling line moves outward. When the lateral shift of the pure rolling line exceeds the flange clearance, the wheelset is forced to remain inside the pure rolling line, resulting in a condition of sustained flange contact. One wheel of the wheelset must slip or slide on the rail as the wheelset rotates. To satisfy equilibrium, the wheelset adopts a positive yaw angle of attack.

In a rigid truck, the two wheelsets are locked by an infinitely rigid primary suspension preventing any relative lateral or yaw displacement between the wheelsets. As a rigid truck negotiates a curve, it is impossible for both wheelsets to align radially and thus perfect steering cannot be achieved. The rigid truck will assume an equilibrium configuration. (See [6, 25] for analytic expressions for the rigid truck equilibrium geometry based on linear curving models.)

A realistic truck with some wheelset bending and shear flexibility will assume a steady-state geometry in between the free wheelset and rigid truck configurations. If the shear and bending stiffnesses are fairly soft, the wheelsets of the truck will behave like free wheelsets. For a stiff truck with large shear and bending stiffnesses, the behavior will be closer to that of a rigid truck. Figure 4.1 shows pictorially the equilibrium geometry of a truck with intermediate shear and bending stiffnesses negotiating a tight curve. This flexible truck allows bending deflection to occur, resulting in a lead wheelset angle of attack and flange force lower than those which occur for the rigid truck configuration. Also contributing to the reduced angle of

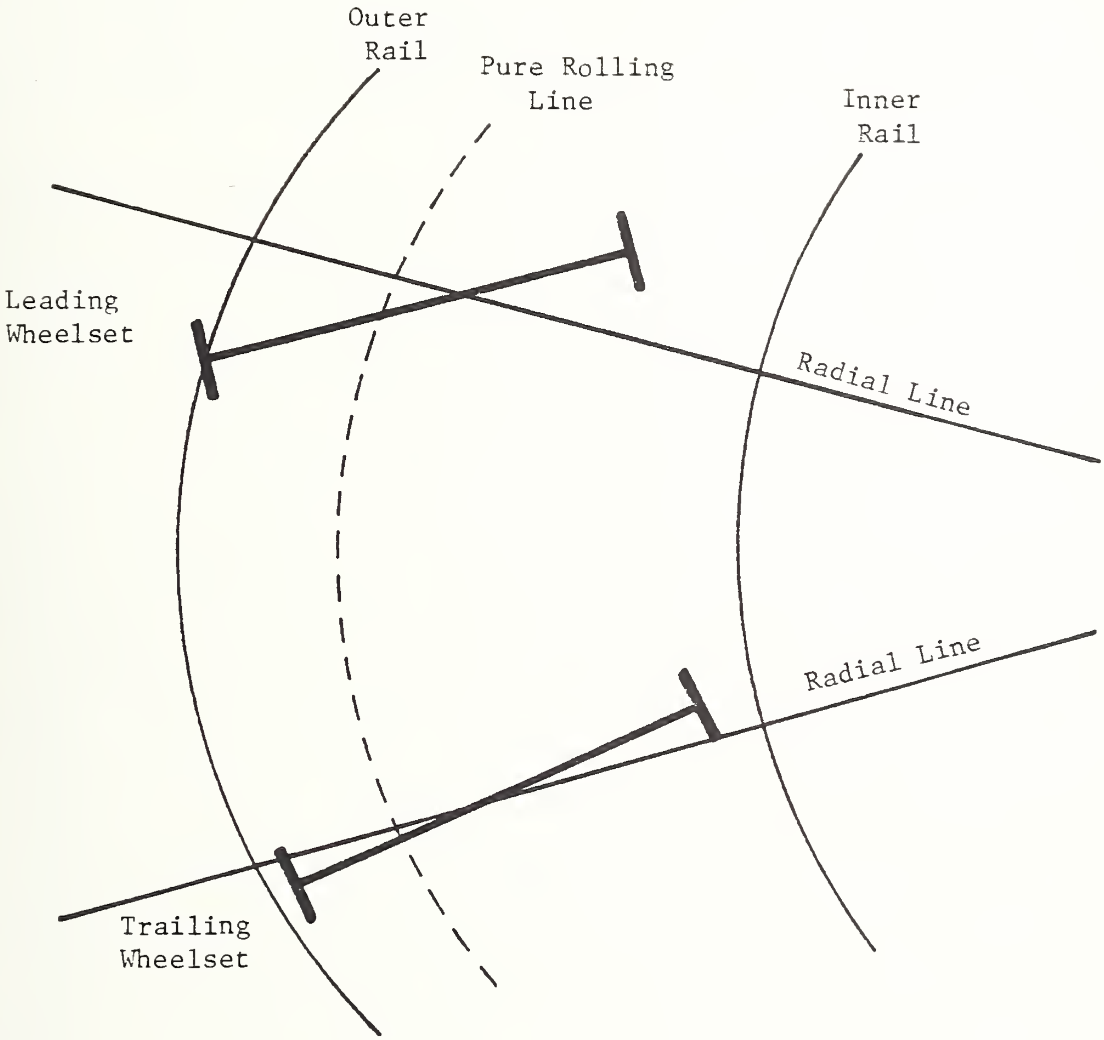

Figure 4.1 Steady-State Equilibrium Configuration for the Wheelsets of a Flexible Truck

attack is the equilibrium requirement that the rear wheelset swing toward the outer rail and maintain near radial alignment.

In this chapter the curving performance of rail vehicles employing conventional, self-steered, and forced-steered radial trucks are investigated using the detailed steady state nonlinear model described in Section 2.4.* The effects of track curvature, suspension design, and wheel/rail profile are evaluated.

The work in the contact patch(es) at the flanging wheel is selected as the principal curving performance index. The work index is receiving increasing acceptance as an indicator of curving performance since it is related to wheel and rail wear and train rolling resistance [9, 29].

The wheel/rail profile has a strong influence on vehicle curving performance. The profile determines the nature of the wheel/rail contact at the flanging wheel as the wheelset is displaced laterally. Some profiles, such as the Heumann wheel profile shown in Figure 4.2 and discussed in Appendix F, are characterized by a smooth transition of a single point of contact from tread to flange with increasing lateral excursion. Other profiles such as the new AAR 1 in 20 wheel profile, have steep flanges, for which simultaneous two point contact occurs at the tread and flange when the net wheelset lateral excursion equals the flange clearance. Single point wheel/rail contact occurs at other lateral excursions, i.e., in the tread region and high up on the flange, as discussed in Appendix F.

The forces and moments acting on a wheelset in steady state curving are significantly different when single-point and two-point contact occur at the flanging wheel. When two-point contact occurs large longitudinal

---

*The results of the curving parametric studies of these trucks with new and Heumann wheels are summarized in Appendix I.

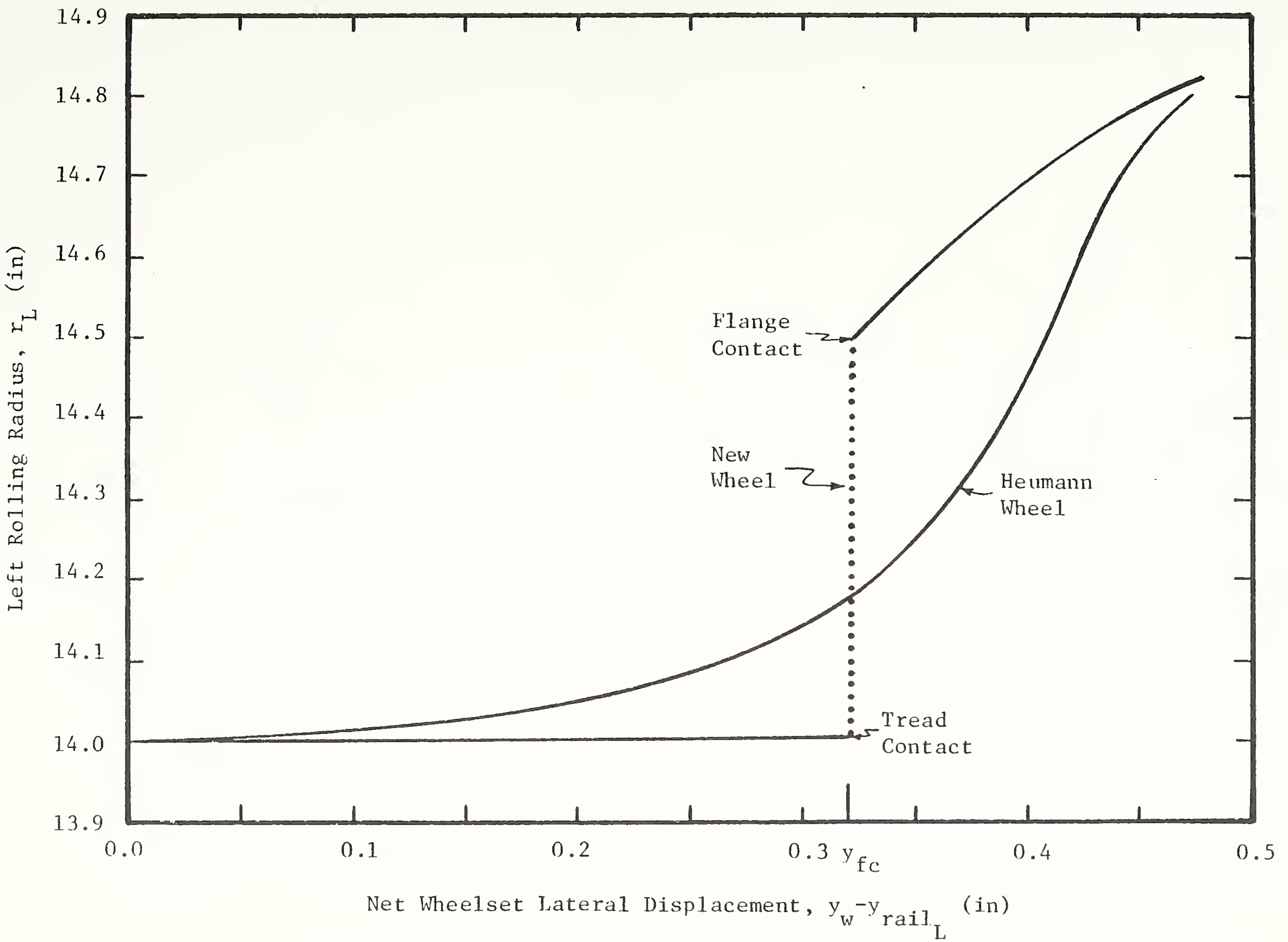

Figure 4.2 Comparison of Flanging Wheel Rolling Radii vs. Wheelset Lateral Displacement for New and Heumann Wheel/Rail Profiles.

creep forces develop in opposite directions at the tread and flange contact patches of the flanging wheel which partially cancel one another. With single-point contact a longitudinal creep force develops at the flanging wheel which is larger than the net longitudinal creep force which acts when two-point contact occurs. The larger longitudinal creep forces which develop when single point contact occurs result in a larger yaw restoring moment which helps the wheelset to position radially. Thus, a wheelset with Heumann wheels develops a larger restoring moment (at the same lateral force) than a wheelset with new wheels, as shown in Figure 4.3 for the case of zero angle of attack and a 10° curve. For a wheelset with Heumann wheels the lateral excursion is less than flange clearance at low levels of lateral force. The outer (flanging) wheel is in tread contact and a small longitudinal creep force develops. As the wheelset with Heumann wheels is displaced laterally, corresponding to higher wheelset lateral force, the outer wheel begins to flange and the longitudinal creep force at the single contact patch becomes large (due to the large rolling radius). This results in a significant increase in the wheelset yaw moment. Eventually the creep forces saturate as the outer wheel rides high up on the flange and a maximum wheelset yaw moment develops. This occurs for wheelset lateral forces greater than 8000 lb. For the wheelset with new wheels, the lateral excursion equals the flange clearance and the outer wheel is in two point tread-flange contact for the range of lateral forces plotted in Figure 4.3. The longitudinal creep forces at the flange and tread contact patches act in opposite directions, because the longitudinal creep force at the flange contact patch is less than at the tread contact patch, while at higher levels of lateral force, the longitudinal creep force

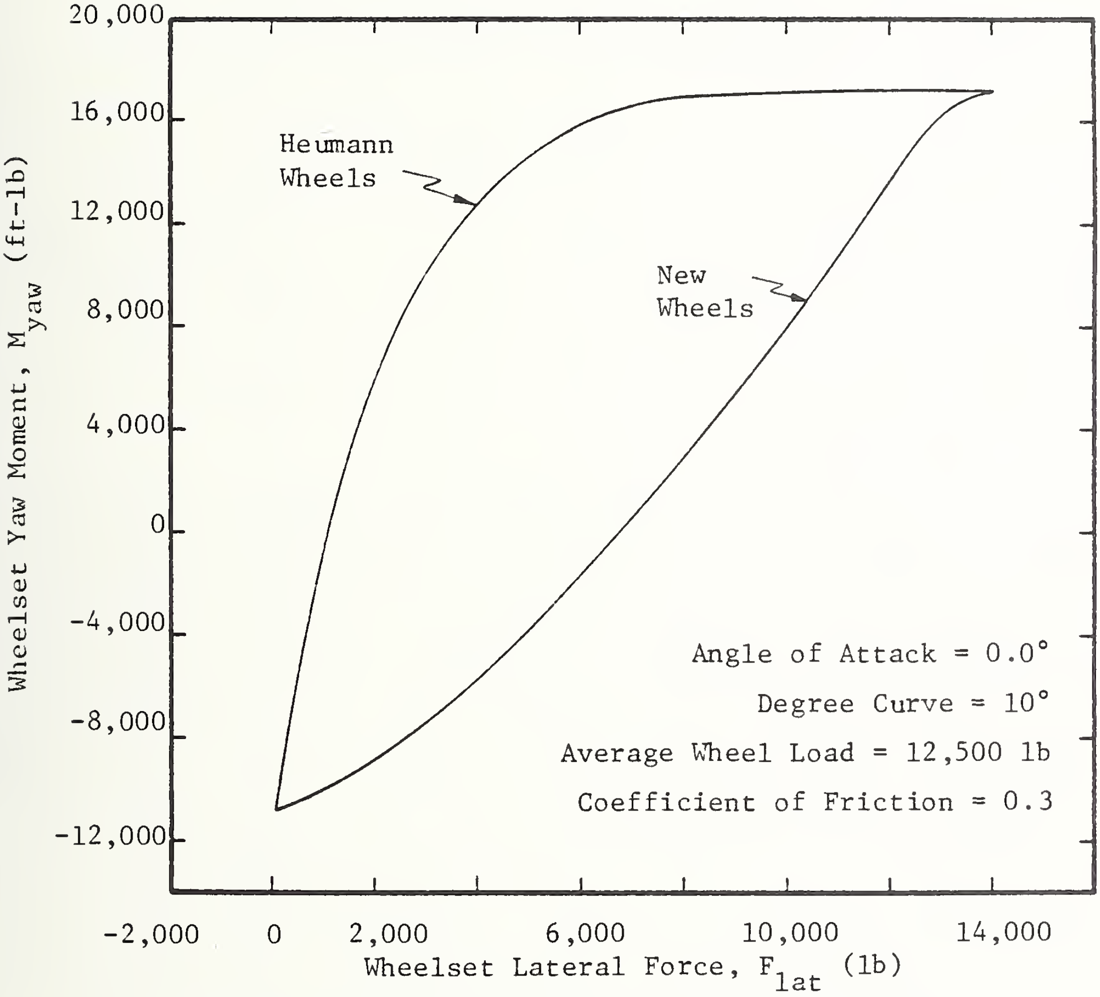

Figure 4.3 Wheelset Yaw Moment vs. Wheelset Lateral Force for New and Heumann Wheels.

at the flange contact patch is larger. This shift in direction of the net longitudinal creep force at the flanging wheel is responsible for the change from negative to positive yaw moments with increasing levels of lateral force. The creep forces at the flange contact patch do not saturate until the lateral force exceeds 14,000 lb. Results of further study have shown that the difference in yaw moments with wheelsets having new and Heumann wheels diminishes with increasing curvature. This is due to creep forces which saturate earlier because of the larger longitudinal creepage which occurs with increased curvature. In summary, the results of Figure 4.3 show that a wheelset with Heumann wheels provides a larger restoring yaw moment than a wheelset with new wheels, which suggest that the Heumann wheel profile would be advantageous for curving.

The improved steady-state curving performance of a wheelset with Heumann wheels as compared to new wheels is borne out by considering the work which occurs at the flanging wheel. Figure 4.4 is a plot of the work versus lateral-to-vertical (L/V) force ratio at the flanging wheel for a wheelset with new and Heumann wheels negotiating a 10° curve with zero angle of attack. Lower levels of work are expended for the wheelset with Heumann wheels at the same (L/V) ratio. This is due to the fact that only single point contact occurs at the outer wheel for all lateral excursions. For the wheelset with Heumann wheels, the work increases with increasing (L/V) ratios as the components of creep force and creepage grow. The work reaches a maximum at (L/V) $\simeq$ 0.7 (equivalent to a wheelset lateral force of $\simeq$ 9000 lb), when the creep force at the flange contact patch saturates. Further increases in (L/V) ratio result in constant work since the creep forces are fully saturated. For the wheelset with new wheels, two-point contact occurs. The work at the flanging wheel is the sum of

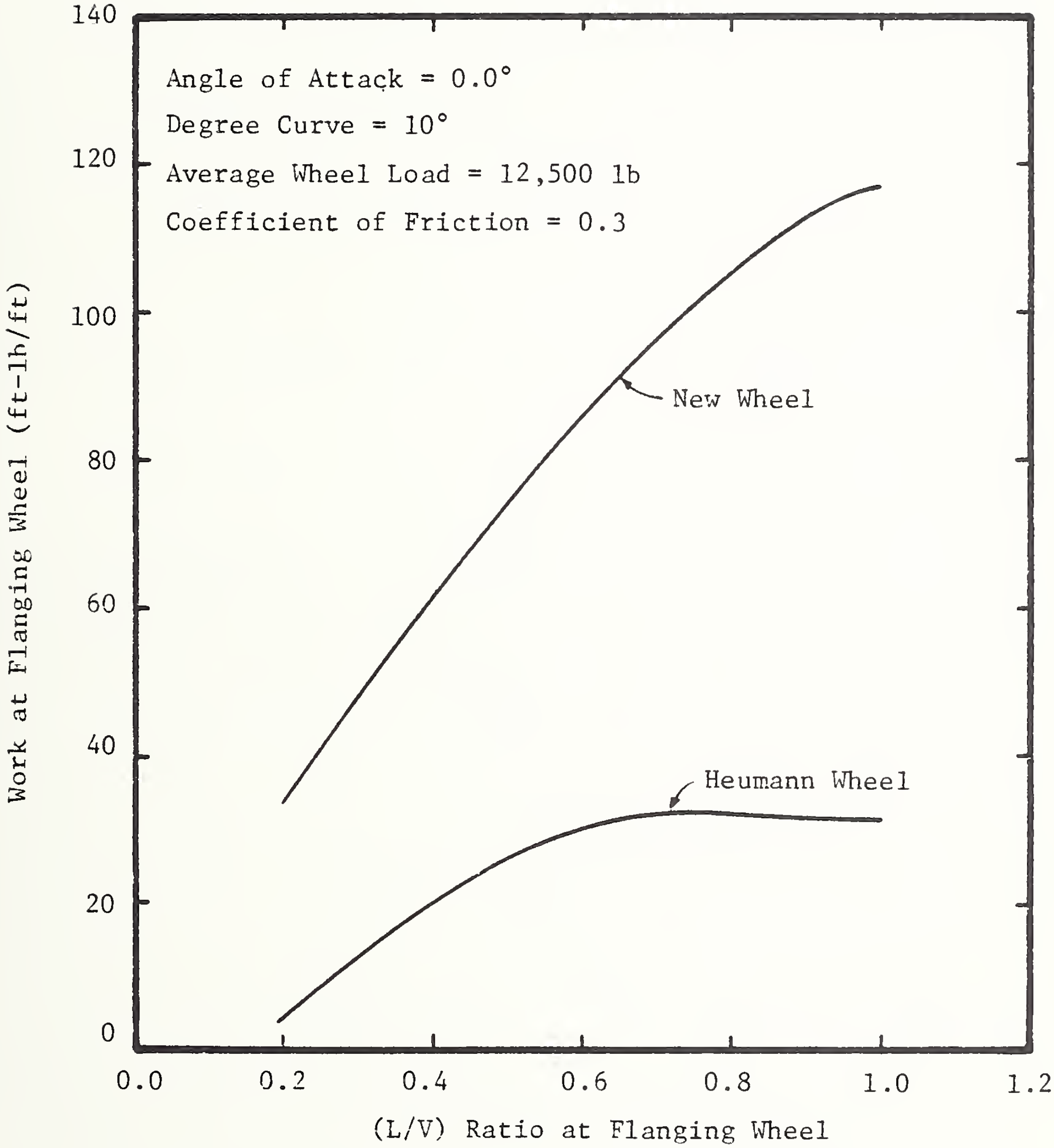

Figure 4.4 Flanging Wheel Work vs. (L/V) Ratio for New and Heumann Wheels.

the work at the tread and flange contact patches. The work at the flange contact patch increases significantly with increasing (L/V) ratio due to the large increase in creep force, while the work at the tread contact patch diminishes as the distribution of forces shifts from the tread to flange patches. The creep forces at the flange do not saturate until (L/V) $\simeq$ 1.2 (equivalent to a wheelset lateral force of 14,000 lb), which is out of the range of values plotted in Figure 4.3. Again, the difference in flanging wheel work for wheelsets with new and Heumann wheels decreases with increasing curvature due to the earlier onset of creep force saturation.

These single wheelset model results are important because they strongly govern the vehicle curving performance.

4.2 Curving Performance of Conventional Trucks

The dominant parameters influencing the steady-state curving behavior of conventional trucks are the primary longitudinal stiffness and the wheel/rail profile geometry. The primary longitudinal stiffness, k_{px}, is equivalent to the total truck bending stiffness: $k_b = d_p^2 k_{px}$. For low values of truck bending stiffness or of k_{px} the wheelsets can adopt yaw displacements which are decoupled from the truck orientation. This allows the wheelsets to align radially in curves, which is beneficial for curving performance.

In Chapter 3, baseline stiffnesses were selected to give truck critical speeds of 120 mph. As a result, the baseline primary longitudinal stiffness of a conventional truck with new wheels is $k_{px} = 1.35 \times 10^5$ lb/ft, while the baseline stiffness of a conventional truck with Heumann wheels is $k_{px} = 6.50 \times 10^5$ lb/ft. These values are in the range of typical stiffnesses of current transit trucks: 1.0×10^5 lb/ft $< k_{px} < 2.0 \times 10^6$ lb/ft. As mentioned in Chapter 3, the primary spring of the Chicago CTA 2400 rapid transit truck has a relatively soft longitudinal stiffness of 2.0×10^5 lb/ft [19]. The standard WMATA car/Rockwell truck has a moderately stiff primary longitudinal stiffness of 1.38×10^6 lb/ft, while the Budd Pioneer III truck has a very stiff primary longitudinal stiffness of 3.5×10^6 lb/ft [2, 28]. Attempts have been made to reduce the longitudinal stiffness through redesign of the primary bushing/shear pad assembly. The proposed primary springs must fit in the space available in the existing trucks. A modified bonded rubber bushing built for the WMATA car/Rockwell truck was designed to achieve a minimum longitudinal stiffness of approximately 3.0×10^5 lb/ft [2]. Metalastick Canada has designed a new primary spring consisting of flat rubber shear pads for the CTA 2400 rapid transit truck which has a longitudinal stiffness of 5.0×10^4 lb/ft [28].

In the following paragraphs, the combined influence of k_{px} and curvature on the curving behavior of a conventional truck with new wheels on worn rails is discussed. In Figure 4.5 the effect of k_{px} on the work at the flanging wheel is plotted for four curvatures: 2.5°, 5°, 10°, and 20° curves. For shallow and moderate curves (2.5°, 5°, and 10°), the work increases as k_{px} is stiffened; for the tight 20° curve, the work rises sharply and then asymptotically reaches a constant as k_{px} is increased. For low values of k_{px}, the wheelsets are loosely restrained in yaw, and can adopt yaw displacements independent of the truck yaw position. The dominant creep forces which act on the wheelsets are the lateral creep forces required to balance forces from the primary lateral stiffness. On the other hand, a rigid wheelset-truck configuration is approached at high stiffnesses, and the work approaches a constant. This is expected since the increased bending stiffness will yaw the wheelsets away from radial alignment. The wheelsets will develop

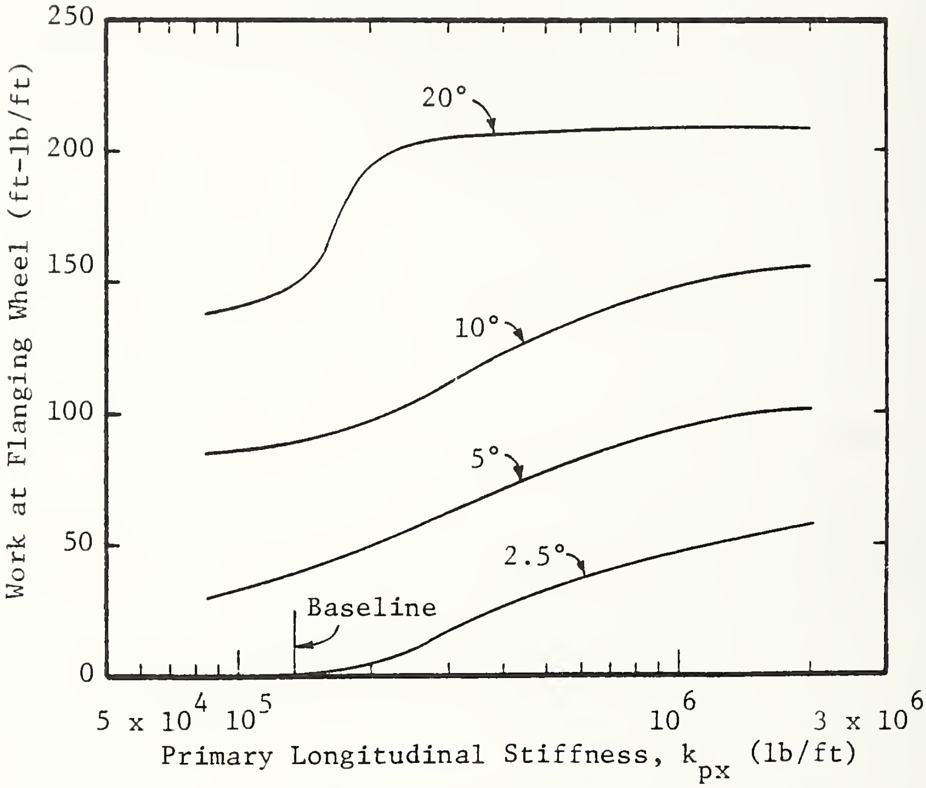

Figure 4.5 Work at Flanging Wheel vs. Primary Longitudinal Stiffness for a Conventional Truck with New Wheels Negotiating 2.5°, 5°, 10°, and 20° Curves

longitudinal creep forces to partially counteract the increase in yaw stiffness, and these forces help to yaw the wheelsets back toward radial positions. Eventually, the creep forces saturate at the adhesion limit and the work at the flanging wheel reaches a constant. Further increases in k_{px} have negligible effect.

In addition to the effect of stiffness, the creep forces which develop are a function of curvature. At very low curvatures, the track is essentially tangent and the pure rolling line coincides with, or is just slightly to the outside of, the track centerline. As the degree curve increases, the pure rolling line moves farther to the outside of the track centerline and the leading wheelset attempts to follow it by displacing laterally until it reaches the flange clearance. The condition of two point tread-flange contact occurs at the outer wheel, with forces at the tread patch dominating. With still tighter curves, the leading wheelset lateral excursion remains fixed at the flange clearance, as the pure rolling line moves further out. At the outer wheel the forces decrease at the tread contact patch and grow larger at the flange patch. The creep forces which develop at the flange contact patch increase, due to the substantial creepages, until they saturate at the adhesion limit. The fact that the creep forces saturate for increased curvature is the reason that the work at the flanging wheel reaches a constant at the lowest k_{px} for the tight 20° curve in Figure 4.5.

The behavior of the trailing wheelset is also a function of the k_{px} and curvature. In general, the trailing wheelset displaces laterally inward and the angle of attack decreases slightly with increasing k_{px} as the truck becomes stiffer and the wheelsets and truck assume a more rigid configuration. This is shown schematically in Figure 4.6. For a tight curve, the trailing

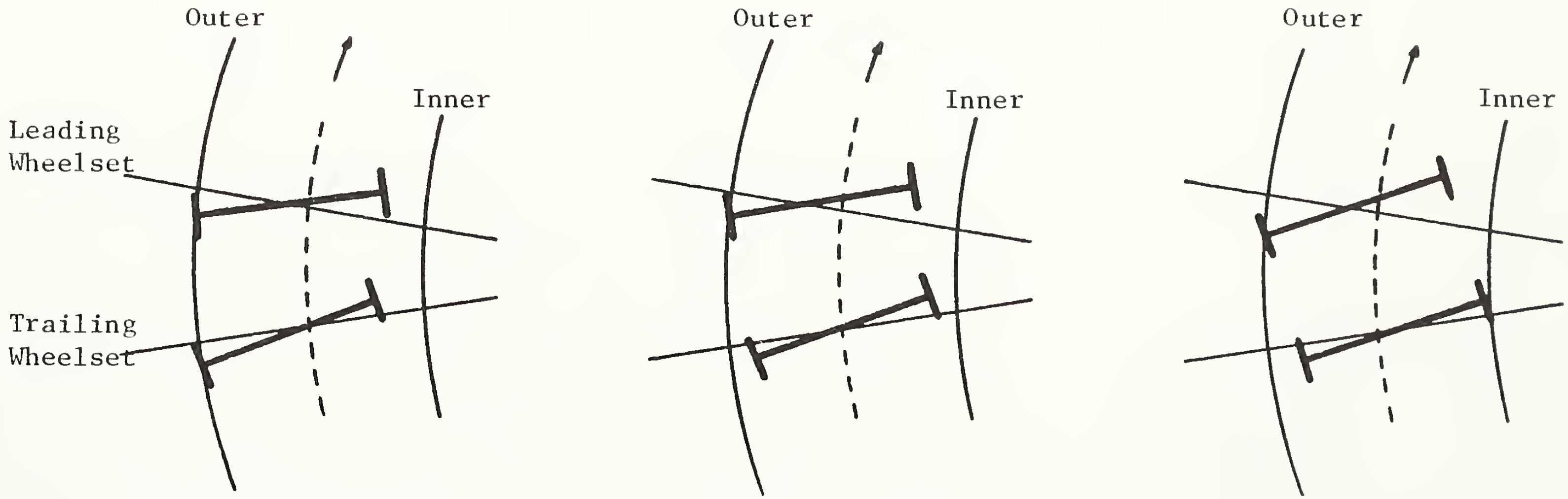

(a) Floating Truck:
Very Soft k_{px}

(b) Flexible Truck:
Intermediate k_{px}

(c) Rigid Truck:
Very Stiff k_{px}

Figure 4.6 Effect of Increasing Primary Longitudinal Stiffness on the Curving Behavior of a Conventional Truck Negotiating a Tight Curve.

wheelset moves from flange contact at the outer wheel for a truck with very soft k_{px} to flange contact at the inner wheel for a rigid truck with very stiff k_{px}. Thus, two-point contact occurs at the leading and trailing wheels of a truck with very low k_{px} negotiating a high degree curve, whereas for a truck with very soft k_{px} the outer wheel of the leading wheelset and the inner wheel of the trailing wheelset are in two-point contact. For a shallow curve, the trailing wheelset of a truck with very soft k_{px} does not displace to flange clearance at the outer wheel, and displaces inward only slightly as the truck becomes more rigid. Thus, single-point contact occurs at all wheels of a truck with very low k_{px} traversing a shallow curve, and two point contact develops at the lead outer wheel of a stiff truck.

The leading wheelset angle of attack of a conventional truck with new wheels as a function of primary longitudinal stiffness and curvature is plotted in Figure 4.7. It is very similar to the graph of flanging wheel work shown in Figure 4.5. The angle of attack of the leading wheelset increases as k_{px} is increased for shallow and moderate degree curves (2.5°, 5° and 10°), whereas it increases sharply and then approaches a constant with increasing k_{px} for the sharp 20° curve. At very low values of k_{px}, the truck has wheelsets which are essentially "free" to adopt angles of attack independent of the truck yaw. The predominate creep forces which act on the wheelsets of a truck with soft k_{px} are the lateral creep forces which occur for equilibrium with the lateral forces from the primary lateral suspension and normal loads. These lateral creep forces are a function of the angle of attack. For positive angles of attack, positive lateral creep forces develop which push the wheelset toward the outer rail, whereas for negative angles of attack negative lateral creep forces occur which restrain the wheelset from displacing out. A

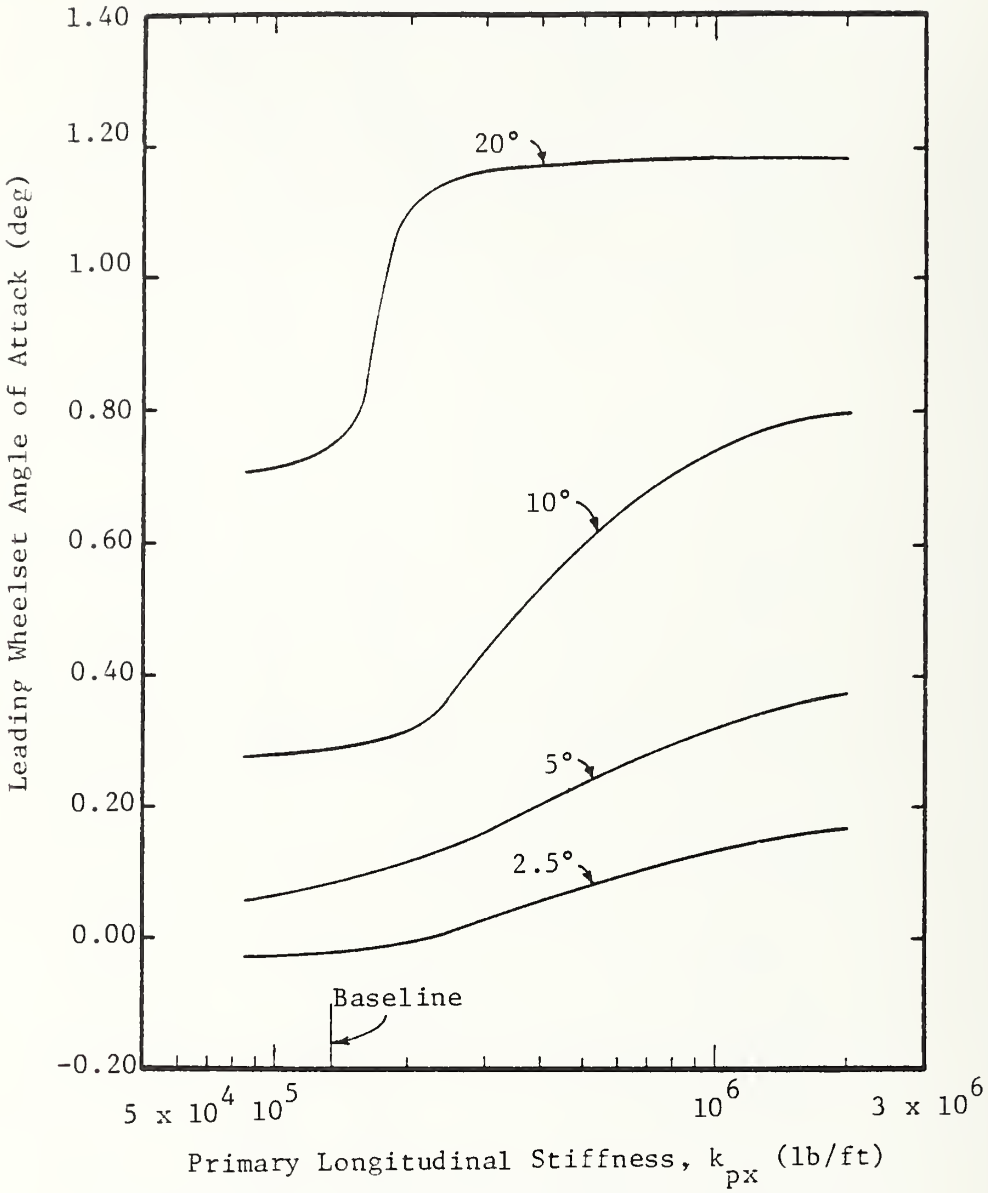

Figure 4.7 Leading Wheelset Angle of Attack vs. Primary Longitudinal Stiffness of a Conventional Truck with New Wheels Negotiating 2.5°, 5°, 10°, and 20° Curves.

conventional truck with soft k_{px} traversing moderate and high degree curves (5°, 10°, and 20° curves) has a positive leading wheelset angle of attack and thus develops positive lateral creep forces, which are needed for equilibrium. A truck with soft k_{px} negotiating a shallow curve (2.5° curve) develops a slightly negative angle of attack, needed to generate lateral creep forces in the opposite direction to balance the lateral components of primary suspension and normal forces. At high values of k_{px}, the wheelsets are almost rigidly coupled to the truck and follow it in yaw due to the high yaw bending stiffness. Longitudinal creep forces develop which create wheelset yaw moments to help balance the large yaw bending moment from k_{px}. As k_{px} is increased still further, larger longitudinal creep forces develop until the resultant creep force at each contact patch saturates at the adhesion limit. Eventually, the wheelset-truck configuration becomes fully-rigid and the wheelset angles of attack approach a constant.

A suspension yaw moment acts on the leading wheelset due to k_{px} and is balanced predominantly by a yaw moment provided by the longitudinal creep forces. As mentioned, for a truck with soft k_{px} the longitudinal creep forces are small (in comparison to the lateral creep forces which are large) corresponding to a small wheelset yaw moment. Large longitudinal creep forces and thus a large wheelset yaw moment occur for a truck with very stiff k_{px} negotiating shallow curves. As this almost rigid truck negotiates tighter curves, severe flanging at the outer wheel of the leading wheelset occurs and the creep forces at the flange contact patch saturate. Larger lateral creep forces are needed for equilibrium (to balance the larger lateral normal forces) and thus the angle of attack becomes larger. As a result of the creep force saturation and the requirement for larger lateral creep forces, smaller longitudinal creep forces are available and thus the wheelset yaw moment decreases. This information is summarized in Figure 4.8 which shows the effect of primary longitudinal stiffness and curvature on the leading wheelset angle of attack and leading wheelset yaw moment of a conventional truck with new wheels. The leading wheelset of a truck with soft k_{px} negotiating shallow curves develops small negative angles of attack which correspond with negative lateral creep forces needed for equilibrium.

The effect of primary longitudinal stiffness and curvature on the leading outer wheel lateral force of a conventional truck with new wheels is shown in Figure 4.9. This lateral force is the sum of the lateral components of the creep and normal forces which act at the contact patches of the flanging wheel. As with the work and angle of attack versus stiffness functions (Figures 4.5 and 4.7, respectively), the lateral force (1) increases and then approaches a constant as k_{px} is increased, and (2) increases as tighter curves are negotiated. At high values of k_{px}, the creep forces saturate at the adhesion limit and the normal forces approach a constant since the truck assumes a rigid configuration. The lead outer wheel lateral force remains constant with further increases in k_{px}.

Lateral equilibrium of the wheelsets represents a balance of lateral normal forces, lateral creep forces, and forces from the primary lateral suspension. The latter suspension forces are determined by the primary lateral stiffness and the relative wheelset-truck lateral strokes. These strokes are influenced by the secondary suspension yaw moments exerted on the trucks by the carbody. The moments are normally similar in magnitude, but opposite in directions on the two trucks as shown in Figure 4.10. A positive moment acts on the front truck, which hinders curving by turning the

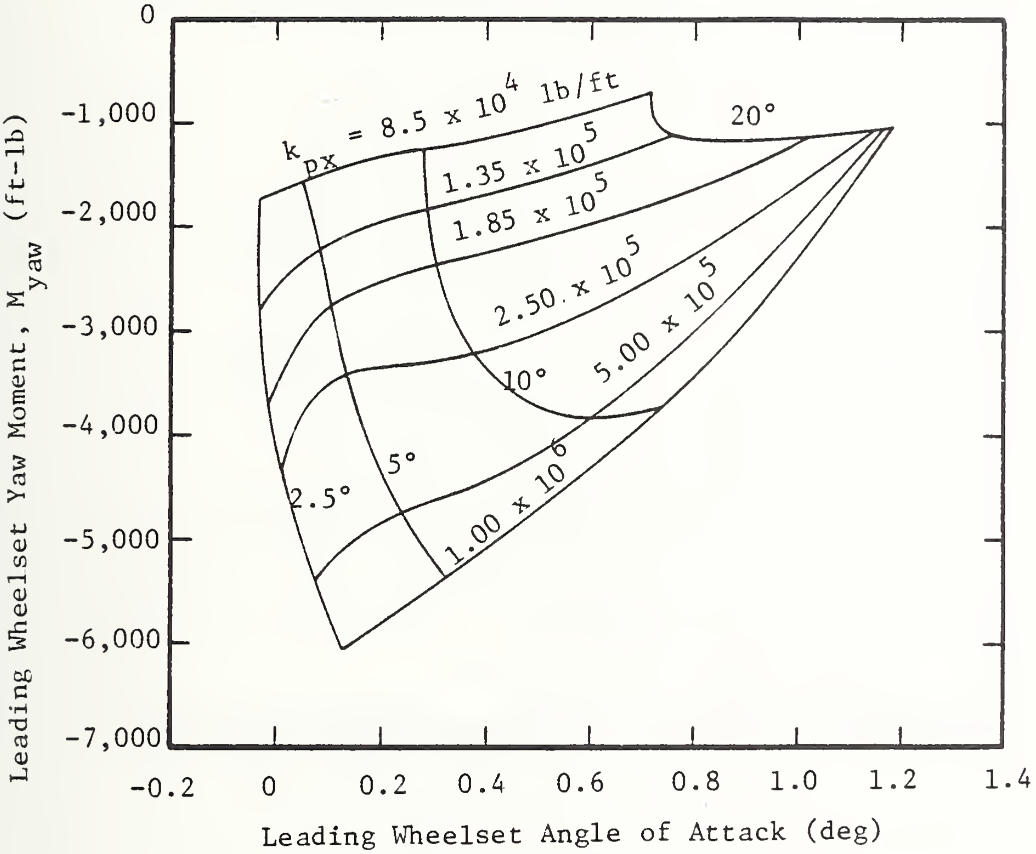

Figure 4.8 Effect of Curvature and Primary Longitudinal Stiffness on the Leading Wheelset Angle of Attack and Yaw Moment of a Conventional Truck with New Wheels.

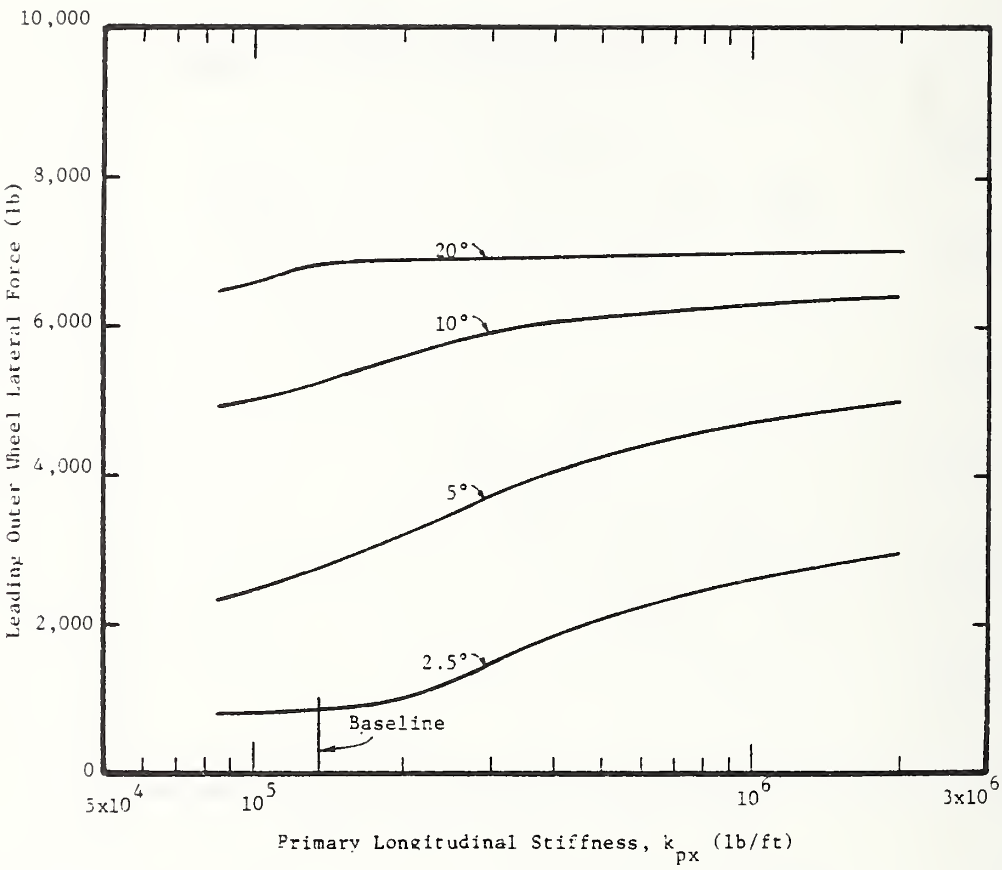

Figure 4.9 Leading Outer Wheel Lateral Force vs. Primary Longitudinal Stiffness of a Conventional Truck with New Wheels Negotiating 2.5°, 5°, 10°, and 20° Curves.

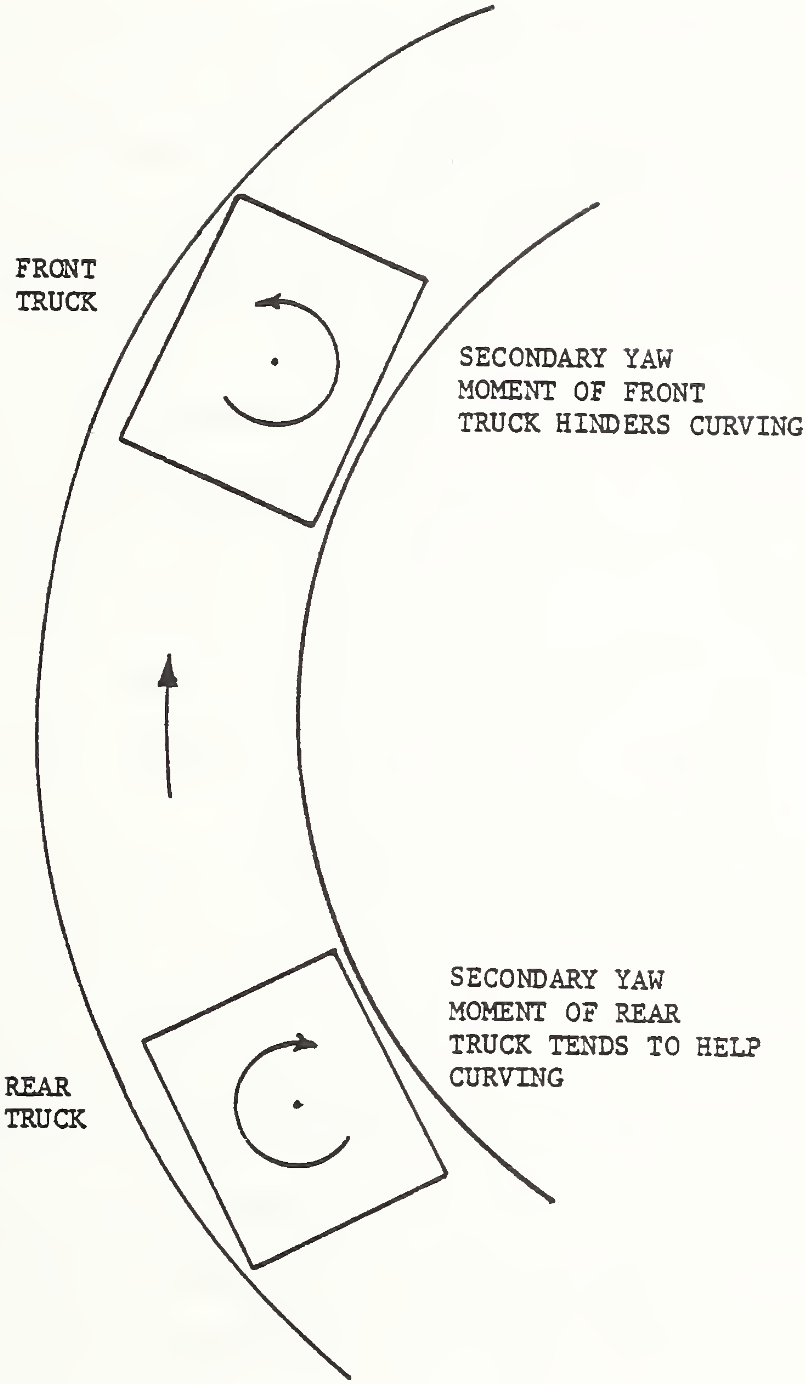

Figure 4.10 Direction of Secondary Yaw Moment on Front and Rear Trucks During Curve Negotiation.

truck toward the outside rail, while a negative moment acts on the rear truck, which tends to help curving by steering the truck toward the inside rail. (If secondary yaw breakaway has already occurred, however, the above moments change direction in the curve exit spiral. In the present study, this reversal is not considered.) In summary, the primary lateral suspension force included in the lateral force equilibrium of a wheelset depends upon the yaw moment from the secondary suspension. The secondary suspension yaw moment acting on the front truck degrades curving performance by pushing the outer wheel of the leading wheelset of the front truck into the flange (assuming a moderate or stiff value of primary lateral stiffness, k_{py}). This leading outer wheel experiences the most severe flanging of all the wheels of the full vehicle. The effect of secondary yaw breakaway torque on the work at the leading outer wheel will be discussed later.

The effect of primary lateral stiffness, k_{py}, on the work at the flanging wheel of a baseline conventional truck with new wheels negotiating a 10° curve is shown in Figure 4.11. As k_{py} is increased from low values, the work decreases slightly (about 10%) and then asymptotically reaches a constant. At low values of k_{py}, the wheelsets are loosely restrained laterally relative to the truck frame. The leading wheelset displaces laterally until the flange clearance, and two-point wheel/rail contact occurs at the outer wheel. As k_{py} is increased, the lateral displacement of the wheelsets becomes more coupled to the truck position and eventually a laterally rigid configuration is approached. The leading wheelset is still fixed at the flange clearance and two-point contact occurs at the outer wheel. However, the laterally stiffer truck somewhat restrains the wheelset and thus smaller creep forces and work develop.

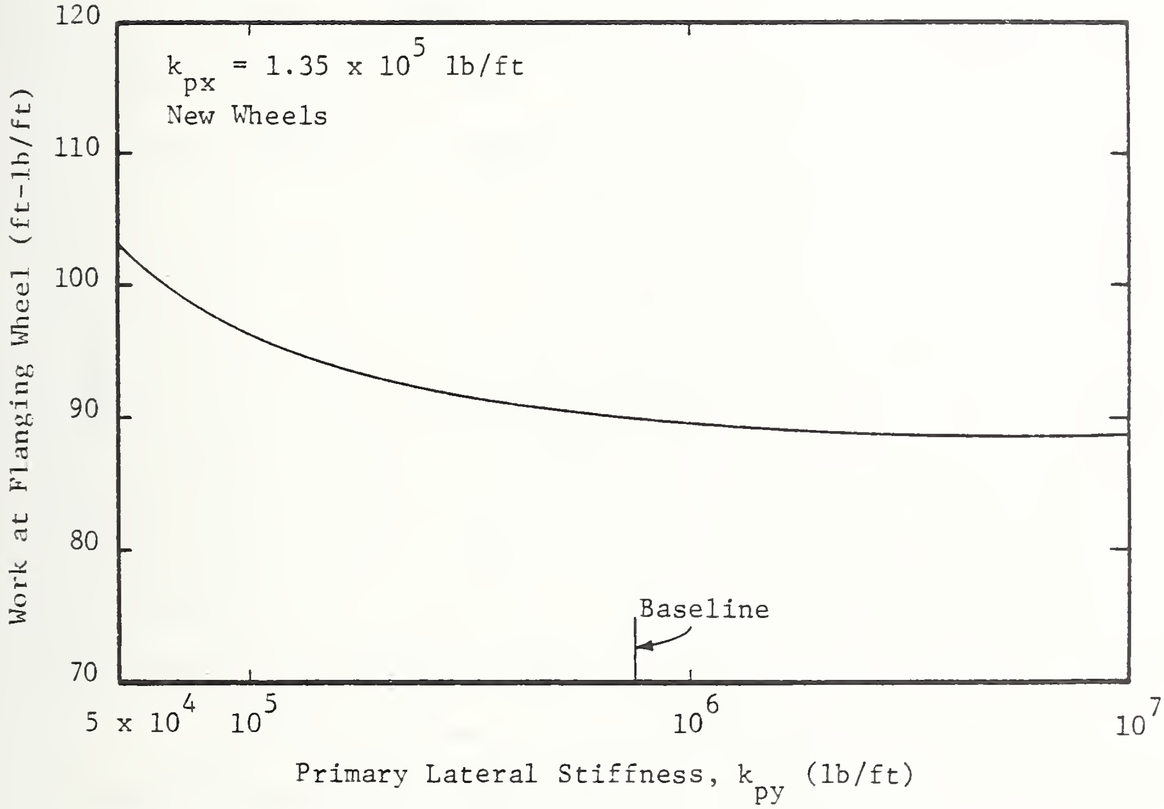

Figure 4.11 Work at Flanging Wheel vs. Primary Lateral Stiffness of a Conventional Truck with New Wheels Negotiating a 10° Curve.

Figures 4.12 and 4.13 show the influence of the two curving inputs, curvature and cant deficiency, respectively, on the work at the flanging wheel of a baseline conventional truck with new wheels. In Figure 4.12, the degree curve is varied from 0° for tangent track to 20° representing a tight curve of radius 290 ft. For small degree curves (less than 2.5°), the leading wheelset lateral excursion is less than flange clearance and thus single point contact occurs at all wheels. Small amounts of work (less than 1 ft-lb/ft) are expended at the flanging wheel. As the truck (in balanced running) negotiates tighter curves (2.5° and greater), the leading wheelset is fixed at the flange clearance and two point contact occurs at the outer wheel. Significant increases in work occur; at 5°, 10°, and 20° the work is 39 ft-lb/ft, 90 ft-lb/ft, and 149 ft-lb/ft, respectively. The majority of transit curves are less than 7.5°, although some systems have curves as high as 20°. Yard curves are typically greater than 7.5°, and most often restraining rails are present. In this study, the behavior of trucks (at balanced running) negotiating 2.5°, 5°, 10° and 20° curves is investigated.

In Figure 4.13 the work at the flanging wheel of a baseline conventional truck with new wheels negotiating a 10° curve is shown as the cant deficiency is varied from $\phi_d = 0$ for balanced running to a lateral unbalance of 0.1 g's. The curving performance is slightly degraded with increasing cant deficiency. Larger forces develop at the flange contact patch to counteract the increased lateral force on the wheelset and, as a result, the work at the flanging wheel increases. Wheel lift at the inner wheel occurs when cant deficiency is large, for instance $\phi_d > 0.5$ g corresponding to $V > 75$ ft/sec negotiating a 20° curve with a superelevation of 6 inches. Cant

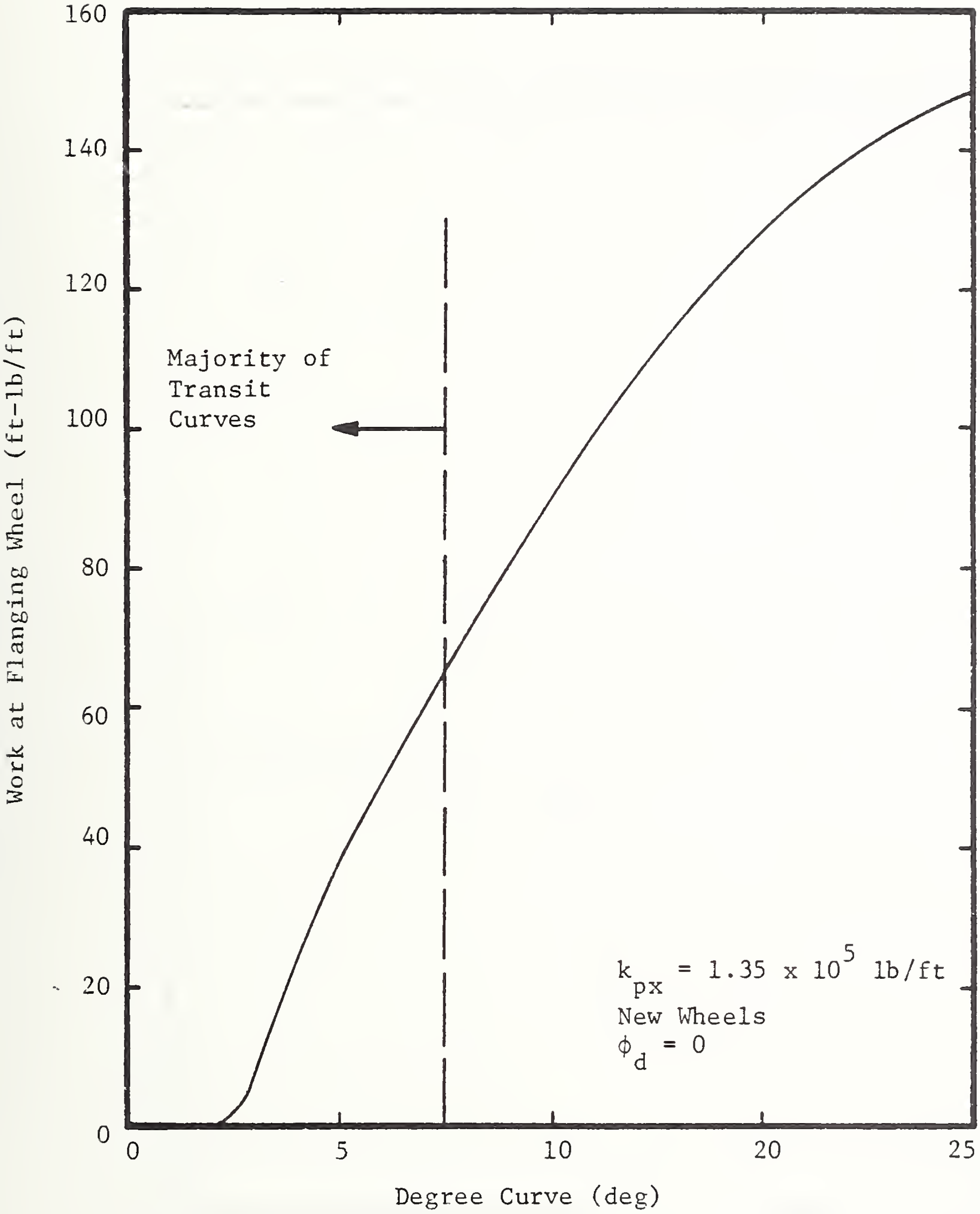

Figure 4.12 Effect of Curvature on the Work at the Flanging Wheel of a Conventional Truck with New Wheels at Balanced Running.

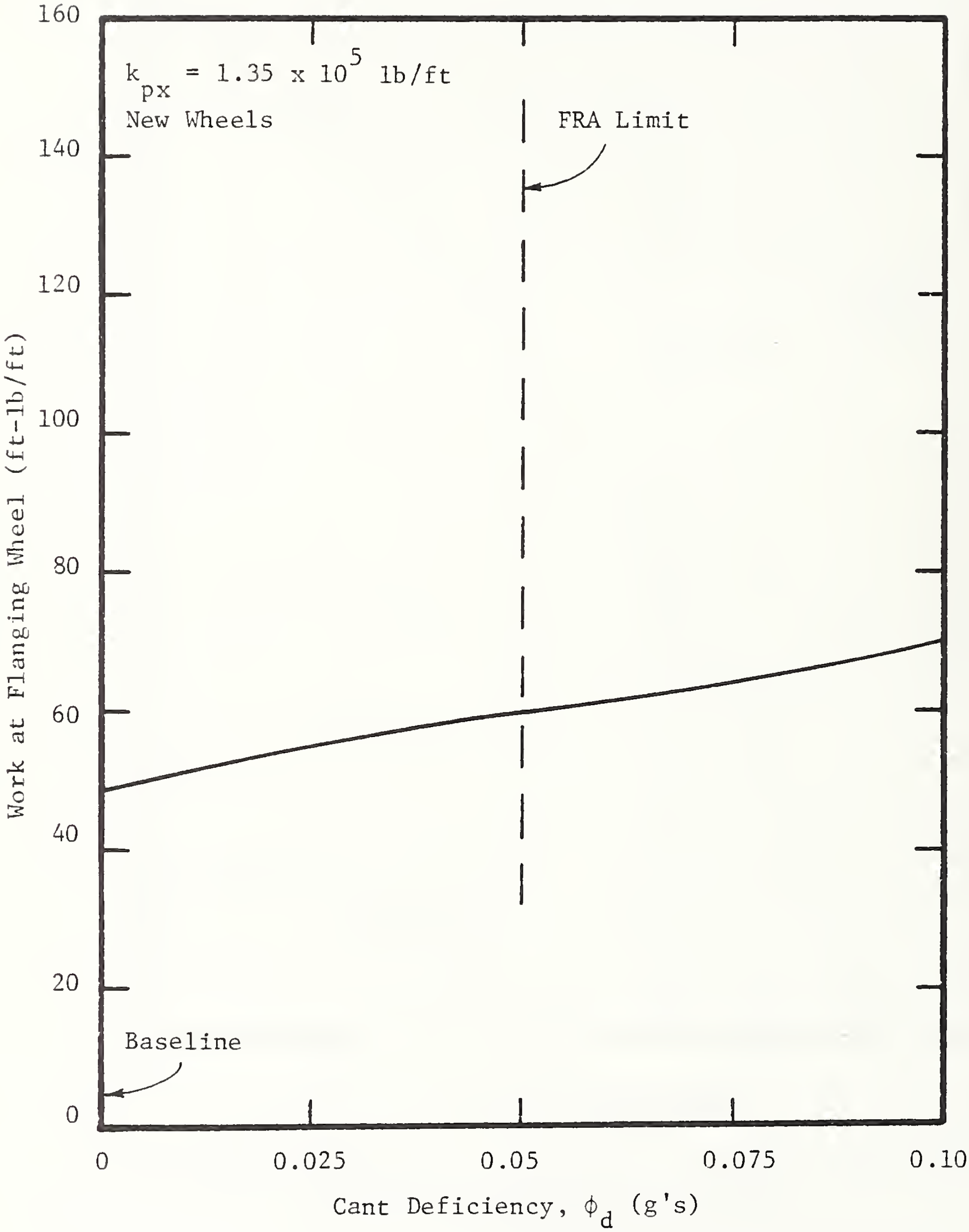

Figure 4.13 Effect of Cant Deficiency on the Work at the Flanging Wheel of a Conventional Truck with New Wheels Negotiating a 10° Curve.

deficiency is the less important of the two curving inputs, especially within the range of the Federal Railway Administration limit of $\phi_d < 0.05$ g's [30]. In this report, all curving performance studies are performed for trucks at balanced running, i.e., $\phi_d = 0$.

Figure 4.14 illustrates the effect of secondary yaw breakaway torque on the curving performance of a baseline conventional truck operating on a 10° curve. As the breakaway torque increases, the work at the leading outer wheel of the front truck increases and the work at the leading outer wheel of the rear truck decreases. This is consistent with the predicted behavior when considering the directions of the yaw breakaway torques on the two trucks, shown in Figure 4.10. On the front truck, the torque acts to steer the truck toward the outer rail. (The lateral and longitudinal creep forces acting on the wheelset also turn the truck toward the outer rail.) This creates larger forces at the leading outer wheel as well as a larger leading wheelset angle of attack, both of which increase the work. On the rear truck, the torque acts in the opposite direction and relieves the forces at the leading outer wheel and the work decreases. In this report, the baseline value of breakaway torque is 7500 ft-lb and the work at the flanging wheel of the front truck is the principal curving performance index. Furthermore, it is assumed that secondary yaw breakaway has occured, which is true for trucks negotiating curves greater than 1 degree.

Figure 4.15 shows the work at the flanging wheel of a baseline conventional truck negotiating a 10° curve as the creep coefficients are varied from zero to 100 percent of the values predicted by Kalker's Linear

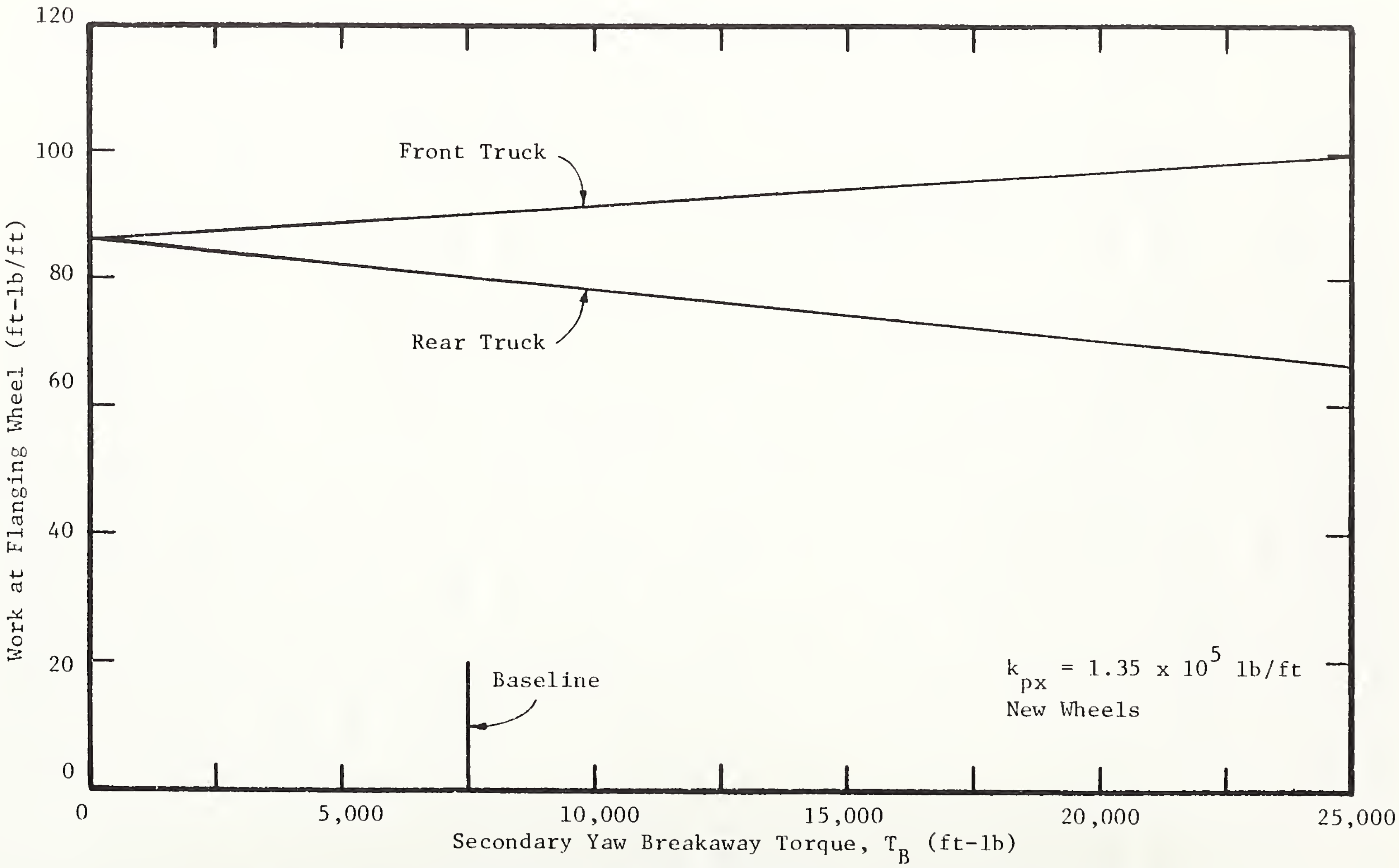

Figure 4.14 Effect of Secondary Yaw Breakaway Torque on the Work at the Flanging Wheel of a Conventional Truck with New Wheels Negotiating a 10° Curve.

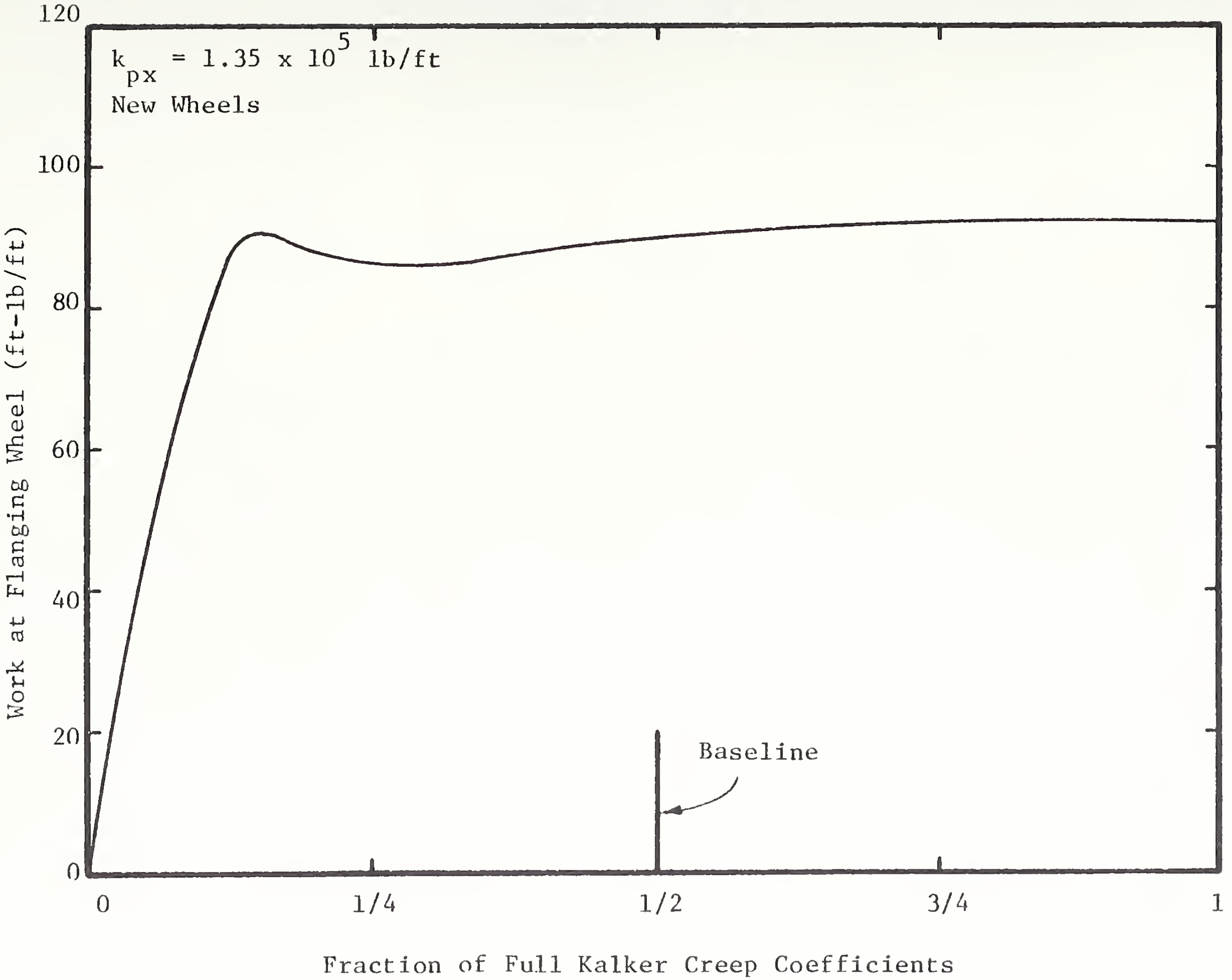

Figure 4.15 Work at Flanging Wheel vs. Fraction of Full Kalker Creep Coefficients for a Conventional Truck with New Wheels Negotiating a 10° Curve.

theory of creep [31]. With zero creep coefficients, no creep forces develop and thus the work is zero. With increasing fractions of full Kalker coefficients, the creep forces grow until saturation occurs. Creep forces at the flange contact patch are fully saturated for fractions greater than about one-eighth. The work is constant for further increases in creep coefficients. The fact that the curving performance is insensitive to creep coefficients over a wide range suggests that the use of more sophisticated creep force models would probably not change the conclusions of the curving analysis.

The influence of the coefficient of friction on the work at the flanging wheel for the same truck is shown in Figure 4.16. Creep forces are saturated and performance is virtually linear with the friction coefficient for $\mu < 0.4$. The magnitude of the creep force is dictated by the coefficient of friction. For higher coefficients of friction, $\mu > 0.4$, severe flanging occurs leading to wheel climb and eventually derailment may occur. Field experiments show that the coefficient of friction between wheel and rail varies over a wide range, from $\mu = 0.1$ for wet surfaces to $\mu = 0.6$ for very clean dry surfaces [13]. A baseline value of 0.3 is used in this report.

The influence of axle drive torque on the work at the flanging wheel of a baseline conventional truck with new wheels negotiating a 10° curve is shown in Figure 4.17. The work increases slightly with drive torque due to increased longitudinal creepage and grows rapidly as the wheel/rail friction limit is approached for which significant creepage occurs. Typical transit vehicles have small drive torques which correspond to the portion of the graph with slightly increasing work. Thus, drive torque has little influence on curving performance.

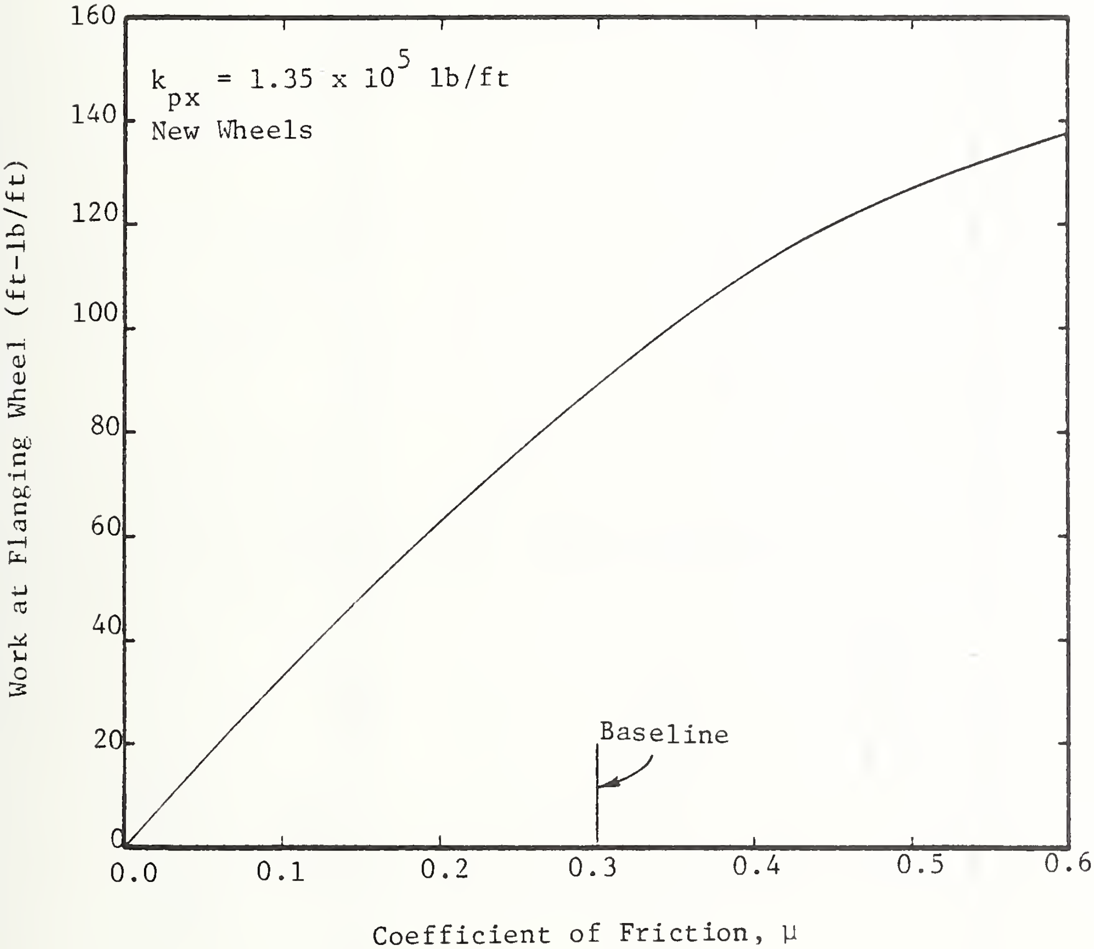

Figure 4.16 Effect of Coefficient of Friction on the Work at the Flanging Wheel of a Conventional Truck With New Wheels Negotiating a 10° Curve.

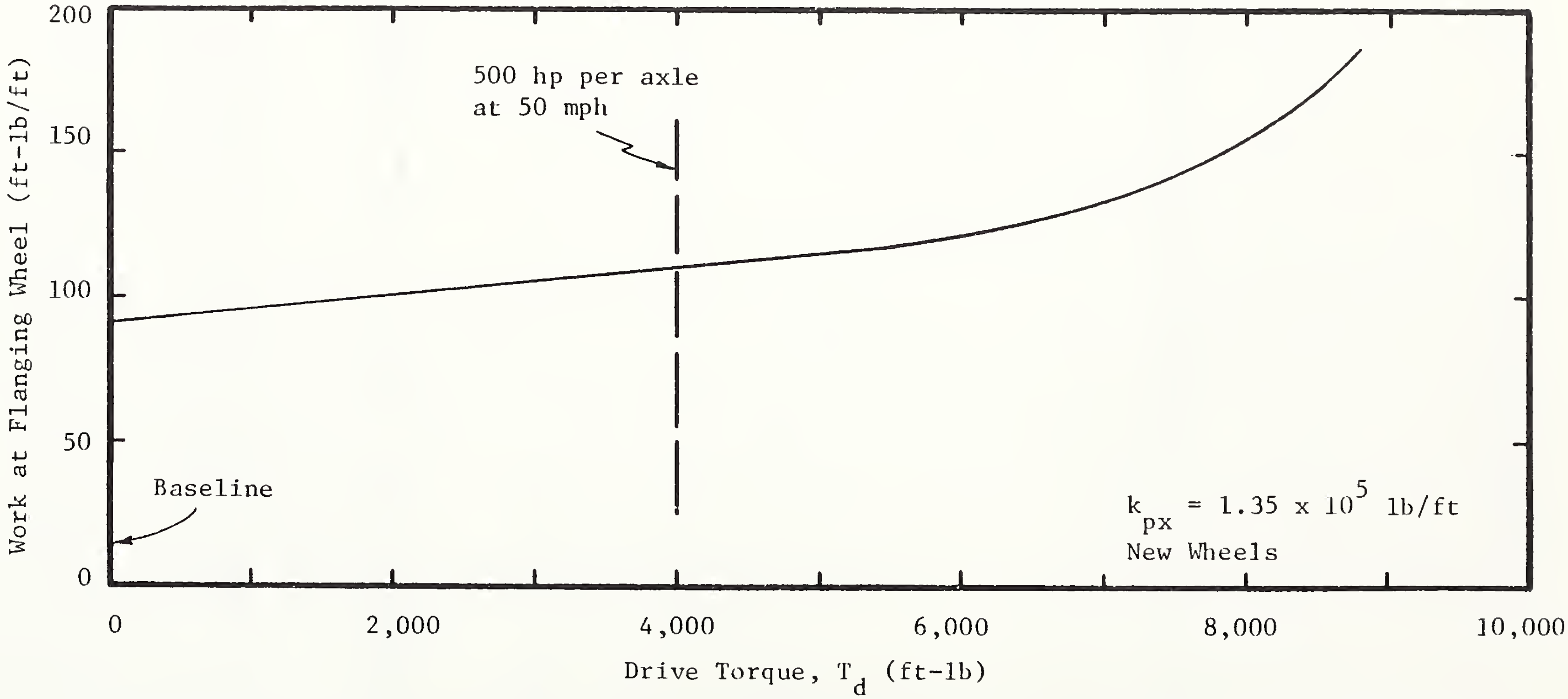

Figure 4.17 Effect of Axle Drive Torque on the Work at the Flanging Wheel of a Conventional Truck with New Wheels Negotiating a 10° Curve.

The curving studies assume that the rail and rail bed are rigid. In actuality, the rails are not rigid but deflect laterally with lateral loading. A simple model for lateral rail flexibility is discussed in Appendix F. The effects of lateral rail flexibility on the curving performance of a conventional truck with $k_{px} = 5.0 \times 10^5$ lb/ft and new wheels negotiating a 10° curve are listed in Table 4.1. With flexibility, the high rail deflects out resulting in an increased leading wheelset lateral excursion. However, the geometry of the truck, the wheel/rail forces, and the wheel/rail work are practically insensitive to rail flexibility. Thus, in this report the results of the curving studies in terms of flanging wheel work are meaningful even though they assume rigid rails.

The curving behavior of a conventional truck with Heumann wheels on worn rails is shown in Figure 4.18, where the effect of k_{px} on the work at the flanging wheel is plotted for 2.5°, 5°, 10° and 20° curves. For all degree curves, the flanging wheel work increases and eventually reaches a constant as k_{px} is stiffened. Figure 4.18 is similar to Figure 4.5, the graph of flanging wheel work of a conventional truck with new wheels. For very low values of k_{px}, the wheelsets are loosely restrained in yaw and the dominant frictional forces are the lateral creep forces. The flanging wheel work is small: less than 5 ft-lb/ft for 2.5°, 5° and 10° curves, and less than 50 ft-lb/ft for the tight 20° curve. At very high values of k_{px}, the wheelsets are locked to the truck frame in yaw. Longitudinal creep forces

Table 4.1 Effects of Rail Flexibility on the Steady-State Curving of a Conventional Truck with New Wheels Negotiating a 10° Curve

$k_{px} = 5.0 \times 10^5$ lb/ft

	Rigid Rail ($k_{flex}=1.0\text{x}10^{10}$ lb/ft)	Flexible Rail ($k_{flex}=5.0\text{x}10^{6}$ lb/ft)
Lead Wheelset Lateral Displacement, y_{w1} (in)	0.3210*	0.3357
Lead Wheelset Angle of Attack, (deg)	0.6000	0.5993
Trailing Wheelset Lateral Displacement, y_{w2} (in)	-0.0922	-0.0763
Trailing Wheelset Angle of Attack (deg)	0.1028	0.1012
Lead Left Rail Lateral Displacement (in)	0.0000	0.0147
Lead Right Rail Lateral Displacement (in)	0.0000	-0.0011
Lead Left Wheel Lateral Force (lb)	-6140.	-6135.
Lead Right Wheel Lateral Force (lb)	3998.	3999.
Work at Lead Left Wheel (ft-lb/ft)	130.	130.
Total Work = Work at all Wheels (ft-lb/ft)	196.	195.

*Flange Clearance

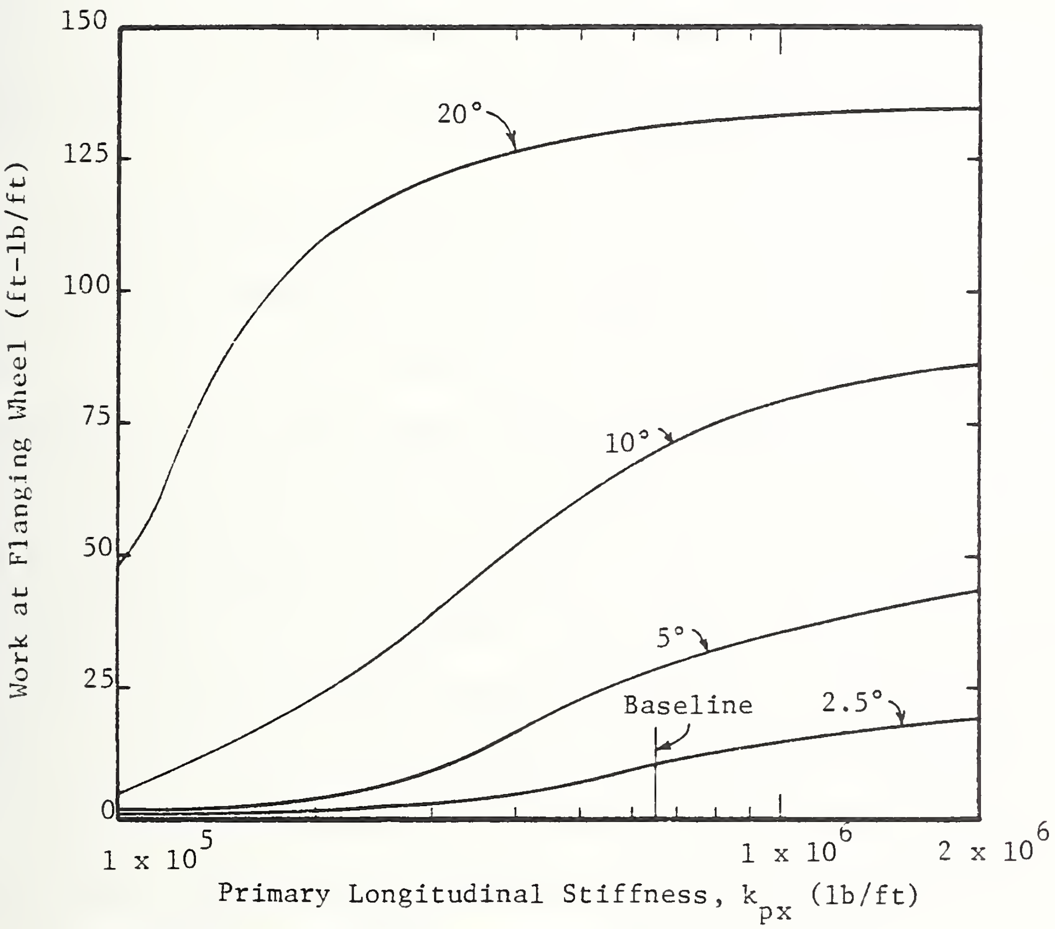

Figure 4.13 Work at Flanging Wheel vs. Primary Longitudinal Stiffness of a Conventional Truck with Heumann Wheels Negotiating 2.5°, 5°, 10°, and 20° Curves.

are present which provide a wheelset yaw moment to counteract the large suspension bending stiffness due to the stiff k_{px}. Eventually the creep forces saturate at the adhesion limit and the work becomes constant. Creep force saturation occurs at the lowest k_{px} for tight curves due to the large lateral creep forces which develop for equilibrium with large lateral components of normal forces. As a result, the work approaches a constant level for the 20° curve at the lowest k_{px} in Figure 4.18. For a conventional truck with Heumann wheels the baseline value of k_{px} is 6.50×10^5 lb/ft, which gives a critical speed of 120 mph.

The choice of wheel profile strongly influences the curving behavior of a conventional truck in terms of the magnitude of the flanging wheel work. Table 4.2 shows that at all degree curves substantially less work is expended for a conventional truck with Heumann wheels than a truck with new wheels, for trucks of identical stiffness. This is due to the fact that the Heumann wheel profile maintains single-point wheel/rail contact at all lateral excursions, and that a larger restoring moment is available to help align the wheelsets radially leading to improved curving performance. The advantage of employing Heumann wheels is greatest at low degree curves. More than a four-fold decrease in flanging wheel work is obtained at 2.5° (33 ft-lb/ft for new wheels versus 8 ft-lb/ft for Heumann wheels), whereas less than a two-fold decrease is obtained at 20° (206 ft-lb/ft versus 130 ft-lb/ft). This agrees with the results of the single wheelset model which shows that the differences in curving behavior decrease with increasing curvature due to the earlier onset of creep force saturation.

Table 4.2 The Effect of New and Heumann Wheel/Rail Profiles on the Work at the Flanging Wheel of a Conventional Truck With $k_{px} = 5.0 \times 10^5$ lb/ft Negotiating 2.5°, 5°, 10°, and 20° Curves

Work at Flanging Wheel (ft-lb/ft) / Wheel/Rail Profile	Degree Curve			
	2.5°	5°	10°	20°
New	33	80	130	206
Heumann	8	24	62	130

4.3 Curving Performance of Self-Steered Radial Trucks

The curving performance of a self-steered radial truck is determined primarily by the primary longitudinal stiffness, k_{px}, the interaxle bending stiffness, k_{b2}, and the wheel/rail profile geometry. The value of the primary longitudinal stiffness is associated with the ability of the wheelsets to align radially. For soft k_{px}, the yaw of the wheelsets is almost decoupled from the yaw of the truck. For stiff k_{px}, the wheelsets and the truck frame are almost locked into a rigid configuration in yaw which prevents the wheelsets from independently adopting radial orientations. The interaxle bending stiffness, k_{b2}, provides direct communication between the wheelsets. Steering action results when the value of k_{b2} is low and the value of the interaxle shear stiffness, k_{s2}, is high. A yaw motion of one wheelset causes the other wheelset to yaw in the opposite direction, thus allowing the wheelsets to align radially in curves. The stiff shear spring can increase the total truck shear stiffness of the self-steered truck above the value achievable by a conventional truck, thus opening the possibility for improved curving (and stability) performance. As before, the wheel/rail profile geometry is important since it dictates the character of the wheel/rail contact by determining whether or not two point contact occurs at the flanging wheel.

The effect of increasing the primary longitudinal stiffness, k_{px}, of a self-steered radial truck with new wheels on worn rails is to degrade the curving performance. Figure 4.19 shows the work at the flanging wheel of a self steered radial truck with a low interaxle bending stiffness, k_{b2} = 1.0×10^3 ft-lb/rad, and a high interaxle shear stiffness, $k_{s2} = 1.0 \times 10^6$ lb/ft, as a function of k_{px} as the truck negotiates 2.5°, 5°, 10°, and 20° curves. In all cases, the flanging wheel work rises with increasing k_{px} and then asymptotically approaches a constant value. The effect of k_{px} on the work is similar to that observed for the conventional truck. However, with the self-steered radial truck some steering action is provided due to the interaxle stiffnesses helping to align the wheelsets radially especially around tight curves. The higher total truck shear stiffness of the self-steered radial truck is advantageous since it helps to minimize the angle of attack and flange forces for negotiation around high degree curves. As a result, lower magnitudes of work are expended for the self-steered radial truck negotiating the tight 20° curve (Fig. 4.19) in comparison to the conventional truck (Fig. 4.5). For the shallow and moderate degree curves, insignificant differences in flanging wheel work occur for the conventional and self-steered radial trucks especially at high k_{px}. For negotiation of low degree curves, the conventional truck with low total truck shear stiffness is desirable since it helps to minimize the wheelset lateral excursion and angle of attack. In contrast, the high total truck shear stiffness of the self-steered radial truck keeps the wheelset at flange clearance, and can

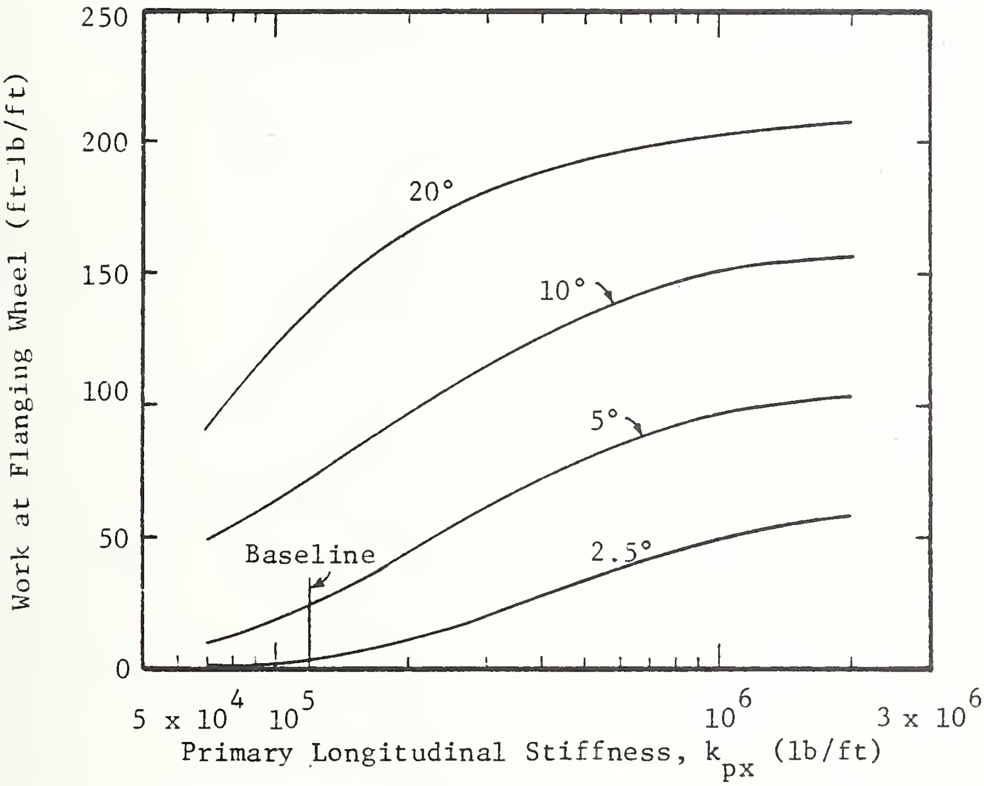

Figure 4.19 Work at Flanging Wheel vs. Primary Longitudinal Stiffness of a Self-Steered Radial Truck with New Wheels Negotiating 2.5°, 5°, 10°, and 20° Curves.

result in more work at the outer wheel, as will be discussed later.

A self-steered radial truck with Heumann wheels on worn rails demonstrates the same characteristic behavior of inferior curving performance with increased k_{px} as shown in Figure 4.20. Lower levels of work are expended at the same stiffness for all degree curves in comparison to the work for a self-steered radial truck with new wheels, shown in Figure 4.19. Results are summarized in Table 4.3 for a stiffness of $k_{px} = 5.0 \times 10^5$ lb/ft. The single-point contact nature of the Heumann wheel profile is responsible for the improvement in curving performance. As before with the conventional truck, the advantage of employing Heumann wheels in comparison to new wheels decreases with tighter curves. For a shallow 2.5° curve, the work is 14 ft-lb/ft for Heumann wheels versus 34 ft-lb/ft for new wheels. For a tight 20° curve, the work is 122 ft-lb/ft for the Heumann wheels versus 194 ft-lb/ft for new wheels. The decrease in relative advantage of the truck with Heumann wheels as curvature is increased is due to creep forces which saturate earlier. The trucks with new and Heumann wheels, compared in Table 4.3 have the same stiffness but different stability properties. To obtain identical critical speeds the truck with Heumann wheels must be made stiffer than the truck with new wheels to offset the destabilizing effect of the higher conicity Heumann profile. The baseline value of k_{px} for a self-steered radial truck with new wheels is 1.20×10^5 lb/ft, and for a truck with Heumann wheels is 5.00×10^5 lb/ft. The baseline interaxle stiffnesses are: $k_{b2} = 1.0 \times 10^3$ ft-lb/rad and $k_{s2} = 1.0 \times 10^6$ lb/ft. These values were selected to yield critical speeds of 120 mph.

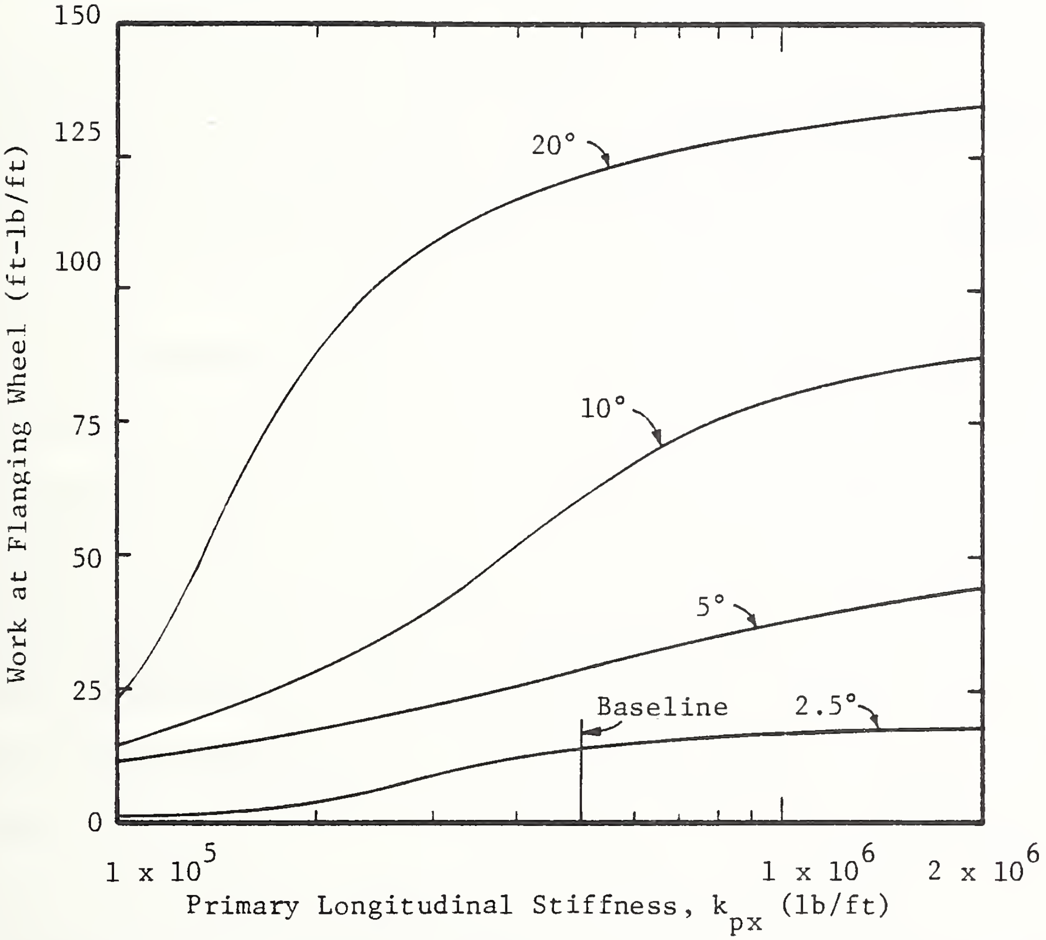

Figure 4.20 Work at Flanging Wheel vs. Primary Longitudinal Stiffness of a Self-Steered Radial Truck with Heumann Wheels Negotiating 2.5°, 5°, 10°, and 20° Curves.

Table 4.3 The Effect of New and Heumann Wheel/Rail Profiles on the Work at the Flanging Wheel of a Self-Steered Radial Truck Negotiating 2.5°, 5°, 10°, and 20° Curves with Stiffnesses:
$k_{px} = 5.0 \times 10^5$ lb/ft, $k_{b2} = 1.0 \times 10^3$ ft-lb/rad, $k_{s2} = 1.0 \times 10^6$ lb/ft

Work at Flanging Wheel (ft-lb/ft) / Wheel/Rail Profile	Degree Curve			
	2.5°	5°	10°	20°
New	34	81	131	194
Heumann	14	29	61	122

The self-steered radial truck of Table 4.3 is obtained by adding inter-axle stiffnesses to the conventional truck of Table 4.2. The resulting radial truck has a higher total shear stiffness (and a slightly higher bending stiffness) which is intended to improve the curving performance. The higher shear stiffness of the radial truck makes it slightly better for negotiating high degree curves since it helps to minimize the leading wheelset angle of attack and lateral forces during flanging. For example, by adding interwheel-set stiffnesses the work decreases from 206 to 194 ft-lb/ft for trucks with new wheels and from 130 to 122 ft-lb/ft for trucks with Heumann wheels negotiating 20° curves. However, the added shear stiffness can actually degrade the performance for negotiation of low degree curves by forcing the leading wheelset into the flange and creating an increased angle of attack. For instance, when converting to the self-steered radial configuration for 2.5° curve negotiation the work remains essentially constant increasing from 33 to 34 ft-lb/ft for trucks with new wheels, while it increases from 8 to 14 ft-lb/ft for trucks with Heumann wheels. The results indicate that the curving performance of conventional and self-steered radial trucks with new wheels are essentially identical for low and moderate degree curves. In contrast, the performance of the self-steered radial truck is worse than that of the conventional truck at low and moderate degree curves when the trucks employ Heumann wheels. The leading wheelsets of the trucks with new wheels are at flange clearance, and two-point contact occurs at the leading outer wheels. The added shear stiffness of the radial truck changes only slightly the distribution and magnitude of forces at the two contact patches of the flanging wheel and as a result the work remains essentially constant at low degree curves. On the other hand, the leading wheelsets of the trucks with the single-point contact Heumann wheels are not fixed at the flange clearance. The lower truck shear stiffness of the conventional truck minimizes the leading wheelset lateral excursion and angle of attack, and thus the work at the flanging wheel is less for the conventional truck than for the self-steered radial truck.

4.4 Curving Performance of Forced-Steered Radial Trucks

Vehicles with forced-steered radial trucks employ passive linkages between the wheelsets and carbody to sense track curvature and/or cant deficiency, and use this information to steer the wheelsets into radial alignment. The curving performance of these vehicles is a function of the primary longitudinal stiffness, the effective interaxle bending stiffness (due to forced-steered linkages), the steering action gain(s), and the wheel/rail profile geometry. In the studies described below an L-type forced-steered radial truck has been used with the curvature steering action gain set to the pure rolling line gain, $G_{pr\ell}$. This is the appropriate gain required for the wheelsets to track the pure rolling line and achieve radial alignment, based upon kinematic arguments which assume rigid steering linkages. Due to nonrigid linkages and the action of flange forces, however, the pure rolling line gain may result in imperfect steering of the wheelsets as discussed later in this section.

The curving properties of a forced-steered truck are not unique since different combinations of primary longitudinal stiffness, k_{px}, and effective interaxle bending stiffness, k_{b2}, can yield the same behavior. As such, two forced-steered truck designs, FSR I, with a low value of k_{px} (k_{px} = 7.0 x 10^4 lb/ft) and FSR II, with a very low value of k_{px} (k_{px} = 1.0 x 10^3 lb/ft) are investigated.

Figures 4.21 and 4.22 show the flanging wheel work as a function of k_{b2} for the two forced-steered truck designs, FSR I and FSR II, with new wheels on worn rails. The curving performance is relatively insensitive to changes in k_{b2} for negotiation of low degree curves (2.5° for FSR I; 2.5° and 5° for FSR II). For forced-steered trucks with low values of k_{b2} negotiating shallow curves, the wheelsets maintain almost radial orientations due to longitudinal creep forces which support the small yaw bending moment from the soft primary longitudinal suspensions, and self-steered behavior is approached. With stiffer values of k_{b2}, the wheelsets become more restrained in yaw and the forced steering action is used to achieve radial alignment and overcome the stiffer truck. For negotiation of higher degree curves, the flanging wheel work rises slightly with increasing k_{b2}. This is due to the fact that the pure rolling line steering gain, which was selected to kinematically align both wheelsets radially, actually results in a slight understeer of the leading wheelset for higher degree curves as is discussed later. With increasing k_{b2}, the leading wheelset adopts a slightly increasing positive angle of attack due to insufficient steering action which is the reason for

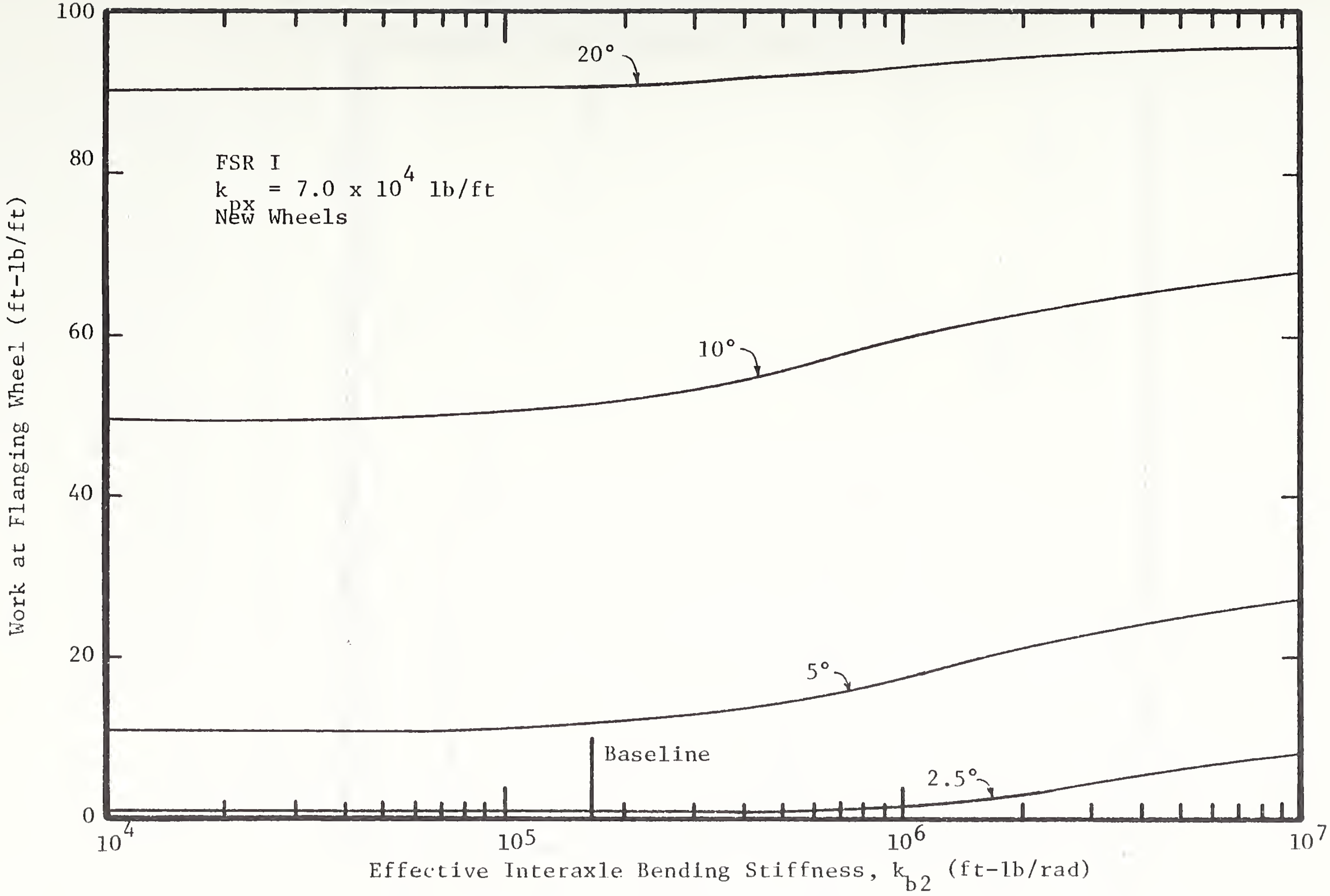

Figure 4.21 Work at Flanging Wheel vs. Interaxle Bending Stiffness of a Forced-Steered Radial Truck, FSR I, with New Wheels Negotiating 2.5°, 5°, 10°, and 20° Curves

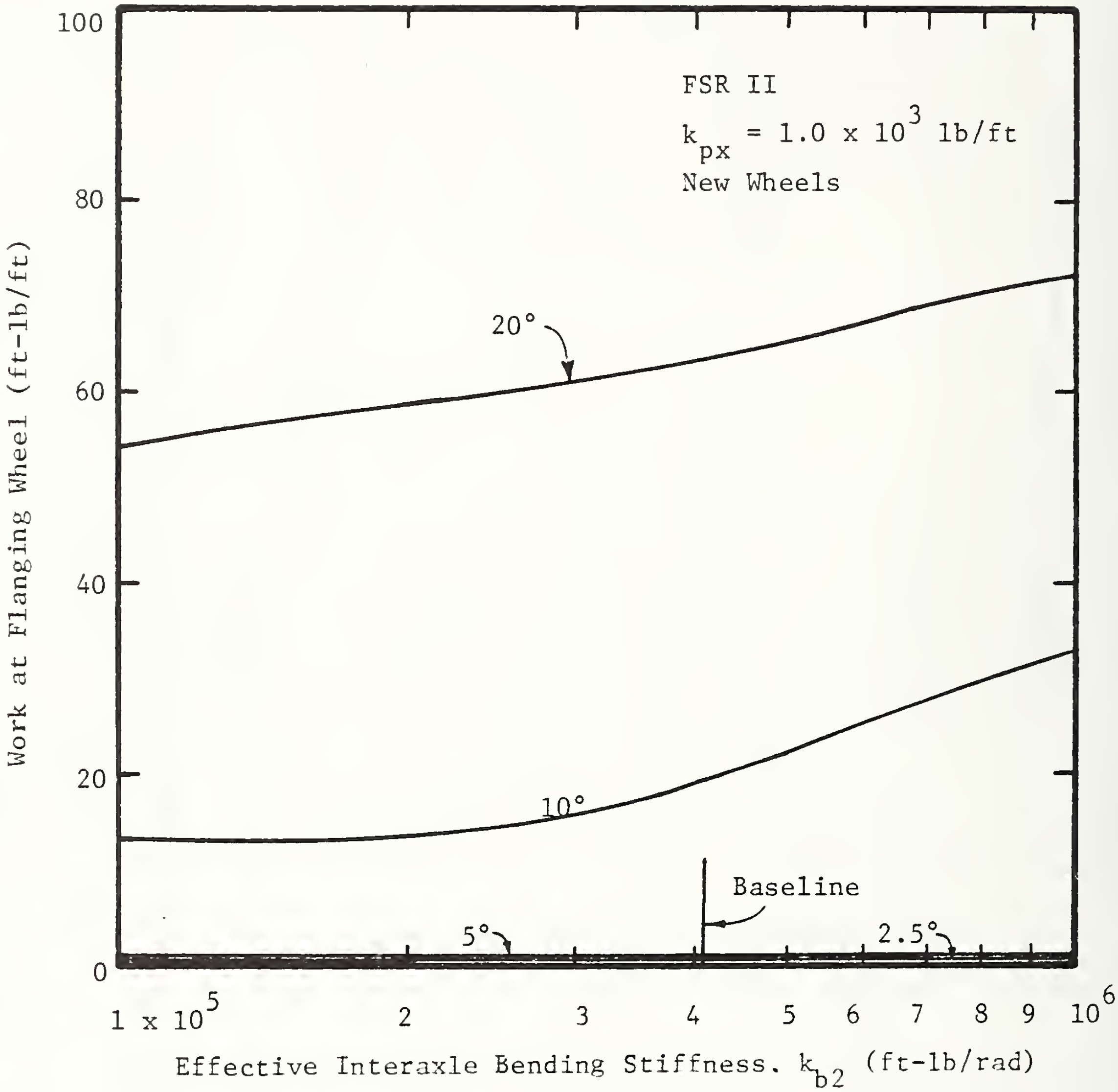

Figure 4.22 Work at Flanging Wheel vs. Interaxle Bending Stiffness of a Forced-Steered Radial Truck, FSR II, with New Wheels Negotiating 2.5°, 5°, 10°, and 20° Curves.

the slight increase in flanging wheel work.

The slight increase in work which occurs with increasing k_{b2} is minimized by the effects of forced steering. In Figure 4.23 the flanging wheel work of a forced-steered radial truck (FSR I) with new wheels negotiating a 10° curve, reproduced from Figure 4.21, is compared to the work associated with a truck with no forced-steering (G = 0), i.e., a self-steered radial truck. As k_{b2} is increased, the creep forces are not sufficient to steer the wheelsets of the self-steered truck causing the lead wheelset angle of attack and thus the flanging wheel work to rise. Eventually, as the wheelsets become rigidly connected the creep forces at the flanging wheel saturate and the work asymptotically reaches a constant. The work increases over 300% in the transition from very soft to very stiff interaxle bending stiffness. In comparison, in the forced-steered truck (with new wheels), the angle of attack remains relatively constant, increasing only slightly with increasing k_{b2}, giving rise to a 35% increase in the flanging wheel work. A high value of k_{b2} is desirable to ensure maximum use of the forced-steering action. Furthermore, Figure 4.23 demonstrates the importance of designing a self-steered radial truck with a low value of k_{b2} to permit the wheelsets to yaw due to action of the longitudinal creep forces.

A comparison of Figures 4.21 and 4.22 shows that the work for the first design forced-steered truck, FSR I is greater than the work for the second design truck, FSR II, at all degree curves. The FSR I truck has a larger k_{px}, and thus a larger yaw bending stiffness, than the FSR II truck. The forced-steering action must overcome this additional bending resistance in the FSR I truck and, as a result, the FSR I truck does not steer the wheelsets as successfully and the flanging wheel work is greater.

The effect of increasing k_{b2} on the flanging wheel work for the two forced-steered truck designs with Heumann wheels on worn rails is shown in Figures 4.24

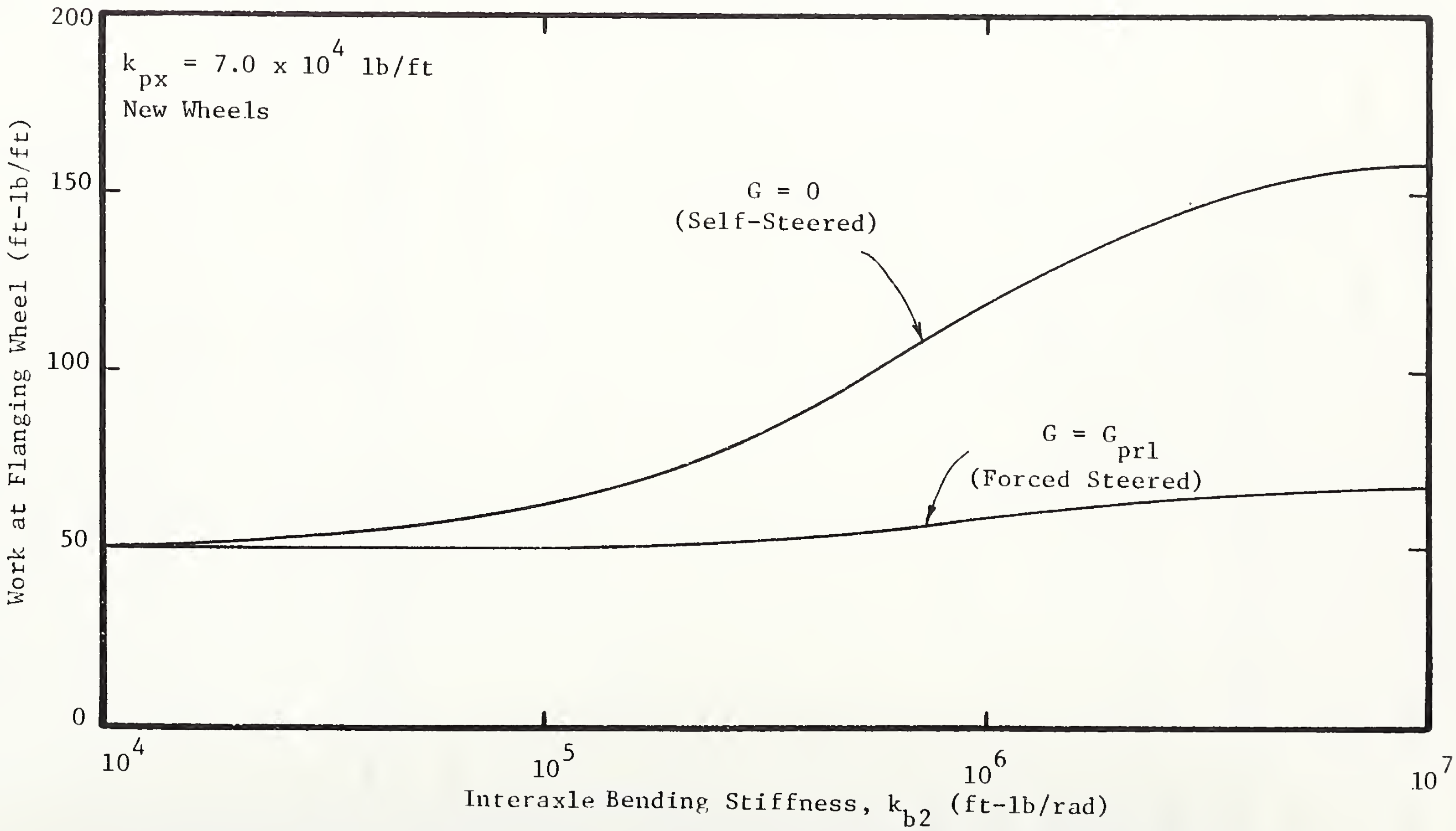

Figure 4.23 Work at Flanging Wheel vs. Interaxle Bending Stiffness of Self-Steered and Forced-Steered Radial Trucks with New Wheels Negotiating 10° Curves.

and 4.25 From Figure 4.24 as the FSR I truck negotiates shallow curves, the work increases slightly with increasing k_{b2} but always is small (less than 2 ft-lb/ft for 2.5° and less than 3 ft-lb/ft for 5°). For the tighter 10° and 20° curves, the work decreases slightly with increasing k_{b2}. For the 20° curve, the outer wheel of the trailing wheelset experiences more work than the outer wheel of the leading wheelset, and thus the work at the trailing outer wheel is reported. For the second design truck, FSR II, shown in Figure 4.25 the work is essentially insensitive to changes in k_{b2}, showing a very slight decrease with increasing stiffness. The work associated with negotiation of the 2.5°, 5° and 10° curves is very small, less than 2.5 ft-lb/ft. Again, the data reported for the 20° curve is the work at the trailing outer wheel since it exceeded the work at the other wheels.

The decrease in work with increasing k_{b2} occurs for forced-steered trucks with Heumann wheels due to effective steering of the wheelsets. As k_{b2} becomes stiffer, the steering linkages become more rigid and "force" the wheelsets into radial alignment. For the Heumann wheel the pure rolling line steering gain results in almost perfect steering, showing slight understeering for high degree curves.

The values of stiffnesses for baseline forced-steered truck designs with critical speeds of 120 mph were listed in Table 3.2, and are marked in Figures 4.21, 4.22, 4.24, and 4.25. The curving performances of the two forced-steered truck designs with new and Heumann wheels and identical interaxle stiffnesses are summarized in Tables 4.4 and 4.5 for FSR I and FSR II, respectively. In both tables, the results for the Heumann wheel profile demonstrate the improvement in curving performance in comparison to the new wheel profile. The single-point contact Heumann profile develops less work and, has been shown,

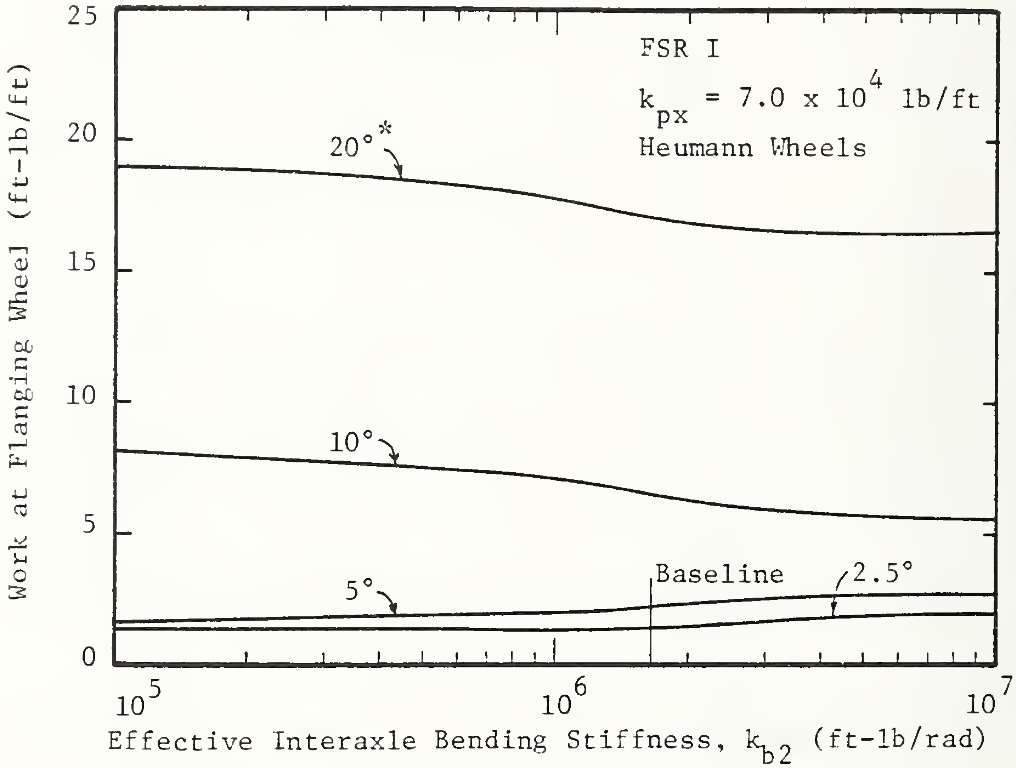

Figure 4.24 Work at Flanging Wheel vs. Interaxle Bending Stiffness of a Forced-Steered Radial Truck, FSR I, with Heumann Wheels Negotiating 2.5°, 5°, 10°, and 20° Curves. (*Work at Trailing Outer Wheel)

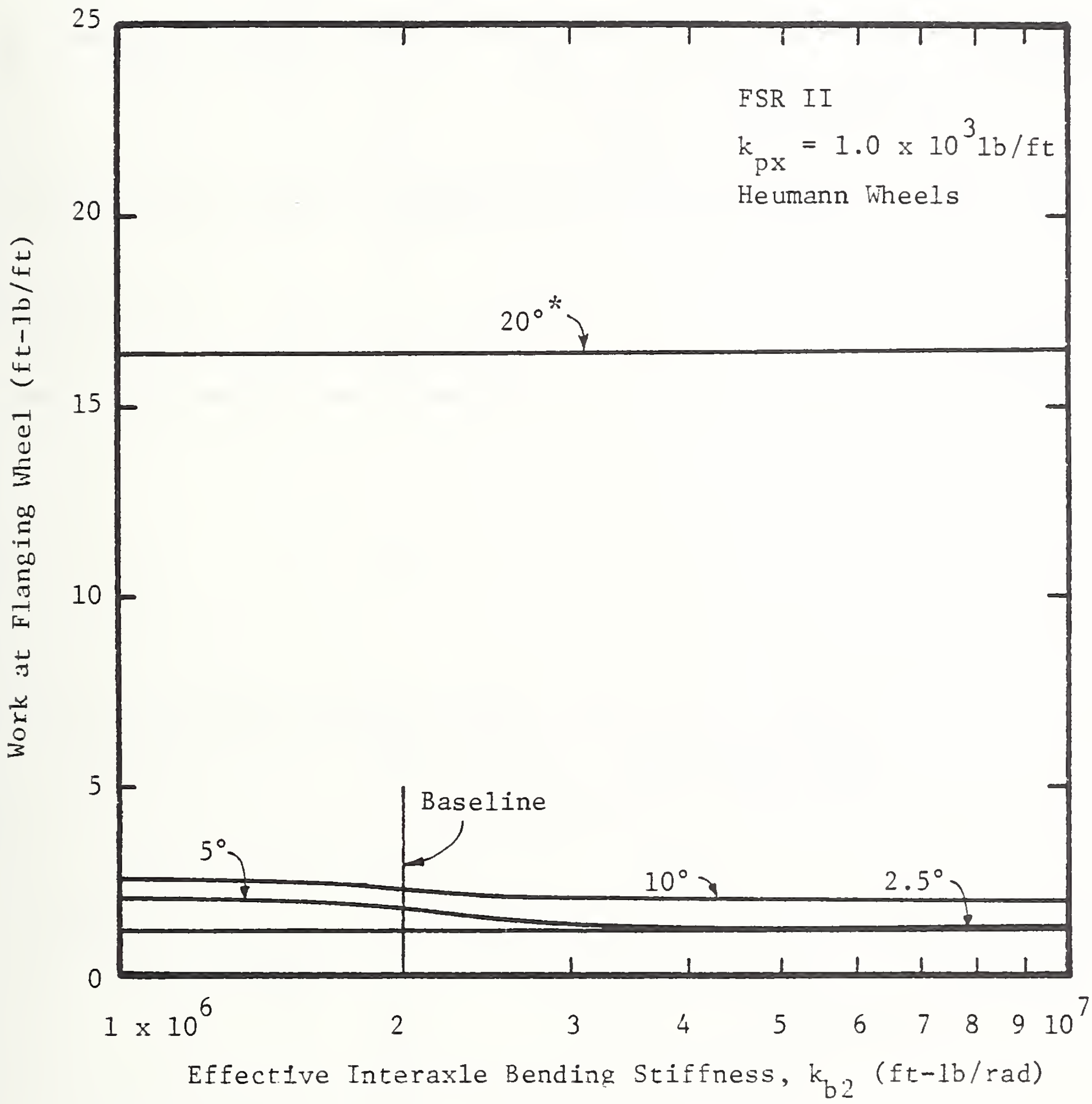

Figure 4.25 Work at Flanging Wheel vs. Interaxle Bending Stiffness of a Forced-Steered Radial Truck, FSR II, with Heumann Wheels Negotiating 2.5°, 5°, 10°, and 20° Curves (*Work at Trailing Outer Wheel)

Table 4.4 The Effect of New and Heumann Wheel/Rail Profiles On the Work at the Flanging Wheel of a Forced-Steered Radial Truck, FSR I, Negotiating 2.5°, 5°, 10°, and 20° Curves with Stiffnesses:

$k_{px} = 7.0 \times 10^4$ lb/ft, $k_{b2} = 1.0 \times 10^6$ ft-lb/rad, $k_{s2} = 1.0 \times 10^6$ lb/ft

Wheel/Rail Profile \ Work at Flanging Wheel (ft-lb/ft)	Degree Curve			
	2.5°	5°	10°	20°
New	1	18	60	93
Heumann	1	2	7	19

Table 4.5 The Effect of New and Heumann Wheel/Rail Profiles On the Work at the Flanging Wheel of a Forced-Steered Radial Truck, FSR II, Negotiating 2.5°, 5°, 10°, and 20° Curves with Stiffnesses:

$k_{px} = 1.0 \times 10^3$ lb/ft, $k_{b2} = 1.0 \times 10^6$ ft-lb/rad, $k_{s2} = 1.0 \times 10^6$ lb/ft

Wheel/Rail Profile \ Work at Flanging Wheel (ft-lb/ft)	Degree Curve			
	2.5°	5°	10°	20°
New	1	2	33	72
Heumann	1	2	3	16

is advantageous for curving. Since identical k_{b2} and k_{s2} were selected, Tables 4.4 and 4.5 can be used to compare the two truck designs with the same wheel profile. With both the new and Heumann wheel profiles, less work occurs for the FSR II design, with the lower k_{px}, than for the FSR I design. With new wheels, the work to negotiate a 10° curve is 60 ft-lb/ft for the FSR I design versus 33 ft-lb/ft for the FSR II design, whereas with Heumann wheels, the work is 7 ft-lb/ft for the FSR I design versus 3 ft-lb/ft for the FSR I design. The FSR II design has minimal wheelset yaw bending resistance due to the very low primary stiffness, and the forced-steering action can better align the wheelsets radially.

For a forced-steered truck with a stiff k_{b2}, the value of steering gain determines the leading wheelset angle of attack, and thus strongly influences the work at the flanging wheel. The curvature steering gain used in this report is the gain which kinematically aligns the wheelsets radially, called the pure rolling line steering gain, $G_{pr\ell}$, derived in Appendix B. It positions the wheelsets radially assuming that no primary longitudinal and secondary yaw stiffnesses exist and no flange forces are present. These assumptions are violated for forced-steered trucks, and thus the pure rolling line steering gain may result in yaw misalignment of the wheelsets.

Figures 4.26 and 4.27 show the effect of steering gain on the flanging wheel work and the leading wheelset angle of attack, respectively, of a forced steered radial truck, FSR I, with stiff k_{b2} negotiating a 20° curve with both new and Heumann wheel profiles. At G = 0 the behavior of a forced-steered truck is similar to that of a self-steered truck with a high value of stiffness k_{b2} since no forced-steering action is involved. With increasing steering gain, the flanging wheel work decreases as the wheelsets are forced toward radial

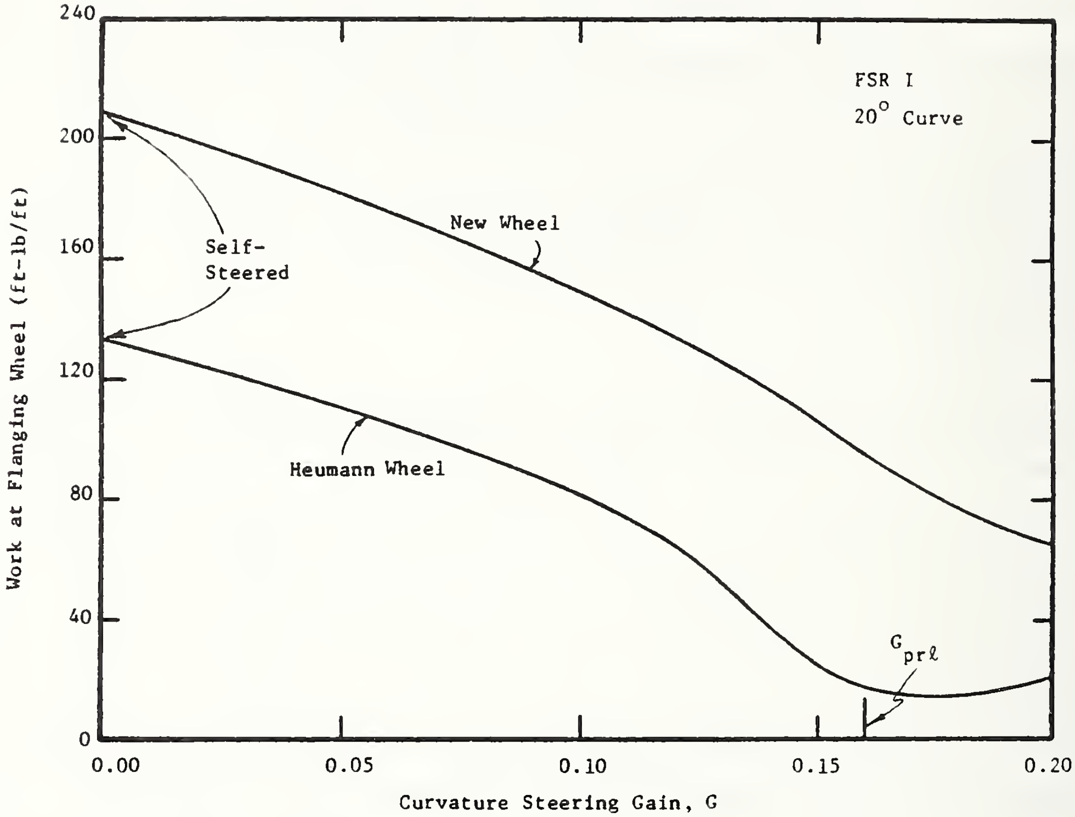

Figure 4.26 Work at Flanging Wheel vs. Curvature Steering Gain for a Forced-Steered Radial Truck, FSR I, with New and Heumann Wheels Negotiating a 20° Curve.
(k_{px} = 7.0 x 10^4 lb/ft, k_{b2} = 1.0 x 10^7 ft-lb/sec,
k_{s2} = 1.0 x 10^6 lb/ft)

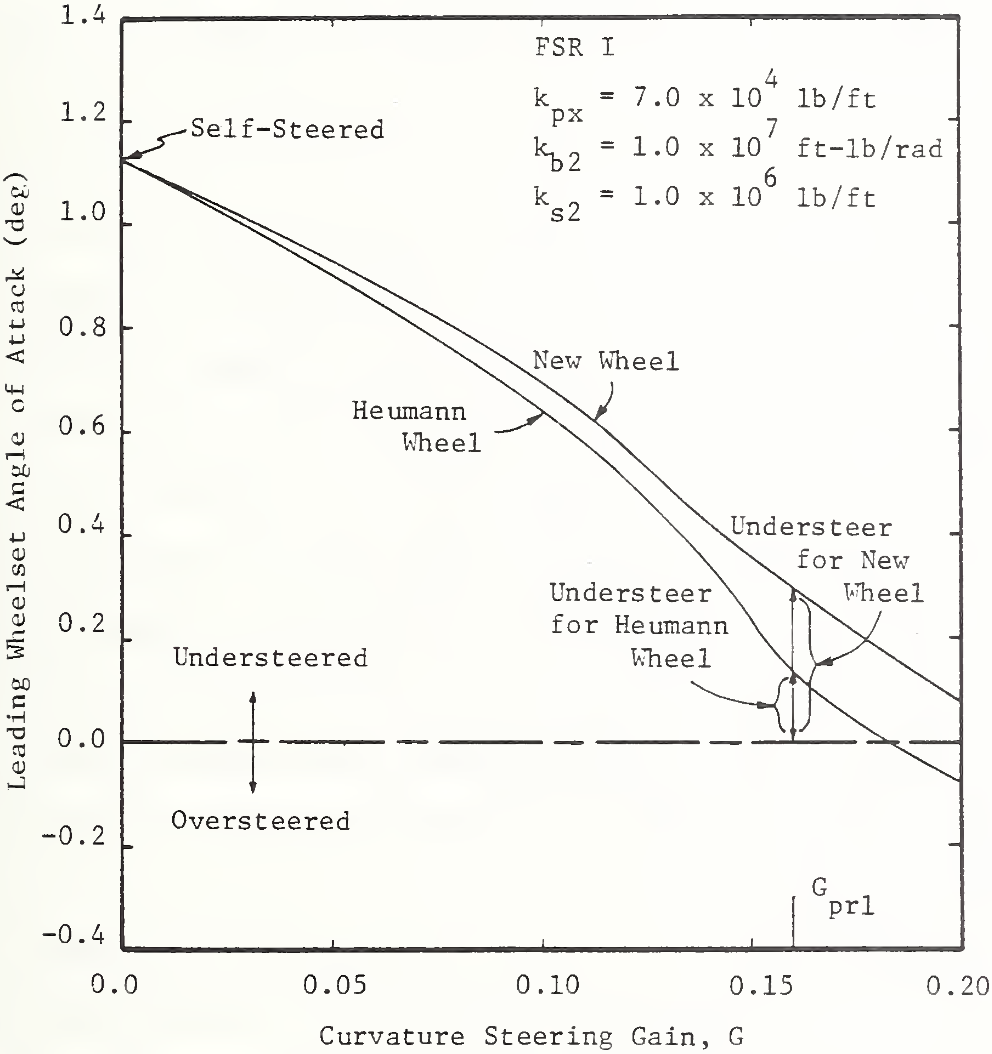

Figure 4.27 Leading Wheelset Angle of Attack vs. Curvature Steering Gain for a Forced-Steering Radial Truck, FSR I, with New and Heumann Wheels Negotiating a 20° Curve.

alignment. At a certain gain, perfect steering is achieved and minimum work occurs. Further increases in steering gain result in oversteering of the wheelsets away from radial alignment and the flanging wheel work increases. For the truck with Heumann wheels, the steering gain associated with perfect radial alignment is slightly higher than the pure rolling line gain ($G_{pr\ell} = 0.1579$). For the truck with new wheels, a steering gain larger than $G = 0.20$, the maximum value plotted in Figures 4.26 and 4.27, is required to achieve perfect steering.

At the pure rolling line steering gain, $G_{pr\ell}$, a larger angle of attack occurs for the truck with new wheels than for the truck with Heumann wheels. Thus, the gain $G_{pr\ell}$ results in substantial understeering of the leading wheelset of the truck with new wheels in comparison to the leading wheelset of the truck with Heumann wheels. To eliminate wheelset misalignment, the steering gains of both trucks must be increased, slightly for the truck with Heumann wheels and significantly for the truck with new wheels. The results shown in Figures 4.26 and 4.27 are for negotiation of a 20° curve, for which the flanging forces are high. For forced-steered trucks negotiating smaller degree curves, the pure rolling line steering gain results in improved steering, i.e., decreased understeering.

The flanging wheel work of the forced-steered trucks with new wheels and steering gain $G_{pr\ell}$, shown in Figures 4.21 and 4.22, increases with stiffer k_{b2} because the leading wheelset is being forced to adopt a positive yaw misalignment. A larger gain is needed to eliminate the understeering, and would give improved curving performance with increasing k_{b2}. Too large a steering gain would result in oversteering, which would also be detrimental to the curving performance. The selection of an optimal steering gain for a forced-steered truck is not addressed in this study, but represents an important area of future research.

Forced-steered trucks adjust their geometry with track curvature to align their wheelsets in nominally radial positions. Because of the reduced wheelset misalignment in curves, the work expended at the flanging wheel decreases. In comparison to the performance of conventional and self-steered radial trucks, a significant improvement is achieved with forced steering of wheelsets, as is discussed in Chapter 5.

4.5 Effect of Wheelset Misalignment on Curving Performance

Wheelset misalignments may occur in transit trucks during construction or as a result of operation and maintenance practice. Misalignments position the wheelsets in offset or skewed initial positions and influence truck performance. In general, they hinder the tracking performance and contribute to asymmetric wear patterns on wheels.

Wheelset misalignments can be resolved into radial and lateral components. In radial misalignments, the wheelsets have equal and opposite yaw angles with respect to the truck centerline, whereas in lateral misalignment the wheelsets are offset laterally with respect to one another. Previous analyses [2, 13] have indicated that the radial component of misalignment has the more detrimental influence on the curving behavior. The results of this study confirm that radial misalignment has a significant effect on curved as well as tangent track negotiation.

The effect of wheelset misalignments on truck curving performance is a function of both the magnitude and direction of the radial and lateral misalignment components. The ability of a truck to negotiate a curve is improved by misalignments which position the wheelsets radially with the curve, and is hindered by misalignments in the opposite direction. Curving performance is degraded by misalignments for a vehicle which negotiates an equal number of right and left handed curves. In addition to direction, the magnitudes of the wheelset misalignment influence truck tracking ability. In the misalignment studies that follow, magnitudes of both lateral and radial misalignments are used which are consistent with observed values [13]. For lateral misalignment, the two wheelsets are each displaced 0.06 in (0.005 ft) in opposite directions relative to the truck centerline, whereas for radial misalignment the two wheelsets are each yawed 0.0573° (0.001 rad) in opposite directions from the perpendicular to the truck centerline. The directions of the misalignments are chosen to degrade the tracking performance.

The effects of wheelset misalignments on the work at the flanging wheel and the wheel/rail lateral force at the flanging wheel are compared in Tables 4.6a and 4.6b, respectively, for conventional, self-steered, and forced-steered radial trucks negotiating a 5° curve. Baseline and increased stiffness truck suspension designs are considered. For the conventional truck, radial misalignment has a stronger influence than the lateral misalignment, especially for the stiffer suspension design. For instance, for the stiff conventional truck with lateral misalignment, the flanging wheel work is 105 ft-lb/ft versus 119 ft-lb/ft with radial misalignment. For the baseline self-steered and forced-steered radial trucks the lateral component of misalignment increases the work and lateral wheel/rail force at the flanging wheel more than the radial component. The work at the flanging wheel of the baseline self-steered truck is 50 ft-lb/ft with lateral misalignment and 34 ft-lb/ft with radial misalignment. A reverse effect occurs for the self-steered and forced-steered radial trucks of stiff suspension design. The radial component

Table 4.6 Work at Flanging Wheel (a) and Wheel/Rail Force at Flanging Wheel (b) vs. Misalignment Condition for Different Trucks Operating on 5° Curve

		Baseline	Stiff
CONV	k_{px}	$= 1.35 \times 10^5$	1.0×10^7 lb/ft
	k_{py}	$= 7.5 \times 10^5$	7.5×10^6 lb/ft
SSR	k_{px}	$= 1.20 \times 10^5$	1.0×10^7 lb/ft
	k_{py}	$= 7.5 \times 10^5$	7.5×10^6 lb/ft
FSR	k_{px}	$= 7.0 \times 10^4$	7.0×10^4 lb/ft
	k_{b2}	$= 1.68 \times 10^5$	1.0×10^7 ft-lb/rad

Work at Flanging Wheel (ft-lb/ft) / Misalignment Condition	Conventional		Self-Steered Radial		Forced-Steered Radial (FSR I)	
	Baseline	Stiff	Baseline	Stiff	Baseline	Stiff
No Misalignment	39	105	24	108	12	27
Lateral Misalignment	47	105	50	117	45	36
Radial Misalignment	49	119	34	123	20	59

(a)

Lateral Force at Flanging Wheel (lb) / Misalignment Condition	Conventional		Self-Steered Radial		Forced-Steered Radial (FSR I)	
	Baseline	Stiff	Baseline	Stiff	Baseline	Stiff
No Misalignment	2700	5065	2260	5190	1720	2370
Lateral Misalignment	2910	5180*	2760	5840*	2490	1650*
Radial Misalignment	3100	5310	2660	5450	2090	3540

(b)

*Misalignment of Opposite Sign

of misalignment increases the work more than the lateral component. For the stiff self-steered truck design, the work is 117 ft-lb/ft with lateral misalignment and 123 ft-lb/ft with radial misalignment. For the stiff forced-steered truck, the work is 36 ft-lb/ft with lateral misalignment and 59 ft-lb/ft with radial misalignment. Thus, both radial and lateral misalignments increase the work to negotiate a curve, with the influence of the radial component most dominant on stiffer truck designs. However, lateral misalignment most significantly increases the work of baseline self-steered and forced-steered radial truck designs.

To improve their ability to negotiate curved track, radial truck designs typically have increased total truck shear stiffness in comparison to the limiting conventional truck value.

Due to the increased shear stiffness, the steady-state performance of radial trucks on tangent track is influenced more strongly by wheelset misalignments than the performance of conventional trucks. In Tables 4.7a and 4.7b the effects of wheelset misalignments on the tangent track negotiation of baseline conventional, self-steered, and forced-steered radial trucks are summarized in terms of wheelset lateral excursion and wheel/rail lateral force (at the leading axle, and leading outer wheel, respectively, except where noted). The results show that the radial component of misalignment has a more significant effect than the lateral component for tangent track negotiation, especially for the radial trucks. The self-steered and forced-steered radial trucks have large lateral excursions of 0.310 and 0.308 in, respectively, which indicate near-flanging conditions at the leading outer wheels. The high shear properties of the radial trucks result in the large excursions and the increased wheel/rail lateral forces (1030 lb for both trucks) on tangent

Table 4.7 Wheelset Lateral Excursion (a) and Wheel/Rail Force (b) vs. Misalignment Condition for Baseline Trucks Operating on Tangent Track

Misalignment Condition \ Wheelset Lateral Excursion (in)	Conventional	Self-Steered Radial	Forced-Steered Radial (FSR I)
No Misalignment	-0.001	-0.006	-0.004
Lateral Misalignment	-0.150*	-0.100*	-0.100*
Radial Misalignment	0.229	0.310	0.308

*Trailing Wheelset

(a)

Misalignment Condition \ Wheel/Rail Lateral Force (lb)	Conventional	Self-Steered Radial	Forced-Steered Radial (FSR I)
No Misalignment	400	410	410
Lateral Misalignment	530*	440*	450*
Radial Misalignment	580	1030	1030

*Trailing Inner Wheel

(b)

track. Thus, self-steered and forced-steered radial truck performance on tangent track is sensitive to wheelset misalignments which implies that minimizing misalignments due to construction and tolerance errors in radial trucks is an important design consideration.

CHAPTER 5

STABILITY/CURVING PERFORMANCE TRADEOFF

5.1 Introduction

The ideal rail truck must simultaneously satisfy two design objectives: (1) minimize wheel/rail forces and wheelset angles of attack during curving; and (2) provide adequate vehicle stability to prevent the onset of hunting during which large lateral accelerations result in large wheel/rail forces. Studies have indicated the value of minimizing wheel/rail forces and wheelset angles since large forces and radial misalignment lead to increased wheel/rail wear resulting in wheel and track deterioration and noise, increase the potential danger of derailment due to wheel climb, and raise fuel consumption because of increased rolling resistance. The two design goals of improved curve negotiation and stability performance are usually represented as a tradeoff which is well documented [17, 25]. Designers of conventional rail trucks have traditionally achieved more stable designs through the use of stiff primary suspension elements. However, the resulting improvement in stability performance is obtained at the expense of degraded curving ability, which creates special problems on the tight curves associated with urban transit applications.

In this study, the lateral stability is characterized by the linear critical speed and the curving performance is represented by the work at the flanging wheel. An increased critical speed implies a more stable truck design, whereas a higher level of flanging wheel work indicates a design with decreased curve negotiation capability.

Studies of the stability performances of conventional, self-steered radial, and two forced-steered radial truck designs have been presented in Chapter 3 and the results are summarized in Table 5.1 for trucks with new wheels and in Table 5.2 for trucks with Heumann wheels. To obtain the same critical speed, the suspensions of the trucks with Heumann wheels are stiffer than the suspensions of the trucks with new wheels since for trucks of the same stiffness the effect of the higher conicity Heumann wheel is to decrease the critical speed. The stiffnesses of Tables 5.1 and 5.2 were used to determine the location of the conventional and steered truck designs in the total truck shear versus bending stiffness plane, shown in Figure 5.1 for trucks with new wheels and in Figure 5.2 for trucks with Heumann wheels. To provide increased critical speed, the self- and forced-steered trucks have increased total truck bending stiffnesses while maintaining approximately the same total shear stiffnesses. The conventional trucks increase both total bending and shear stiffnesses, but are restricted to stiffness values below the $k_s = k_b/b^2$ line. Due to this limitation, the total shear stiffnesses of the self-steered and forced-steered truck designs are significantly higher than the values achievable by conventional trucks. The results of the parametric curving studies were presented in Chapter 4 where the functional relationship of truck suspension on flanging wheel work was established for the different trucks with new and Heumann wheels.

In this chapter, the stability/curving characteristics are studied by combining the stability and curving performance results. The results allow identification of truck designs which minimize the inherent tradeoffs, and suggest modifications in future designs. Tradeoff studies for the conventional,

Table 5.1 Stiffnesses vs. Critical Speed for Four Truck Designs with New Wheels

Vcr (mph)	CONV. k_{px} (lb/ft)	SSR k_{px} (lb/ft) ($k_{b2}=10^3$ ft-lb/rad $k_{s2}=10^6$ lb/ft)	FSR I k_{b2} (ft-lb/rad) ($k_{px}=7.0\times10^4$ lb/ft $k_{s2}=10^6$ lb/ft)	FSR II k_{b2} (ft-lb/rad) ($k_{px}=1.0\times10^3$ lb/ft $k_{s2}=10^6$ lb/ft)
100	8.5×10^4	7.0×10^4	1.0×10^4	2.4×10^5
110	1.08×10^5	9.5×10^4	9.0×10^4	3.3×10^5
120*	1.35×10^5	1.20×10^5	1.68×10^5	4.1×10^5
130	1.60×10^5	1.47×10^5	2.55×10^5	5.0×10^5
140	1.85×10^5	1.70×10^5	3.4×10^5	5.8×10^5

Table 5.2 Stiffnesses vs. Critical Speed for Four Truck Designs with Heumann Wheels

Vcr (mph)	CONV k_{px} (lb/ft)	SSR k_{px} (lb/ft) ($k_{b2}=10^3$ ft-lb/rad $k_{s2}=10^6$ lb/ft)	FSR I k_{b2} (ft-lb/rad) ($k_{px}=7.0\times10^4$ lb/ft $k_{s2}=10^6$ lb/ft)	FSR II k_{b2} (ft-lb/rad) ($k_{px}=1.0\times10^3$ lb/ft $k_{s2}=10^6$ lb/ft)
90	3.45×10^5	3.10×10^5	9.5×10^5	1.25×10^6
100	4.25×10^5	3.70×10^5	1.18×10^6	1.50×10^6
110	5.25×10^5	4.32×10^5	1.42×10^6	1.75×10^6
120*	6.50×10^5	5.00×10^5	1.66×10^6	2.00×10^6
130	8.50×10^5	6.00×10^5	2.00×10^6	2.35×10^6

*Baseline

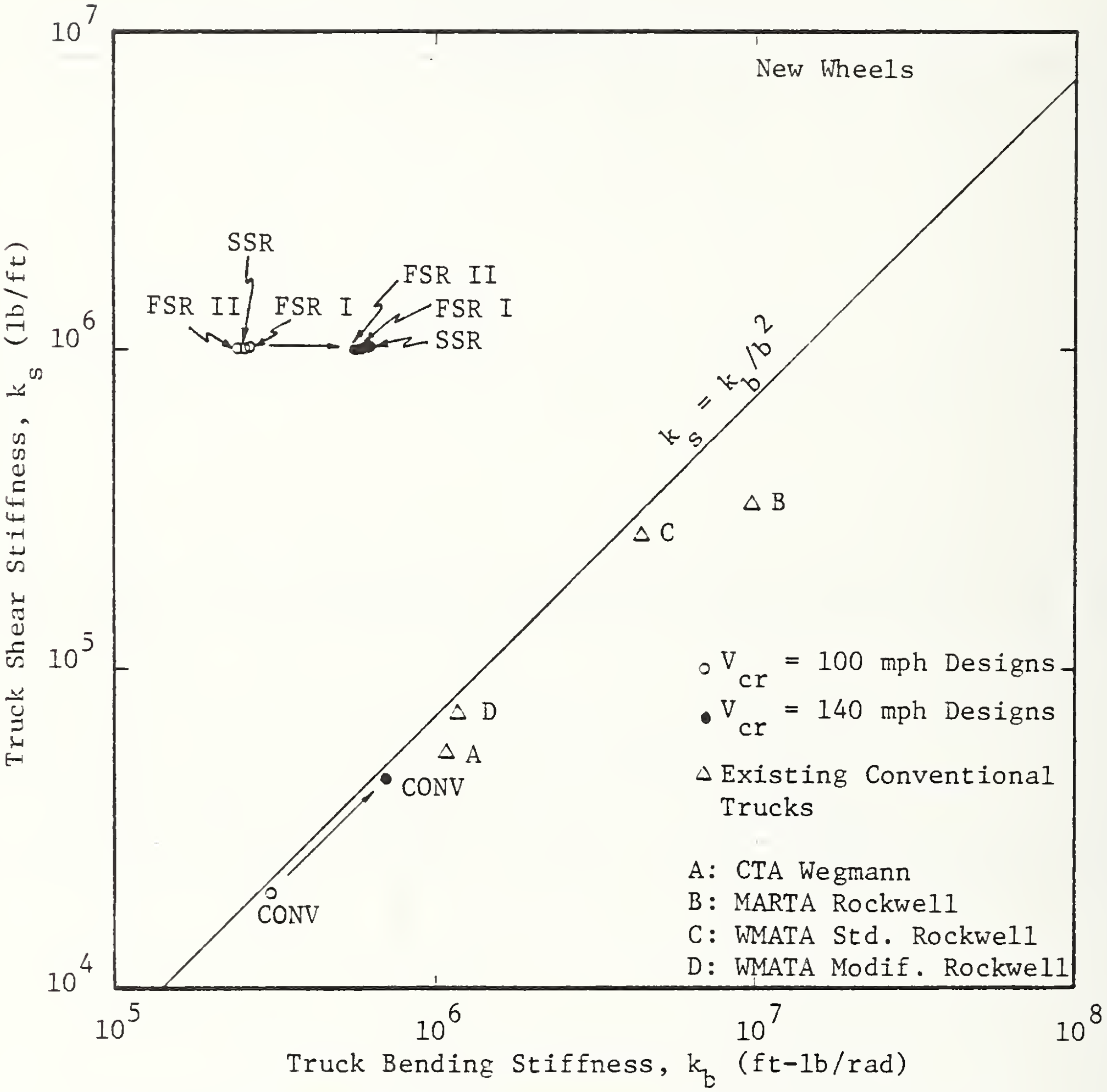

Figure 5.1 Location of Conventional and Radial Trucks with New Wheels in the Truck Shear vs. Bending Stiffness Plane.

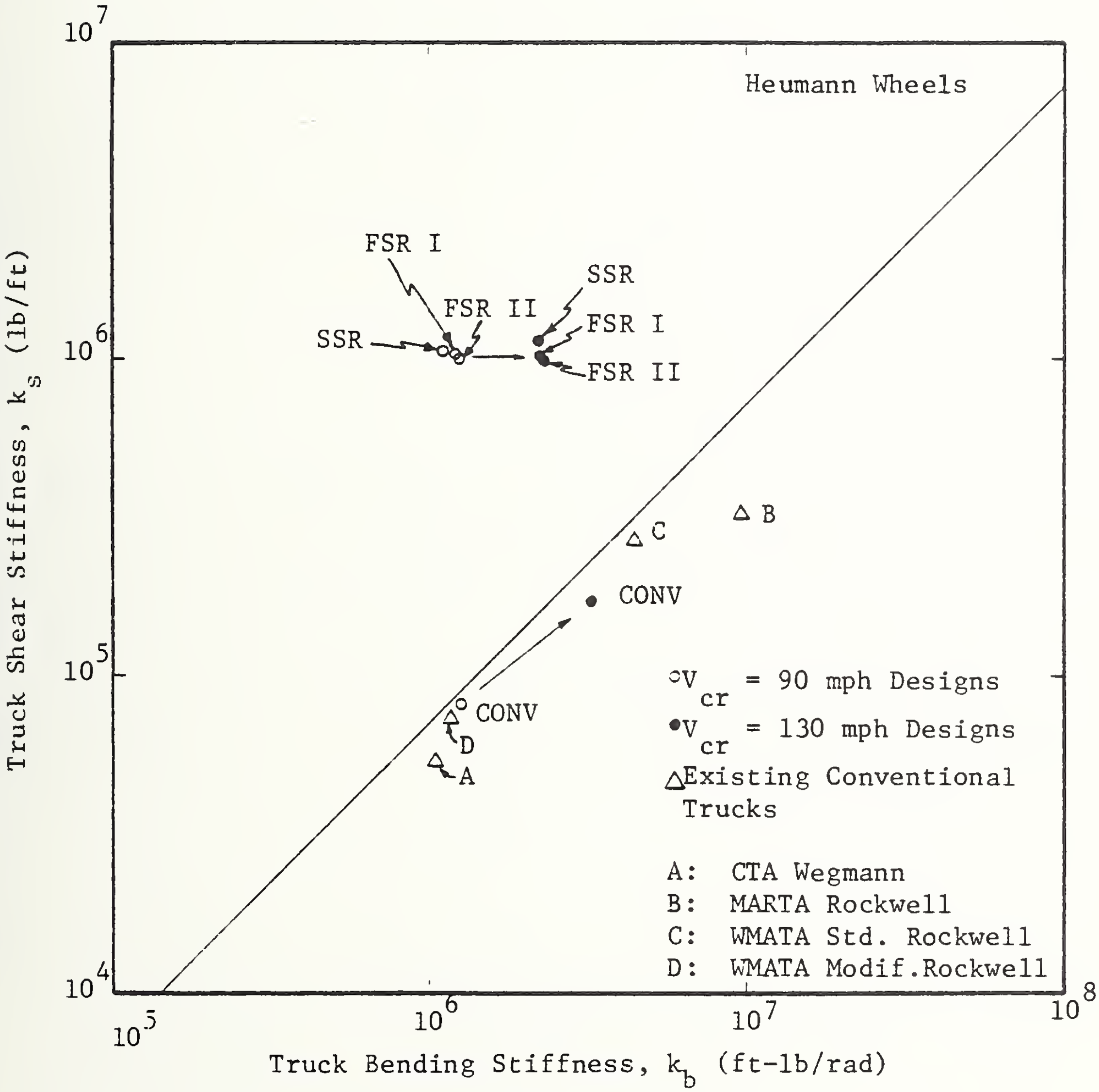

Figure 5.2 Location of Conventional and Radial Trucks with Heumann Wheels in the Truck Shear vs. Bending Stiffness Plane.

self-steered radial, and two forced-steered radial truck designs previously described are presented in this chapter.

5.2 Parametric Tradeoff Studies

In the tradeoff study of conventional trucks, the work at the flanging wheel is plotted against the critical speed as a truck with different values of k_{px} negotiates 2.5°, 5°, 10° and 20° curves. Stability/curving performance tradeoff results are shown in Figure 5.3 for a conventional truck with new wheels and in Figure 5.4 for a truck with Heumann wheels. These figures demonstrate the inherent tradeoff between stability and curving performance for which lower critical speeds correspond to decreased work. For a conventional truck with new wheels negotiating a 20° curve as k_{px} is stiffened the work increases from 139 to 189 ft-lb/ft and the critical speed changes from 100 to 140 mph. For lower degree curves in Figure 5.3, the work increases only slightly with increasing k_{px}, implying that a higher critical speed can be obtained with minimal decrease in curving performance. For the 2.5° curve, the work is insensitive to changes in k_{px}. The stability/curving performance tradeoff for the conventional truck with Heumann wheels shows that as the critical speed is increased from 90 to 130 mph the work at the flanging wheel increases only slightly (6%) for the 20° curve and more significantly for lower degree curves (64% for the 10° curve; 250% for the 2.5° curve).

The stability/curving tradeoff plots for self-steered radial trucks with new and Heumann wheels are shown in Figures 5.5 and 5.6, respectively. In these figures, the primary longitudinal stiffness, k_{px}, is the independent variable, while the interaxle bending stiffness, k_{b2}, is fixed at a low value of 1.0×10^3 ft-lb/rad to permit the wheelsets to orient themselves in yaw. These figures imply that the self-steered radial trucks with new and Heumann wheels are subject to the traditional design conflicts between improved

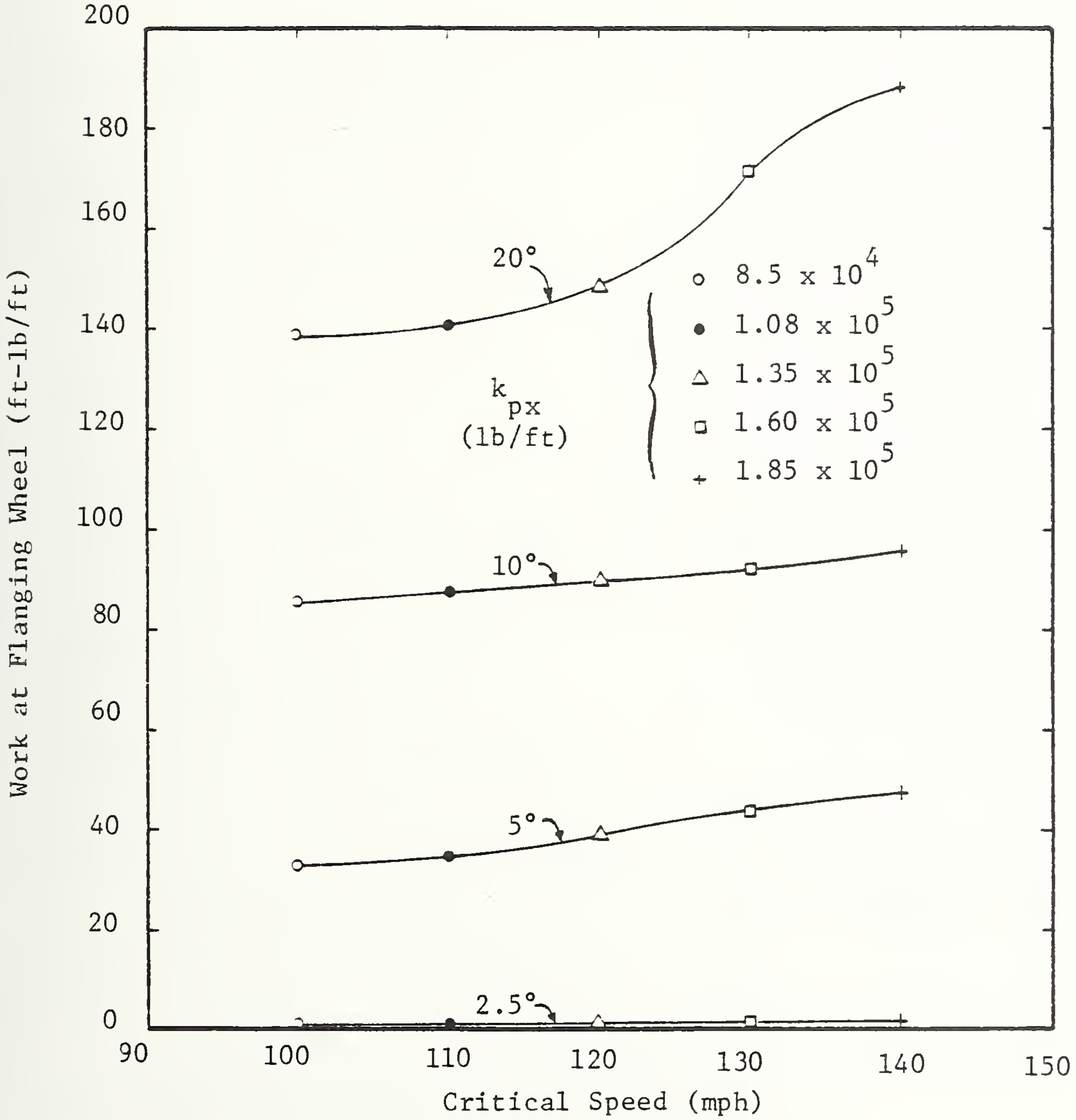

Figure 5.3 Curving Performance/Stability Tradeoff in Terms of Work at Flanging Wheel vs. Critical Speed of a Conventional Truck with New Wheels Negotiating 2.5°, 5°, 10°, and 20° Curves.

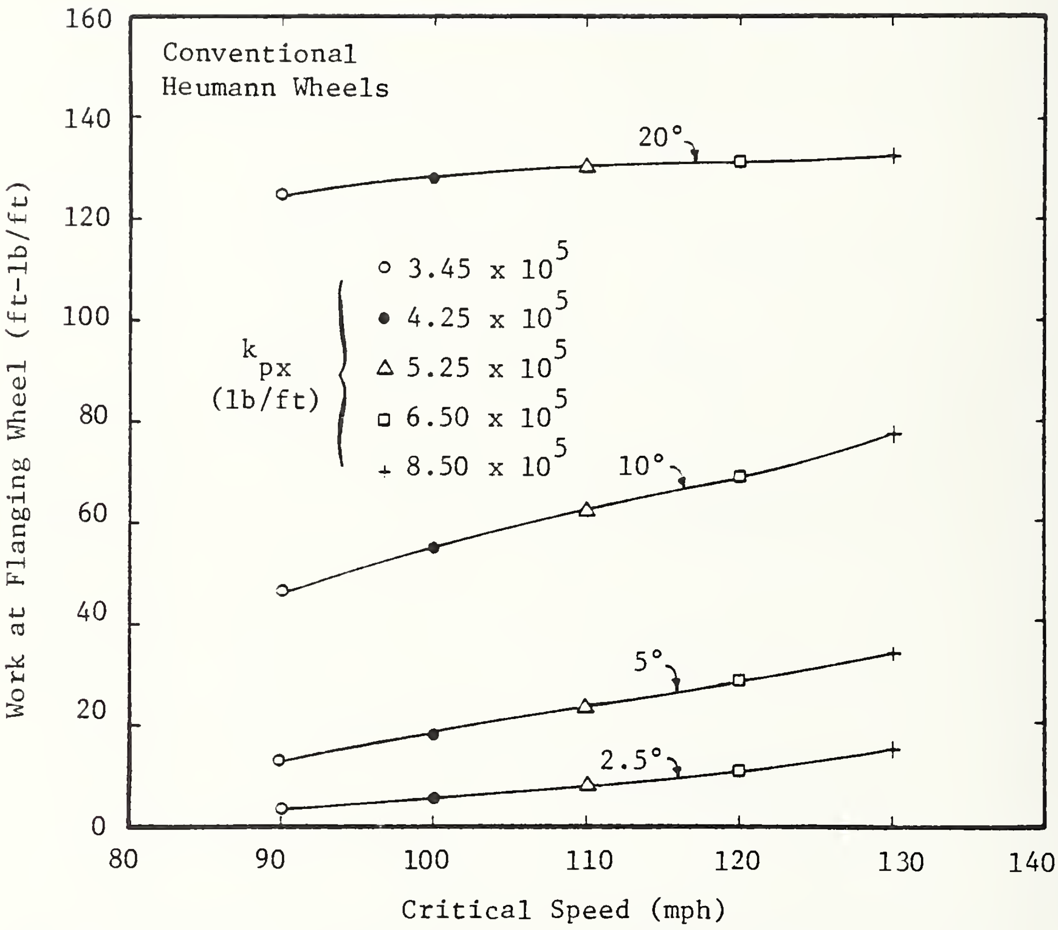

Figure 5.4 Curving Performance/Stability Tradeoff in Terms of Work at Flanging Wheel vs. Critical Speed of a Conventional Truck with Heumann Wheels Negotiating 2.5°, 5°, 10°, and 20° Curves.

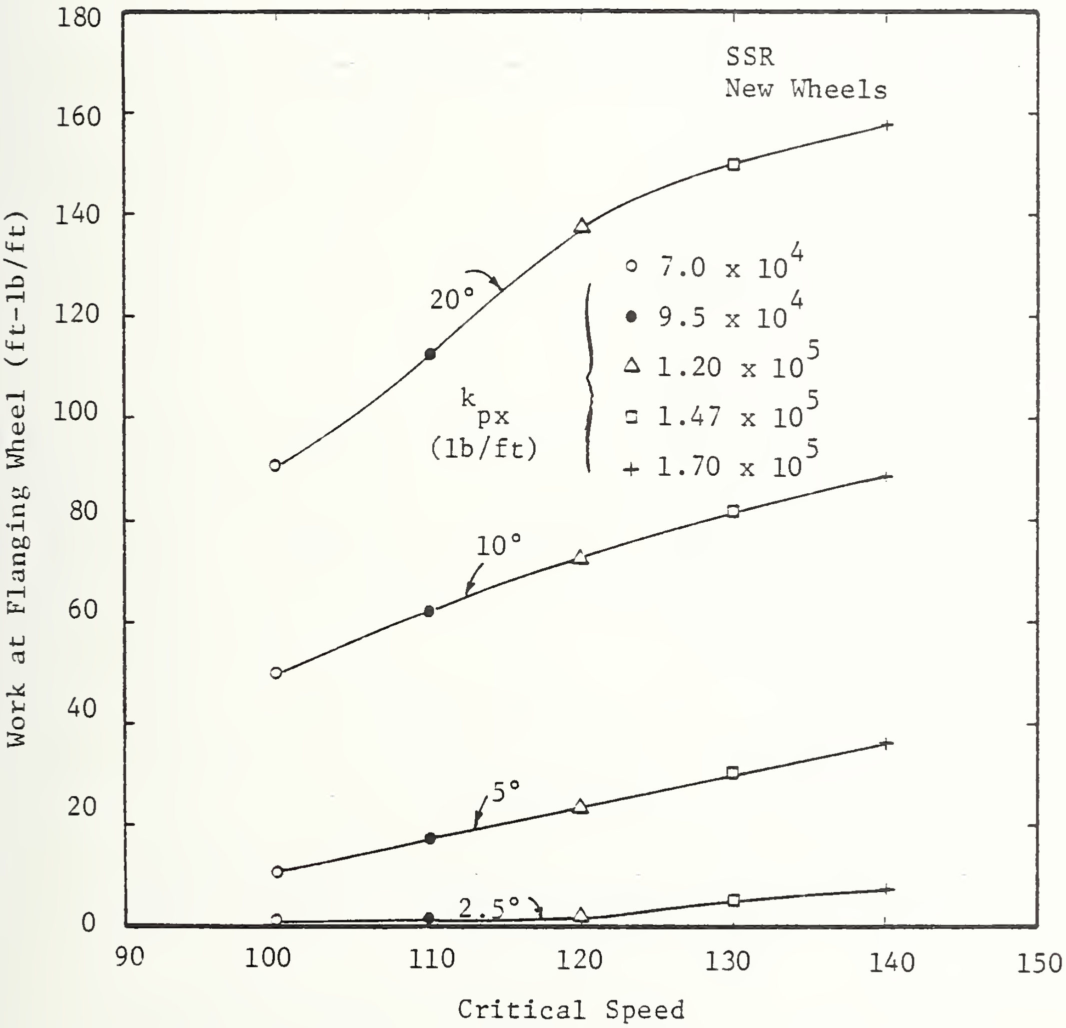

Figure 5.5 Curving Performance/Stability Tradeoff in Terms of Work at Flanging Wheel vs. Critical Speed of a Self-Steered Radial Truck with New Wheels Negotiating 2.5°, 5°, 10°, and 20° Curves.

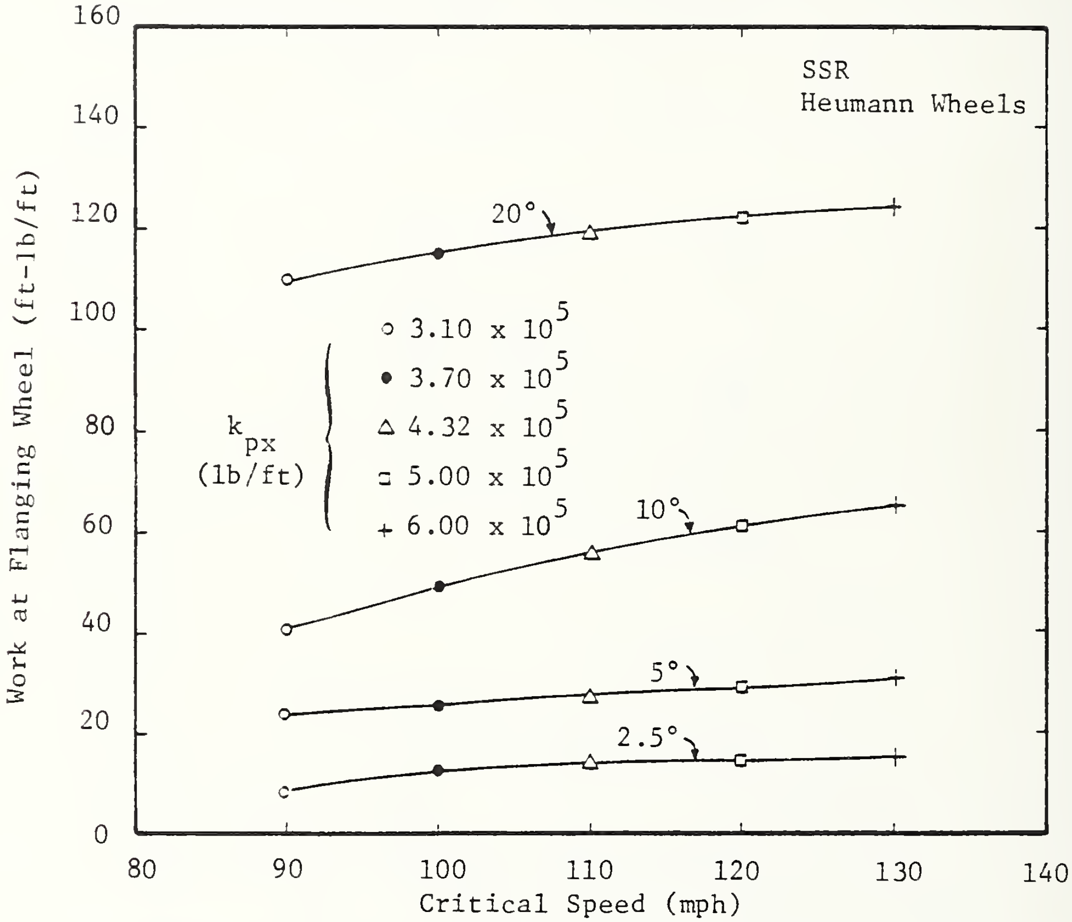

Figure 5.6 Curving Performance/Stability Tradeoff in Terms of Work at Flanging Wheel vs. Critical Speed of a Self-Steered Radial Truck with Heumann Wheels Negotiating 2.5°, 5°, 10°, and 20° Curves.

stability and curving performance. For a self-steered radial truck with new wheels traversing 10° and 20° curves, the work increases approximately 75% as the critical speed changes from 100 to 140 mph due to increasing k_{px}. For a truck with Heumann wheels, the work increases 65% for the 10° curve and 14% for the 20° curve with changes in critical speed from 90 to 130 mph. At lower degree curves, the work increases more for the truck with new wheels (from 1 to 8 ft-lb/ft at 2.5° as critical speed increases from 100 to 140 mph) than for the truck with Heumann wheels (10 to 15 ft-lb/ft at 2.5° as critical speed changes from 90 to 130 mph).

Two forced-steered truck designs are considered in the tradeoff study. The first design, FSR I, has a soft primary longitudinal stiffness (k_{px} = 7.0×10^4 lb/ft); the second design, FSR II, practically has negligible primary longitudinal suspension ($k_{px} = 1.0 \times 10^3$ lb/ft). In Figures 5.7 and 5.8 graphs of flanging wheel work versus critical speed are shown for the FSR I and FSR II designs with new wheels, respectively; in Figures 5.9 and 5.10 the corresponding graphs are shown for the trucks with Heumann wheels. In these figures the independent variable is the interaxle bending stiffness, k_{b2}. For both designs with new and Heumann wheels, the work is almost insensitive to increases in k_{b2} at low degree curves. The work in negotiating a 2.5° curve is 1 ft-lb/ft for the range of k_{b2} values. Thus for negotiation of low degree curves, it is advantageous to stiffen k_{b2} to maximize the critical speed while the work remains relatively constant (and small). For the two forced-steered truck designs with new wheels negotiating higher degree curves, the work increases slightly with increasing critical speed, as k_{b2} is stiffened. The work increases because of understeering of the lead wheelset which was shown to occur for forced-steered trucks with new wheels and pure

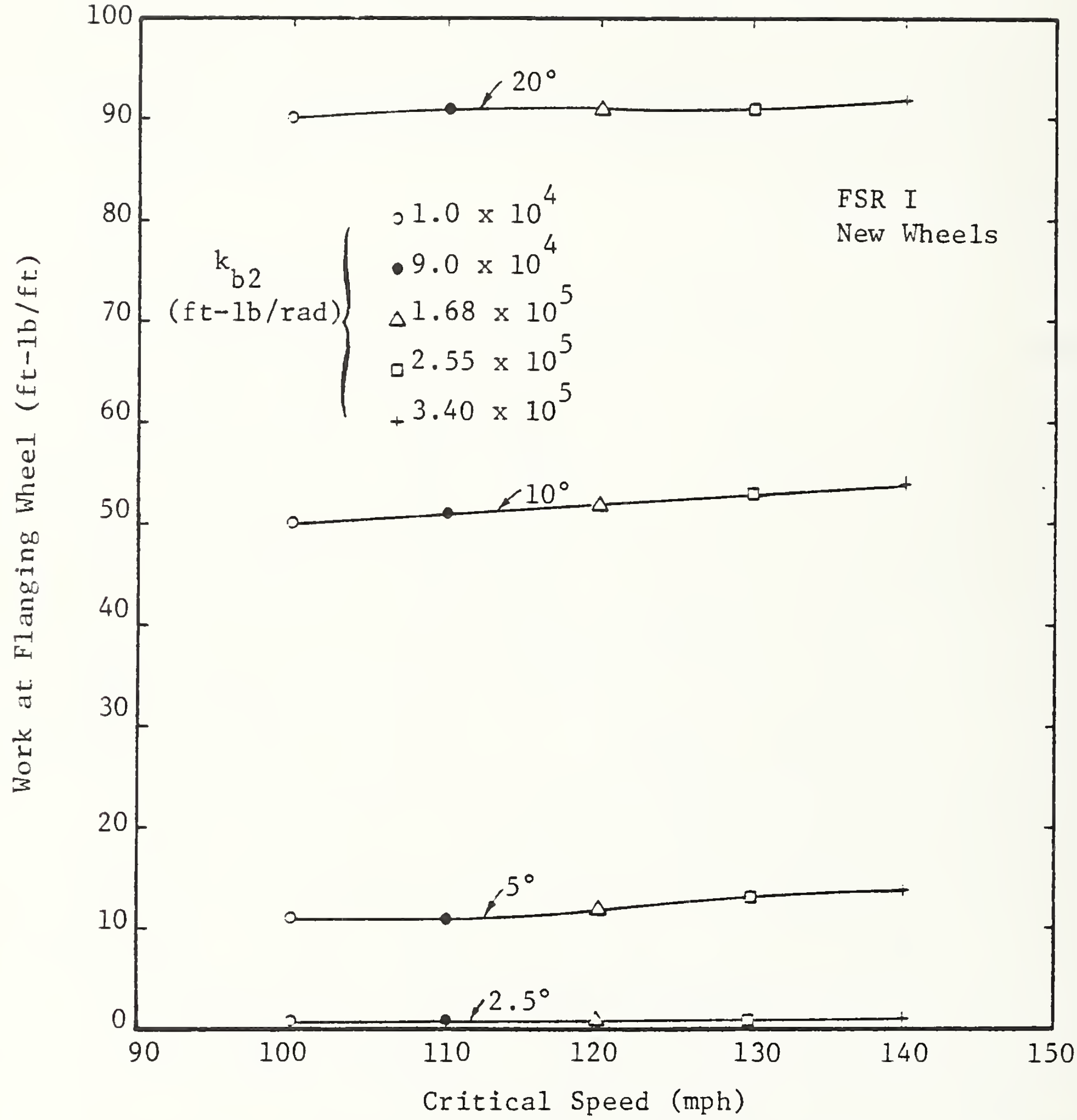

Figure 5.7 Curving Performance/Stability Tradeoff in Terms of Work at Flanging Wheel vs. Critical Speed of a Forced-Steered Radial Truck, FSR I, With New Wheels Negotiating 2.5°, 5°, 10°, and 20° Curves.

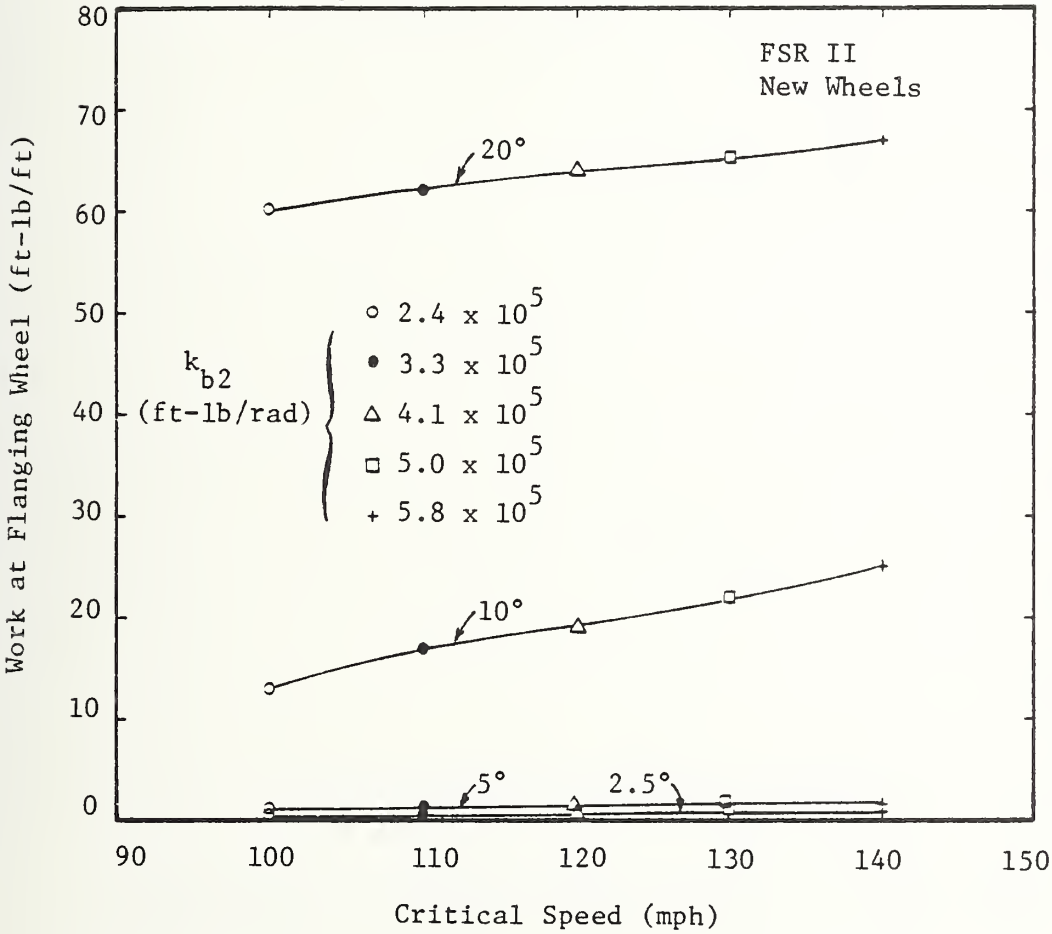

Figure 5.8 Curving Performance/Stability Tradeoff in Terms of Work at Flanging Wheel vs. Critical Speed of a Forced-Steered Radial Truck, FSR II, With New Wheels Negotiating 2.5°, 5°, 10°, and 20° Curves.

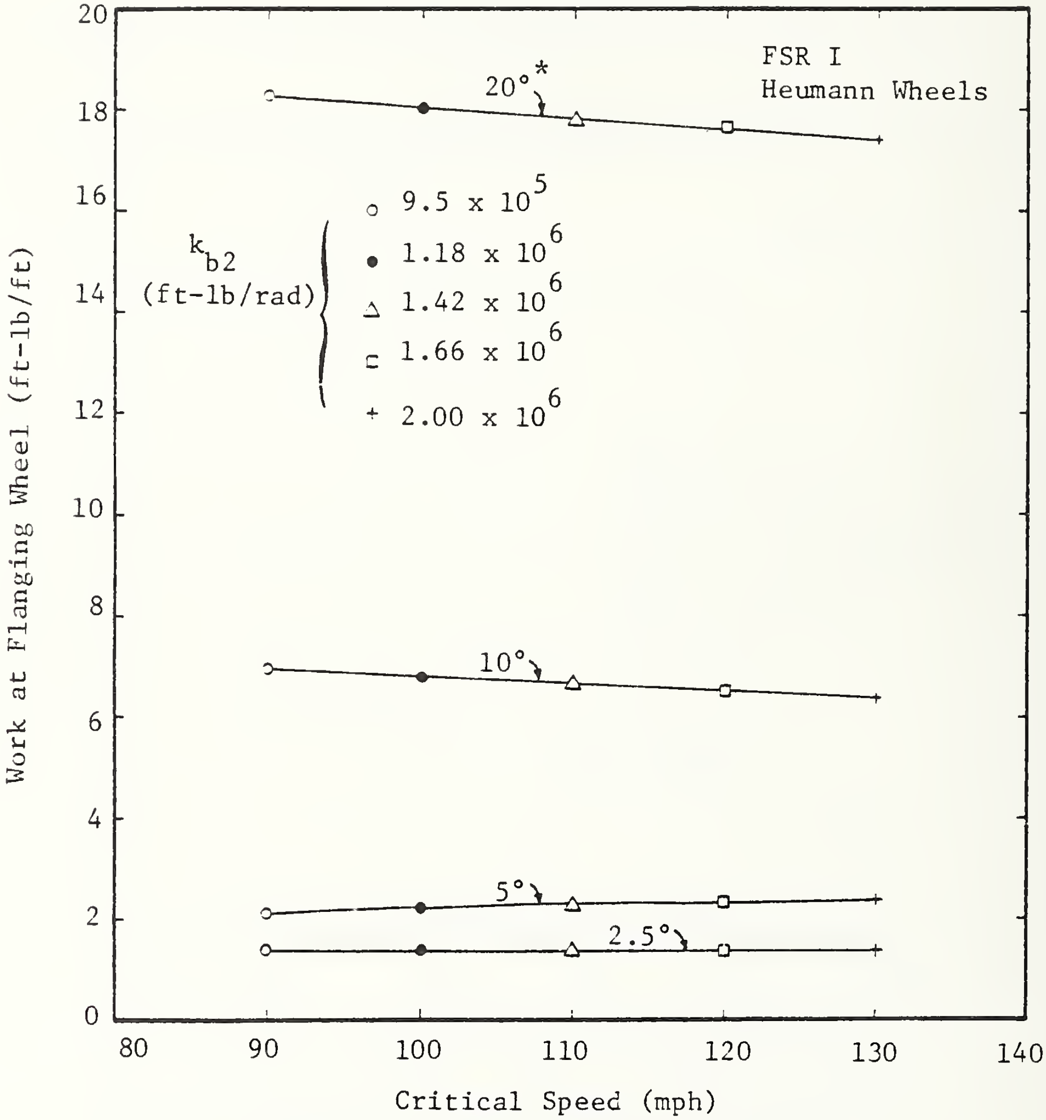

Figure 5.9 Curving Performance/Stability Tradeoff in Terms of Work at Flanging Wheel vs. Critical Speed of a Forced-Steered Radial Truck, FSR I, With Heumann Wheels Negotiating 2.5°, 5°, 10°, and 20° Curves. (*Work at Trailing Outer Wheel).

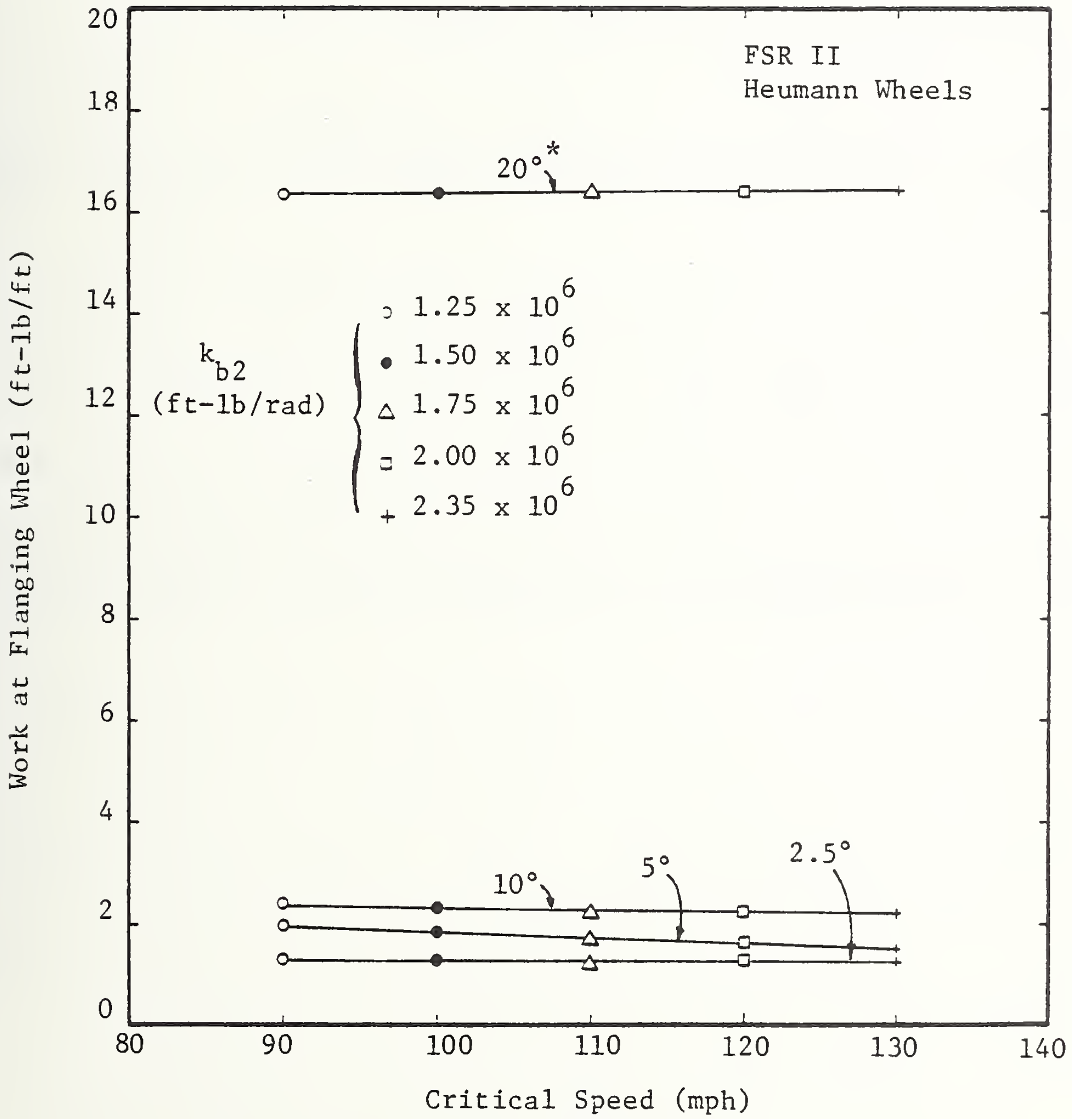

Figure 5.10 Curving Performance/Stability Tradeoff in Terms of Work at Flanging Wheel vs. Critical Speed of a Forced-Steered Radial Truck, FSR II, With Heumann Wheels Negotiating 2.5°, 5°, 10°, and 20° Curves. (*Work at Trailing Outer Wheel).

rolling line steering gains. As the FSR I truck design with Heumann wheels negotiates higher degree curves the work at the flanging wheel decreases as the critical speed increases with stiffer k_{b2}. The work for a FSR II truck with Heumann wheels negotiating higher degree curves remains essentially constant. For these trucks with Heumann wheels the pure rolling line steering gain provides effective steering of the wheelsets and thus the work decreases or stays constant as k_{b2} is increased. This represents an ideal situation since no tradeoff exists. A stiffer k_{b2} is desirable since it gives a more stable truck with the same or improved curving properties.

5.3 Comparative Performance of Conventional, Self-Steered, and Forced-Steered Trucks

The tradeoff plots of the previous section are summarized in Tables 5.3 and 5.4 for trucks with new and Heumann wheels, respectively. These tables list the work at the flanging wheel for a conventional, self-steered radial, and two forced-steered radial truck designs negotiating 2.5°, 5°, 10°, and 20° curves as a function of critical speed. Tables 5.3 and 5.4 can be used to compare the curving performance of the different trucks at the same critical speed.

The forced-steered radial truck designs exhibit superior performance when negotiating tight curves, since they can take advantage of the large relative yaw angle between the truck and carbody to steer the wheelsets into radial alignment. In Tables 5.3 and 5.4 the work of the two forced-steered radial truck designs negotiating 20° curves is appreciably lower than that of the self steered radial or conventional truck having the same critical speed. For instance, for trucks with new wheels and 120 mph critical speeds the work for the FSR I truck is 91 ft-lb/ft as compared with 138 ft-lb/ft for the self-steered radial truck and 149 ft-lb/ft for the conventional truck. The work for the FSR II truck is 64 ft-lb/ft.

Table 5.3 Curving Performance/Stability Tradeoff in Terms of Work at Flanging Wheel vs. Critical Speed for Four Truck Designs with New Wheels Negotiating 2.5°, 5°, 10°, and 20° Curves

Critical Speed (mph) \ Work at Flanging Wheel (ft-lb/ft)	Conventional				Self-Steered Radial				Forced Steered Radial FSR I				Forced Steered Radial FSR II			
	2.5°	5°	10°	20°	2.5°	5°	10°	20°	2.5°	5°	10°	20°	2.5°	5°	10°	20°
V_{cr} = 100	1	30	86	139	1	10	50	90	1	11	50	90	0	1	13	60
V_{cr} = 110	1	34	88	141	1	17	62	112	1	11	51	91	0	1	17	62
V_{cr} = 120*	1	39	90	149	2	24	72	138	1	12	52	91	0	1	19	64
V_{cr} = 130	1	44	92	171	5	31	82	150	1	13	53	91	1	1	22	65
V_{cr} = 140	1	48	95	189	8	37	89	158	1	14	54	92	1	1	25	67

*Baseline

Table 5.4 Curving Performance/Stability Tradeoff in Terms of Work at Flanging Wheel vs. Critical Speed for Four Truck Designs with Heumann Wheels Negotiating 2.5°, 5°, 10°, and 20° Curves

Critical Speed (mph) \ Work at Flanging Wheel (ft-lb/ft)	Conventional				Self-Steered Radial				Forced Steered Radial FSR I				Forced Steered Radial FSR II			
	2.5°	5°	10°	20°	2.5°	5°	10°	20°	2.5°	5°	10°	20°**	2.5°	5°	10°**	20°**
V_{cr} = 90	4	13	47	124	10	24	41	110	1	2	7	18	1	2	2	16
V_{cr} = 100	5	18	55	128	13	25	49	115	1	2	7	18	1	2	2	16
V_{cr} = 110	8	24	63	130	14	27	55	119	1	2	7	18	1	2	2	16
V_{cr} = 120*	11	29	69	131	15	29	61	122	1	2	7	18	1	2	2	16
V_{cr} = 130	14	34	77	132	15	31	68	125	1	2	6	17	1	2	2	16

*Baseline **Work at Trailing Outer Wheel

The advantage of the forced-steered radial trucks is most evident at higher critical speeds. For example, at a critical speed of 140 mph the work is 189, 158, 92 and 67 ft-lb/ft for conventional, self-steered radial, forced steered FSR I and FSR II trucks, respectively, with new wheels. Higher critical speeds for the conventional and self-steered radial trucks are achieved by increasing the primary longitudinal stiffness, k_{px}, resulting in significantly degraded curving performance indicated by increased work. On the other hand, increasing the interaxle bending stiffness, k_{b2}, of the forced-steered radial trucks (up to a certain value) increases the critical speed and only slightly degrades the curving performance for trucks with new wheels resulting in a minimal increase in work, and actually improves or maintains the curving performance of trucks with Heumann wheels resulting in a decrease in work.

In comparison of the different trucks with new wheels (Table 5.3) at low critical speeds, the first forced-steered truck design, FSR I, behaves similar to the self-steered radial truck which performs better than the conventional truck. At a 100 mph critical speed design, the work for a conventional truck is 86 ft-lb/ft versus 50 ft-lb/ft for both the self-steered and forced-steered FSR I trucks negotiating a 10° curve. The forced-steered design FSR I does not possess sufficient steering action due its the soft interaxle bending stiffness, k_{b2}, at low critical speeds (at V_{cr} = 100 mph the k_{b2} is 1.0 x 10^4 ft-lb/rad for FSR I) and thus behaves like the self-steered radial truck. The second forced-steered truck design, FSR II, offers superior curving performance due to the practical absence of primary longitudinal stiffness and higher value of k_{b2} (at V_{cr} = 100 mph, k_{b2} = 2.4 x 10^5 ft-lb/rad). The work is 13 ft-lb/ft for a FSR II truck designed for a

100 mph critical speed traversing a 10° curve.

The work at the flanging wheel as a function of curvature is shown in Figure 5.11 for the different (baseline) trucks with new wheels, all at the same critical speed of 120 mph. The improvement in curving performance by employing self-steered over conventional designs and by utilizing forced-steered instead of self-steered truck designs is demonstrated. Further the curving performance of the forced-steered truck FSR II at all degree curves is shown to offer over a factor of two reduction in the work at the flanging wheel in comparison to the conventional truck.

The steady-state lateral force at the leading outer wheel as a function of curvature is compared in Figure 5.12 for the baseline trucks. Lower lateral forces are predicted for the forced-steered truck designs than the conventional and self-steered trucks. The self-steered truck has slightly lower forces in comparison to the conventional truck, except at very steep curvatures (> 15°) for which the lateral force predicted for the conventional truck is slightly less than that associated with the self-steered design. This occurs because at very tight curvatures the leading outer wheel lateral force is approaching its theoretical maximum, i.e., the adhesion limit, and the self-steered truck has a higher normal load due to the added weight of the steering linkages.

In Table 5.4 the different trucks with Heumann wheels are compared. The self-steered radial truck offers a slight improvement in curving performance in comparison to the conventional truck for moderate and tight curves. For low degree curves, the conventional truck performs better than the self-steered radial truck, as high values of shear stiffness cause the wheelsets of the radial truck to flange somewhat sooner than those of the conventional

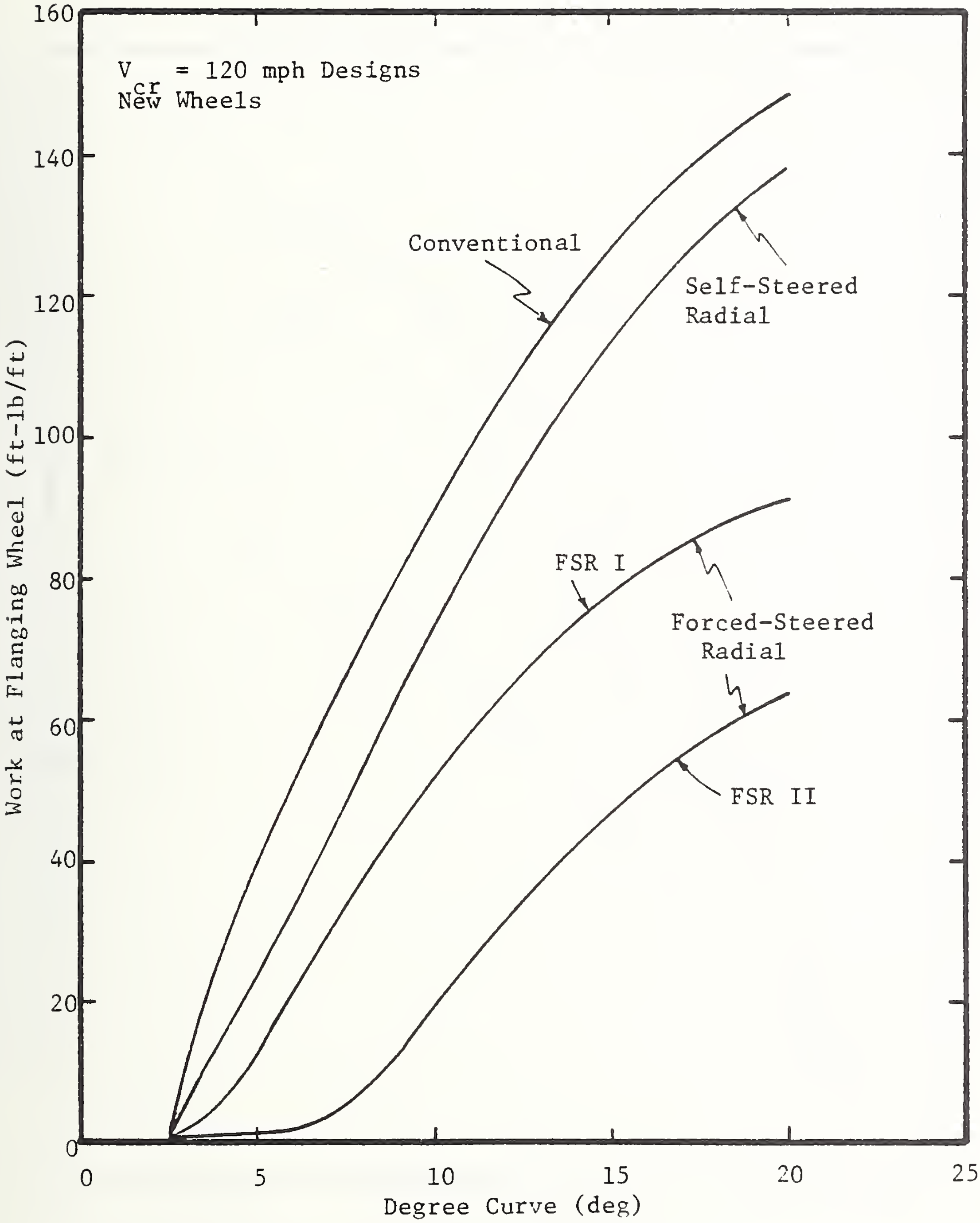

Figure 5.11 Work at Flanging Wheel vs. Curvature for Baseline Truck Designs with New Wheels (Critical Speeds = 120 mph).

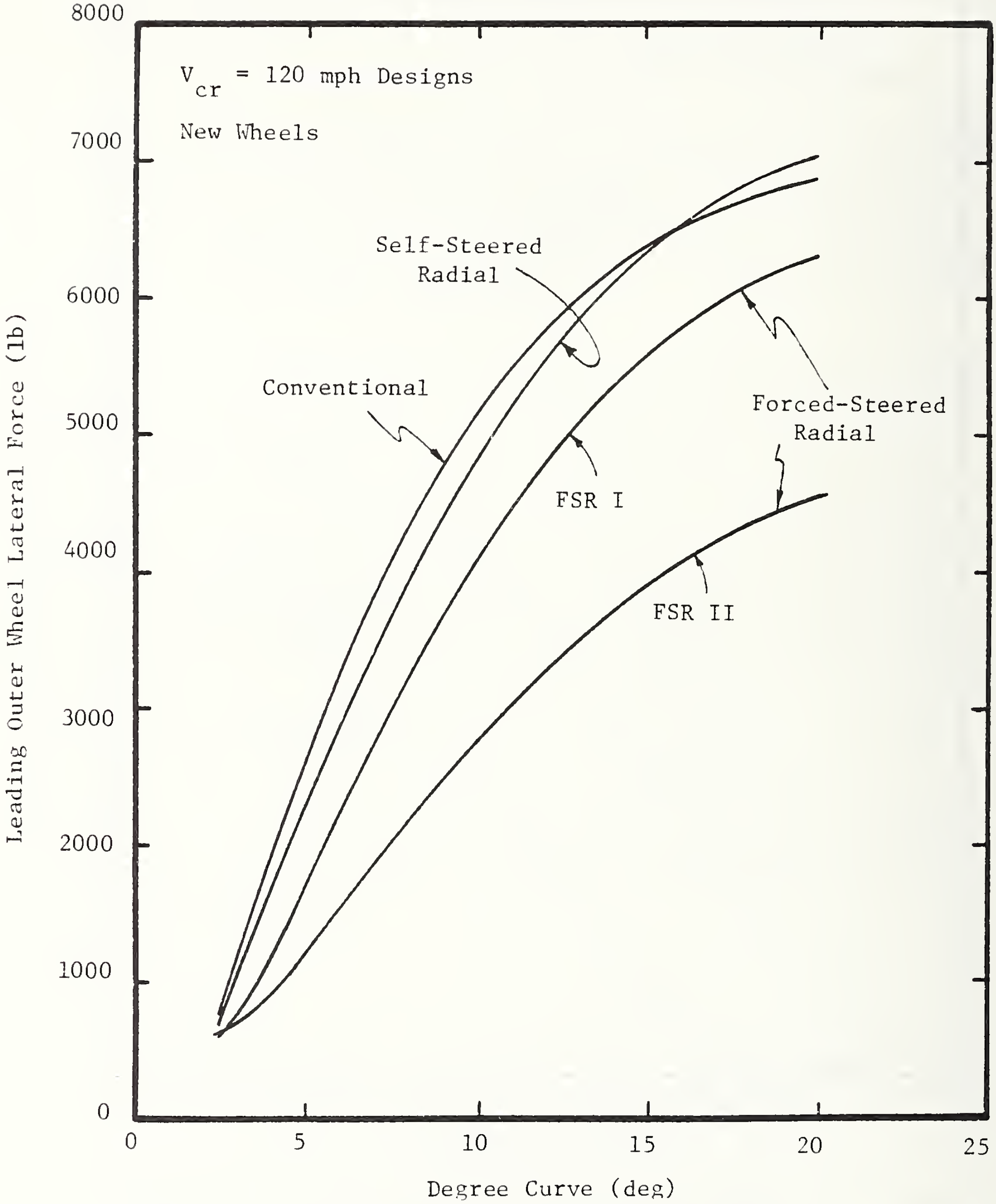

Figure 5.12 Leading Outer Wheel Lateral Force vs. Curvature for Baseline Truck Designs with New Wheels (Critical Speeds = 120 mph).

truck. Significant advantages are gained by employing the forced steered truck designs over the conventional or self-steered trucks at all degree curves, especially for designs at high critical speeds.

Figures 5.13 and 5.14 are graphs of the work and lateral force at the flanging wheel, respectively, versus degree curve for the different (baseline) trucks with Heumann wheels and critical speeds of 120 mph. The slight reduction in work of the conventional truck in comparison to the self-steered radial truck at low degree curves is due to the earlier onset of flanging. In contrast, at high degree curves (> 10°) the lateral force of the self-steered radial truck is slightly larger than the force of the conventional truck. This is due to the larger adhesion limit for the self-steered truck as a result of the added weight of the steering linkages. Both figures demonstrate the potential of employing forced-steered trucks in contrast to conventional and self-steered trucks.

The forced-steered truck designs are advantageous in comparison to the conventional truck not only because they reduce the work (and force) at the flanging wheel, but because they more equally distribute the work at the four wheels. The total work and distribution of work at the contact patches for the different trucks with new wheels is shown in Figure 5.15 and for trucks with Heumann wheels in Figure 5.16, where all trucks have critical speeds of 120 mph and are negotiating 10° curves. A reduction and equalization of work occurs for the forced-steered truck designs with Heumann wheels.

In this report, the curving performance (and stability) studies have focused on the behavior of the front truck. In general, as a vehicle negotiates a curve, more work is expended for the front truck than for the rear truck. This is due to the directions of the secondary suspension yaw moments which

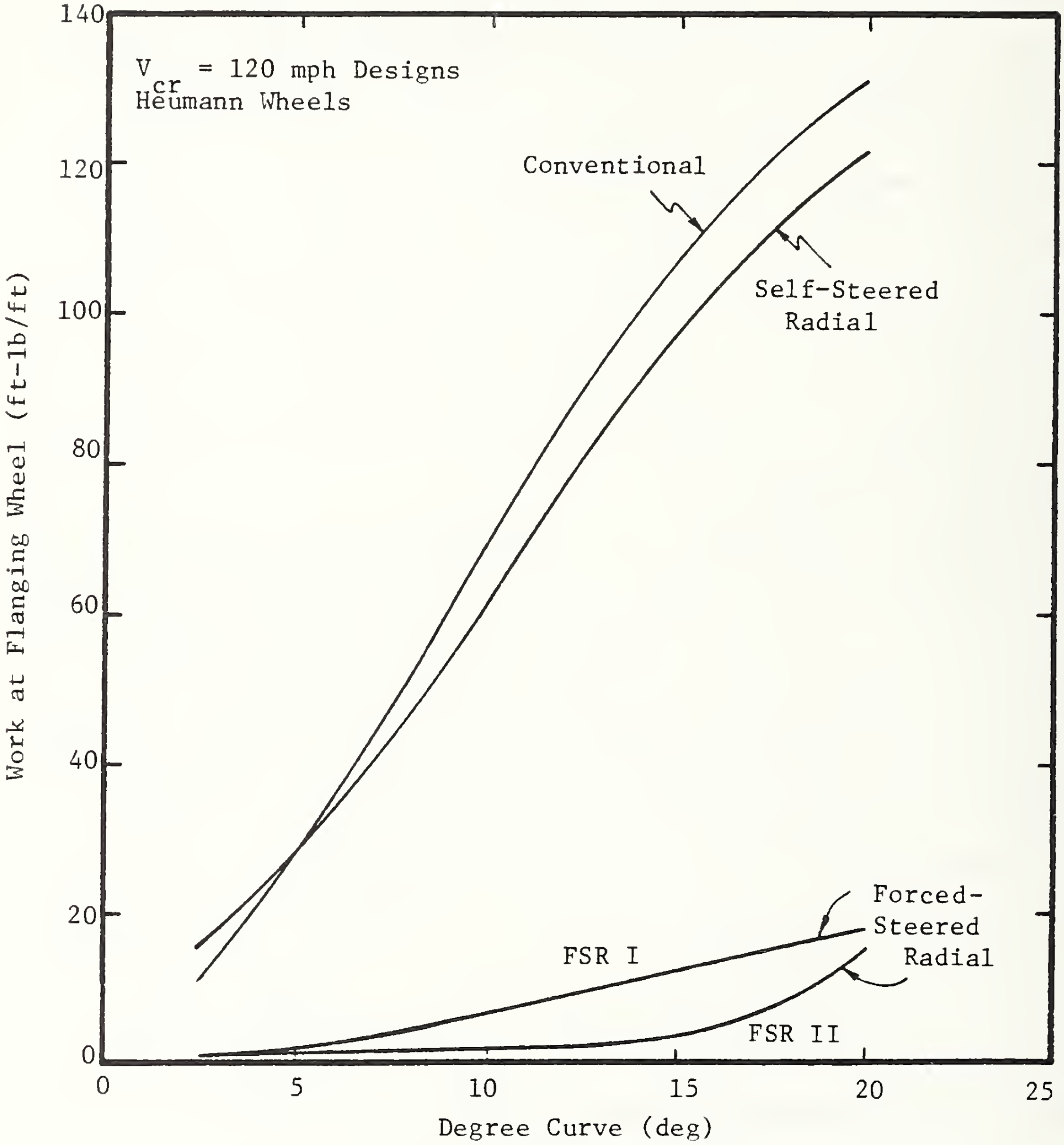

Figure 5.13 Work at Flanging Wheel vs. Curvature for Baseline Truck Designs with Heumann Wheels (Critical Speeds = 120 mph).

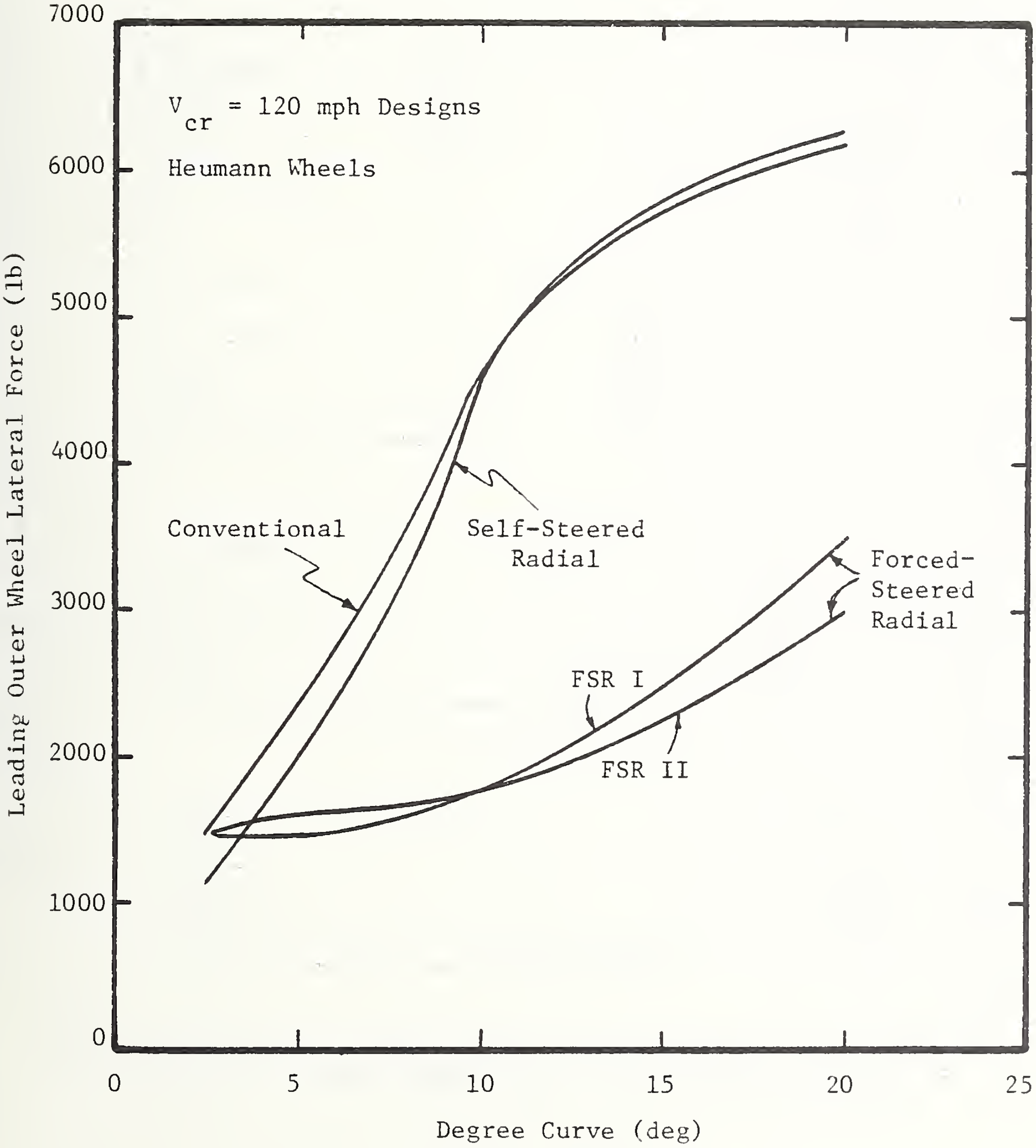

Figure 5.14 Leading Outer Wheel Lateral Force vs. Curvature for Baseline Truck Designs with Heumann Wheels (Critical Speeds = 120 mph).

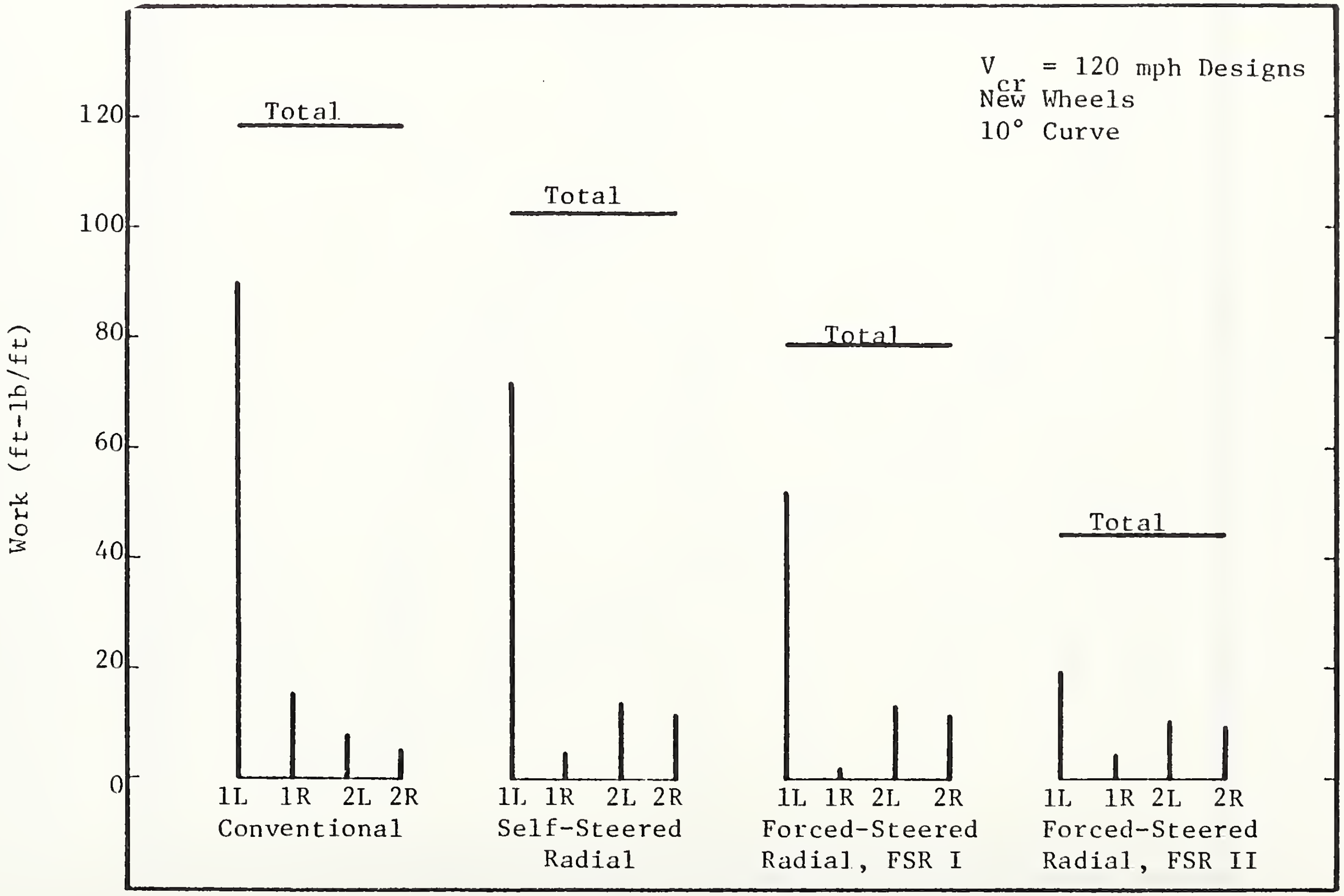

Figure 5.15 Total Work and Distribution of Work at Contact Patches for Baseline Trucks with New Wheels Negotiating 10° Curves (1L = Leading Left, 1R = Leading Right, 2L = Trailing Left, 2R = Trailing Right).

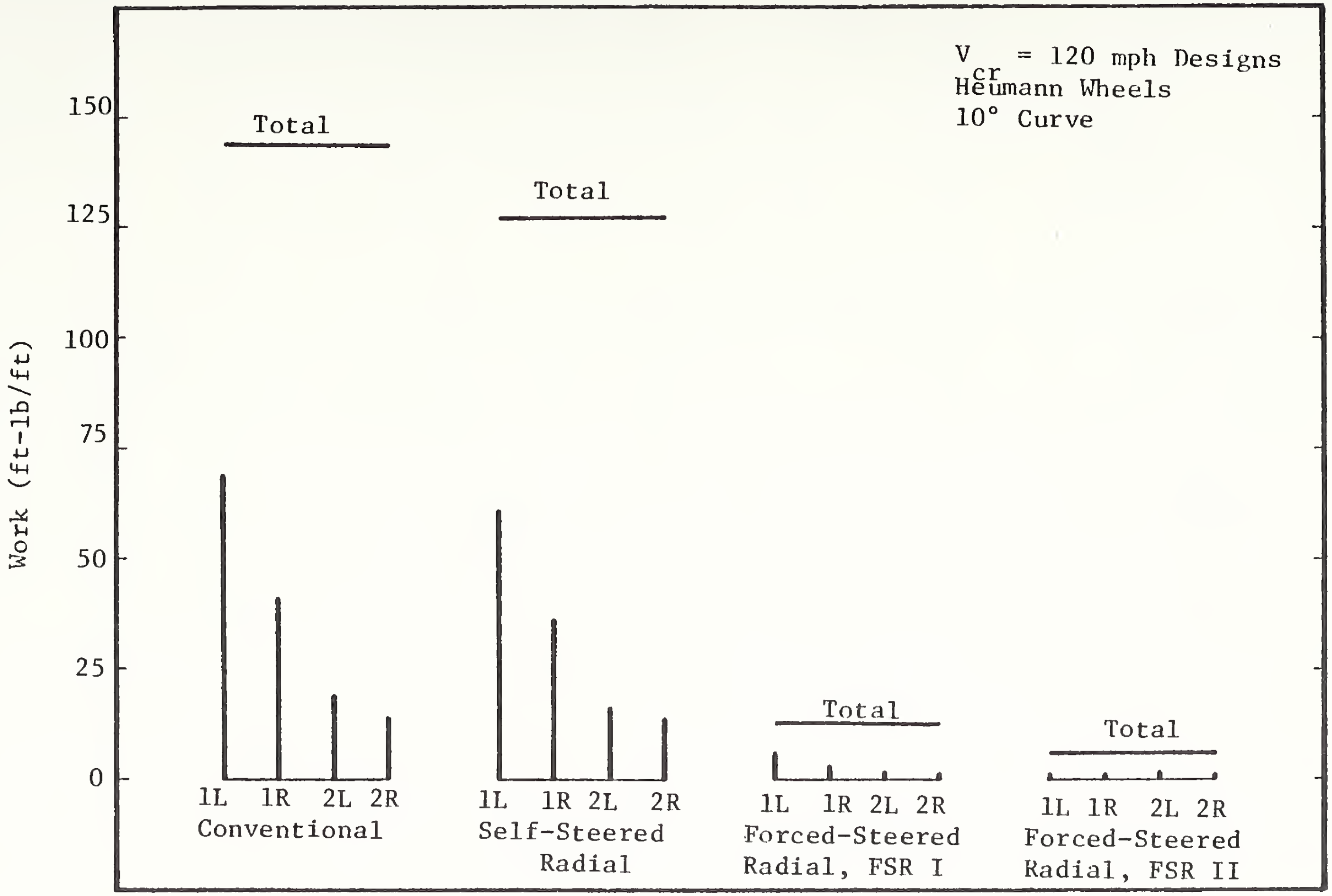

Figure 5.16 Total Work and Distribution of Work at Contact Patches for Baseline Trucks with Heumann Wheels Negotiating 10° Curves (1L = Leading Left, 1R = Leading Right, 2L = Trailing Left, 2R = Trailing Right).

act on the trucks, as shown in Figure 4.10. The yaw moment on the front truck hinders curving by helping to push the leading outer wheel into the flange, whereas the yaw moment on the rear truck helps curving by yawing the truck in the direction of the curve. As a result, in general it is the leading outer wheel of the vehicle which experiences the majority of the contact patch work. Thus, in the curving performance studies the work generated at the leading outer or flanging wheel of the front truck is used as the principal curving performance index.

Considerations of the power dissipated by the different trucks as they negotiate a curve illustrates the potential performance improvements possible with advanced designs. Table 5.5 is a summary comparison of the flanging wheel work, total work, and power requirements of the front and rear trucks for baseline designs (i.e., 120 mph critical speed designs) with new wheels negotiating 10° curves. The table shows that more work is expended for the front truck than for the rear truck, especially for the steered truck designs which have additional moments helping to steer the rear truck around the curve. Furthermore, the table shows the front truck, rear truck, and total vehicle power for negotiation of the 10° curve at 50 ft/sec (34 mph) for the different truck designs. The significantly reduced dissipated power of the forced-steered vehicles, especially the FSR II design with 6.4 HP, in comparison to the conventional vehicle with 21.4 HP emphasizes the potential advantages of employing forced-steering to reduce fuel consumption.

In general, forced-steered truck designs offer significant advantages over the conventional and self-steered trucks. This is especially true for trucks with Heumann wheels and for trucks negotiating tight curves.

Table 5.5 Comparison of Flanging Wheel Work, Total Work, and Power Requirements of Front and Rear Trucks for Baseline Designs With New Wheels Negotiating 10° Curves

		Conventional	Self-Steered Radial	Forced-Steered Radial	
				FSR I	FSR II
FRONT TRUCK	Flanging Wheel Work (ft-lb/ft)	90	72	52	19
	Truck Work (ft-lb/ft)	118	103	79	45
	Truck Power* (HP)	10.7	9.4	7.2	4.1
REAR TRUCK	Flanging Wheel Work (ft-lb/ft)	80	48	37	11
	Truck Work (ft-lb/ft)	118	84	57	25
	Truck Power* (HP)	10.7	7.6	5.2	2.3
Vehicle Total Power* (HP)		21.4	17.0	12.4	6.4

*@ 50 ft/sec (34 mph)

CHAPTER 6

CONCLUSIONS

This study has evaluated the stability and curving performance of conventional and advanced design rail transit trucks. A general performance model which incorporates conventional, self-steering radial and forced-steering trucks has been formulated. This model is sufficiently general so that it can be utilized to represent transit track designs currently in use as well as those which have been proposed at this point in time for possible development.

The general model has been incorporated into two computer programs for performance evaluation. The first program, the dynamic stability program, is used to compute the truck critical speed at which sustained hunting occurs using linear eigenvalue analysis techniques. The second program, the steady-state curving program determines the curving forces, angles of attack and wheel/rail contact patch work performed as a vehicle negotiates a constant radius curve at constant speed. The curving analysis is based upon nonlinear representations of vehicle suspension elements and nonlinear geometry including single- and multiple-point wheel/rail contact and creep force saturation.

Parametric studies have been conducted to determine the influence of vehicle suspension parameters and wheel profile on vehicle critical speed and curving performance measured in terms of work generated in the wheel/rail contact patch per unit distance traveled.

For conventional trucks, parametric studies have shown that the two dominant design parameters in stability and curving are truck primary longitudinal suspension stiffness and wheel profile. Broad ranges of values for truck primary lateral suspension stiffness and secondary suspension yaw stiffness were found for which both stability and curving performance parameters were insensitive. For new AAR wheel profiles with a 0.05 conicity it was found that typical truck primary suspension stiffness varied from 1×10^5 lb/ft to 2×10^6 lb/ft and resulted in designs with critical speeds ranging from 110 mph to 210 mph. Increases in longitudinal stiffness above this range resulted in decreases in critical speed. As the stiffness is decreased the work required to negotiate a curve decreases. For a 10° curve with operation at balanced speed, the work developed at the flanging wheel is 155 ft-lb/ft at a design longitudinal stiffness of 2×10^6 lb/ft and 85 ft-lb/ft at a design longitudinal stiffness of 10^5 lb/ft. Thus, a direct tradeoff exists between critical speed and work performed during curving with respect to primary longitudinal stiffness. Trucks with relatively high values of stiffness (approaching 10^6 lb/ft) will have improved curving performance if lower stiffnesses are used and the associated lower critical speeds are acceptable.

The use of Heumann wheels with an effective conicity of 0.2 in the conventional truck results in a tradeoff between stability and curving. To achieve a given value of critical speed with the higher conicity Heumann wheel profile requires a higher primary longitudinal stiffness than for the 0.05 conicity wheel truck designs. For example at a critical speed of 125 mph the 0.2 conicity wheel requires a stiffness of 6.5×10^5 lb/ft while a 0.05 conicity wheel suspension design requires a stiffness of 1.04×10^5 lb/ft. At this critical speed the higher conicity wheel requires 22% less work per unit distance traveled than the truck designed for the 0.05 conicity wheel to negotiate a 10° curve. Conventional truck designs with the same critical speed but with higher conicity wheels result in reduced work required in curving. It should be noted, however that in the range of practical longitudinal primary stiffnesses, the 0.2 conicity wheel was found to have a maximum design critical speed of 130 mph and if higher critical speeds are desired reduced conicity wheels are required.

Parametric studies of self-steering radial trucks identified interaxle bending stiffness, primary longitudinal stiffnesses and wheel profile to be the primary parameters influencing the stability/curving tradeoff. For trucks with tapered or Heumann wheels, stability was found to be insensitive to increases in interaxle shear stiffness once a value of 5×10^5 lb/ft is exceeded and also independent of secondary suspension yaw stiffness for values approaching the baseline design value. Stability studies conducted on self-steering trucks have shown that stability may be achieved with a combination of interaxle bending stiffness and primary suspension stiffness. As these quantities are increased critical speed increases; however, the work performed during curving also increases. The studies have concentrated on designs with low interaxle bending stiffnesses of 10^3 ft-lb/rad and a high interaxle shear stiffness of 10^6 lb/ft since this combination provides a relatively good stability/curving tradeoff. The primary suspension longitudinal stiffness has been selected as the primary design parameter used to achieve desired levels of critical speed. Data have shown that the critical speed increases from 100 mph to 130 mph and the work to negotiate a 10° curve increases from 50 to 82 ft-lb/ft as primary suspension stiffness is increased from 7.0×10^4 lb/ft to 1.5×10^5 lb/ft for 0.05 conicity wheels. For 0.2 conicity Heumann wheels, the stiffness required to achieve critical speeds of 100 mph and 130 mph is higher, 3.7×10^5 lb/ft and

6×10^5 lb/ft, respectively, and the corresponding work required to negotiate a 10° curve is 50 ft-lb/ft and 68 ft-lb/ft. For a lower critical speed design of 100 mph the work required to negotiate a 10° curve for low conicity tapered and high conicity Heumann wheel suspension designs is similar while for the higher critical speed designs of 130 mph, the higher conicity Heumann wheel uses 20% less work than the lower conicity wheel.

Data comparing the work required to negotiate 10° curves for conventional and self-steering radial trucks designed for a critical speed of 130 mph have shown for both the low and high wheel conicity designs that approximately a 12% decrease in work is required for the radial truck in comparison to the conventional truck.

An extensive parametric study of forced-steering trucks employing steering links between the carbody and the axles has been conducted. As a result of this study it has been shown that principal stability/curving tradeoff design parameters include truck primary suspension longitudinal stiffness, steering link stiffness and wheel conicity while secondary design parameters which may be selected within relatively broad ranges include primary suspension lateral stiffness and secondary suspension yaw stiffness. The geometric gain of the steering linkage was selected in the studies to yield a design which nominally tracks the pure rolling line of a given degree curve. As a result of the studies two designs designated FSR I and FSR II were selected. Design FSR I employs a relatively low value of primary suspension longitudinal stiffness of 7×10^4 lb/ft, while design FSR II employs a very low value of longitudinal stiffness of 1×10^3 lb/ft which was selected to represent a lower limit of stiffness. Low values of primary suspension longitudinal stiffness are desired in forced-steering trucks to allow the wheelsets to adopt a radial orientation during curving. Stability is achieved in these low primary stiffness designs by increasing the steering link stiffness. As the steering link stiffness is increased, critical speed increases until a sufficiently large value of steering link stiffness is achieved for which further increases in stiffness decrease critical speed. Data comparing the work required to negotiate a 10° curve for designs with suspension parameters selected to yield a critical speed of 130 mph have shown for 0.05 conicity wheels that design FSR I requires 53 ft-lb/ft while FSR II requires 22 ft-lb/ft and for 0.2 conicity wheels that design FSR I requires 6 ft-lb/ft and FSR II requires 2 ft-lb/ft. These data show that for the same critical speed suspension designs, lower values of primary suspension longitudinal stiffness result in decreased work during curving and that the higher conicity wheels also result in decreased work during curving. The practical lower limit on primary suspension stiffness is determined by a combination of factors involving details of the truck propulsion and braking systems and requires study beyond the scope of this report.

Work required during curve negotiation for the forced-steering truck designs is less than that for conventional and radial tracks with similar critical speeds. For a critical speed of 130 mph using 0.05 conicity wheels, the work required to negotiate a 10° curve is 92 ft-lb/ft for the conventional design, 82 ft-lb/ft for the radial design, 56 ft-lb/ft for forced-steering design I and 28 ft-lb/ft for forced-steering design II. And for 0.2 conicity wheels, the work is 77 ft-lb/ft, 68 ft-lb/ft, 6 ft-lb/ft and 2 ft-lb/ft. These data show significant reductions in work for forced-steering truck designs in comparison to conventional and radial truck designs. The reductions in work are more significant with the higher conicity 0.2 Heumann wheels than the 0.05 conicity tapered wheels. Thus, forced-steering trucks show potential to utilize high conicity wheels to reduce work generated during curving in comparison to conventional and radial trucks with the same critical speeds. This potential with high conicity wheels can be most effectively realized for truck designs with critical speeds in the range up to 130 mph. If higher critical speed designs are required, then a wheel conicity less than 0.2 is required for the range of truck suspension parameters explored in this report.

For specific transit authorities, the selection of an appropriate truck design depends upon the number and severity of curves which influence the relative importance of the wheel wear performance parameters measured in terms of work and depends upon the required truck critical speed which is related to maximum system operating speed. The potential for reduction in wheel wear during curving offered by forced-steering truck designs must be assessed in terms of the increased complexity associated with the forced steering linkage designs, the practicality of maintaining the required high relative stiffness in the forced-steering links, and the capability to accommodate braking and propulsion forces with relatively low primary longitudinal stiffnesses. These issues can best be resolved through analysis and testing of prototype forced-steering truck designs.

This report summarizes data and analysis for conventional and advanced truck designs based upon stability and steady-state curve negotiation. A continuation of this study is planned to determine the dynamic behavior of these trucks during spiral curve entry and exit as well as during track anomoly negotiation.

APPENDIX A

DERIVATION OF CURVATURE STEERING GAIN AND INTERAXLE BENDING STIFFNESS FOR THREE FORCED STEERING TRUCK PROTOTYPES

In this Appendix the curvature steering gains and interaxle bending stiffnesses for three forced-steering truck prototypes are derived. Each curvature steering gain is derived by assuming the linkages are perfectly rigid, and calculating the resultant steering action $\Delta\psi$ between the wheelsets (i.e., when yaw angles of the two wheelsets are in equal and opposite directions) as a result of yawing the carbody. As expressed in the steering law, the curvature steering gain is a ratio between the resultant steering action $\Delta\psi$ and the motion that causes the steering action (the carbody yaw in this case). The interaxle bending stiffness is derived by performing an experiment, where the two wheelsets are yawed in opposite directions to form a steering angle $\Delta\psi$ between them. The external moment that has to be applied on each wheelset, which is due to the steering linkage stiffnesses only, is calculated from static force and moment balances on the truck and its parts. During the experiment the bolster is restrained from yawing, but is permitted to follow the truck laterally to achieve static equilibrium. The primary suspension system, which is not part of the steering linkage, has been left out of the analysis, except in the case of the L prototype, where the primary lateral stiffness has an effect on the interaxle bending stiffness. The interaxle bending stiffness is given by the ratio of the symmetrical external moment on each wheelset, and the resultant steering action $\Delta\psi$.

A.1 The S Truck Prototype

The schematic of the S prototype is shown in Figure A.1. The steering linkages lie in the vertical plane such that the lateral distance from the truck centerline to any node shown is d. The steering law for the prototype is:

$$\Delta\psi = \pm 2G\left[\frac{\psi_1+\psi_2}{2} - \psi_c\right] \quad \text{(A-1)}$$

where the plus sign is for the front truck and the minus sign for the rear one.

To illustrate the effect on the steering linkages due to the carbody yaw (and hence bolster yaw) only, the steering law is reduced to

$$\Delta\psi = \pm 2G(-\psi_c) \quad \text{(A-2)}$$

which, for the front truck, gives the curvature steering gain as:

$$G = \frac{\Delta\psi}{(-2\psi_c)} \quad \text{(A-3)}$$

with the assumption of rigid steering linkages, yawing the carbody in the negative direction produces $\Delta\psi$ as shown in Figure A.2.

With small motion assumptions, $s_3 = \frac{\Delta\psi}{2} \times d$ (A-4)

$$s_1 + s_2 = \ell_1 \quad \text{(A-5)}$$

From the expanded diagram of the linkages:

$$s_1 \times \theta = s_3 \quad \text{(A-6)}$$

$$s_2 \times \theta = s_3 \quad \text{(A-7)}$$

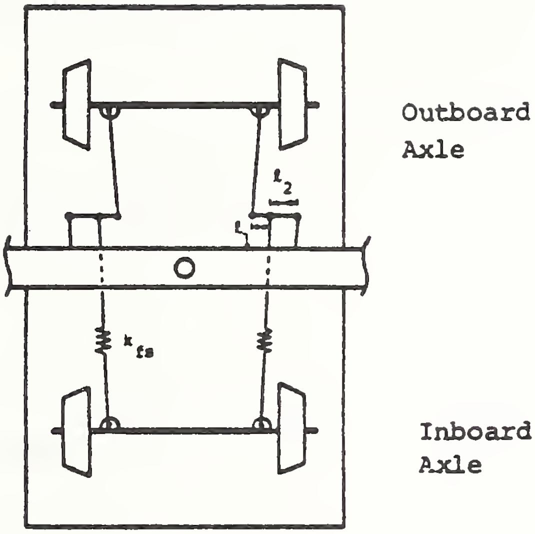

S Prototype

$$\Delta\psi = \pm 2G\left(\frac{\psi_1+\psi_2}{2} - \psi_c\right)$$

$$G = \frac{\ell_1}{\ell_1 + 2\ell_2}$$

$$k_{b2} = \frac{1}{2} d^2 k_{fs}\left(1 + \frac{\ell_2}{\ell_1 + \ell_2}\right)^2$$

Figure A.1 Schematic of the S Forced-Steering Truck Prototype

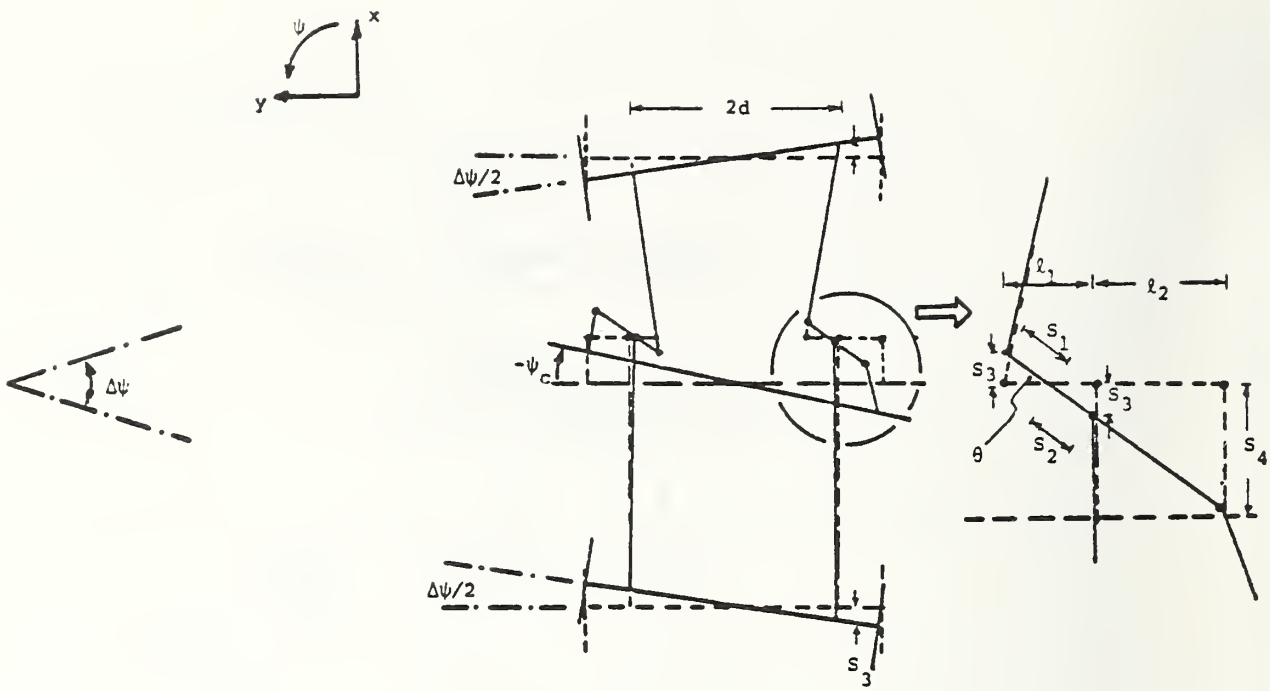

Figure A.2 Kinematic Steering of the S Truck Prototype (Front Truck)

Combining equations (A-4) through (A-7) yields

$$\theta = \frac{\Delta\psi \times d}{\ell_1} \tag{A-8}$$

and

$$s_1 = s_2 = \frac{1}{2}\ell_1 \tag{A-9}$$

Recalling that the steering linkages lie in the vertical plane and not in the horizontal plane as shown in the diagram, the following relation is obtained:

$$s_4 = \theta x(s_2 + \ell_2) = (-\psi_c) \times d \tag{A-10}$$

which, upon substitution of equation (A-8) and (A-9), yields

$$\frac{\Delta\psi}{\ell_1}\left(\frac{\ell_1}{2} + \ell_2\right) = (-\psi_c) \tag{A-11}$$

Rearranging equation (A-11) according to the definition of equation (A-3), the curvature steering gain is given by:

$$G = \frac{\Delta\psi}{(-2\psi_c)} = \frac{\ell_1}{\ell_1 + 2\ell_2} \tag{A-12}$$

The gain G can also be derived by having zero carbody yaw and yawing the whole truck with its wheelsets, which leads to the same result as given by equation (A-12). The interaxle bending stiffness is calculated by yawing each wheelset through an angle $\Delta\psi/2$ in opposite directions to form a steering angle $\Delta\psi$ and calculating the effective resistance provided by the steering linkage stiffness. Figure A.3 shows the free body diagram of the wheelsets after the steering angle $\Delta\psi$ is imposed on them. (Because of symmetry about the truck lateral midplane only half of the truck is analyzed).

Assuming small motions, $h_1 = \frac{\Delta\psi}{2} \times d$ (A-13)

The distance h_2 is found by using similar triangles to be:

$$h_2 = \frac{\ell_2}{\ell_1 + \ell_2} h_1 \tag{A-14}$$

The deflection of spring k_{fs} is $\Delta = h_1 + h_2$ (A-15)

which, after substitution of equation (A-13) and (A-14), is given by

$$\Delta = \left(1 + \frac{\ell_2}{\ell_1 + \ell_2}\right) \frac{\Delta\psi}{2} d \tag{A-16}$$

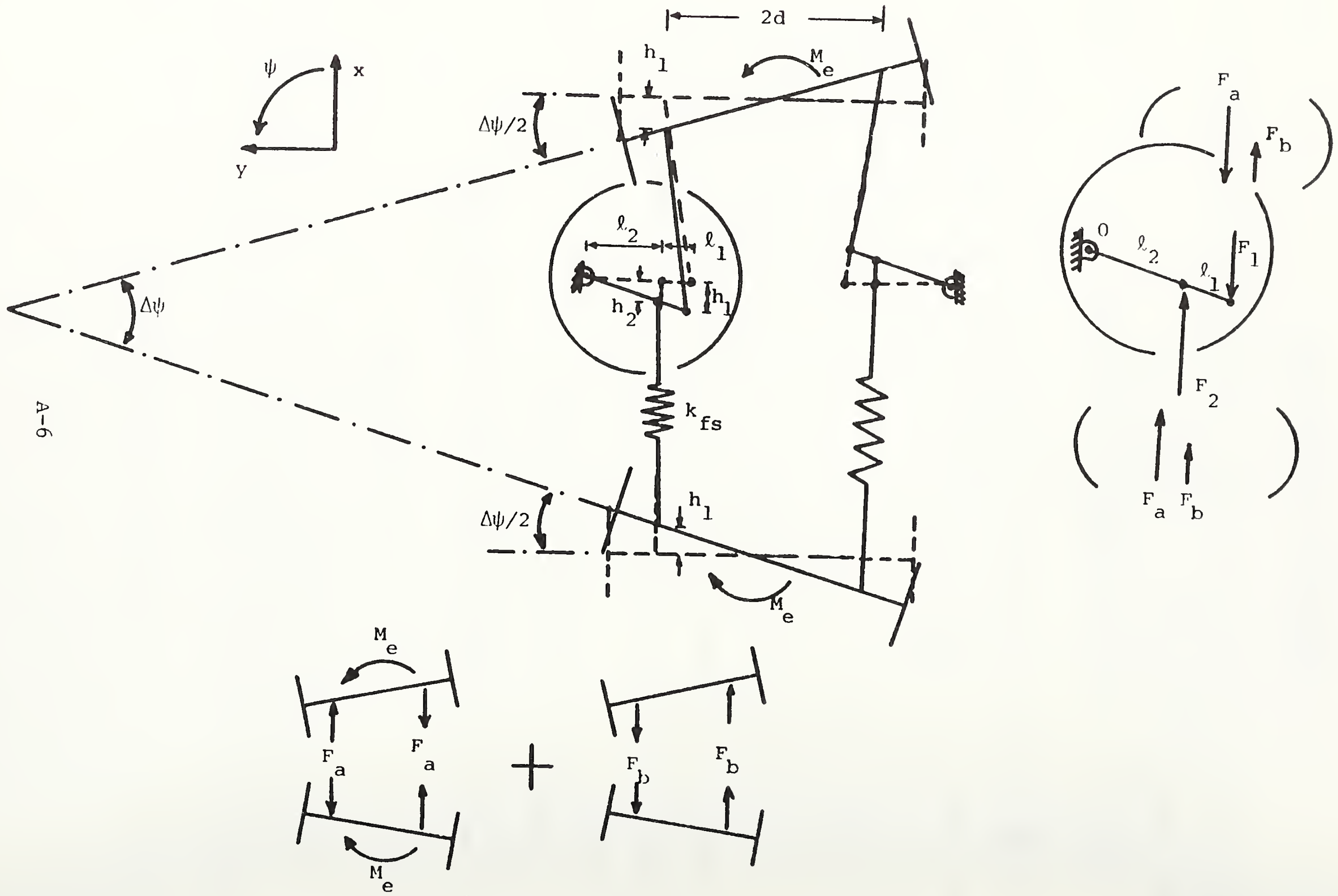

Figure A.3 Free Body Diagram of The S Prototype

The force F_2 is equal to the spring force and is

$$F_2 = k_{fs} d\left(1 + \frac{\ell_2}{\ell_1 + \ell_2}\right) \frac{\Delta\psi}{2} \tag{A-17}$$

Writing a moment balance about point 0 gives F_1 as

$$F_1 = k_{fs} d\left(1 + \frac{\ell_2}{\ell_1 + \ell_2}\right) \left(\frac{\ell_2}{\ell_1 + \ell_2}\right) \frac{\Delta\psi}{2} \tag{A-18}$$

The forces F_1 and F_2 can each be decomposed into two components F_a and F_b where

$$F_1 = F_a - F_b \tag{A-19}$$

$$F_2 = F_a + F_b \tag{A-20}$$

Equations (A-17) through (A-20) can be used to calculate F_a,

$$F_a = k_{fs} d \left(1 + \frac{\ell_2}{\ell_1 + \ell_2}\right)^2 \frac{\Delta\psi}{4} \tag{A-21}$$

The force component F_b acts in the same direction on both wheelsets and represents the tendency of the spring k_{fs} to yaw both wheelsets in the same direction. On the other hand, the force component F_a acts in opposite directions on the two wheelsets. It is the resistance from the spring k_{fs} against yawing the two wheelsets in opposite directions (i.e., against imposing the steering angle $\Delta\psi$ on the wheelsets). Thus the interaxle bending stiffness is due to F_a, which should be overcome by applying external moment M_e,

$$M_e = 2d \times F_a \tag{A-22}$$

The interaxle bending stiffness is defined as

$$k_{b2} = \frac{M_e}{\Delta\psi} \tag{A-23}$$

and is given by $$k_{b2} = \frac{1}{2} k_{fs} \left(1 + \frac{\ell_2}{\ell_1 + \ell_2}\right)^2 d^2 \tag{A-24}$$

after substitution of equations (A-21) and (A-22) into equation (A-23).

A.2 The L Truck Prototype

The steering law for the L prototype, shown in Figure A.4, is:

$$\Delta\psi = \pm 2G\left[\frac{y_1-y_2}{2b} - \psi_c\right] + \underbrace{2\left(\frac{G+1}{b}\right)}_{G*} \left[\frac{y_1+y_2}{2} - y_T\right] \tag{A-25}$$

The gain consists of two terms; the first term is the primary steering action which senses the track curvature and steers the wheelsets into a radial alignment around a curve. The second term is a secondary effect that results from the linkage arrangement of the prototype. This effect is usually negligible unless the truck has very soft primary lateral stiffnesses, in which case the wheelset pair can move laterally with respect to the truck frame. The derivation of the curvature steering gain is done separately for the two steering actions mentioned above. The curvature steering gain due to the primary steering action, G, is most easily derived by having zero (y_1-y_2) and yawing the carbody in the negative direction, where G (for the front truck) is defined as:

$$G = \frac{\Delta\psi}{(-2\psi_c)} \tag{A-26}$$

Figure A.5 shows the kinematic steering of the front L truck prototype with the truck stays stationary, assuming perfectly rigid steering linkage. To

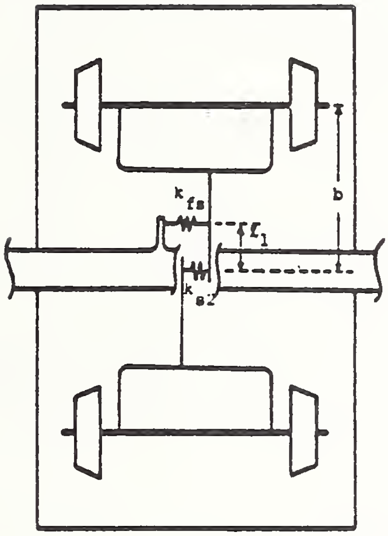

L Prototype

$$\Delta\psi = \pm 2G\left(\frac{y_1-y_2}{2b} - \psi_c\right)$$

$$+2\left(\frac{G+1}{b}\right)\left(\frac{y_1+y_2}{2} - y_T\right)$$

$$G = \frac{\ell_1}{b-\ell_1}$$

$$k_{b2} = \frac{(b-\ell_1)^2 k_{fs} k_{py}}{(4k_{py}+k_{fs})}\ ^*$$

---

*Assumes stiff k_{s2} for symmetry

Figure A.4 Schematic of the L Forced-Steering Truck Prototype

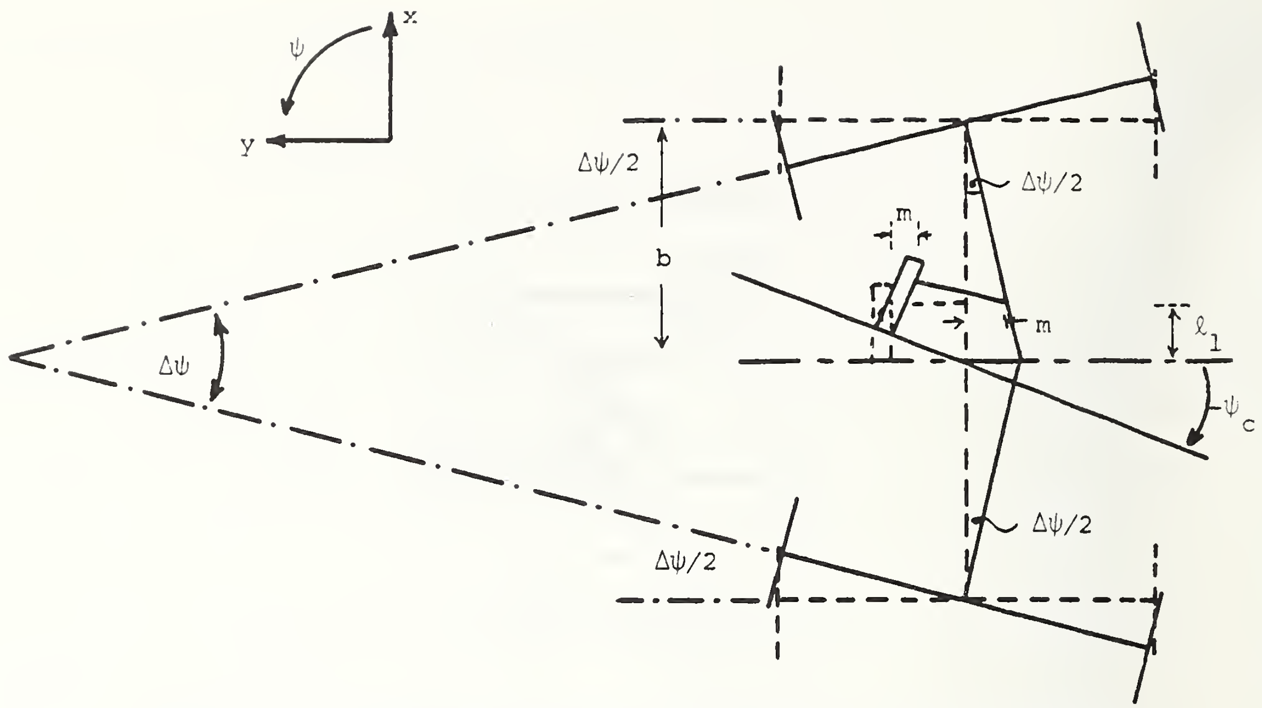

Figure A.5 Kinematic Steering of the Front L Truck Prototype

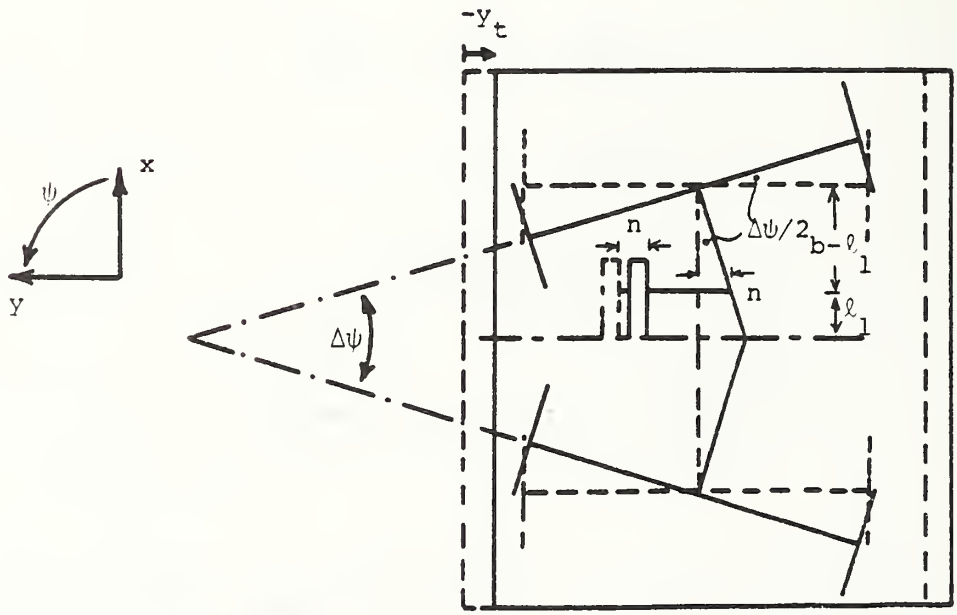

Figure A.6 Secondary Kinematic Steering of the Front L Truck Prototype achieve a symmetrical configuration, a very high value of interaxle shear stiffness has been assumed. This assumption is justified by the fact that the physical prototype does have a high value of interaxle shear stiffness. The mathematical model can still be used with low interaxle shear stiffness provided the physical linkage arrangement is modified to include symmetrical steering linkages with respect to both wheelsets. One possible such modification is shown in reference [19].

From Figure A.5, as a result of $(-\psi_c)$ carbody yaw, each wheelset is yawed through an angle $\Delta\psi/2$, forming a steering angle $\Delta\psi$ between the wheelsets. With a small motion assumption the following relations are obtained:

$$m = (-\psi_c) \times \ell_1 \tag{A-27}$$

$$\Delta\psi/2 = \frac{m}{b-\ell_1} \tag{A-28}$$

Equations (A-26) through (A-28) are combined to give

$$G = \frac{\ell_1}{b - \ell_1} \tag{A-29}$$

as the primary effect curvature steering gain.

The secondary effect curvature steering gain can be derived by moving the truck frame laterally with respect to the wheelset pair, as shown in Figure A.6. Since the bolster follows the truck motion in the lateral direction,

$$n = -y_t \tag{A-30}$$

For small motion,

$$\Delta\psi/2 = \frac{n}{b-\ell_1} \quad \text{(A-31)}$$

The secondary steering gain is defined by the steering law as

$$G^* = \frac{\Delta\psi}{(-2y_t)} \quad \text{(A-32)}$$

which, after substitution of equations (A-30) and (A-31) is given by

$$G^* = \frac{1}{b-\ell_1} \quad \text{(A-33)}$$

Comparing with equation (A-29), G^* can be rewritten as

$$G^* = \frac{G+1}{b} \quad \text{(A-34)}$$

The secondary steering effect acts in the same direction on both the leading and trailing trucks and hence has the same sign for both trucks in the steering law.

Figure A.7 shows the free body diagram of the L truck prototype after the external moment M_e' is applied on both wheelsets to achieve a steering angle $\Delta\psi$ between the wheelsets. As a result the truck frame moves laterally a distance y_T and yaws through an angle ψ_T, both in the negative direction, to achieve a new equilibrium configuration. Taking a moment balance about point C (center of the truck), and lateral force balance on the truck yields:

$$2k_{py}(y_T + b\psi_T)b = 2\, k_{py}(y_T - b\psi_T)b + F_{fs}\,\ell_1 \quad \text{(A-35)}$$

$$F_{fs} = 4k_{py}y_T \quad \text{(A-36)}$$

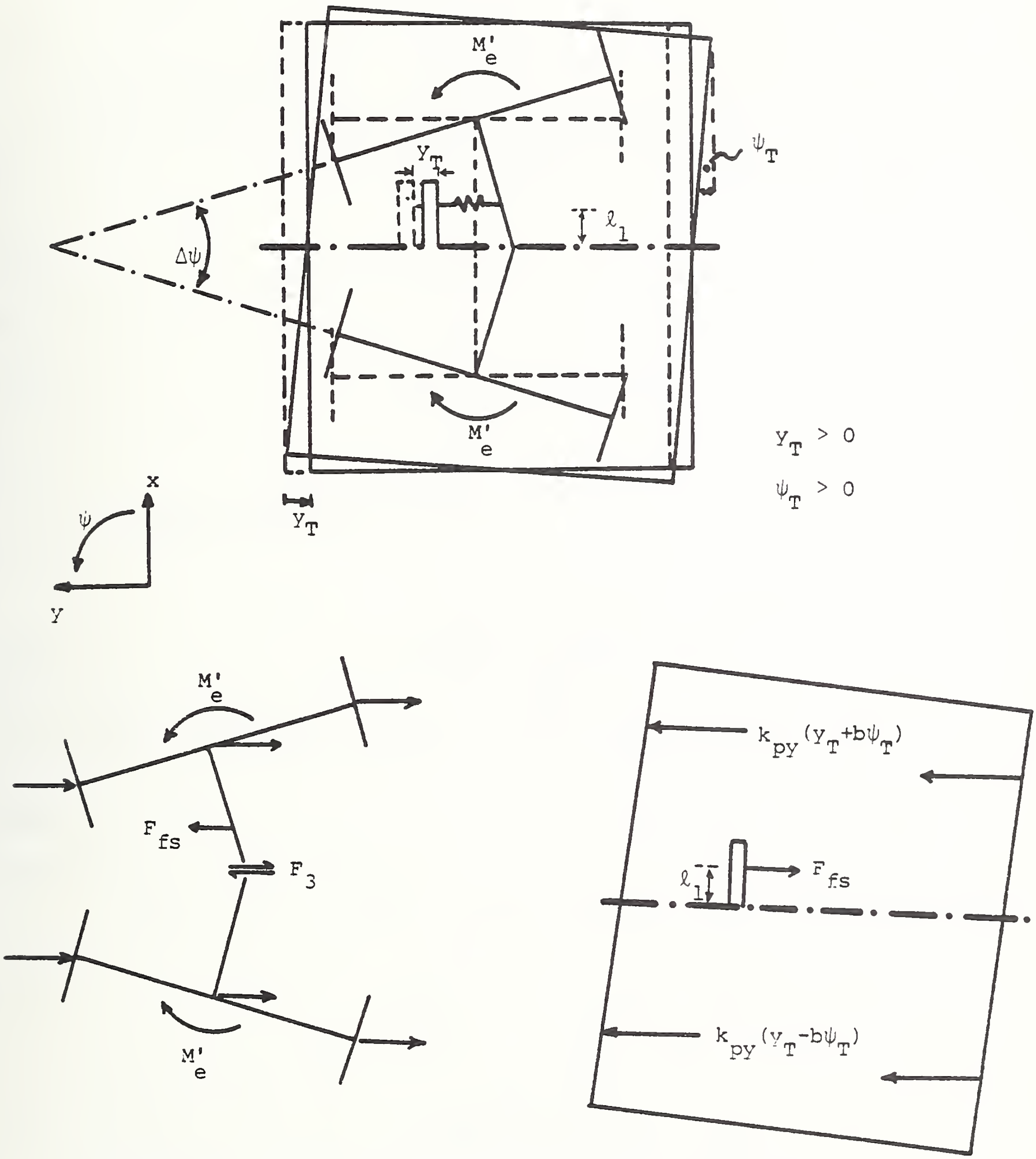

Figure A.7 Free Body Diagram of the L Truck Prototype

Substituting equation (A-36) into (A-35):

$$\psi_T = \frac{y_T \ell_1}{b^2} \tag{A-37}$$

The deflection of spring k_{fs} can be determined from the spring force F_{fs} as given by equation (A-36) or from the geometry as:

$$\Delta_{fs} = \frac{F_{fs}}{k_{fs}} = \frac{4\,k_{py}\,y_T}{k_{fs}} \tag{A-38}$$

$$\Delta_{fs} = \frac{\Delta\psi}{2}(b - \ell_1) - y_T \tag{A-39}$$

respectively.

Solving for y_T from equations (A-38) and (A-39) and substituting the result into equation (A-36) leads to:

$$F_{fs} = \frac{2k_{py}\,\Delta\psi\,(b-\ell_1)k_{fs}}{(4k_{py} + k_{fs})} \tag{A-40}$$

Taking a moment balance on the trailing wheelset about point B gives

$$F_3 b = M_e' \tag{A-41}$$

while doing the same on the leading wheelset about point A yields

$$F_3 b + M_e' = F_{fs} \times (b-\ell_1) \tag{A-42}$$

Combining equations (A-40) through (A-42)

$$M_e' = \frac{\Delta\psi\,(b-\ell_1)^2 k_{fs} k_{py}}{(4k_{py} + k_{fs})} \tag{A-43}$$

The interaxle bending stiffness, defined by the ratio of M_e' and $\Delta\psi$, is thus given by

$$k_{b2} = \frac{(b-\ell_1)^2 \, k_{fs} \, k_{py}}{(4k_{py} + k_{fs})} \tag{A-44}$$

A.3 The U Truck Prototype

The steering action for the U prototype is given by the following steering gain:

$$\Delta\psi = \pm 2G(\psi_T - \psi_c) \tag{A-45}$$

which utilizes the relative yaw angle between the truck and the carbody to sense the track curvature. The following derivation of the curvature steering gain assumes zero truck yaw so that the relative yaw angle between the truck and the carbody is given by the carbody yaw. With this assumption, equation (A-45) gives the gain G for the front truck as:

$$G = \frac{\Delta\psi}{(-2\psi_c)} \tag{A-46}$$

Figure A.8 shows the kinematic steering of the front truck as a result of yawing the carbody in the negative direction. Each wheelset is yawed through an angle $\Delta\psi/2$ in opposite directions, creating a steering angle $\Delta\psi$ between them. Assuming small motions,

$$d_1 = (-\psi_c) \times \ell_6 \tag{A-47}$$

$$d_2 = \frac{\Delta\psi}{2} \times \ell_3 \tag{A-48}$$

Relative dimensions of the linkages can be expressed in terms of a lever ratio, defined as:

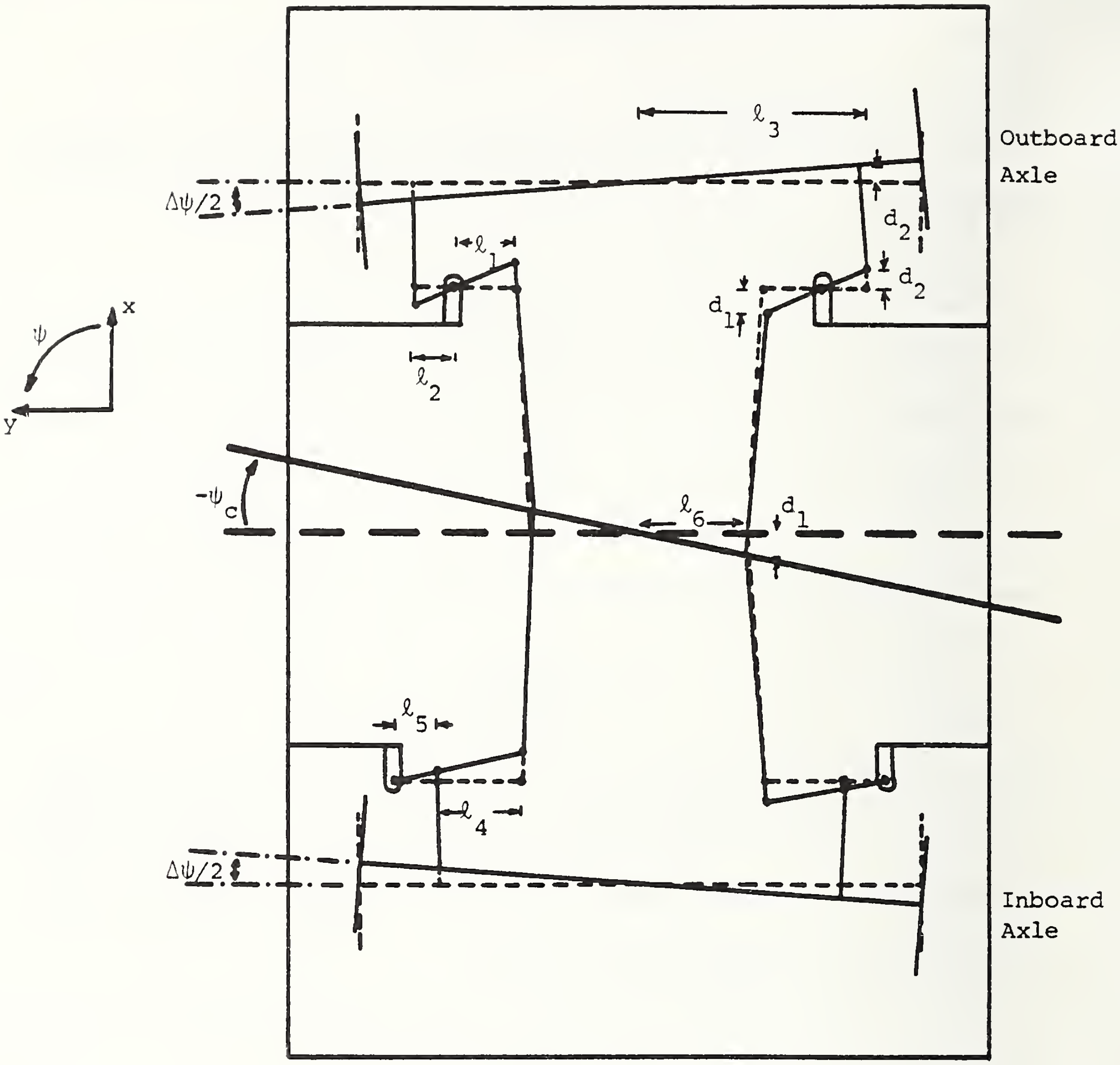

$$\text{lever ratio, } \ell_R = \begin{cases} \dfrac{\ell_1}{\ell_2} & \text{for the outboard axle} \\[2ex] \dfrac{\ell_4+\ell_5}{\ell_5} & \text{for the inboard axle} \end{cases}$$

Figure A.8 Kinematic Steering of the Front U Truck Prototype

$$
\ell_R = \begin{cases} \ell_1/\ell_2 & \text{for outboard axle} \qquad \text{(A-49)} \\[2ex] \dfrac{\ell_4+\ell_5}{\ell_5} & \text{for inboard axle} \qquad \text{(A-50)} \end{cases}
$$

which is usually designed to be the same for both axles to achieve a symmetrical truck configuration.

From similar triangles, the following relation is established:

$$
\frac{d_1}{d_2} = \frac{\ell_1}{\ell_2} \qquad \text{(A-51)}
$$

Upon combining equations (A-46) through (A-49) and equation (A-51), the curvature steering gain G is given by:

$$
G = \frac{\ell_6}{\ell_R \, \ell_3} \qquad \text{(A-52)}
$$

For a symmetrical truck with the same lever ratio ℓ_R for both axles, equation (A-52) applies for both axles.

The modeling of the U prototype steering linkages is slightly different from that of the previous two prototypes. The steering linkage stiffnesses of the U prototype are actually modelled as an effective bending stiffness between the truck and each wheelset in series with the geometric offset, as shown in Figure A.9. This is true since yawing one of the wheelsets, in the absence of carbody yaw, only directly affects the truck frame and not the other wheelset. For uniformity this effective bending stiffness is considered as an "inter-axle bending stiffness". Thus the term "interaxle bending stiffness"

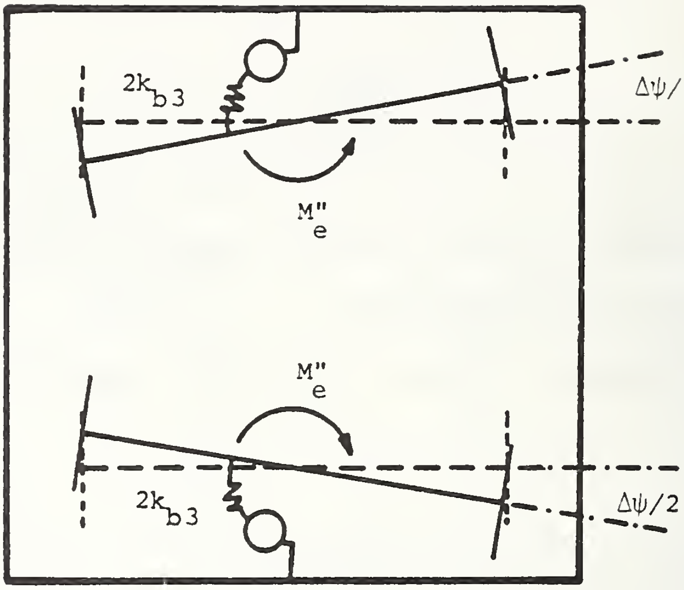

Figure A.9 Schematic Diagram of Simplified U Prototype Model

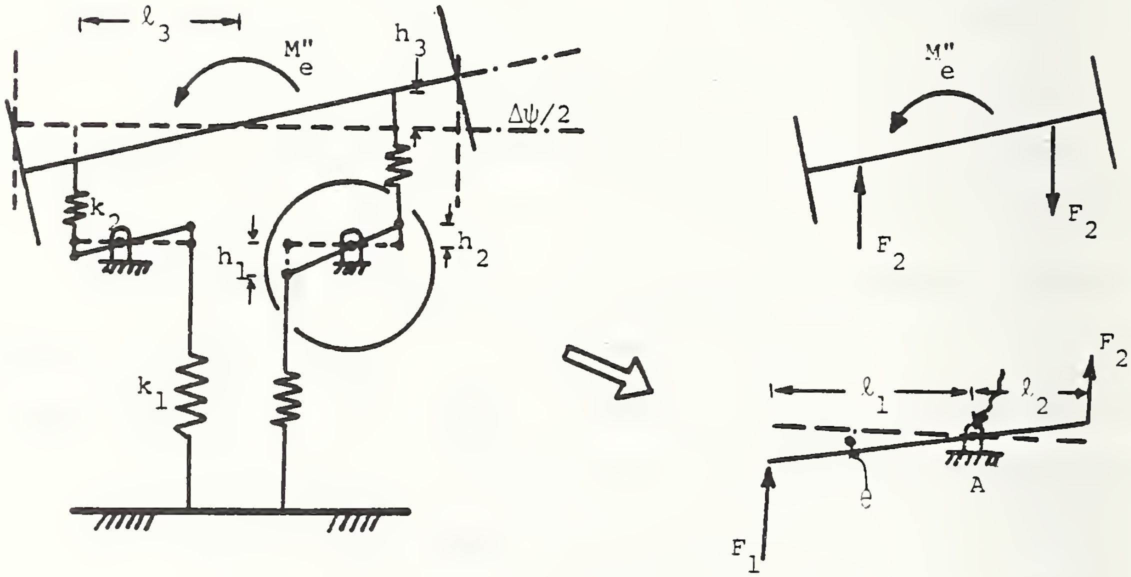

Figure A.10 Free Body Diagram of the Outboard Axle of The U Prototype for forced-steering trucks refers to the effective bending stiffness in series with the geometric offset.

A moment balance on one of the wheelsets of Figure A.9 defines the effective bending stiffness as:

$$k_{b3} = \frac{M''_e}{\Delta\psi} \tag{A-53}$$

Figure A.10 shows the free body diagram of the outboard axle of the U prototype after an external moment M''_e is applied on it to produce a wheelset yaw $\Delta\psi/2$. Using small motions assumption:

$$h_1 = \theta\ell_1 \tag{A-54}$$

$$h_2 = \theta\ell_2 \tag{A-55}$$

$$h_3 = \frac{\Delta\psi}{2}\ \ell_3 \tag{A-56}$$

Deflections of springs k_1 and k_2 on the right half of the truck are given, respectively, by:

$$\Delta_1 \text{ (compression)} = h_1 = \theta\ell_1 \tag{A-57}$$

$$\Delta_2 \text{(extension)} = h_3 - h_2 = \frac{\Delta\psi}{2}\ell_3 - \theta\ell_2 \tag{A-58}$$

creating spring forces F_1 and F_2:

$$F_1 = k_1\Delta_1 \tag{A-59}$$

$$F_2 = k_2\Delta_2 \tag{A-60}$$

which are related, from a moment balance about point A, as:

$$F_1 \ell_1 = F_2 \ell_2 \tag{A-61}$$

Solving for θ from equations (A-57) through (A-61) and using the definition of equation (A-49):

$$\theta = \frac{k_2 \, \ell_3 \, \Delta\psi}{2\ell_2(\ell_R^2 k_1 + k_2)} \tag{A-62}$$

A moment balance on the wheelset yields:

$$M''_e = 2F_2 \, \ell_3 \tag{A-63}$$

The effective bending stiffness is found by combining equations (A-58), (A-60), (A-62), (A-63) and (A-53) and is given by:

$$k_{b_3} = \frac{k_1 \, k_2 \, \ell_3^2 \, \ell_R^2}{(\ell_R^2 \, k_1 + k_2)} \tag{A-64}$$

The effective bending stiffness for the inboard axle can be derived in a similar fashion. For a symmetrical truck, it yields the same result as for the outboard axle given by equation (A-64).

APPENDIX B

DERIVATION OF CURVATURE STEERING GAIN

For tracking the pure rolling line in curves the yaw geometry offset is

$$\Delta\psi_{pr\ell} = -\frac{2b}{R} \tag{B-1}$$

when T_B and k_{b1} are negligible. From simple geometry (assuming small angles), the following relations hold when the wheelsets track the pure rolling line in equilibrium in the absence of cant deficiency:

$$\psi_T = \mp \frac{\ell_s}{R} \tag{B-2}$$

$$\psi_c = 0 \tag{B-3}$$

Substituting into the curvature steering law yields:

$$\Delta\psi_{pr\ell} = -\frac{2b}{R} = \mp 2\, G_{pr\ell} \frac{\ell_s}{R} \tag{B-3}$$

The curvature gain for tracking the pure rolling line is thus

$$G_{pr\ell} = \frac{b}{\ell_s} \tag{B-5}$$

APPENDIX C

LINEARIZED EQUATIONS FOR THE 6 DOF STABILITY MODEL (CONVENTIONAL TRUCK)

C.1 Conventional Truck Model

A schematic diagram of the six degree of freedom model for a conventional truck is shown in Figure C.1. The truck is attached to an "inertial" carbody by the secondary suspension. The degrees of freedom are:

- leading wheelset lateral displacement
- leading wheelset yaw angle
- trailing wheelset lateral displacement
- trailing wheelset yaw angle
- truck lateral displacement
- truck yaw angle

The following assumptions are made:

- all masses are rigid
- the vertical and longitudinal motions are assumed to be decoupled from the lateral
- the vehicle is moving at a constant forward speed
- the truck roll angle is assumed to be the average of the roll angles of its two wheelsets
- all displacements are assumed to be small
- all wheel/rail and suspension forces are assumed to be linear
- the effect of track irregularities is neglected.

C.2 Wheel/Rail Geometry

In the stability analysis the displacements of the wheelset from its centered position are assumed to be small and thus the geometric wheel/rail constraint functions are linearized. Therefore, the various parameters can

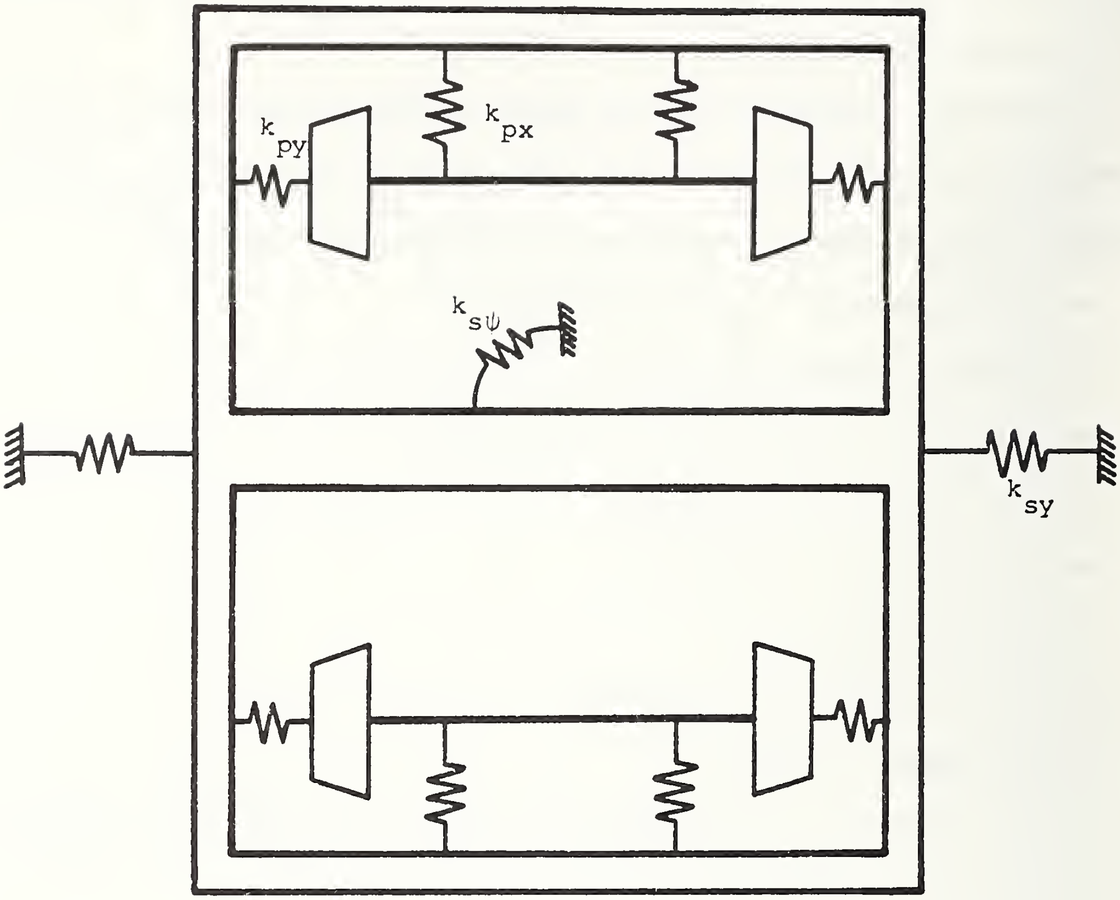

Figure C.1 6 DOF Conventional Truck Model Connected to an Inertial Reference Frame be described as a function of the lateral displacement of the wheelset, y_w. The parameters of importance are:

r_L, r_R = rolling radius of the left and right wheel

$\delta_L\ \delta_R$ = contact angle of the left and right wheel

ϕ_w = roll angle of the wheelset

The relations between these parameters and the parameters when the wheelset is centered on the track are:

$$\frac{r_L - r_R}{2} = \lambda y_w \tag{C-1}$$

$$\frac{r_L + r_R}{2} = r_o \tag{C-2}$$

$$\frac{\delta_L - \delta_R}{2} = \frac{\Delta}{a} y_w \tag{C-3}$$

$$\frac{\delta_L + \delta_R}{2} = \delta_o \tag{C-4}$$

$$\phi_w = \frac{a_{11}}{a} y_w \tag{C-5}$$

where λ = effective conicity of the wheel

r_o = centered (nominal) wheel rolling radius

δ_o = centered contact angle

Δ = contact angle difference coefficient

a = half of wheelset contact distance

a_{11} = wheelset roll coefficient

The assumption of a linearly profiled wheel is usually quite good in the tread region. When the wheelset lateral displacement is such that the rail contacts the flange, there is a sudden jump in the wheel rolling radius and contact angle which is neglected in this analysis.

C.3 Wheel/Rail Forces and Moments

The nature of contact between steel wheel and steel rail is commonly known as creep, which is a state between pure rolling and sliding. Many theories exist to describe this phenomenon, ranging from a simple linear theory to a nonlinear three-dimensional exact creep theory [31, 33].

The creepages developed at the wheel/rail interface include lateral, longitudinal and spin creepages, defined respectively as:

$$\xi_y = \frac{(\text{lateral velocity of wheel-lateral velocity of rail})_{\text{at contact point}}}{\text{nominal velocity}}$$

$$\xi_x = \frac{(\text{longitudinal velocity of wheel-longitudinal velocity of rail})_{\text{at contact point}}}{\text{nominal velocity}}$$

$$\xi_{sp} = \frac{(\text{angular velocity of wheel-angular velocity of rail})_{\text{at contact point}}}{\text{nominal velocity}}$$

The derivation of linearized creepages has been treated in many studies e.g. [34], with the following result (in the contact planes):

Left Wheel:

$$\begin{aligned}
\xi_{xL} &= \frac{1}{V}[V(1 - \frac{r_L}{r_o}) - a\dot{\psi}] \\
\xi_{yL} &= \frac{1}{V}[\dot{y} + r_L\dot{\phi} - V\psi] \qquad \text{(C-6)} \\
\xi_{spL} &= \frac{1}{V}[\dot{\psi} + \Omega_o\delta_L]
\end{aligned}$$

Right Wheel:

$$\xi_{xR} = \frac{1}{V}[V(1 - \frac{r_R}{r_o}) + a\dot{\psi}]$$

$$\xi_{yR} = \frac{1}{V}[\dot{y} + r_R\dot{\phi} - V\psi] \qquad \text{(C-7)}$$

$$\xi_{spR} = \frac{1}{V}[\dot{\psi} + \Omega_o\delta_R]$$

where $\Omega_o = \frac{V}{\bar{r}_o}$ is the nominal angular velocity

V = forward velocity

The above result uses the assumption of small roll, yaw, and contact angles, and of small wheelset vertical velocity.

The most widely accepted linear creep law is due to Kalker [31], which relates the creep forces/moment and the creepages according to:

Lateral Creep Force:

$$F_y = -f_{11}\xi_y - f_{12}\xi_{sp} \qquad \text{(C-8)}$$

Longitudinal Creep Force:

$$F_x = -f_{33}\xi_x \qquad \text{(C-9)}$$

Spin Creep Moment:

$$M_z = f_{12}\xi_y - f_{22}\xi_{sp} \qquad \text{(C-10)}$$

where f_{11} = lateral creep coefficient

f_{12} = lateral/spin creep coefficient

f_{22} = spin creep coefficient

f_{33} = longitudinal creep coefficient

The total lateral creep force consists of a lateral creepage component which is related to the wheelset yaw angle, and a lateral/spin component that is a function of the contact angle.

The creep coefficients are functions of the normal load N, given by the following relations:

$$f_{11} = \left(\frac{N}{N_N}\right)^{2/3} f_{11_N}$$

$$f_{12} = \left(\frac{N}{N_N}\right) f_{12_N}$$

$$f_{22} = \left(\frac{N}{N_N}\right)^{4/3} f_{22_N} \qquad \text{(C-11)}$$

$$f_{33} = \left(\frac{N}{N_N}\right)^{2/3} f_{33_N}$$

where f_{ij_N} are the nominal values computed for the nominal normal load N_N, while f_{ij} are the values for normal load N.

The linearized creep theory does not consider the fact that the magnitude of the resultant creep force is physically limited by the adhesion limit μN, where μ is the coefficient of friction. However, for operation in the tread region of the wheel, the magnitude of the resultant creep force is usually less than the friction force μN, justifying the use of the linearized creep theory in the model.

The other force acting at the wheel/rail interface is the normal force, which can be resolved into vertical and horizontal components. The horizontal component is sometimes referred to as the lateral "gravitational stiffness force". The gravitational stiffness forces of the two wheels create a net yaw moment on the wheelset. The linearized expressions for the gravitational stiffness force and the resulting yaw moment are, respectively [35]:

$$F_g = -\frac{N}{a}(a_{11} + \Delta)y_{wi} \tag{C-12}$$

$$T_g = aN\delta_o\ \psi_{wi} \tag{C-13}$$

where N = axle load

y_{wi} = lateral displacement of the i^{th} wheelset

ψ_{wi} = yaw of the i^{th} wheelset

The vertical component of the normal force does not enter the lateral or yaw equations of motion. The model assumes constant wheel/rail loads.

C.4 Suspensions

C.4.1 Primary Suspension

The primary suspension connects the axle to the truck frame. For the stability analysis the primary suspension is assumed to be linear parallel spring/damper combinations for both the lateral and the longitudinal suspensions. Since primary suspensions are generally rubber chevrons or donuts the damping is assumed to be a fixed ratio of the spring constant. In general the primary suspension damping forces are negligible when compared to the wheel/rail friction damping forces but they are included for completeness.

C.4.2 Secondary Suspension

For the stability analysis the lateral and yaw secondary suspensions, between the carbody and the trucks, are modelled as linear parallel spring/damper combinations. The lateral suspension is generally achieved by the shear properties of the vertical airbag or coiled spring group as well as possible lateral hydraulic dampers. A possible physical arrangement for the secondary yaw suspension is shown in Figure C.2. For the

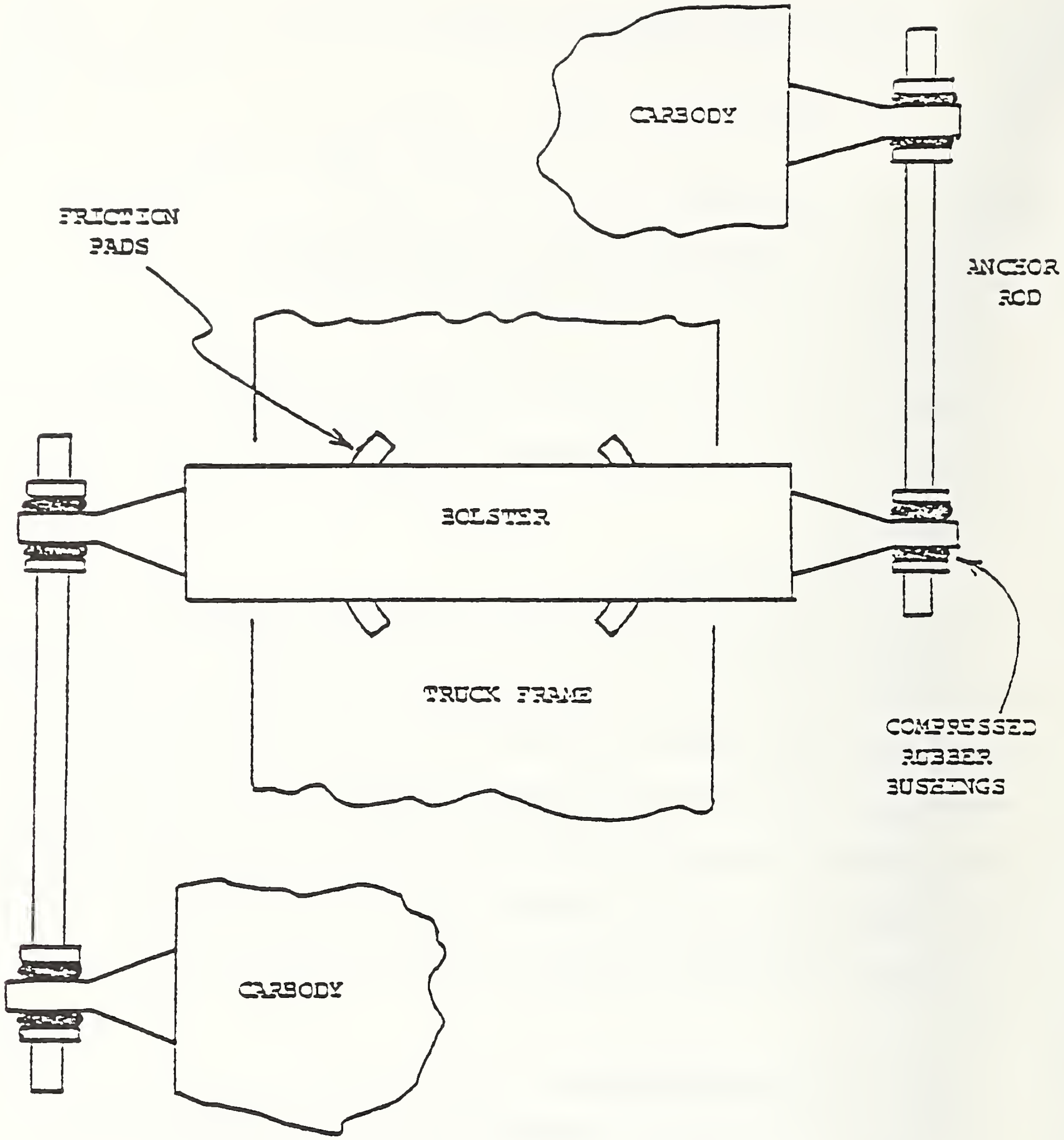

Figure C.2 Physical Arrangement of the Secondary Yaw Suspension stability analysis it is assumed that the bolster has not broken away with respect to the friction pads of the centerplate and thus the yaw stiffness is obtained by the compressed bushings in the anchor rods.

C.5 Equations of Motion

The linearized equations of motion for the six degree of freedom conventional truck model have been derived previously in the literature [35]. In the derivation (not presented here) the contributions to the generalized forces due to the action of the steering laws are derived in the generalized coordinates similar to those used by Wickens. These generalized forces are then transformed into the physical coordinates. In this section the complete equations for a conventional truck are listed. The equations of motion for steered trucks include additional terms due to steering linkages. These are derived in Appendix D.

As mentioned in Section C.1 the degrees of freedom in the physical coordinates for a truck are the lateral and yaw motions of the two wheelsets and of the truck frame. The degrees of freedom in the generalized coordinates are:

$y_1 + y_2$: equal lateral displacements of the wheelsets

$y_1 - y_2$: equal and opposite lateral displacements of the wheelsets

$\psi_1 + \psi_2$: equal yaw displacements of the wheelsets

$\psi_1 - \psi_2$: equal and opposite yaw displacements of the wheelsets

y_T : lateral displacement of the truck frame

ψ_T : yaw displacement of the truck frame

These are shown in Figure C.3.

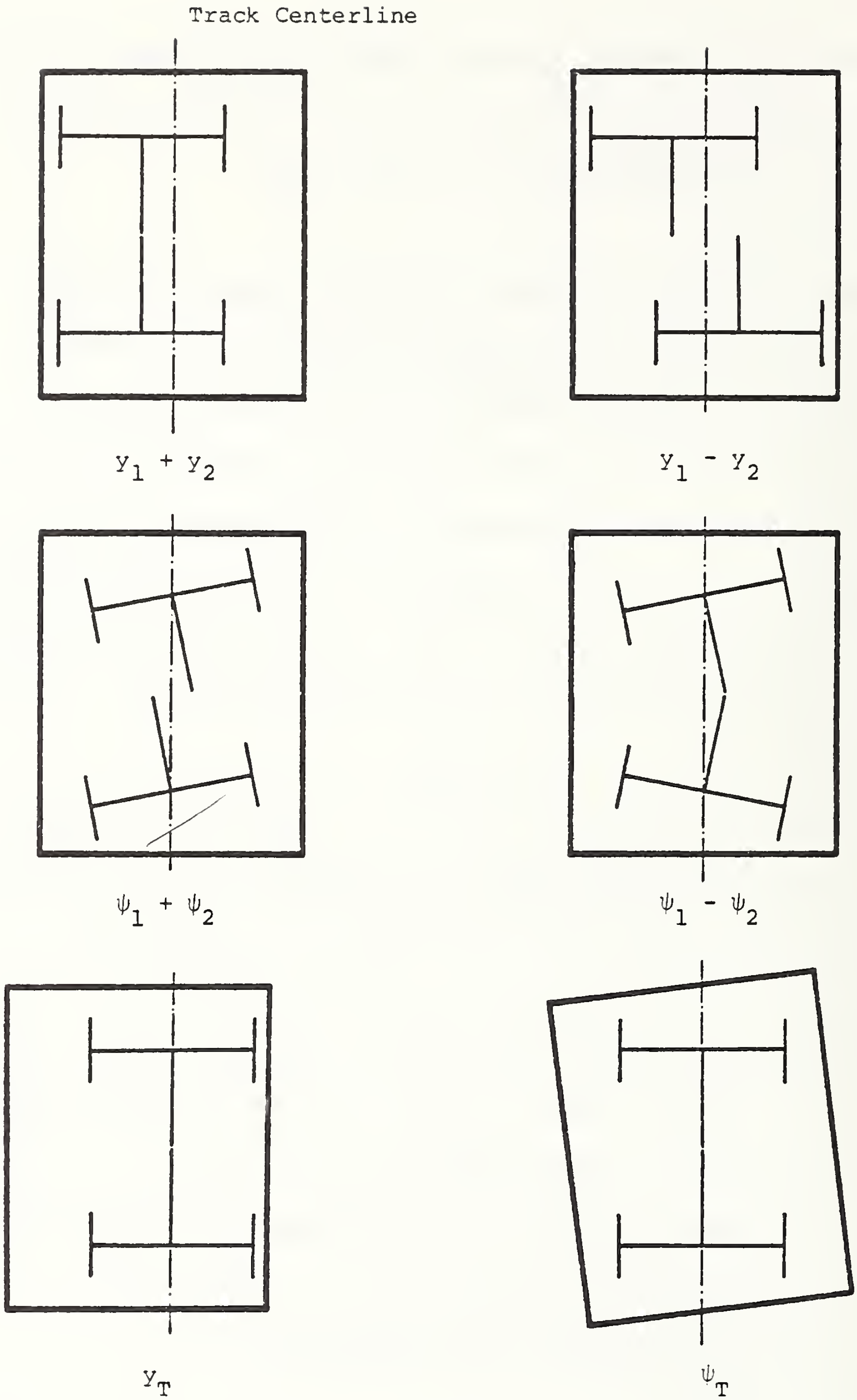

Figure C.3 Generalized Coordinates of the Generic Truck

The linearized equations for the 6 DOF conventional truck stability model follow:

Truck Frame Equations

$$M_T\ddot{y}_T = 2k_{py}y_{w1} + 2C_{py}\dot{y}_{w1} + 2k_{py}y_{w2} + 2C_{py}\dot{y}_{w2} - [4k_{py} + 2k_{sy}]y_T$$

$$- [4C_{py} + 2C_{sy}]\dot{y}_T \tag{C-14}$$

$$I_{Tz}\ddot{\psi}_T = 2bk_{py}y_{w1} + 2bC_{py}\dot{y}_{w1} + 2d_p^2k_{px}\psi_{w1} + 2d_p^2C_{px}\dot{\psi}_{w1} - 2bk_{py}y_{w2}$$

$$- 2bC_{py}\dot{y}_{w2} + 2d_p^2k_{px}\psi_{w2} + 2d_p^2C_{px}\dot{\psi}_{w2} - [4b^2k_{py} + 4d_p^2k_{px}$$

$$+ k_{s\psi}]\psi_T - [4b^2C_{py} + 4d_p^2C_{px} + C_{s\psi}]\dot{\psi}_T \tag{C-15}$$

Wheelset Equations

$$M_w\ddot{y}_{wi} = F_{cr} + F_{si} + F_g + F_j \tag{C-16}$$

$$I_{wz}\ddot{\psi}_{wi} = T_{cr} + T_{si} + T_g + T_j \tag{C-17}$$

where F_{cr} = net lateral force on wheelset due to creepages

F_{si} = net lateral force on wheelset i due to primary lateral suspension elements

F_g = lateral force on wheelset due to lateral gravitational stiffness

F_j = lateral force on wheelset due to gyroscopic effect of the wheelset

T_{cr} = net yaw moment from creepages

T_{si} = net yaw moment applied on wheelset i by the primary suspension elements

T_g = yaw moment contribution from gravitational stiffness

T_j = yaw moment contribution from gyroscopic effect of the wheelset.

The above equations are applicable to both wheelsets, with the corresponding values of forces and moments.

The suspension forces and moments are:

$$F_{s1} = 2k_{py}(y_T + b\psi_T - y_{w1}) + 2C_{py}(\dot{y}_T + b\dot{\psi}_T - \dot{y}_{w1}) \quad \text{(C-18)}$$

$$F_{s2} = 2k_{py}(y_T - b\psi_T - y_{w2}) + 2C_{py}(\dot{y}_T - b\dot{\psi}_T - \dot{y}_{w2}) \quad \text{(C-19)}$$

$$T_{s1} = 2d_p^2k_{px}(\psi_T - \psi_{w1}) + 2d_p^2C_{px}(\dot{\psi}_T - \dot{\psi}_{w1}) \quad \text{(C-20)}$$

$$T_{s2} = 2d_p^2k_{px}(\psi_T - \psi_{w2}) + 2d_p^2C_{px}(\dot{\psi}_T - \dot{\psi}_{w2}) \quad \text{(C-21)}$$

The creep, gravitational and gyroscopic forces and moments are [35]:

$$F_{cr} = -2f_{11}\left(\frac{\dot{y}_{wi}}{V} - \psi_{wi}\right) + \frac{2f_{12}\Delta}{ar_o}\, y_{wi} - \frac{2f_{12}}{V}\,\dot{\psi}_{wi} \quad \text{(C-22)}$$

$$F_g = -\frac{N}{a}(a_{11} + \Delta)y_{wi} \quad \text{(C-23)}$$

$$F_j = \frac{V\, I_{wy}a_{11}}{ar_o}\,\dot{\psi}_{wi} \quad \text{(C-24)}$$

$$T_{cr} = -2f_{33}\left(\frac{\lambda a}{r_o}\, y_{wi} + \frac{a^2}{V}\,\psi_{wi}\right) - \frac{2f_{22}}{V}\,\dot{\psi}_{wi}$$

$$-2f_{12}\psi_{wi} + \frac{2f_{22}\Delta}{ar_o}\, y_{wi} \quad \text{(C-25)}$$

$$T_g = aN\delta_o \psi_{wi} \tag{C-26}$$

$$T_j = -\frac{V I_{wy} a_{11}}{a r_o} \dot{y}_{wi} \tag{C-27}$$

where I_{wy} is the wheelset pitch moment of inertia

and where, M_T = truck frame mass

y_T = lateral displacement of truck frame c.g.

y_{w1} = lateral displacement of the leading wheelset c.g.

y_{w2} = lateral displacement of the trailing wheelset c.g.

k_{py} = primary lateral stiffness

C_{py} = primary lateral damping

k_{sy} = secondary lateral stiffness

C_{sy} = secondary lateral damping

I_{Tz} = truck frame yaw moment of inertia

ψ_T = yaw of truck frame

ψ_{w1} = yaw of the leading wheelset

ψ_{w2} = yaw of the trailing wheelset

k_{px} = primary longitudinal stiffness

C_{px} = primary longitudinal damping

$k_{s\psi}$ = secondary yaw stiffness

$C_{s\psi}$ = secondary yaw damping

APPENDIX D

DERIVATION OF ADDITIONAL TERMS DUE TO STEERING LINKAGES

The generalized forces in the physical coordinates due to the action of the steering linkages in Figure 2.10 are derived in this Appendix. These generalized forces can be written in matrix form, which is equivalent to the negative of the stiffness matrix:

$$\underline{F}_{fs} = \overline{\underline{K}}_{fs}\,\underline{y} \tag{D-1}$$

where $\underline{F}_{fs}$ is the vector of generalized force due to the steering linkages, as defined in equations (D-20) through (D-33)

$\overline{\underline{K}}_{fs}$ is the stiffness matrix contribution from the steering linkages

$\underline{y}$ is the vector of position degrees of freedom

For generality, the self-steering radial truck model is allowed to have dampers in parallel with all stiffnesses to accommodate interaxle damping although in this study all interaxle damping is set to zero. The contribution to the generalized forces by these dampers is found by replacing stiffnesses of all the terms without steering gains in the vector $\underline{F}_{fs}$ with damping constants, and the degrees of freedom by their derivatives. This contribution can also be written in matrix form:

$$\underline{F}'_{fs} = -\overline{\underline{C}}_{fs}\,\dot{\underline{y}} \tag{D-2}$$

where $\underline{F}'_{fs}$ is the vector of damper forces, as defined in equations (D-34) to (D-45)

$\overline{\underline{C}}_{fs}$ is the damping matrix contribution from the interaxle connection (for self steering radial truck only)

$\dot{\underline{y}}$ is the velocity vector in the direction of the degrees of freedom

The equations of motion of the 6 DOF generic truck model are obtained by adding the additional terms due to the steering linkages to the equations of motion of the truck and wheelsets of a conventional vehicle.

To derive the contribution of the forced steering linkages to the stiffness matrix, the steering laws are rewritten and expressed in the generalized coordinates:

$$\Delta\psi_1^{*} = \Delta\psi_2 = G_3(y_1+y_2) \pm \frac{G_2+G_6}{b}(y_1-y_2) \pm (G_1+G_5)(\psi_1+\psi_2)$$

$$-2G_3y_T \pm (2G_4-2G_5-2G_6)\psi_T \mp (2G_1+2G_2+2G_4)\psi_c \qquad \text{(D-3)}$$

$$\Delta y_1 = \Delta y_2 = (H_1+H_3)(y_1+y_2)+2(H_2-H_3)y_T-2(H_1+H_2)y_c \qquad \text{(D-4)}$$

With the assumption that the linkages have no inertia or damping, energy is conserved and the linkages can be treated as a transformer with $\Delta\psi$ or Δy as the modulus. This technique has been used in writing the back reaction forces and moments in the directions which activate $\Delta\psi$ and Δy.

First we consider the contribution of $\Delta\psi_1$ and k_{b2} only, in the generalized coordinates as discussed in Section 2.3.1.4. The derivation for the contribution of $\Delta\psi_2$ and k_{b3} is analogous, except for a few terms as discussed below.

Because $\Delta\psi_1$ is positive in the direction of positive $(\psi_1-\psi_2)$, a $\Delta\psi_1$ offset creates a moment $k_{b2}x\ \Delta\psi_1$ in the spring k_{b2} in the direction of $(\psi_1-\psi_2)$. Deflecting the spring k_{b2} in the direction of $(\psi_1-\psi_2)$ also creates a reaction equal to $-k_{b2}x(\psi_1-\psi_2)$. Thus the total moment in the k_{b2} spring is:

---

*The subscripts 1 and 2 refer to the leading and trailing wheelset respectively, of either the leading or trailing truck.

$$M^{*}_{\psi_1-\psi_2} = M_{\Delta\psi} = k_{b2}\Delta\psi_1 - k_{b2}(\psi_1-\psi_2) \qquad \text{(D-5)}$$

This moment has a back reaction in every direction that activates $\Delta\psi_1$ according to the steering law. For example, the back reaction in the direction (y_1+y_2) is derived as follows:

A displacement in the (y_1+y_2) direction causes a displacement in the $\Delta\psi$ or the $(\psi_1-\psi_2)$ direction equal to $G_3(y_1+y_2)$ to generate a moment $M_{\Delta\psi}$ in the k_{b2} spring. The force in the (y_1+y_2) direction is given by the effective transformer modulus (G_3 in this case) times the moment $M_{\Delta\psi}$:

$$F_{y1+y2} = -G_3M_{\Delta\psi} \qquad \text{(D-6)}$$

The sign is negative because of the assumption that energy is conserved in the linkages, so that the output energy is the negative of the input energy. Similarly the back reaction forces and moments in the other direction are:

$$F_{y1-y2} = \mp \frac{G_2+G_6}{b} M_{\Delta\psi} \qquad \text{(D-7)}$$

$$M_{\psi_1+\psi_2} = \mp (G_1+G_5)M_{\Delta\psi} \qquad \text{(D-8)}$$

$$F_{yT} = 2G_3M_{\Delta\psi} \qquad \text{(D-9)}$$

$$M_{\psi_T} = \mp(2G_4 - 2G_5 - 2G_6)M_{\Delta\psi} \qquad \text{(D-10)}$$

$$M_{\psi_c} = \pm(2G_1 + 2G_2 + 2G_4)M_{\Delta\psi} \qquad \text{(D-11)}$$

---

*The subscript on the force or moments denotes the direction in which the particular force or moment is acting.

The forces and moments due to $\Delta\psi_2$ and k_{b3} are similar to those due to $\Delta\psi_1$ and k_{b2}, except for the following additional effect due to the interconnection between the truck and the wheelset:

$$M_{\psi_1+\psi_2} = -k_{b3}(\psi_1+\psi_2) + 2\,k_{b3}\psi_T \tag{D-12}$$

$$M_{\psi_T} = 2\,k_{b3}(\psi_1+\psi_2) - 4\,k_{b3}\psi_T \tag{D-13}$$

Similarly, the contribution of Δy_1 and k_{s2} is derived by first writing the force $F_{\Delta y} = -F_{y1-y2}$ caused by the offset Δy_1 and by the reaction to deflection in the (y_1-y_2) direction

$$F_{\Delta y} = -F_{y1-y2} = \Delta y_1\,k_{s2} + k_{s2}(y_1-y_2) - b\,k_{s2}(\psi_1+\psi_2) \tag{D-14}$$

The back reaction forces and moments are derived using the same argument as before, given by:

$$M_{\psi_1+\psi_2} = b\,\Delta y_1\,k_{s2} + b\,k_{s2}(y_1-y_2) - b^2\,k_{s2}(\psi_1+\psi_2) \tag{D-15}$$

$$F_{y_1+y_2} = -(H_1+H_3)F_{\Delta y} \tag{D-16}$$

$$F_{y_T} = -2(H_2-H_3)F_{\Delta y} \tag{D-17}$$

$$F_{y_c} = 2(H_1+H_2)F_{\Delta y} \tag{D-18}$$

The contribution of Δy_2 and k_{s3} are similar, with the additional effect due to the interconnection between the truck and the wheelset:

$$F_{y_1+y_2} = -k_{s3}(y_1+y_2) + bk_{s3}(\psi_1-\psi_2) + 2\,k_{s3}y_T \tag{D-19}$$

$$M_{\psi_1-\psi_2} = bk_{s3}(y_1+y_2) - b^2k_{s3}(\psi_1-\psi_2) - 2bk_{s3}y_T \tag{D-20}$$

$$F_{y_T} = 2k_{s3}(y_1+y_2) - 2bk_{s3}(\psi_1-\psi_2) - 4k_{s3}y_T \qquad \text{(D-21)}$$

The total effect of $\Delta\psi_1$, $\Delta\psi_2$, Δy_1 and Δy_2 is found by substituting equation (D-3) into equations (D-5) through (D-11) and equation (D-4) into equations (D-14) through (D-18), and combining the results together. These generalized forces are expressed in the generalized coordinates. Transforming them into the physical coordinates the following results are obtained, with expressions for the front and rear trucks written separately:

$$\begin{aligned}
F_{y_{w1}} = & -[(G_3 + \frac{G_2+G_6}{b})^2(k_{b2}+k_{b3}) + (H_1+H_3+1)^2(k_{s2}+k_{s3})+k_{s3}]y_{w1} \\
& -[\left\{G_3{}^2-(\frac{G_2+G_6}{b})^2\right\}(k_{b2}+k_{b3}) + \left\{(H_1+H_3)^2-1\right\}(k_{s2}+k_{s3})+k_{s3}]y_{w2} \\
& +[(G_3+\frac{G_2+G_6}{b})\left\{1-(G_1+G_5)\right\}(k_{b2}+k_{b3})+b(H_1+H_3+1)(k_{s2}+k_{s3})+bk_{s3}]\psi_{w1} \\
& +[-(G_3+\frac{G_2+G_6}{b})\left\{1+(G_1+G_5)\right\}(k_{b2}+k_{b3})+b(H_1+H_3+1)(k_{s2}+k_{s3})-bk_{s3}]\psi_{w2} \\
& +[2G_3(G_3+\frac{G_2+G_6}{b})(k_{b2}+k_{b3})-2(H_2-H_3)(H_1+H_3+1)(k_{s2}+k_{s3})+2k_{s3}]y_{T1} \\
& -(2G_4-2G_5-2G_6)(G_3+\frac{G_2+G_6}{b})(k_{b2}+k_{b3})\psi_{T1} \\
& +2(H_1+H_2)(H_1+H_3+1)(k_{s2}+k_{s3})y_c \\
& +(2G_1+2G_2+2G_4)(G_3+\frac{G_2+G_6}{b})(k_{b2}+k_{b3})\psi_c
\end{aligned} \qquad \text{(D-22)}$$

$$M_{\psi_{w1}} = [(G_3 + \frac{G_2+G_6}{b})\left\{1-(G_1+G_5)\right\} (k_{b2}+k_{b3})+b(H_1+H_3+1)(k_{s2}+k_{s3})+bk_{s3}]y_{w1}$$

$$+[(G_3 - \frac{G_2+G_6}{b}) \left\{1-(G_1+G_5)\right\} (k_{b2}+k_{b3})+b(H_1+H_3-1)(k_{s2}+k_{s3})+bk_{s3}]y_{w2}$$

$$-[(G_1+G_5-1)^2(k_{b2}+k_{b3})+b^2(k_{s2}+k_{s3})+k_{b3}+b^2k_{s3})\psi_{w1}$$

$$+[\left\{1-(G_1+G_5)^2\right\} (k_{b2}+k_{b3})-b^2(k_{s2}+k_{s3})-k_{b3}+b^2k_{s3}]\psi_{w2}$$

$$+[2G_3\left\{-1+(G_1+G_5)\right\} (k_{b2}+k_{b3})+2b(H_2-H_3)(k_{s2}+k_{s3})-2bk_{s3}]y_{T1}$$

$$+[(2G_4-2G_5-2G_6) \left\{1-(G_1+G_5)\right\} (k_{b2}+k_{b3})+2k_{b3}]\psi_{T1}$$

$$-2b(H_1+H_2)(k_{s2}+k_{s3})y_c$$

$$+(2G_1+2G_2+2G_4) \left\{(G_1+G_5)-1\right\} (k_{b2}+k_{b3})\psi_c \tag{D-23}$$

$$F_{y_{w2}} = -[\left\{G_3^2-(\frac{G_2+G_6}{b})^2\right\} (k_{b2}+k_{b3})+ \left\{(H_1+H_3)^2-1\right\} (k_{s2}+k_{s3})+k_{s3}]y_{w1}$$

$$-[(G_3- \frac{G_2+G_6}{b})^2 (k_{b2}+k_{b3})+(H_1+H_3-1)^2(k_{s2}+k_{s3})+k_{s3}]y_{w2}$$

$$+[(G_3- \frac{G_2+G_6}{b}) \left\{1-(G_1+G_5)\right\} (k_{b2}+k_{b3})+b(H_1+H_3-1)(k_{s2}+k_{s3})+bk_{s3}]\psi_{w1}$$

$$+[(-G_3+ \frac{G_2+G_6}{b}) \left\{1+(G_1+G_5)\right\} (k_{b2}+k_{b3})+b(H_1+H_3-1)(k_{s2}+k_{s3})-bk_{s3}]\psi_{w2}$$

$$+[2G_3(G_3- \frac{G_2+G_6}{b})(k_{b2}+k_{b3})-2(H_2-H_3)(H_1+H_3-1)(k_{s2}+k_{s3})+2k_{s3}]y_{T1}$$

$$+(2G_4-2G_5-2G_6)(-G_3 + \frac{G_2+G_6}{b})(k_{b2}+k_{b3})\psi_{T1}$$

$$+2(H_1+H_2)(H_1+H_3 - 1)(k_{s2}+k_{s3})y_c$$

$$+(2G_1+2G_2 + 2G_4)(G_3 - \frac{G_2+G_6}{b})(k_{b2}+k_{b3})\psi_c \tag{D-24}$$

$$M_{\psi_{w2}} = [-(G_3+ \frac{G_2+G_6}{b}) \left\{1+(G_1+G_5)\right\} (k_{b2}+k_{b3})+b(H_1+H_3+1)(k_{s2}+k_{s3})-bk_{s3}]y_{w1}$$

$$+[-(G_3- \frac{G_2+G_6}{b}) \left\{1+(G_1+G_5)\right\} (k_{b2}+k_{b3})+b(H_1+H_3-1)(k_{s2}+k_{s3})-bk_{s3}]y_{w2}$$

$$+[\left\{1-(G_1+G_5)^2\right\} (k_{b2}+k_{b3})-b^2(k_{s2}+k_{s3})-k_{b3}+b^2k_{s3}]\psi_{w1}$$

$$+[- \left\{1+(G_1+G_5)\right\}^2 (k_{b2}+k_{b3})-b^2(k_{s2}+k_{s3})-k_{b3}-b^2k_{s3}]\psi_{w2}$$

$$+[2G_3 \left\{1+(G_1+G_5)\right\} (k_{b2}+k_{b3})+2b(H_2-H_3)(k_{s2}+k_{s3})+2bk_{s3}]y_{T1}$$

$$+[-(2G_4-2G_5-2G_6) \left\{1+(G_1+G_5)\right\} (k_{b2}+k_{b3})+2k_{b3}]\psi_{T1}$$

$$-2b(H_1+H_2)(k_{s2}+k_{s3})y_c$$

$$+(2G_1+2G_2+2G_4) \left\{1+(G_1+G_5)\right\} (k_{b2}+k_{b3})\psi_c \tag{D-25}$$

$$F_{y_{T1}} = [2G_3(G_3+ \frac{G_2+G_6}{b})(k_{b2}+k_{b3})-2(H_2-H_3)(H_1+H_3+1)(k_{s2}+k_{s3})+2k_{s3}]y_{w1}$$

$$+[2G_3(G_3 - \frac{G_2+G_6}{b})(k_{b2}+k_{b3})-2(H_2-H_3)(H_1+H_3-1)(k_{s2}+k_{s3})+2k_{s3}]y_{w2}$$

$$+[-2G_3 \left\{1-(G_1+G_5)\right\} (k_{b2}+k_{b3})+2b(H_2-H_3)(k_{s2}+k_{s3})-2bk_{s3}]\psi_{w1}$$

$$+[2G_3 \left\{1+(G_1+G_5)\right\} (k_{b2}+k_{b3})+2b(H_2-H_3)(k_{s2}+k_{s3})+2bk_{s3}]\psi_{w2}$$

$$-[4G_3^2(k_{b2}+k_{b3})+4(H_2-H_3)^2(k_{s2}+k_{s3})+4k_{s3}]y_{T1}$$

$$+2G_3(2G_4-2G_5-2G_6)(k_{b2}+k_{b3})\psi_{T1} + 4(H_1+H_2)(H_2-H_3)(k_{s2}+k_{s3})y_c$$

$$-2G_3(2G_1+2G_2+2G_4)(k_{b2}+k_{b3})\psi_c \tag{D-26}$$

$$M_{\psi_{T1}} = -(G_3+ \frac{G_2+G_6}{b})(2G_4-2G_5-2G_6)(k_{b2}+k_{b3})y_{w1}$$

$$-(G_3- \frac{G_2+G_6}{b})(2G_4-2G_5-2G_6)(k_{b2}+k_{b3})y_{w2}$$

$$+[(2G_4-2G_5-2G_6) \left\{1-(G_1+G_5)\right\} (k_{b2}+k_{b3})+2k_{b3}]\psi_{w1}$$

$$+[-(2G_4-2G_5-2G_6) \left\{1+(G_1+G_5)\right\} (k_{b2}+k_{b3})+2k_{b3}]\psi_{w2}$$

$$+2G_3(2G_4-2G_5-2G_6)(k_{b2}+k_{b3})y_{T1}$$

$$-[(2G_4-2G_5-2G_6)^2(k_{b2}+k_{b3})+4k_{b3}]\psi_{T1}$$

$$+(2G_4-2G_5-2G_6)(2G_1+2G_2+2G_4)(k_{b2}+k_{b3})\psi_c \tag{D-27}$$

$$
\begin{aligned}
F_{y_{w3}} = & -[(G_3 - \frac{G_2+G_6}{b})^2 (k_{b2}+k_{b3}) + (H_1+H_3+1)^2 (k_{s2}+k_{s3}) + k_{s3}] y_{w3} \\
& -[\left\{ G_3^2 - (\frac{G_2+G_6}{b})^2 \right\} (k_{b2}+k_{b3}) + \left\{ (H_1+H_3)^2 - 1 \right\} (k_{s2}+k_{s3}) + k_{s3}] y_{w4} \\
& +[(G_3 - \frac{G_2+G_6}{b}) \left\{ 1+G_1+G_5 \right\} (k_{b2}+k_{b3}) + b(H_1+H_3+1)(k_{s2}+k_{s3}) + bk_{s3}] \psi_{w3} \\
& +[(-G_3 + \frac{G_2+G_6}{b}) \left\{ 1-(G_1+G_5) \right\} (k_{b2}+k_{b3}) + b(H_1+H_3+1)(k_{s2}+k_{s3}) - bk_{s3}] \psi_{w4} \\
& +[2G_3(G_3 - \frac{G_2+G_6}{b})(k_{b2}+k_{b3}) - 2(H_2-H_3)(H_1+H_3+1)(k_{s2}+k_{s3}) + 2k_{s3}] y_{T2} \\
& +(2G_4-2G_5-2G_6)(G_3 - \frac{G_2+G_6}{b})(k_{b2}+k_{b3}) \psi_{T2} \\
& +2(H_1+H_2)(H_1+H_3+1)(k_{s2}+k_{s3}) y_c \\
& -(2G_1+2G_2+2G_4)(G_3 - \frac{G_2+G_6}{b})(k_{b2}+k_{b3}) \psi_c
\end{aligned}
\tag{D-28}
$$

$$
\begin{aligned}
M_{\psi_{w3}} = & [(G_3 - \frac{G_2+G_6}{b}) \left\{ 1+(G_1+G_5) \right\} (k_{b2}+k_{b3}) + b(H_1+H_3+1)(k_{s2}+k_{s3}) + bk_{s3}] y_{w3} \\
& +[(G_3 + \frac{G_2+G_6}{b}) \left\{ 1+(G_1+G_5) \right\} (k_{b2}+k_{b3}) + b(H_1+H_3-1)(k_{s2}+k_{s3}) + bk_{s3}] y_{w4} \\
& -[(G_1+G_5+1)^2 (k_{b2}+k_{b3}) + b^2 (k_{s2}+k_{s3}) + k_{b3} + b^2 k_{s3}] \psi_{w3} \\
& +[\left\{ 1-(G_1+G_5)^2 \right\} (k_{b2}+k_{b3}) - b^2 (k_{s2}+k_{s3}) - k_{b3} + b^2 k_{s3}] \psi_{w4} \\
& +[-2G_3 \left\{ 1+(G_1+G_5) \right\} (k_{b2}+k_{b3}) + 2b(H_2-H_3)(k_{s2}+k_{s3}) - 2bk_{s3}] y_{T2}
\end{aligned}
$$

$$+[-(2G_4-2G_5-2G_6)\left\{1+(G_1+G_5)\right\}(k_{b2}+k_{b3})+2k_{b3}]\psi_{T2}$$

$$-2b(H_1+H_2)(k_{s2}+k_{s3})y_c$$

$$+(2G_1+2G_2+2G_4)\left\{(G_1+G_5)+1\right\}(k_{b2}+k_{b3})\psi_c \qquad \text{(D-29)}$$

$$F_{y_{w4}} = -[\left\{G_3^2-(\frac{G_2+G_6}{b})^2\right\}(k_{b2}+k_{b3})+\left\{(H_1+H_3)^2-1\right\}(k_{s2}+k_{s3})+k_{s3}]y_{w3}$$

$$-[(G_3+\frac{G_2+G_6}{b})^2(k_{b2}+k_{b3})+(H_1+H_3-1)^2(k_{s2}+k_{s3})+k_{s3}]y_{w4}$$

$$+[(G_3+\frac{G_2+G_6}{b})\left\{1+(G_1+G_5)\right\}(k_{b2}+k_{b3})+b(H_1+H_3-1)(k_{s2}+k_{s3})+bk_{s3}]\psi_{w3}$$

$$+[-(G_3+\frac{G_2+G_6}{b})\left\{1-(G_1+G_5)\right\}(k_{b2}+k_{b3})+b(H_1+H_3-1)(k_{s2}+k_{s3})-bk_{s3}]\psi_{w4}$$

$$+[2G_3(G_3+\frac{G_2+G_6}{b})(k_{b2}+k_{b3})-2(H_2-H_3)(H_1+H_3-1)(k_{s2}+k_{s3})+2k_{s3}]y_{T2}$$

$$+(2G_4-2G_5-2G_6)(G_3+\frac{G_2+G_6}{b})(k_{b2}+k_{b3})\psi_{T2}$$

$$+2(H_1+H_2)(H_1+H_3-1)(k_{s2}+k_{s3})y_c$$

$$-(2G_1+2G_2-2G_4)(G_3+\frac{G_2+G_6}{b})(k_{b2}+k_{b3})\psi_c \qquad \text{(D-30)}$$

$$M_{\psi_{w4}} = [(-G_3+\frac{G_2+G_6}{b})\left\{1-(G_1+G_5)\right\}(k_{b2}+k_{b3})+b(H_1+H_3+1)(k_{s2}+k_{s3})-bk_{s3}]y_{w3}$$

$$+[-(G_3+\frac{G_2+G_6}{b})\left\{1-(G_1+G_5)\right\}(k_{b2}+k_{b3})+b(H_1+H_3-1)(k_{s2}+k_{s3})-bk_{s3}]y_{w4}$$

$$+[\left\{1-(G_1+G_5)^2\right\}(k_{b2}+k_{b3})-b^2(k_{s2}+k_{s3})-k_{b3}+b^2k_{s3}]\psi_{w3}$$

$$+[-\left\{1-(G_1+G_5)\right\}^2(k_{b2}+k_{b3})-b^2(k_{s2}+k_{s3})-k_{b3}-b^2k_{s3}]\psi_{w4}$$

$$+[2G_3\left\{1-(G_1+G_5)\right\}(k_{b2}+k_{b3})+2b(H_2-H_3)(k_{s3}+k_{s3})+2bk_{s3}]y_{T2}$$

$$+[(2G_4-2G_5-2G_6)\left\{1-(G_1+G_5)\right\}(k_{b2}+k_{b3})+2k_{b3}]\psi_{T2}$$

$$-2b(H_1+H_2)(k_{s2}+k_{s3})y_c$$

$$+(2G_1+2G_2+2G_4)\left\{-1+(G_1+G_5)\right\}(k_{b2}+k_{b3})\psi_c \qquad \text{(D-31)}$$

$$F_{y_{T2}} = [2G_3(G_3-\frac{G_2+G_6}{b})(k_{b2}+k_{b3})-2(H_2-H_3)(H_1+H_3+1)(k_{s2}+k_{s3})+2k_{s3}]y_{w3}$$

$$+[2G_3(G_3+\frac{G_2+G_6}{b})(k_{b2}+k_{b3})-2(H_2-H_3)(H_1+H_3-1)(k_{s2}+k_{s3})+2k_{s3}]y_{w4}$$

$$+[-2G_3\left\{1+(G_1+G_5)\right\}(k_{b2}+k_{b3})+2b(H_2-H_3)(k_{s2}+k_{s3})-2bk_{s3}]\psi_{w3}$$

$$+[2G_3\left\{1-(G_1+G_5)\right\}(k_{b2}+k_{b3})+2b(H_2-H_3)(k_{s2}+k_{s3})+2bk_{s3}]\psi_{w4}$$

$$-[4G_3^2(k_{b2}+k_{b3})+4(H_2-H_3)^2(k_{s2}+k_{s3})+4k_{s3}]y_{T2}$$

$$-2G_3(2G_4-2G_5-2G_6)(k_{b2}+k_{b3})\psi_{T2} + 4(H_1+H_2)(H_2-H_3)(k_{s2}+k_{s3})y_c$$

$$+2G_3(2G_1+2G_3+2G_4)(k_{b2}+k_{b3})\psi_c \qquad \text{(D-32)}$$

$$M_{\psi_{T2}} = (G_3 - \frac{G_2+G_6}{b})(2G_4-2G_5-2G_6)(k_{b2}+k_{b3})y_{w3}$$

$$+(G_3 + \frac{G_2+G_6}{b})(2G_4-2G_5-2G_6)(k_{b2}+k_{b3})y_{w4}$$

$$+[-(2G_4-2G_5-2G_6)\left\{1+(G_1+G_5)\right\}(k_{b2}+k_{b3})+2k_{b3}]\psi_{w3}$$

$$+[(2G_4-2G_5-2G_6)\left\{1-(G_1+G_5)\right\}(k_{b2}+k_{b3})+2k_{b3}]\psi_{w4}$$

$$-2G_3(2G_4-2G_5-2G_6)(k_{b2}+k_{b3})\ y_{T2}$$

$$-[(2G_4-2G_5-2G_6)^2(k_{b2}+k_{b3})+4k_{b3}]\psi_{T2}$$

$$+(2G_4-2G_5-2G_6)(2G_1+2G_2+2G_4)(k_{b2}+k_{b3})\psi_c \qquad \text{(D-33)}$$

$$F_{yc} = 2(H_1+H_2)(H_1+H_3+1)(k_{s2}+k_{s3})y_{w1} + 2(H_1+H_2)(H_1+H_3-1)(k_{s2}+k_{s3})y_{w2}$$

$$-2b(H_1+H_2)(k_{s2}+k_{s3})\psi_{w1} - 2b(H_1+H_2)(k_{s2}+k_{s3})\psi_{w2}$$

$$+4(H_1+H_2)(H_2-H_3)(k_{s2}+k_{s3})y_{T1} + 2(H_1+H_2)(H_1+H_3+1)(k_{s2}+k_{s3})y_{w3}$$

$$+2(H_1+H_2)(H_1+H_3-1)(k_{s2}+k_{s3})y_{w4} - 2b(H_1+H_2)(k_{s2}+k_{s3})\psi_{w3}$$

$$-2b(H_1+H_2)(k_{s2}+k_{s3})\psi_{w4} + 4(H_1+H_2)(H_2-H_3)(k_{s2}+k_{s3})y_{T2}$$

$$-8(H_1+H_2)^2(k_{s2}+k_{s3})y_c \qquad \text{(D-34)}$$

$$M_{\psi_c} = (2G_1+2G_2+2G_4)(G_3+\frac{G_2+G_6}{b})(k_{b2}+k_{b3})y_{w1}+(2G_1+2G_2+2G_4)(G_3-\frac{G_2+G_6}{b})(k_{b2}+k_{b3})y_{w2}$$

$$+(2G_1+2G_2+2G_4)(G_1+G_5-1)(k_{b2}+k_{b3})\psi_{w1}+(2G_1+2G_2+2G_4)(G_1+G_5+1)(k_{b2}+k_{b3})\psi_{w2}$$

$$-2G_3(2G_1+2G_2+2G_4)(k_{b2}+k_{b3})y_{T1}+(2G_1+2G_2+2G_4)(2G_4-2G_5-2G_6)(k_{b2}+k_{b3})\psi_{T1}$$

$$+(2G_1+2G_2+2G_4)(-G_3+\frac{G_2+G_6}{b})(k_{b2}+k_{b3})y_{w3}-(2G_1+2G_2+2G_4)(G_3+\frac{G_2+G_6}{b})(k_{b2}+k_{b3})y_{w4}$$

$$+(2G_1+2G_2+2G_4)(G_1+G_5+1)(k_{b2}+k_{b3})\psi_{w3}+(2G_1+2G_2+2G_4)(G_1+G_5-1)(k_{b2}+k_{b3})\psi_{w4}$$

$$+2G_3(2G_1+2G_2+2G_4)(k_{b2}+k_{b3})y_{T2}+(2G_1+2G_2+2G_4)(2G_4-2G_5-2G_6)(k_{b2}+k_{b3})\psi_{T2}$$

$$-2(2G_1+2G_2+2G_4)^2(k_{b2}+k_{b3})\psi_c \qquad \text{(D-35)}$$

The contributions to the generalized forces by the dampers in parallel with the interaxle stiffnesses (for self-steering radial trucks) are found by replacing stiffnesses of all the terms without the steering gains in equation (D-22) to (D-35) with damping constants, and the degrees of freedom by their derivatives. These damping forces are:

$$F_{\dot{y}_{w1}} = -(C_{s2} + 2C_{s3})\dot{y}_{w1} + C_{s2}\dot{y}_{w2} + b(C_{s2} + 2C_{s3})\dot{\psi}_{w1}$$

$$+bC_{s2}\dot{\psi}_{w2} + 2C_{s3}\dot{y}_{T1} \qquad \text{(D-36)}$$

$$M_{\dot{\psi}_{w1}} = b(C_{s2} + 2C_{s3})\dot{y}_{w1} - bC_{s2}\dot{y}_{w2} - \left\{ C_{b2}+2C_{b3}+b^2(C_{s2}+2C_{s3}) \right\} \dot{\psi}_{w1}$$

$$+(C_{b2}-b^2C_{s2})\dot{\psi}_{w2} - 2bC_{s3}\dot{y}_{T1} + 2C_{b3}\dot{\psi}_{T1} \qquad \text{(D-37)}$$

$$F_{\dot{y}_{w2}} = C_{s2}\dot{y}_{w1} - (C_{s2}+2C_{s3})\dot{y}_{w2} - bC_{s2}\dot{\psi}_{w1} - b(C_{s2}+2C_{s3})\dot{\psi}_{w2}$$

$$+2C_{s3}\dot{y}_{T1} \qquad \text{(D-38)}$$

$$M_{\dot{\psi}_{w2}} = bC_{s2}\dot{y}_{w1}-b(C_{s2}+2C_{s3})\dot{y}_{w2}+(C_{b2}-b^2C_{s2})\dot{\psi}_{w1} - \left\{ C_{b2}+2C_{b3} + \right.$$

$$\left. b^2(C_{s2}+2C_{s3}) \right\} \dot{\psi}_{w2}+2bC_{s3}\dot{y}_{T1} + 2C_{b3}\dot{\psi}_{T1} \qquad \text{(D-39)}$$

$$F_{\dot{y}_{T1}} = 2C_{s3}\dot{y}_{w1} + 2C_{s3}\dot{y}_{w2} - 2bC_{s3}\dot{\psi}_{w1}+2bC_{s3}\dot{\psi}_{w2} - 4C_{s3}\dot{y}_{T1} \qquad \text{(D-40)}$$

$$M_{\dot{\psi}_{T1}} = 2C_{b3}\dot{\psi}_{w1} + 2C_{b3}\dot{\psi}_{w2} - 4C_{b3}\dot{\psi}_{T1} \qquad \text{(D-41)}$$

$$F_{\dot{y}_{w3}} = -(C_{s2}+2C_{s3})\dot{y}_{w3} + C_{s2}\dot{y}_{w4} + b(C_{s2}+2C_{s3})\dot{\psi}_{w3}$$

$$+bC_{s2}\dot{\psi}_{w4} + 2C_{s3}\dot{y}_{T2} \qquad \text{(D-42)}$$

$$M_{\dot{\psi}_{w3}} = b(C_{s2}+2C_{s3})\dot{y}_{w3} - bC_{s2}\dot{y}_{w4} - \quad C_{b2}+2C_{b3}+b^2(C_{s2}+2C_{s3}) \quad \dot{\psi}_{w3}$$

$$+(C_{b2}-b^2C_{s2})\dot{\psi}_{w4} - 2bC_{s3}\dot{y}_{T2} + 2C_{b3}\dot{\psi}_{T2} \qquad \text{(D-43)}$$

$$F_{\dot{y}_{w4}} = C_{s2}\dot{y}_{w3} - (C_{s2}+2C_{s3})\dot{y}_{w4} - bC_{s2}\dot{\psi}_{w3} - b(C_{s2}+2C_{s3})\dot{\psi}_{w4} + 2C_{s3}\dot{y}_{T2} \qquad \text{(D-44)}$$

$$M_{\dot{\psi}_{w4}} = bC_{s2}\dot{y}_{w3} - b(C_{s2}+2C_{s3})\dot{y}_{w4} + (C_{b2}-b^2C_{s2})\dot{\psi}_{w3} - \left\{C_{b2} + 2C_{b3}\right.$$

$$\left. + b^2(C_{s2}+2C_{s3})\right\} \dot{\psi}_{w4} + 2bC_{s3}\dot{y}_{T2} + 2C_{b3}\dot{\psi}_{T2} \qquad \text{(D-45)}$$

$$F_{\dot{y}_{T2}} = 2C_{s3}\dot{y}_{w3} + 2C_{s3}\dot{y}_{w4} - 2bC_{s3}\dot{\psi}_{w3} + 2bC_{s3}\dot{\psi}_{w4} - 4C_{s3}\dot{y}_{T2} \qquad \text{(D-46)}$$

$$M_{\dot{\psi}_{T2}} = 2C_{b3}\dot{\psi}_{w3} + 2C_{b3}\dot{\psi}_{w4} - 4C_{b3}\dot{\psi}_{T2} \qquad \text{(D-47)}$$

APPENDIX E

LINEARIZED EQUATIONS FOR THE 15 DOF STABILITY MODEL (CONVENTIONAL TRUCK)

The 6 DOF truck stability model developed for the conventional truck in Appendix C and extended to the generic truck* in Appendix D can be used to represent a truck quite accurately, provided the carbody motions are not significant in the speed range of interest. When the carbody motions become significant, the model has to be extended to include both trucks and the carbody to be able to represent all the significant modes. This extension increases the degrees of freedom of the model from six to 15. Figure E.1 shows the degrees of freedom and Figure E.2 shows the suspension system for conventional trucks.

The 15 second order linear differential equations of motion for a conventional vehicle are included in this Appendix [35]. The equations are based on the assumptions that the vehicle runs at constant speed on rigid, tangent, level track and that no external forces such as wind or coupling loads exist. These equations can be written in matrix form as:

$$\underline{\bar{M}}\,\underline{\ddot{y}} + [\underline{\bar{C}}_s + \underline{\bar{C}}_r]\underline{\dot{y}} + [\underline{\bar{K}}_s + \underline{\bar{K}}_r]\underline{y} = 0 \qquad \text{(E-1)}$$

where $\underline{y}$ is the vector of position degrees of freedom

$\underline{\bar{M}}$ is the inertia matrix

$\underline{\bar{K}}$ and $\underline{\bar{C}}$ are the suspension stiffness and damping matrices, respectively

$\underline{\bar{K}}_r$ and $\underline{\bar{C}}_r$ are the stiffness and damping matrices resulting from the wheel/rail interaction

To describe the generic truck with the 15 DOF analysis requires that additional terms from Appendix D representing the steering linkages be

---

*The standard self- and forced-steered trucks are special cases of the generic truck.

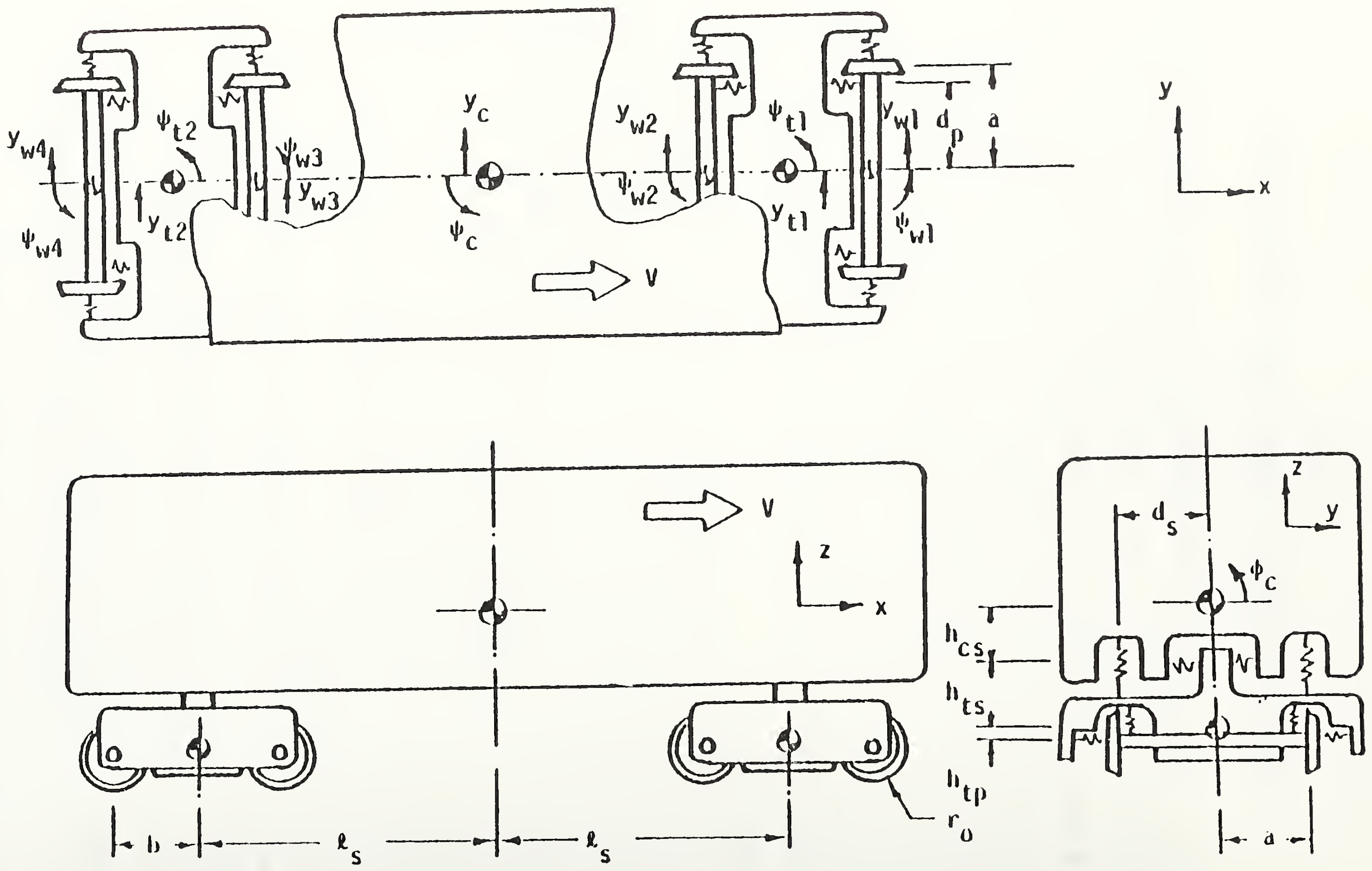

Figure E.1 Conventional Rail Vehicle Lateral Dynamic Model

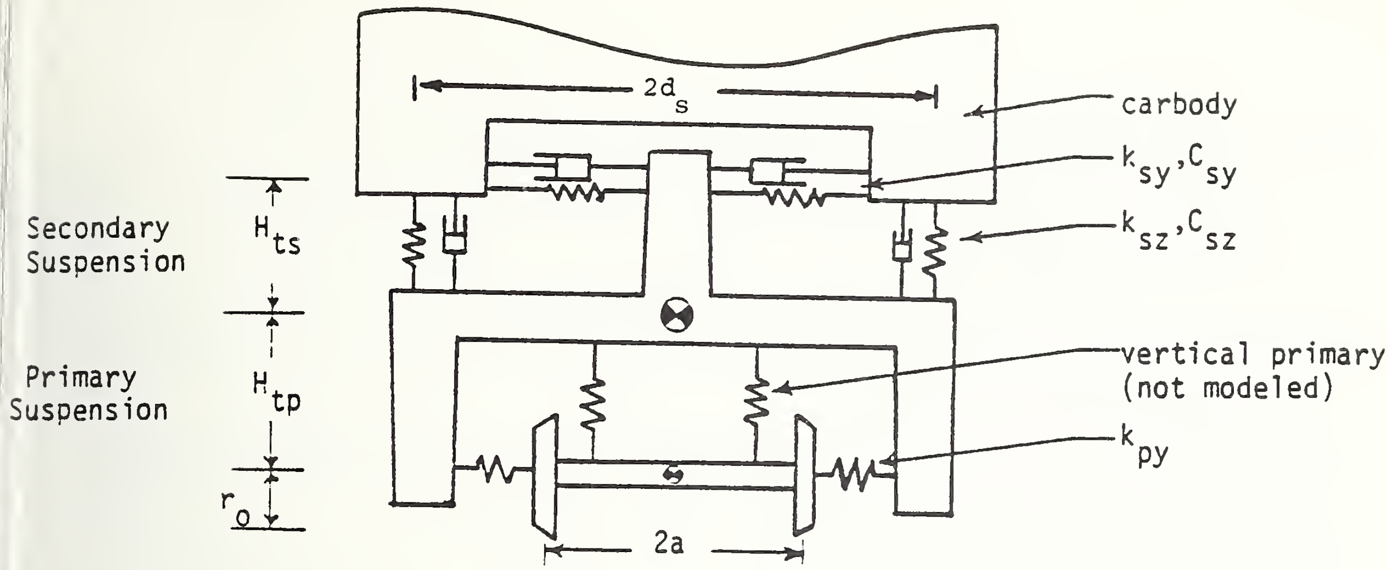

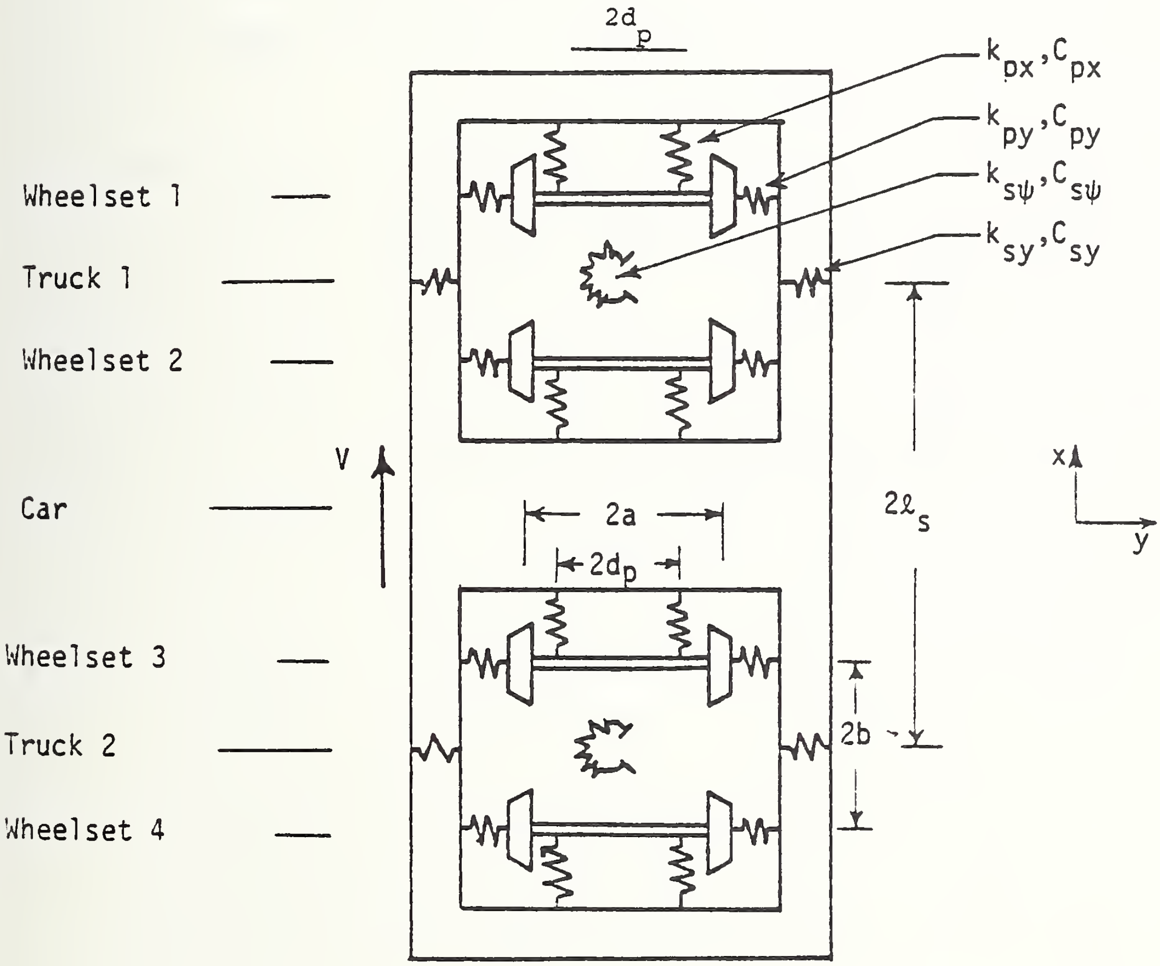

Figure E.2 Model of Conventional Rail Vehicle Suspension System appropriately added to the equations given in this Appendix E.

Despite the advantage of being able to represent all the important modes, the 15 DOF full vehicle model has some disadvantages such as:

- increased complexity, which makes it difficult to solve analytically.
- longer computational time

For these reasons, the 6 DOF model is used in the parametric studies whenever it is deemed appropriate.

The lateral equations of motion of a conventional rail vehicle are presented here. The state variables of the 15 DOF full vehicle model are defined in Table E.1 and are shown in Figure E.1. The model assumes the following:

- the vehicle runs at constant speed on rigid, tangent, level track
- no external forces as wind or coupling loads exist
- small displacements
- no flange contact

The fifteen linear differential equations of motion are:

Table E.1 Vehicle Model State Definitions

State	Unit	Definition
y_{w1}	ft	Lateral position of c.g., leading wheelset of the leading truck
ψ_{w1}	radian	Yaw of leading wheelset of the leading truck
y_{w2}	ft	Lateral position of c.g., trailing wheelset of the leading truck
ψ_{w2}	radian	Yaw of trailing wheelset of the leading truck
y_{t1}	ft	Lateral position of leading truck c.g.
ψ_{t1}	radian	Yaw of leading truck
y_{w3}	ft	Lateral position of c.g., leading wheelset of the trailing truck
ψ_{w3}	radian	Yaw of leading wheelset of the trailing truck
y_{w4}	ft	Lateral position of c.g., trailing wheelset of the trailing truck
ψ_{w4}	radian	Yaw of trailing wheelset of the trailing truck
y_{t2}	ft	Lateral position of trailing truck c.g.
ψ_{t2}	radian	Yaw of trailing truck
y_c	ft	Lateral position of carbody c.g.
ψ_c	radian	Yaw of carbody
ϕ_c	radian	Roll of carbody

Leading Wheelset Leading Truck

$$M_w\ddot{y}_{w1} = -[\frac{2f_{11}}{V} + 2c_{py} - \frac{c_{py}h_{tp}a_{11}}{a}]\,\dot{y}_{w1}$$

$$-2[k_{py} - \frac{f_{12}\Delta}{ar_o} + \frac{N}{2a}(a_{11}+\Delta) - \frac{k_{py}h_{tp}a_{11}}{2a}]y_{w1}$$

$$-[\frac{2f_{12}}{V} - \frac{VI_{wy}a_{11}}{ar_o}]\dot{\psi}_{w1} + 2f_{11}\psi_{w1}$$

$$+ \frac{c_{py}h_{tp}a_{11}}{a}\,\dot{y}_{w2} + \frac{k_{py}h_{tp}a_{11}}{a}\,y_{w2}$$

$$+ 2c_{py}\dot{y}_{t1} + 2k_{py}y_{t1} + 2c_{py}b\dot{\psi}_{t1} + 2k_{py}b\psi_{t1} \tag{E-2}$$

$$I_{wz}\ddot{\psi}_{w1} = [\frac{2f_{12}}{V} - \frac{VI_{wy}a_{11}}{ar_o}]\dot{y}_{w1} + [\frac{2f_{22}\Delta}{ar_o} - \frac{2af_{33}\lambda}{r_o}]y_{w1}$$

$$-[\frac{2f_{22}}{V} + \frac{2a^2f_{33}}{V} + 2c_{px}d_p^2]\dot{\psi}_{w1}$$

$$-[2k_{px}d_p^2 - aN\delta_o + 2f_{12}]\psi_{w1}$$

$$+ 2c_{px}d_p^2\dot{\psi}_{t1} + 2k_{px}d_p^2\psi_{t1} \tag{E-3}$$

Trailing Wheelset Leading Truck

$$M_w\ddot{y}_{w2} = \frac{c_{py}h_{tp}a_{11}}{a}\,\dot{y}_{w1} + \frac{k_{py}h_{tp}a_{11}}{a}\,y_{w1} - [\frac{2f_{11}}{V} + 2c_{py} - \frac{c_{py}h_{tp}a_{11}}{a}]\dot{y}_{w2}$$

$$-2[k_{py} - \frac{f_{12}\Delta}{ar_o} + \frac{N}{2a}(a_{11}+\Delta) - \frac{k_{py}h_{tp}a_{11}}{2a}]\,y_{w2}$$

$$-2\left[\frac{f_{12}}{V} - \frac{VI_{wy}a_{11}}{ar_o}\right]\dot{\psi}_{w2} + 2f_{11}\psi_{w2}$$

$$+2c_{py}\dot{y}_{t1} + 2k_{py}y_{t1} - 2c_{py}b\dot{\psi}_{t1} - 2k_{py}b\psi_{t1} \qquad \text{(E-4)}$$

$$I_{wz}\ddot{\psi}_{w2} = \left[\frac{2f_{12}}{V} - \frac{VI_{wy}a_{11}}{ar_o}\right]\dot{y}_{w2} + \left[\frac{2f_{22}\Delta}{ar_o} - \frac{2af_{33}\lambda}{r_o}\right]y_{w2}$$

$$-\left[\frac{2f_{22}}{V} + \frac{2a^2f_{33}}{V} + 2c_{px}d_p^2\right]\dot{\psi}_{w2}$$

$$-[2k_{px}d_p^2 - aN\delta_o + 2f_{12}]\psi_{w2}$$

$$+ 2c_{px}d_p^2\dot{\psi}_{t1} + 2k_{px}d_p^2\psi_{t1} \qquad \text{(E-5)}$$

Leading Truck

$$M_t\ddot{y}_{t1} = \left[2c_{py} - \frac{a_{11}}{a}(2c_{py}h_{tp} + c_{sy}h_{ts})\right]\dot{y}_{w1}$$

$$+ \left[2k_{py} - \frac{a_{11}}{a}(2k_{py}h_{tp} + k_{sy}h_{ts})\right]y_{w1}$$

$$+ \left[2c_{py} - \frac{a_{11}}{a}(2c_{py}h_{tp} + c_{sy}h_{ts})\right]\dot{y}_{w2}$$

$$+ \left[2k_{py} - \frac{a_{11}}{a}(2k_{py}h_{tp} + k_{sy}h_{ts})\right]y_{w2}$$

$$-[4c_{py} + 2c_{sy}]\dot{y}_{t1} - [4k_{py} + 2k_{sy}]y_{t1}$$

$$+ 2c_{sy}\dot{y}_c + 2k_{sy}y_c + 2c_{sy}\ell_s\dot{\psi}_c + 2k_{sy}\ell_s\psi_c$$

$$+ 2c_{sy}h_{cs}\dot{\phi}_c + 2k_{sy}h_{cs}\phi_c \tag{E-6}$$

$$I_{tz}\ddot{\psi}_{t1} = 2bc_{py}\dot{y}_{w1} + 2bk_{py}y_{w1} + 2d_p^2c_{px}\dot{\psi}_{w1} + 2d_p^2k_{px}\psi_{w1}$$

$$- 2bc_{py}\dot{y}_{w2} - 2bk_{py}y_{w2} + 2d_p^2c_{px}\dot{\psi}_{w2} + 2d_p^2k_{px}\psi_{w2}$$

$$-[4c_{py}b^2 + c_{s\psi} + 4c_{px}d_p^2]\dot{\psi}_{t1}$$

$$-[4k_{py}b^2 + k_{s\psi} + 4k_{px}d_p^2]\psi_{t1}$$

$$+ c_{s\psi}\dot{\psi}_c + k_{s\psi}\psi_c \tag{E-7}$$

<u>Leading Wheelset, Trailing Truck</u>

$$M_w\ddot{y}_{w3} = -[\frac{2f_{11}}{V} + 2c_{py} - \frac{c_{py}h_{tp}a_{11}}{a}]\dot{y}_{w3}$$

$$-2[k_{py} - \frac{f_{12}\Delta}{ar_o} + \frac{N}{2a}(a_{11} + \Delta) - \frac{k_{py}h_{tp}a_{11}}{2a}]y_{w3}$$

$$-[\frac{2f_{12}}{V} - \frac{VI_{wy}a_{11}}{ar_o}]\dot{\psi}_{w3} + 2f_{11}\psi_{w3}$$

$$+ \frac{c_{py}h_{tp}a_{11}}{a}\dot{y}_{w4} + \frac{k_{py}h_{tp}a_{11}}{a}y_{w4}$$

$$+ 2c_{py}\dot{y}_{t2} + 2k_{py}y_{t2} + 2c_{py}b\dot{\psi}_{t2} + 2k_{py}b\psi_{t2} \tag{E-8}$$

$$I_{wz}\ddot{\psi}_{w3} = [\frac{2f_{12}}{V} - \frac{VI_{wy}a_{11}}{ar_o}]\dot{y}_{w3} + [\frac{2f_{22}\Delta}{ar_o} - \frac{2af_{33}\lambda}{r_o}]\, y_{w3}$$

$$- [\frac{2f_{22}}{V} + \frac{2a^2 f_{33}}{V} + 2c_{px}d_p^2]\dot{\psi}_{w3}$$

$$- [2k_{px}d_p^2 - aN\delta_o + 2f_{12}]\psi_{w3}$$

$$+ 2c_{px}d_p^2\dot{\psi}_{t2} + 2k_{px}d_p^2\psi_{t2} \qquad \text{(E-9)}$$

Trailing Wheelset, Trailing Truck

$$M_w\ddot{y}_4 = \frac{c_{py}h_{tp}a_{11}}{a}\,\dot{y}_{w3} + \frac{k_{py}h_{tp}a_{11}}{a}\,y_{w3} - [\frac{2f_{11}}{V} + 2c_{py} - \frac{c_{py}h_{tp}a_{11}}{a}]\dot{y}_{w4}$$

$$- 2[k_{py} - \frac{f_{12}\Delta}{ar_o} + \frac{N}{2a}\,(a_{11} + \Delta) - \frac{k_{py}h_{tp}a_{11}}{2a}]y_{w4}$$

$$-[\frac{2f_{12}}{V} - \frac{2\,VI_{wy}a_{11}}{ar_o}]\dot{\psi}_{w4} + 2f_{11}\psi_{w4}$$

$$+ 2c_{py}\dot{y}_{t2} + 2k_{py}y_{t2} - 2c_{py}b\dot{\psi}_{t2} - 2k_{py}b\psi_{t2} \qquad \text{(E-10)}$$

$$I_{wz}\ddot{\psi}_{w4} = [\frac{2f_{12}}{V} - \frac{VI_{wy}a_{11}}{ar_o}]\dot{y}_{w4} + [\frac{2f_{22}\Delta}{ar_o} - \frac{2af_{33}\lambda}{r_o}]y_{w4}$$

$$- [\frac{2f_{22}}{V} + \frac{2a^2 f_{33}}{V} + 2c_{px}d_p^2]\dot{\psi}_{w4}$$

$$- [2k_{px}d_p^2 - aN\delta_o + 2f_{12}]\psi_{w4}$$

$$+ 2c_{px}d_p^2\dot{\psi}_{t2} + 2k_{px}d_p^2\psi_{t2} \qquad \text{(E-11)}$$

Trailing Truck

$$M_t \ddot{y}_{t2} = [2c_{py} - \frac{a_{11}}{a}(2c_{py}h_{tp} + c_{sy}h_{ts})]\dot{y}_{w3}$$

$$+ [2k_{py} - \frac{a_{11}}{a}(2k_{py}h_{tp} + k_{sy}h_{ts})]y_{w3}$$

$$+ [2c_{py} - \frac{a_{11}}{a}(2c_{py}h_{tp} + c_{sy}h_{ts})]\dot{y}_{w4}$$

$$+ [2k_{py} - \frac{a_{11}}{a}(2k_{py}h_{tp} + k_{sy}h_{ts})]y_{w4}$$

$$- [4c_{py} + 2c_{sy}]\dot{y}_{t2} - [4k_{py} + 2k_{sy}]y_{t2}$$

$$+ 2c_{sy}\dot{y}_c + 2k_{sy}y_c - 2c_{sy}\ell_s\dot{\psi}_c - 2k_{sy}\ell_s\psi_c$$

$$+ 2c_{sy}h_{cs}\dot{\phi}_c + 2k_{sy}h_{cs}\phi_c \tag{E-12}$$

$$I_{tz}\ddot{\psi}_{t2} = 2bc_{py}\dot{y}_{w3} + 2bk_{py}y_{w3} + 2d_p^2c_{px}\dot{\psi}_{w3} + 2d_p^2k_{px}\psi_{w3}$$

$$- 2bc_{py}\dot{y}_{w4} - 2bk_{py}y_{w4} + 2d_p^2c_{px}\dot{\psi}_{w4} + 2d_p^2k_{px}\psi_{w4}$$

$$-[4c_{py}b^2 + c_{s\psi} + 4c_{px}d_p^2]\dot{\psi}_{t2}$$

$$-[4k_{py}b^2 + k_{s\psi} + 4k_{px}d_p^2]\psi_{t2} \tag{E-13}$$

$$+ c_{s\psi}\dot{\psi}_c + k_{s\psi}\psi_c$$

Carbody

$$M_c\ddot{y}_c = -\frac{a_{11}h_{ts}c_{sy}}{a}\dot{y}_{w1} - \frac{a_{11}h_{ts}k_{sy}}{a}y_{w1} - \frac{a_{11}h_{ts}c_{sy}}{a}\dot{y}_{w2} - \frac{a_{11}h_{ts}k_{sy}}{a}y_{w2}$$

$$+ 2c_{sy}\dot{y}_{t1} + 2k_{sy}y_{t1} - \frac{a_{11}h_{ts}c_{sy}}{a}\dot{y}_{w3} - \frac{a_{11}h_{ts}k_{sy}}{a}y_{w3} - \frac{a_{11}h_{ts}c_{sy}}{a}\dot{y}_{w4}$$

$$- \frac{a_{11}h_{ts}k_{sy}}{a}y_{w4} + 2c_{sy}\dot{y}_{t2} + 2k_{sy}y_{t2} - 4c_{sy}\dot{y}_c - 4k_{sy}y_c$$

$$- 4h_{cs}c_{sy}\dot{\phi}_c - 4h_{cs}k_{sy}\phi_c \qquad \text{(E-14)}$$

$$I_{cz}\ddot{\psi}_c = -\frac{h_{ts}\ell_s a_{11}c_{sy}}{a}\dot{y}_{w1} - \frac{h_{ts}\ell_s a_{11}k_{sy}}{a}y_{w1} - \frac{h_{ts}\ell_s a_{11}c_{sy}}{a}\dot{y}_{w2}$$

$$- \frac{h_{ts}\ell_s a_{11}k_{sy}}{a}y_{w2} + 2\ell_s c_{sy}\dot{y}_{t1} + 2\ell_s k_{sy}y_{t1} + c_{s\psi}\dot{\psi}_{t1}$$

$$+ k_{s\psi}\psi_{t1} + \frac{h_{ts}\ell_s a_{11}c_{sy}}{a}\dot{y}_{w3} + \frac{h_{ts}\ell_s a_{11}k_{sy}}{a}y_{w3}$$

$$+ \frac{h_{ts}\ell_s a_{11}c_{sy}}{a}\dot{y}_{w4} + \frac{h_{ts}\ell_s a_{11}k_{sy}}{a}y_{w4} - 2\ell_s c_{sy}\dot{y}_{t2}$$

$$- 2\ell_s k_{sy}y_{t2} + c_{s\psi}\dot{\psi}_{t2} + k_{s\psi}\psi_{t2}$$

$$- [4\ell_s^2 c_{sy} + 2c_{s\psi}]\dot{\psi}_c - [4\ell_s^2 k_{sy} + 2k_{s\psi}]\psi_c \qquad \text{(E-15)}$$

$$I_{cy}\ddot{\phi}_c = \frac{a_{11}}{a}[d_s^2 c_{sz} - h_{cs}h_{ts}c_{sy}]\dot{y}_{w1} + \frac{a_{11}}{a}[d_s^2 k_{sz} - h_{cs}h_{ts}k_{sy}]y_{w1}$$

$$+ \frac{a_{11}}{a}[d_s^2 c_{sz} - h_{cs}h_{ts}c_{sy}]\dot{y}_{w2} + \frac{a_{11}}{a}[d_s^2 k_{sz} - h_{cs}h_{ts}k_{sy}]y_{w2}$$

$$+ 2h_{cs}c_{sy}\dot{y}_{t1} + 2h_{cs}k_{sy}y_{t1}$$

$$+ \frac{a_{11}}{a}[d_s^2 c_{sz} - h_{cs}h_{ts}c_{sy}]\dot{y}_{w3} + \frac{a_{11}}{a}[d_s^2 k_{sz} - h_{cs}h_{ts}k_{sy}]y_{w3}$$

$$+ \frac{a_{11}}{a}[d_s^2 c_{sz} - h_{cs}h_{ts}c_{sy}]\dot{y}_{w4} + \frac{a_{11}}{a}[d_s^2 k_{sz} - h_{cs}h_{ts}k_{sy}]y_{w4}$$

$$+ 2h_{cs}c_{sy}\dot{y}_{t2} + 2h_{cs}k_{sy}y_{t2} - 4h_{cs}c_{sy}\dot{y}_c - 4h_{cs}k_{sy}y_c$$

$$- [4h_{cs}^2 c_{sy} + 4d_s^2 c_{sz}]\dot{\phi}_c - [4h_{cs}^2 k_{sy} + 4d_s^2 k_{sz} - h_{cs}W]\phi_c \qquad \text{(E-16)}$$

APPENDIX F

STEADY-STATE CURVING EQUATIONS FOR A SINGLE WHEELSET

This Appendix develops the nonlinear curving models used to compute curve negotiation performance indices. Fully nonlinear models are needed since nearly all vehicles experience flange contact and creep force saturation on the majority of transit property curves.

As discussed in Section 2.1.2 the primary curving performance index is the work generated by the flanging or high rail wheel. This index is related to the wear rate of the wheel.

F.1 Single Wheelset Model

This section presents the equation formulation for both single and two point contact situations on an individual wheel.

The basic element of the rail vehicle steering and support system is the wheelset. The contact and friction mechanisms which develop at the wheel/rail interfaces have a dominant effect on vehicle curving behavior. The curving performance of a vehicle is a direct function of the ability of its wheelsets to negotiate a curve.

F.1.1 Coordinate Systems

A free wheelset negotiating a constant radius curve is exposed to track curvature and lateral force unbalance inputs. The track curvature is given by 1/R, where R is the curve radius assumed constant. The lateral force unbalance is usually expressed in terms of cant deficiency, ϕ_d, defined as the angle between (1) the resultant of the "centrifugal force", mV^2/R, and the weight, mg, and (2) the normal into the rail plane. When $\phi_d=0$, a condition of "balanced running" is achieved for which the components of centrifugal force and weight parallel to the rail plane cancel each other. For comfort and safety the maximum cant deficiency loads are limited to low levels in the U. S. (about 6° of inboard unbalance and 3° of outboard unbalance [30]). Track curvature is therefore considered the dominant curving input.

Assuming continuous wheel/rail contact, a wheelset negotiating a constant radius track at constant speed has two independent degrees of freedom: lateral and yaw displacements, y_w and ψ_w, respectively. The convention for positive y_w and ψ_w displacements is shown in Figure 2.1. In this report, right handed curves are considered, and thus positive y_w is associated with displacements toward the left rail. Track and wheelset coordinate systems are introduced in Figure F.1. Contact angles (δ_L, δ_R), rolling radii (r_L, r_R), and wheelset roll angle relative to the track plane (ϕ_w) are defined in Figure F.2.

F.1.2 Wheel/Rail Profile Geometry

For a wheelset which never loses contact with the rails, the rolling radii, contact angles, and wheelset roll angle are functions of the net wheelset-rail lateral excursion for a given wheel/rail profile. These functions (rolling radii and contact angles) are shown in Figure F.3 for a typical new wheel on worn rail profile and in Figure F.4 for a Heumann wheel on worn rail, both for standard gage rails [22]. For the new wheel profile, the flange clearance is y_{fc} = 0.32 in. When the wheelset lateral excursion minus the rail lateral excursion is less than flange clearance, tread contact occurs. Flanging at the left wheel occurs when the wheelset lateral excursion with respect to the left rail equals or exceeds flange clearance.

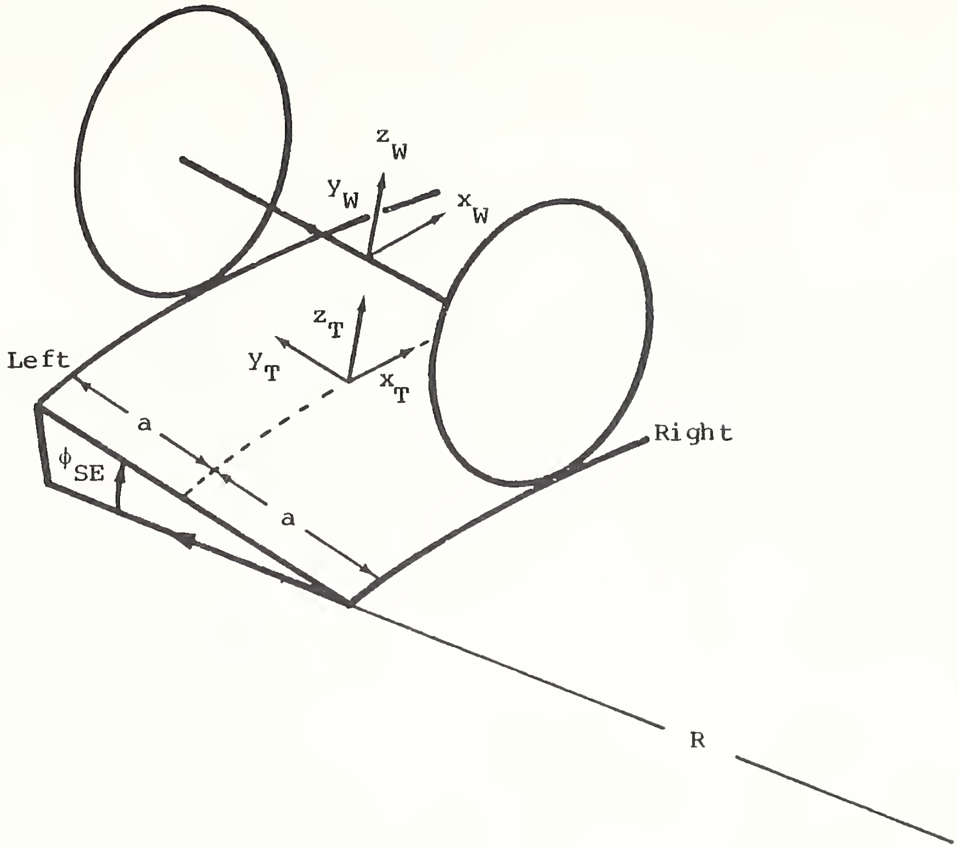

Figure F.1 Track and Wheelset Coordinate Systems

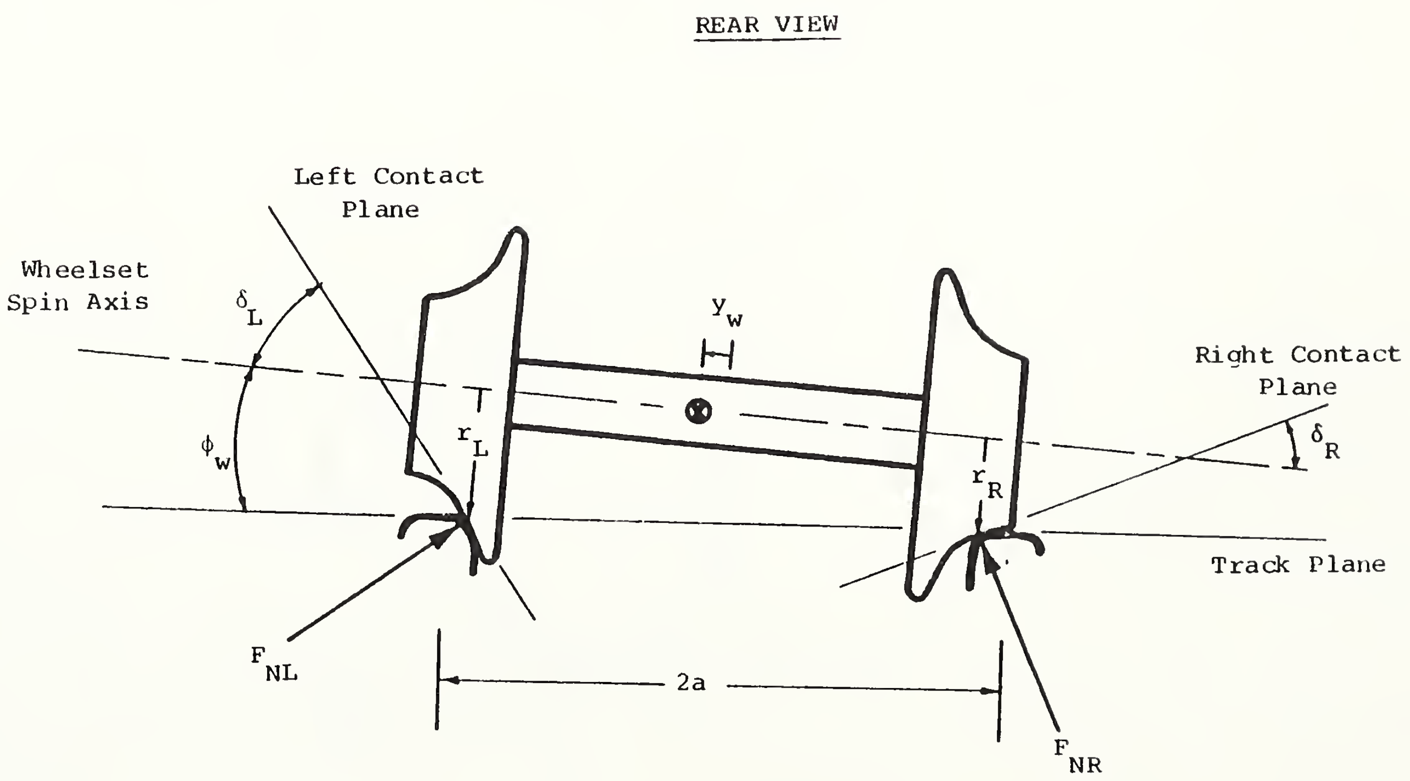

Figure F.2 Wheel/Rail Geometry and Normal Forces Assuming Single-Point Contact

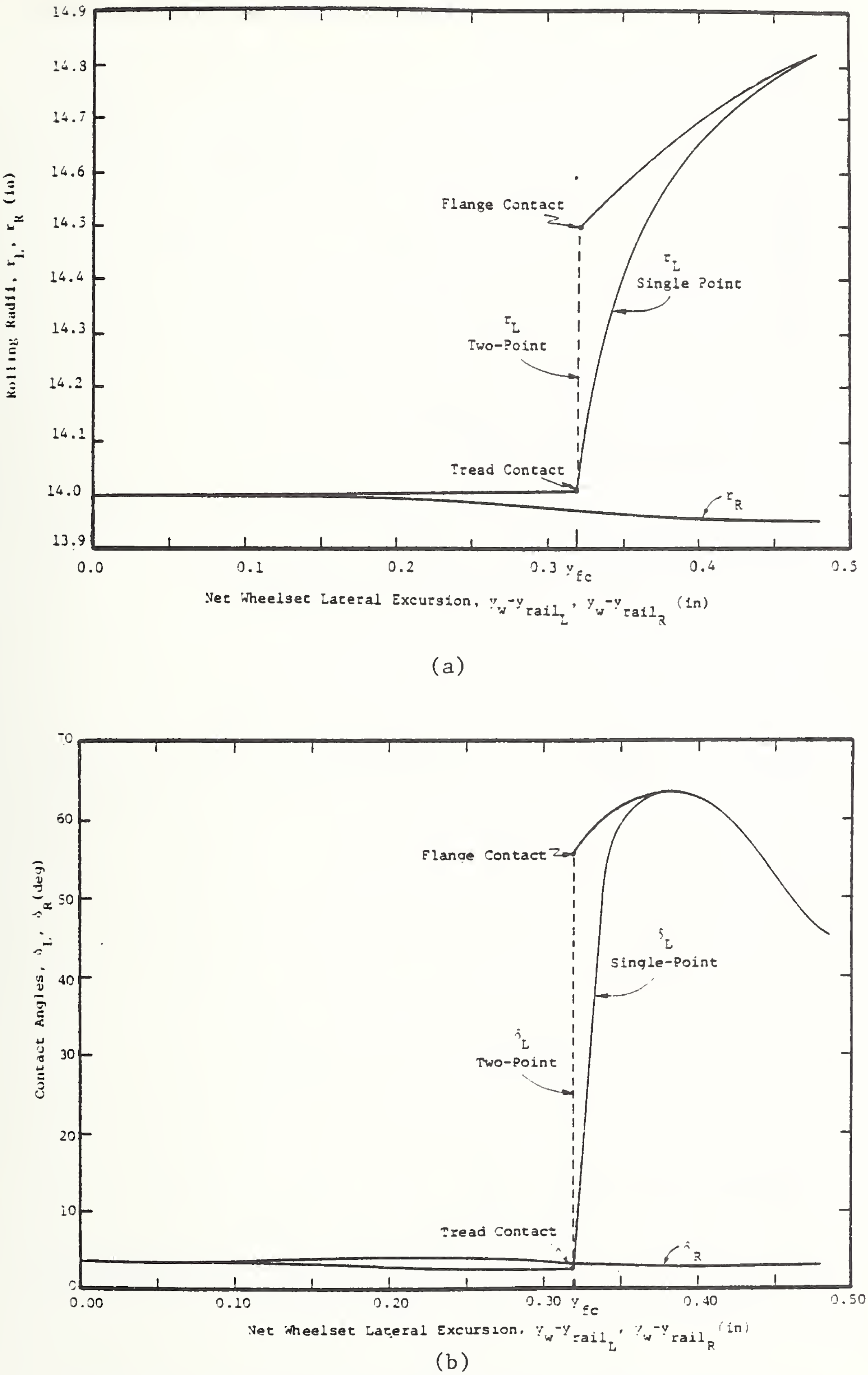

Figure F.3 Rolling Radii (a) and Contact Angles (b) vs. Net Wheelset Lateral Excursion for New Wheel on Worn Rail.

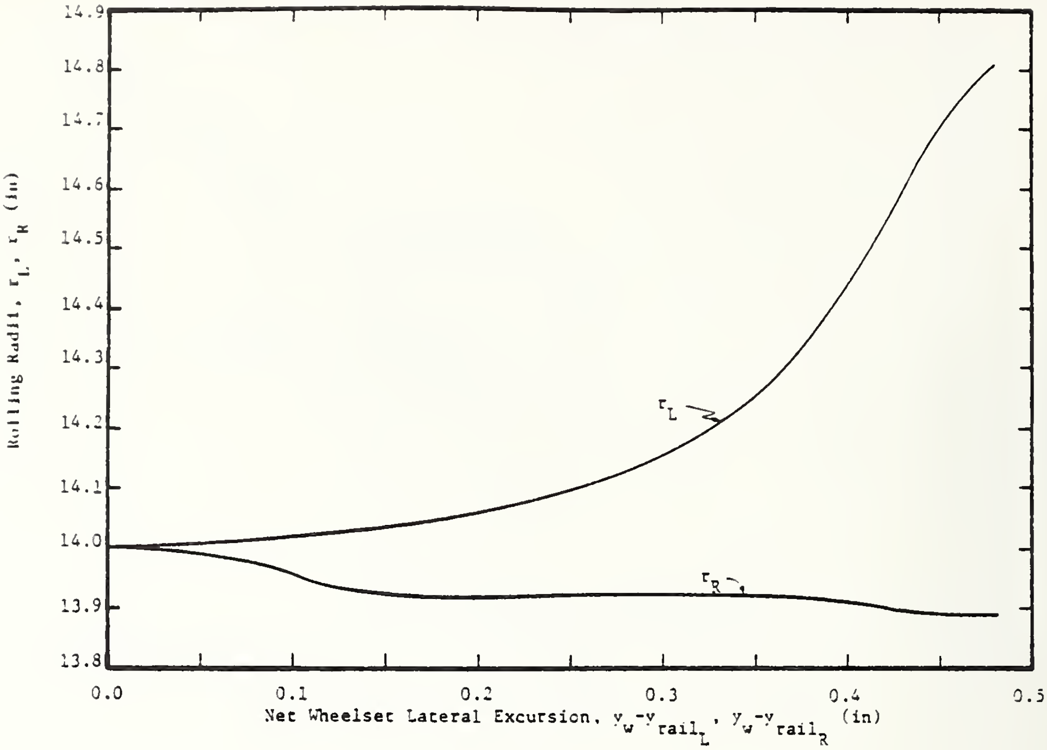

(a)

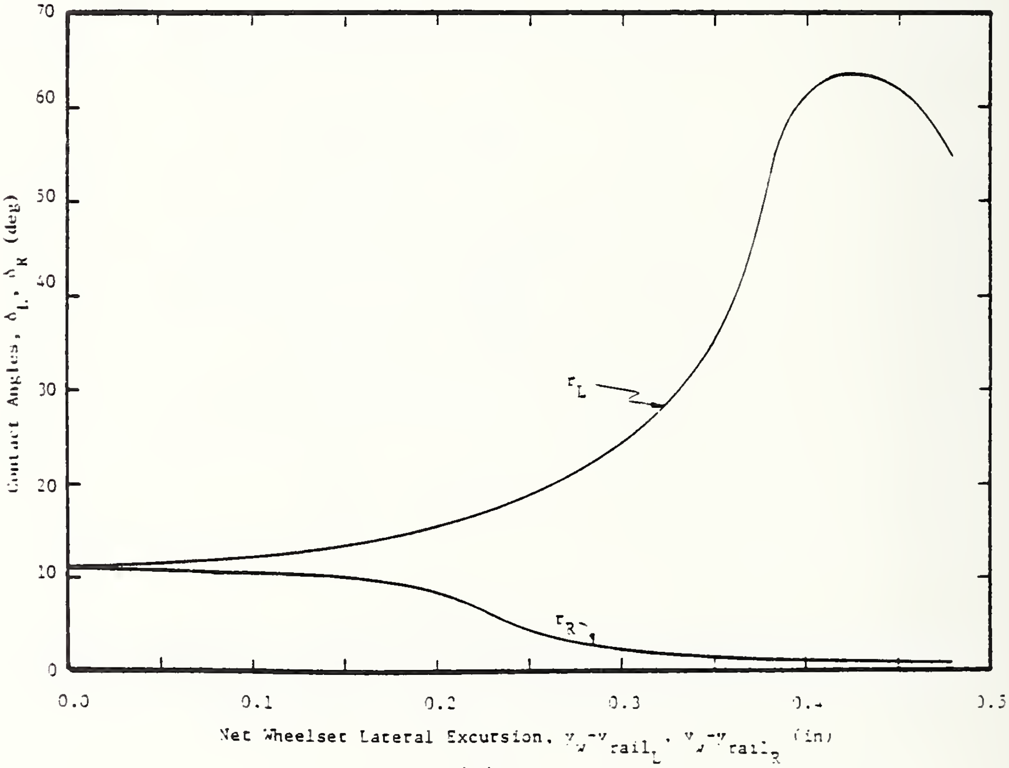

(b)

Figure F.4 Rolling Radii (a) and Contact Angles (b) vs. Net Wheelset Lateral Excursion for Heumann Wheel on Worn Rail.

Note that for severe flanging the contact angle approaches 65°.

The rolling radii, contact angles, and roll angle are wheel/rail geometric constraint variables since they are functions of the net wheelset-rail lateral displacement. These variables indicate the nature of wheel/rail contact as the wheelset is displaced laterally. If the rolling radii and contact angles are single valued functions of the lateral excursion, single point contact occurs at both wheels for all displacements. This represents the continuous single-point contact approximation, shown in Figures F.3 and F.4. As the wheelset is laterally displaced, the left wheel shifts from tread to flange contact, while the inner wheel maintains tread contact. For other profiles (see Figures F.3) the left rolling radius and left contact angle have discontinuous jumps at net lateral excursions equal to flange clearance indicating that multiple wheel/rail contact points exist at the flanging (left) wheel. Single-point tread contact occurs for net lateral excursions less than flange clearance, corresponding to the situation drawn in Figure F.5a. For net lateral excursions equal to flange clearance, it is assumed that two-point contact occurs at the flanging wheel depicted in Figure F.5b, where the rail head is shown to contact simultaneously both the tread and flange of the flanging (outer) wheel. The inner wheel maintains single-point tread contact. For net lateral excursions larger than flange clearance, a situation conducive to derailment exists since single-point flange contact occurs at the flanging wheel (Figure F.5c).

Some profiles are designed to achieve single-point wheel/rail contact for all realistic values of lateral displacement. This is the case for the Heumann wheel profile of Figures F.4. Many new wheel profiles, such as the

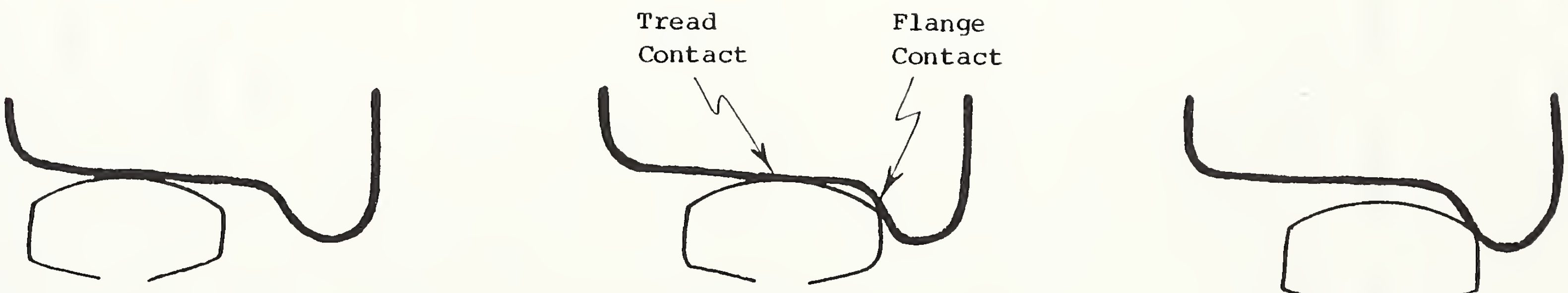

(a) One-Point Tread Contact
$y_w - y_{rail_L} < y_{fc}$

(b) Two-Point Contact
$y_w - y_{rail_L} = y_{fc}$

(c) One-Point Flange Contact
$y_w - y_{rail_L} > y_{fc}$

Figure F.5 Left Wheel/Rail Contact

AAR 1 in 20, contact the rails at multiple points during normal use. Naturally, wheel (and rail) profiles change with time due to wear during service life.

F.1.3 Wheelset Equilibrium Conditions

For a wheelset negotiating a curve, a difference occurs between the actual velocity and the velocity in pure rolling of the contact points resulting in partial slip or creepage of the wheels relative to the rails. Normal loads acting on a slipping wheelset result in the generation of creep forces. Due to the action of creep, the lateral and yaw degrees of freedom of a wheelset are coupled.

Each point of wheel/rail contact is a patch of finite area, where a state between pure-roll and pure-slip exists. During the last ten years there has been a significant improvement in the understanding of this friction mechanism and in computational programs to predict it. Kalker [31] developed linear, simplified nonlinear, and exact nonlinear theories and programs. In this paper a "heuristic" [34] creep force model* is used which is computationally fast and reasonably accurate. The creep forces and moment at each contact patch can be resolved into longitudinal, lateral, and vertical components in the track frame.

Whereas creep forces act in the plane of each contact patch, normal forces act perpendicular to the plane. These forces can be resolved into lateral and vertical components in the track frame. For single-point wheel/rail contact at the left and right wheels, the resolved normal force components from Figure F.2 are:

---

*See Appendix G.

$$F_{NYL} = -F_{NL}\sin(\delta_L + \phi_w)$$

$$F_{NZL} = F_{NL}\cos(\delta_L + \phi_w)$$

$$F_{NYR} = F_{NR}\sin(\delta_R - \phi_w) \tag{F-1}$$

$$F_{NZR} = F_{NR}\cos(\delta_R - \phi_w)$$

The sum of the lateral components of the normal force is sometimes referred to as the "gravitational stiffness force".

The static equilibrium conditions for a wheelset negotiating a constant radius curve can be expressed by eight algebraic equations, six for the wheelset and one for each rail. The rail is assumed to only have a lateral degree of freedom (Figure F.6), i.e., overturning motion has been neglected. The equilibrium equations are

Wheelset

$$\Sigma F_{x_T} = 0 \tag{F-2}$$

$$\Sigma F_{y_T} = 0 \tag{F-3}$$

$$\Sigma F_{z_T} = 0 \tag{F-4}$$

$$\Sigma M_{x_w} = 0 \tag{F-5}$$

$$\Sigma M_{y_w} = 0 \tag{F-6}$$

$$\Sigma M_{z_w} = 0 \tag{F-7}$$

Left Rail: $$\Sigma F_{y_T} = 0 \tag{F-8}$$

Right Rail: $$\Sigma F_{y_T} = 0 \tag{F-9}$$

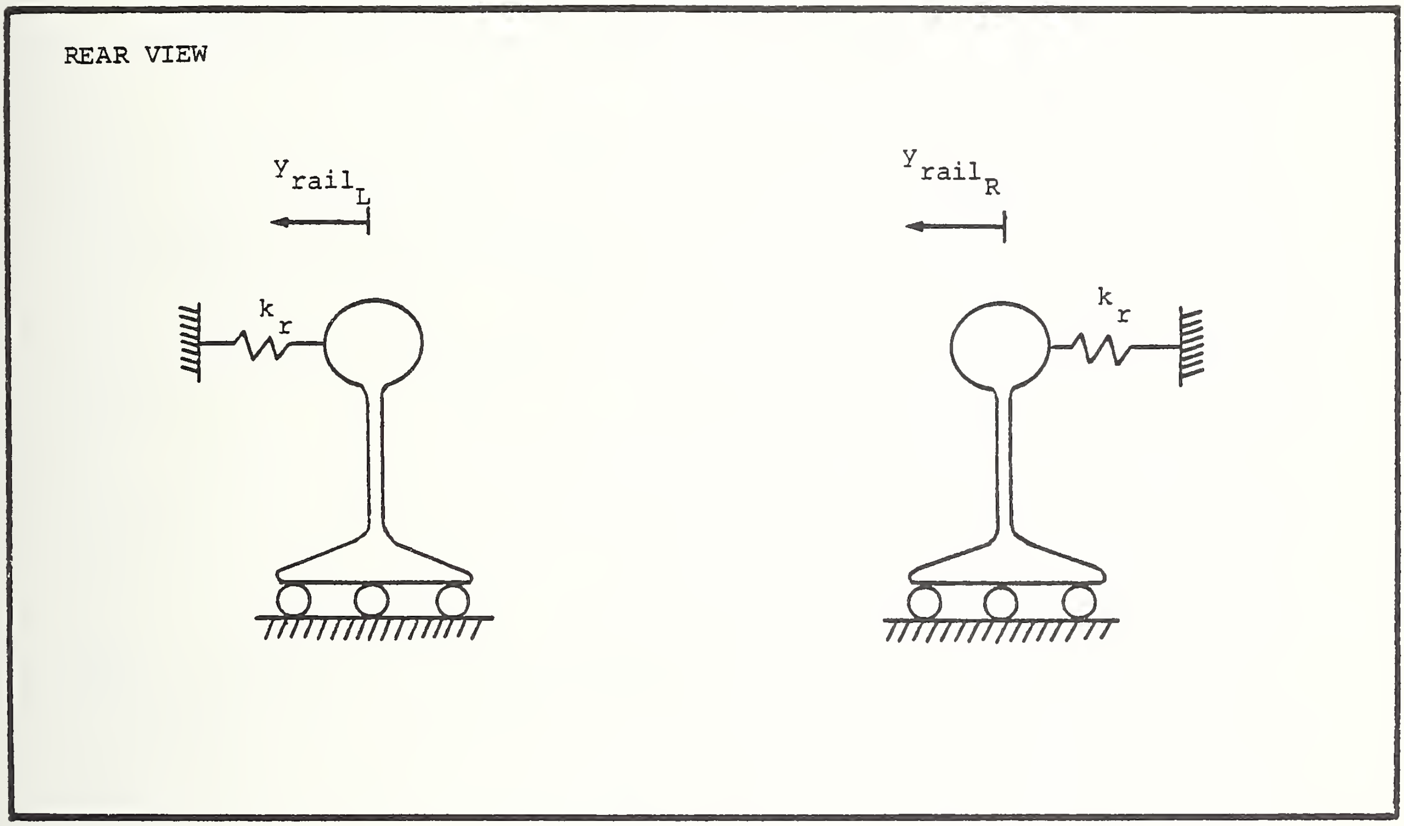

Figure F.6 Flexible Rail Model

where external and inertial forces/moments are summed on the left. Equations (F-2) - (F-4) are wheelset force equilibrium equations, (F-5) - (F-7) are wheelset moment equations and (F-8) - (F-9) are the left and right rail lateral force equations.

In steady state curving the rails can be modeled approximately as linear springs as shown in Figure F.6. Each rail displaces laterally a distance related to the net lateral wheel force, i.e.,

$$y_{rail_L} = \frac{F_{YL}}{k_r} \tag{F-10}$$

$$y_{rail_R} = \frac{F_{YR}}{k_r} \tag{F-11}$$

where F_{YL} and F_{YR} are the net lateral wheel forces and are composed of creep and normal forces. The typical range of effective lateral rail stiffness values is 25,000 lb/in to 80,000 lb/in [36].

Two nonlinear models have been developed to predict the steady-state curving behavior of a single wheelset. Both models assume that the wheelset is in force and moment static equilibrium. The difference between the models is that one assumes that single-point wheel/rail contact occurs at both wheels of the wheelset; the other model assumes that two-point tread-flange contact occurs at the outer wheel and single-point tread contact occurs at the inner wheel of the wheelset. The following two sections formulate the equilibrium conditions for these two models.

F.1.3.1 Single-Point Contact

A free-body diagram of a wheelset with single-point contact at each wheel/rail interface is shown in Figure F.7. All forces and

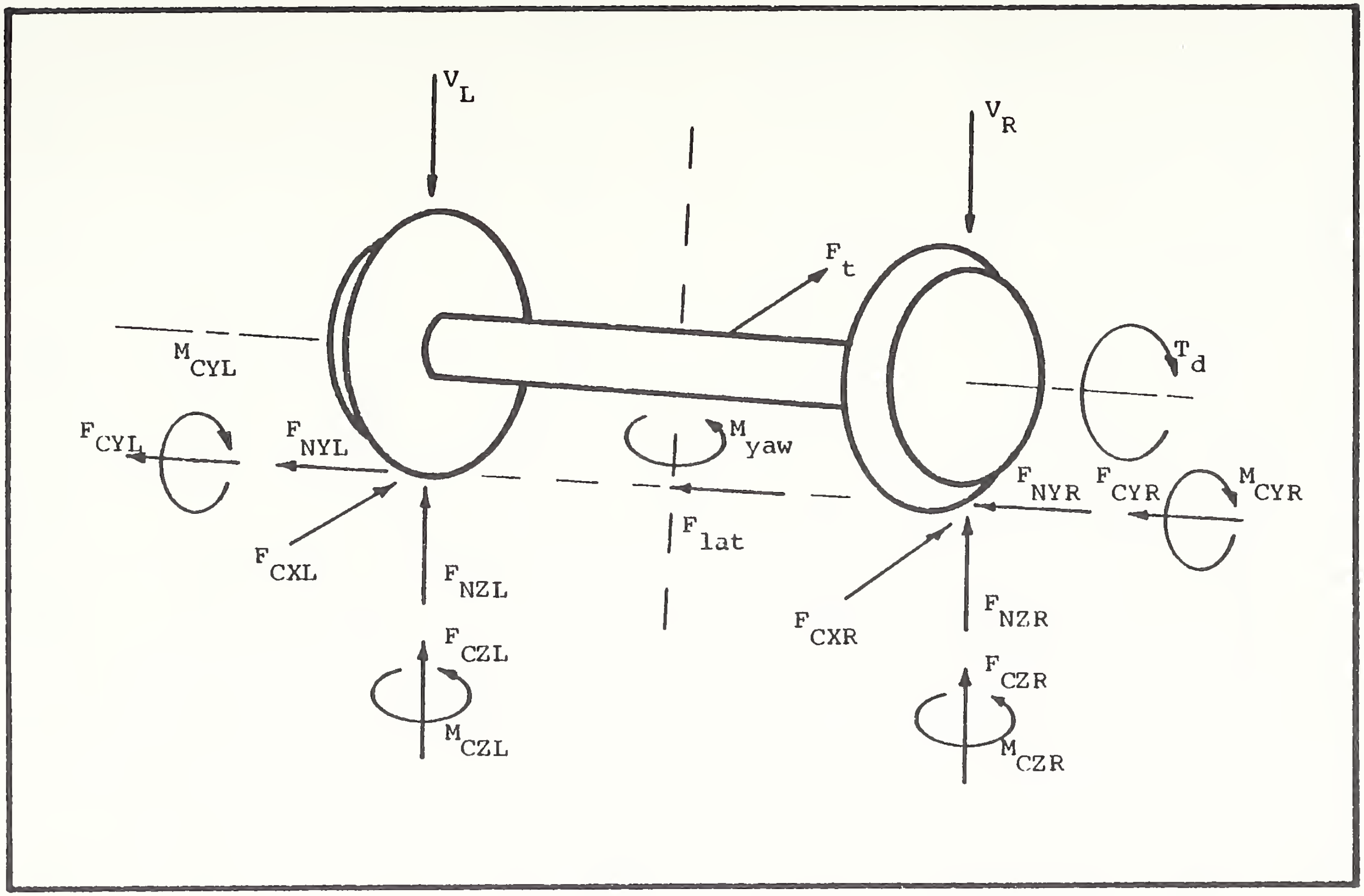

Figure F.7 Wheelset Free-Body Diagram: Single-Point Wheel/Rail Contact.

moments are resolved in track coordinates, except for the wheelset drive/brake torque, T_d, which acts about the spin axis. This drive/brake torque can be considered to be a specified input. Other inputs are: (1) the vertical loads on the left and right wheels, V_L and V_R, respectively, acting in the negative z_T direction, (2) the thrust or drawbar force, F_t, acting at the wheelset center of mass in the x_T direction, (3) the wheelset lateral force, F_{lat}, acting in the track plane in the y_T direction, and (4) the wheelset yaw moment, M_{yaw}, acting about the z_W axis. Figure F.8 shows a rear view of the wheel and rail force equilibrium.

Assuming single-point contact at the left and right wheel/rail interfaces and small roll and yaw angles, the following steady-state equilibrium conditions apply:

WHEELSET

LONGITUDINAL

$$\Sigma F_{x_T} = 0 = F_{CXL} + F_{CXR} + F_t \qquad \text{(F-12)}$$

LATERAL

$$\Sigma F_{y_T} = 0 = F_{NYL} + F_{CYL} + F_{NYR} + F_{CYR} + F_{lat} \qquad \text{(F-13)}$$

VERTICAL

$$\Sigma F_{z_T} = 0 = F_{NZL} + F_{CZL} + F_{NZR} + F_{CZR} - V_L - V_R \qquad \text{(F-14)}$$

ROLL

$$\Sigma M_{x_W} = 0 = (F_{NZL} + F_{CZL} - F_{NZR} - F_{CZR})a + (V_R - V_L)a \qquad \text{(F-15)}$$

REAR VIEW

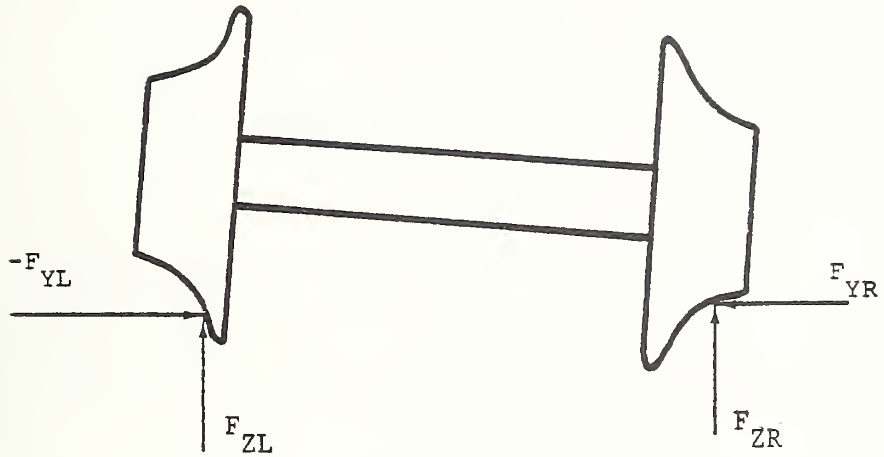

Wheel Forces

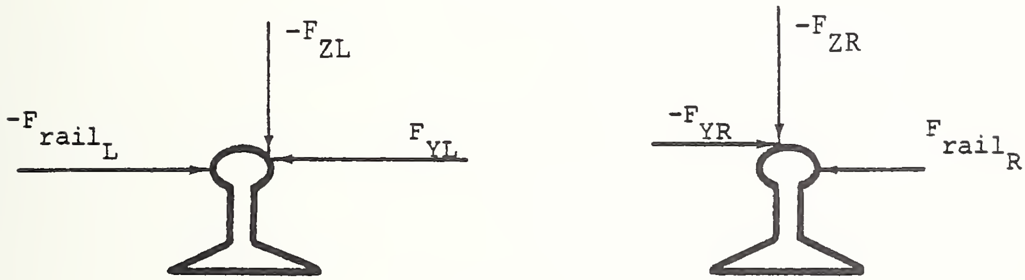

Rail Forces

Figure F.8 Wheel and Rail Forces for Single-Point Contact

SPIN

$$\Sigma M_{y_w} = 0 = -r_L[F_{CXL} + \psi_w\{F_{CYL} + F_{CZL}\tan(\delta_L + \phi_w)\}]$$

$$-r_R[F_{CXR} + \psi_w\{F_{CYR} - F_{CZR}\tan(\delta_R - \phi_w)\}]$$

$$+M_{CYL} + M_{CYR} + \phi_w\,(M_{CZL} + M_{CZR}) + T_d \quad \text{(F-16)}$$

YAW

$$\Sigma M_{z_w} = 0 = -(F_{CXL} - F_{CXR})a - \psi_w\{(F_{NYL} + F_{CYL})(a - r_L\tan(\delta_L + \phi_w))$$

$$-(F_{NYR} + F_{CYR})\,(a - r_R\tan(\delta_R - \phi_w))\} + M_{CZL} + M_{CZR}$$

$$-\phi_w(M_{CYL} + M_{CYR}) + M_{yaw} \quad \text{(F-17)}$$

RAIL

LATERAL LEFT

$$\Sigma F_{y_T} = 0 = F_{NYL} + F_{CYL} + F_{rail_L} \quad \text{(F-18)}$$

LATERAL RIGHT

$$\Sigma F_{y_T} = 0 = F_{NYR} + F_{CYR} + F_{rail_R} \quad \text{(F-19)}$$

Here the lateral rail reaction forces, F_{rail_L} and F_{rail_R}, are functions of $y_w - y_{rail_L}$ and $y_w - y_{rail_R}$, respectively.

Equations (F-12) - (F-19) represent eight coupled nonlinear algebraic equations. Assuming V_L, V_R, F_{lat}, and M_{yaw} are known, the equations can be solved for the following eight independent variables: F_t, y_w, F_{NZL}, F_{NZR}, Ω, ψ_w, y_{rail_L}, y_{rail_R}. These variables can be used to calculate all wheel/rail forces. The contact angle and roll angle are specified since

$y_w - y_{rail_L}$ and $y_w - y_{rail_R}$ are known, and thus the resultant normal forces and the lateral components of the normal forces can be calculated from F_{NZL} and F_{NZR}. The creep forces at the left and right contact patches can be computed since the creepages (which are functions of $y_w - y_{rail_L}$, $y_w - y_{rail_R}$, Ω, and ψ_w) and the normal forces are known. Equations (F-12) - (F-19) can alternatively be solved for the following variables if V_L, V_R, y_w, and ψ_w are specified: F_t, F_{lat}, F_{NZL}, F_{NZR}, Ω, M_{yaw}, Y_{rail_L}, y_{rail_R}. Later in this Appendix, the numerical technique required to solve for this latter set of unknowns is described. Finally, for the case of rigid rails, $y_{rail_L} = y_{rail_R} = 0$ and the wheelset equilibrium equations, equations (F-12) - (F-17) decouple from the lateral rail force equations, equations (F-18) and (F-19), leaving a system of six equations with six unknowns.

The thrust in the longitudinal track direction defines the drawbar force, F_t, which must be applied to the wheelset for it to traverse the curve in steady-state. The lateral force, F_{lat}, is provided by suspension and body (cant deficiency) forces. It equilibrates the lateral components of creep and normal forces to yield static equilibrium in the lateral direction. Suspension forces also give rise to the yaw moment, M_{yaw}, which balances the moments in the yaw direction due to creep and normal forces. The vertical loads whch act on the left and right wheels, V_L and V_R, respectively, are provided by suspension and body forces. The sum and difference of the vertical and roll equations yield the following equations for the vertical loads:

$$V_L = F_{NZL} + F_{CZL} \tag{F-20}$$

$$V_R + F_{NZR} + F_{CZR} \tag{F-21}$$

The rotational velocity of the wheelset is determined by the spin equation, which balances the moments about the wheelset spin (bearing) axis. The wheelset drive/brake torque, T_d, is balanced principally by longitudinal creep forces.

F.1.3.2 Two-Point Contact

The wheelset model appropriate for two-point contact analysis assumes simultaneous tread and flange contact at the outer (flanging) wheel and single-point contact at the inner wheel. The lateral displacement of the wheelset with respect to the left rail is fixed at flange clearance and thus the contact geometry of the tread and flange contact points at the left wheel is fixed even though the forces may vary. Figure F.9 shows the free-body wheel and rail forces for two-point contact. The steady-state force and moment equilibrium equations for the case of two-point contact are similar to equations (F-12) - (F-19) with new terms to account for the additional contact point. The two-point contact formulation is statically determinate due to the facts that (1) the net lateral excursion at the left wheel is constrained to equal the flange clearance, and (2) the normal forces have components in the lateral as well as vertical directions. This implies that the contact geometry at the tread and flange contact points of the flanging wheel is known and that the normal force at the flange contact point can be determined from the lateral force balance equation. The complete equations are shown below:

WHEELSET

LONGITUDINAL

$$F_{x_T} = 0 = F_{CXLT} + F_{CXLF} + F_{CXR} + F_t \tag{F-22}$$

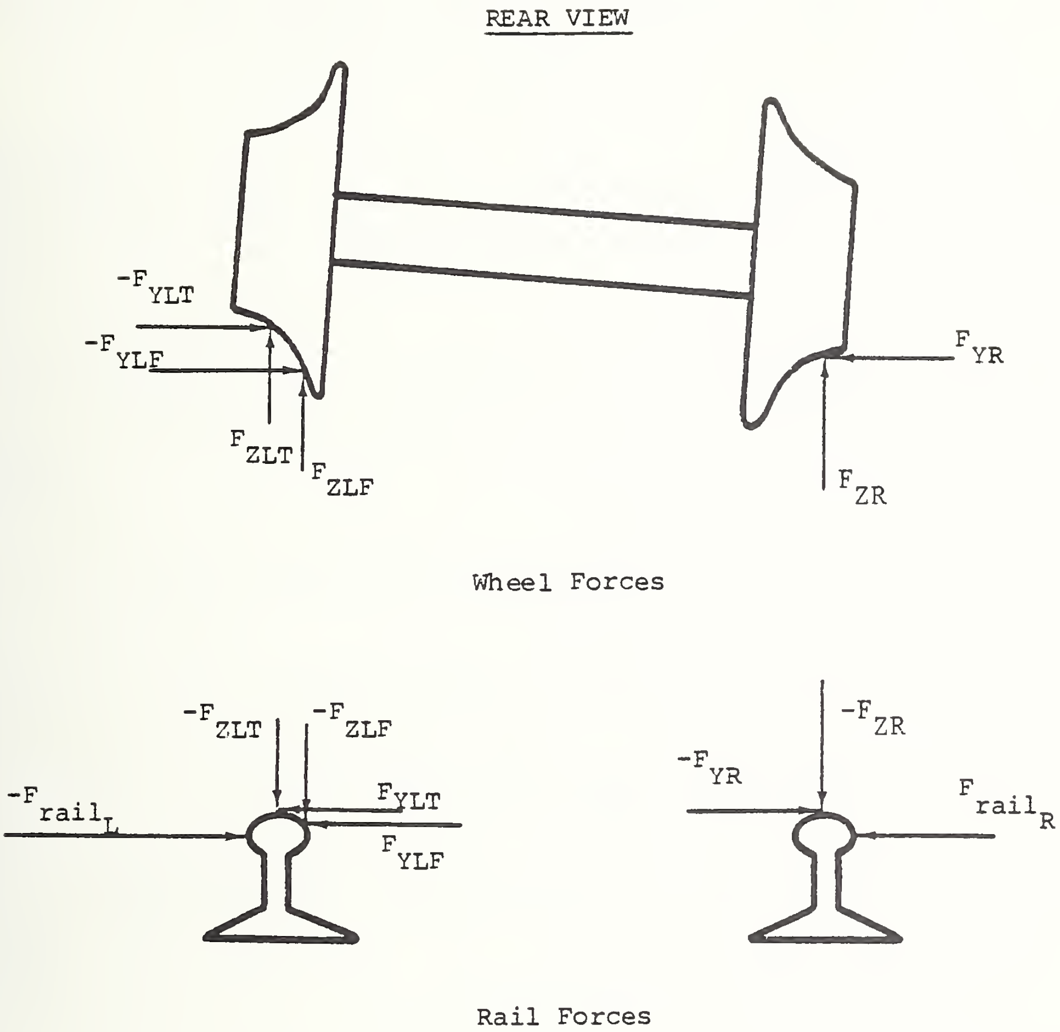

Figure F.9 Wheel and Rail Forces for Two-Point Contact

LATERAL

$$F_{y_T} = 0 = F_{NYLT} + F_{CYLT} + F_{CYLF} + F_{NYR} + F_{CYR} + F_{lat} \quad \text{(F-23)}$$

VERTICAL

$$\Sigma F_{z_T} = 0 = F_{NZLT} + F_{CZLT} + F_{NZLF} + F_{CZLF} + F_{NZR} + F_{CZR} - V_L - V_R \quad \text{(F-24)}$$

ROLL

$$\Sigma M_{x_w} = 0 = (F_{NZLT} + F_{CZLT} + F_{NZLF} + F_{CZLF} - F_{NZR} - F_{CZR})a$$

$$- (V_R - V_L)a \quad \text{(F-25)}$$

SPIN

$$\Sigma M_{y_w} = 0 = -r_{LT}[F_{CXLT} + \psi_w \{F_{CYLT} + F_{CZLT} \tan(\delta_{LT} + \phi_w)\}]$$

$$-r_{LF}[F_{CXLF} + \psi_w \{F_{CYLF} + F_{CZLF} \tan(\delta_{LF} + \phi_w)\}]$$

$$-r_R[F_{CXR} + \psi_w \{F_{CYR} - F_{CZR} \tan(\delta_R - \phi_w)\}]$$

$$+M_{CYLT} + M_{CYLF} + M_{CYR} + \phi_w(M_{CZLT} + M_{CZLF} + M_{CZR})$$

$$+ T_d \quad \text{(F-26)}$$

YAW

$$\Sigma M_{z_w} = 0 = -(F_{CXLT} + F_{CXLF} - F_{CXR})a$$

$$-\psi_w\{(F_{NYLT} + F_{CYLT})(a-r_{LT}\tan(\delta_{LT} + \phi_w))$$

$$+ (F_{NYLF} + F_{CYLF})(a - r_{LF}\tan(\delta_{LF} + \phi_w))$$

$$- (F_{NYR} + F_{CYR}) (a - r_R\tan(\delta_R - \phi_w))\}$$

$$+ M_{CZLT} + M_{CZLF} + M_{CZR} - \phi_w(M_{CYLT} + M_{CYLF} + M_{CYR}) + M_{yaw} \quad \text{(F-27)}$$

RAIL

LATERAL LEFT

$$\Sigma F_{y_T} = 0 = F_{NYLT} + F_{CYLT} + F_{NYLF} + F_{CYLF} + F_{rail_L} \tag{F-28}$$

LATERAL RIGHT

$$\Sigma F_{y_T} = 0 = F_{NYR} + F_{CYR} + F_{rail_R} \tag{F-29}$$

Equations (F-22) - (F-29) represent eight coupled nonlinear algebraic equations. In this case the relative wheelset excursion ($y_w - y_{rail_L}$) is fixed at the flange clearance value (y_{fc}). Assuming V_L, V_R, F_{lat}, and M_{yaw} are known, the equations can be solved for: F_t, y_w, F_{NZLT}, F_{NZLF}, F_{NZR}, Ω, ψ_w, y_{rail_R}. Alternatively, if V_L, V_R, y_w and ψ_w are specified, the equations can be solved for: F_t, F_{lat}, F_{NZLT}, F_{NZLF}, F_{NZR}, Ω, M_{yaw}, y_{rail_R}. For the case of rigid rails the wheelset equations decouple from the rail force equations. The wheelset lateral excursion, y_w, equals the flange clearance, y_{fc}. If V_L, V_R, F_{lat}, and ψ_w are known, the following variables can be determined from equations (F-22) - (F-27): F_t, F_{NZLT}, F_{NZLF}, F_{NZR}, Ω, M_{yaw}.

The two-point contact model is used to determine the distribution of wheel/rail forces acting at the tread and flange contact points at the flanging wheel. For a wheelset negotiating a shallow curve corresponding to "mild" flanging, the forces at the tread contact point dominate. With tighter curves more severe flanging develops, and the wheel/rail forces gradually grow at the flange contact point and decrease at the tread contact point. This tradeoff in forces from tread to flange continues with degree curve until all forces act at the flange contact patch. This would occur for a wheelset negotiating an extremely tight curve, and would indicate the danger of derailment as the outer wheel rides high up against the flange. The single-point contact model is appropriate once contact occurs at only the flange contact patch.

A useful relationship between the work index, W_1, defined in Table 2.1, and the external forces and moments on the wheelset can be derived by manipulating the equilibrium equations or by writing a power balance equation, i.e.,

$$P_{in} = P_{out} \qquad \text{(F-30)}$$

$$P_{in} = V \left[F_t - \frac{M_{yaw}}{R} + \rho T_d\right] \qquad \text{(F-31)}$$

$$P_{out} = -VW_1 = -V \sum_{L,R}[F_{CPX_i}\xi_{x_i} + F_{CPY_i}\xi_{y_i} + M_{CP_i}\xi_{sp_i}] \qquad \text{(F-32)}$$

Noting from equations (F-12) and (F-20) that $F_t = -\sum_{L,R} F_{CXi}$, equation (F-30) yields:

$$W_1 = \sum_{L,R} F_{CXi} + \frac{M_{yaw}}{R} - \rho T_d \qquad \text{(F-33)}$$

Equation (F-33) is a useful check to ensure that a correct numerical solution of the equilibrium equations has been obtained.

In the full vehicle formulation the wheelset yaw moment is not an external moment and thus equation (F-33) reduces to that obtained in [9], i.e.,

$$W_1 = \sum_{L,R} F_{cxi} - \rho T_d \qquad \text{(F-34)}$$

F.1.4 Numerical Methods

The numerical solution procedures used to solve the coupled equilibrium equations of the single-point contact and two-point contact wheelset models are discussed in the following sections. The procedures assume that the wheelset lateral excursion and angle of attack, as well as the vertical loads acting on the left and right wheels are known. By solving the single-point equations, equilibrium values of lateral force and yaw moment are determined as functions of lateral excursion and angle of attack. For lateral excursions less than and larger than flange clearance this model is appropriate. For some profiles, this model is still appropriate at flange clearance, as was discussed above in Section F.1.2. For profiles with discontinuous jumps in the rolling radius-displacement and contact angle-displacement functions at flange clearance, the two-point contact model is applicable since it represents the fact that distinct tread and flange contact points exist simultaneously. Solution of the two-point equations gives the equilibrium yaw moment as a function of lateral force and angle of attack.

F.1.4.1 Single-Point Contact

For the case of rigid rails, the wheelset equilibrium conditions are specified by equations (F-12) through (F-17), and represent nonlinear algebraic equations coupled due to the fact that the normal and creep forces depend upon each other. First, equations (F-16), (F-20) and (F-21) are solved simultaneously for the wheel/rail contact forces and moments. Then, equations (F-12), (F-13) and (F-17) are used to define the drawbar force, the lateral force, and the yaw moment, respectively, needed to maintain the wheelset in equilibrium.

Two nested iteration loops are used to solve simultaneously the spin, vertical and roll equations. The inner loop balances the torque about the wheelset rolling axis by adjusting the spin perturbation rate, $\dot{\beta}$, to satisfy the spin equation. The outer loop adjusts the vertical component of creep force at each wheel to satisfy the sum and difference of the vertical and roll equations. This procedure is continued until vertical force convergence is achieved, as outlined in the flow chart in Figure F.10 and gives the equilibrium values of all contact forces and moments. The longitudinal, lateral, and yaw equations are then applied to solve for the equilibrium values of F_t, F_{lat}, and M_{yaw}, respectively.

A similar routine to solve the coupled wheelset equilibrium equations was developed by Sweet and Sivak [4] in which the two nested iteration loops are reversed. It should be noted that the creep forces are quite sensitive to small changes in the spin perturbation rate, $\dot{\beta}$.

To accommodate rail flexibility, the solution technique is to calculate the net lateral wheel force at each wheel assuming a rigid rail model. Then the lateral rail displacement at each wheel is calculated according to equations (F-10) and (F-11) and used to compute the effective lateral excursion at each wheel ($y_w - y_{rail_L}$, $y_w - y_{rail_R}$). These lateral excursions are used to update the wheel/rail contact geometry at the left and right contact points. The net lateral wheel force at each wheel is then computed, and the process is continued until convergence is achieved. Even with "soft" rail, convergence occurs rapidly, within several iterations.

F.1.4.2 Two-Point Contact

For some profiles, two-point contact occurs at the outer (left) wheel when the net lateral excursion equals the flange clearance. To

Figure F.10 Flow Chart for Wheelset Equilibrium with Rigid Rails: Single-Point Contact Model

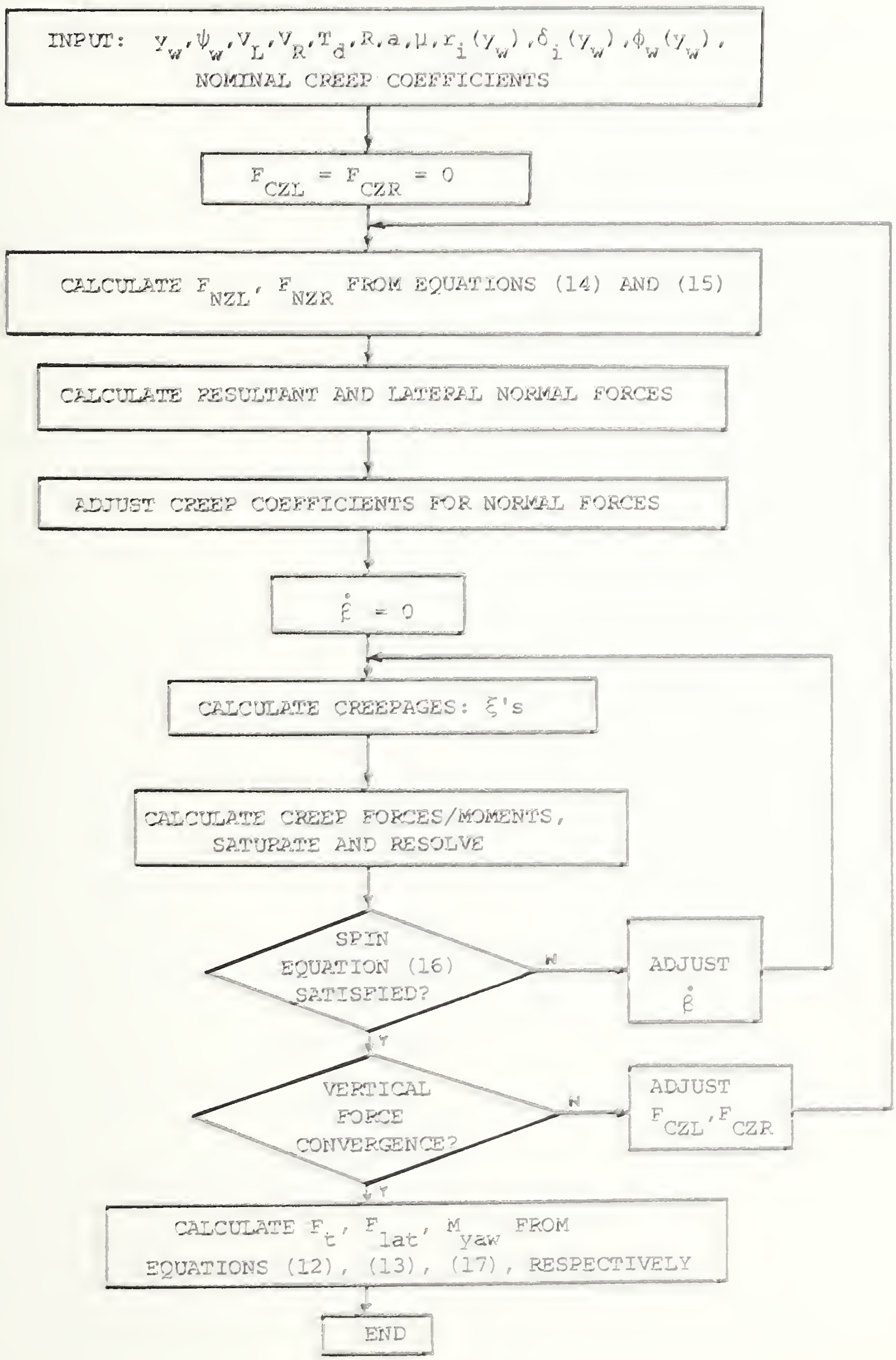

determine the wheel/rail forces and moments at the three contact patches, assuming rigid rails, four coupled equilibrium equations must be solved simultaneously: the spin, vertical, roll, and lateral equations. The lateral equation is then used to determine the equilibrium values of the contact forces and moments. This implies that the wheelset lateral force, derived from body and suspension forces, must be known. Once a solution to these coupled equations is determined, the wheelset yaw moment needed to satisfy yaw equilibrium is calculated from the yaw equation. In a vehicle, this yaw moment is provided by the suspension forces.

The four coupled equations are solved as before using two nested iteration loops as shown in Figure F.11. The inner loop adjusts the spin perturbation rate, $\dot{\beta}$, to satisfy the spin equation. The outer loop adjusts the vertical components of the creep forces at the tread and the flange of the outer wheel and the tread of the inner wheel to simultaneously satisfy the lateral equation and the sum and difference of the vertical and roll equations. Once vertical force convergence is achieved, equilibrium values of all contact forces and moments are known and the yaw equation is used to calculate the wheelset yaw moment which must act for equilibrium.

Rail flexibility is accounted for, as before, by solving first for the net lateral wheel forces assuming rigid rails. Equations (F-10) and (F-11) are used to calculate the lateral rail displacements, where $F_{YL} = F_{YLT} + F_{YLF}$ in equation (F-10). The net lateral excursion at the right, $y_w - y_{rail_R}$, is computed and used to update the right contact geometry. It is assumed that two-point contact at the left wheel is maintained and thus $y_w - y_{rail} = y_{fc}$. The net lateral wheel forces are then computed and the procedure is continued until convergence occurs.

Figure F.11 Flow Chart for Wheelset Equilibrium with Rigid Rails: Two-Point Contact Model

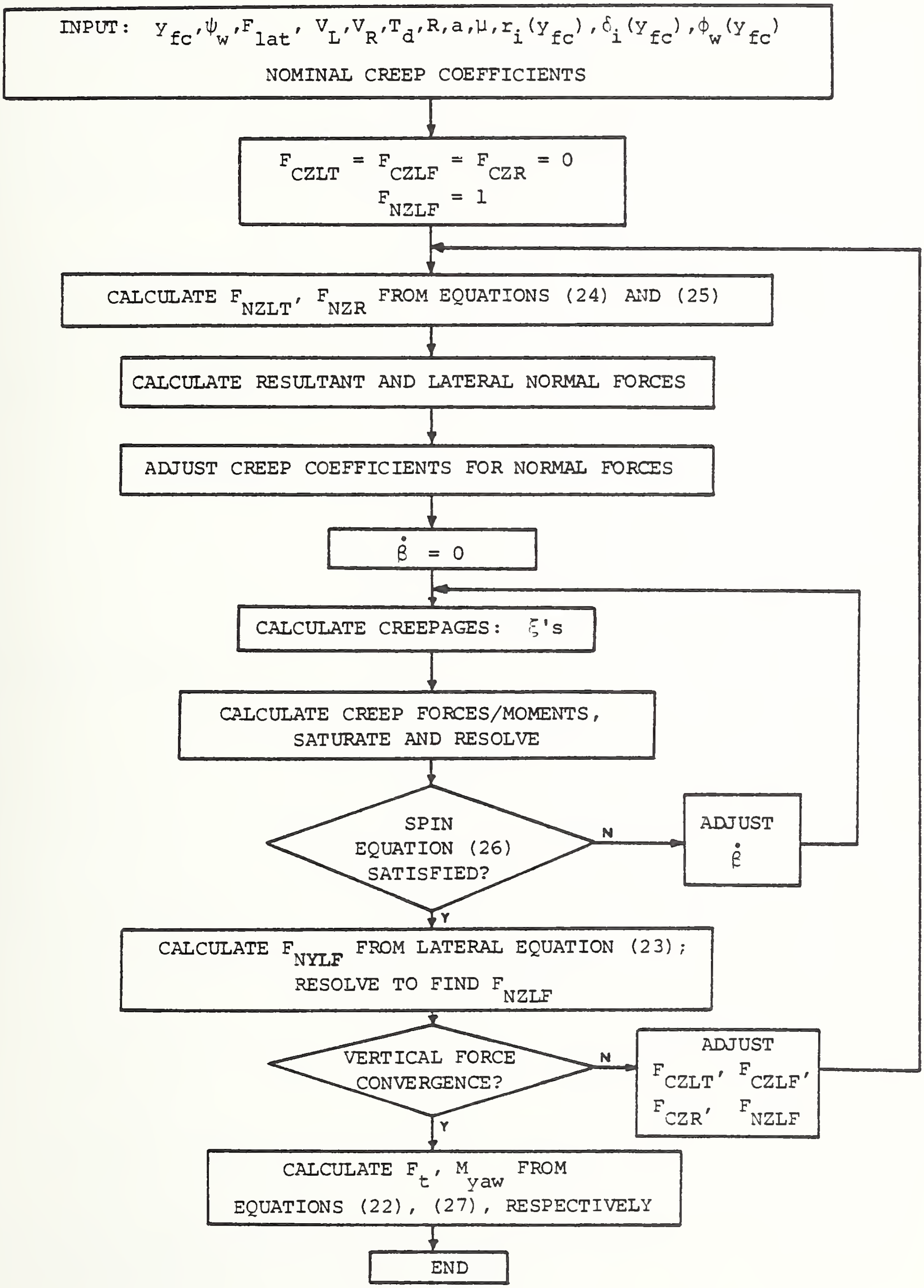

APPENDIX G

NONLINEAR CREEP FORCE MODEL

The "heuristic" nonlinear creep force model mentioned in the text is a modified Vermeulen-Johnson [33] formulation that includes the effect of spin creep.

The creep forces and moments are initially computed using the Kalker linear theory [31]. At each contact patch, the longitudinal and lateral components of creep force are:

$$\begin{aligned} F'_{CPX} &= -f_{33}\xi_x \\ F'_{CPY} &= -f_{11}\xi_y - f_{12}\xi_{SP} \end{aligned} \tag{G-1}$$

and the spin creep moment acting normal to the contact patch is:

$$M'_{CP} = f_{12}\xi_y - f_{22}\xi_{sp} \tag{G-2}$$

where ξ_x, ξ_y and ξ_{sp} are the longitudinal, lateral, and spin creepages*, respectively, in contact patch coordinates. The derivation of these creepages is a complicated application of kinematics [9, 37]. The creepages at the left and right contact patches are:

$$\xi_{x_L} = 1 + \frac{a}{R} - r_L\rho \tag{G-3}$$

$$\xi_{x_R} = 1 - \frac{a}{R} - r_R\rho \tag{G-4}$$

---

*The creepages are the relative velocities between the wheel and rail at the contact patch normalized by the nominal forward velocity.

$$\xi_{y_L} = -r_L \rho \, \psi_w \sec(\delta_L + \phi_w) \tag{G-5}$$

$$\xi_{y_R} = -r_R \rho \, \psi_w \sec(\delta_L + \phi_w) \tag{G-6}$$

$$\xi_{SP_L} = -\rho \sin(\delta_L + \phi_w) - \frac{1}{R} \cos\,(\delta_L + \phi_w) \tag{G-7}$$

$$\xi_{SP_R} = \rho \sin(\delta_R - \phi_w) - \frac{1}{R} \cos\,(\delta_R - \phi_w) \tag{G-8}$$

where $\rho \triangleq \frac{\Omega}{V} = \frac{1}{r_o} + \frac{\dot{\beta}}{V}$. (For the case of two-point contact at the left wheel, equations (G-3), (G-5) and (G-7) are the creepages at the left tread and left flange contact patches when the appropriate rolling radii and contact angles are used). The derivations of equations (G-3) - (G-8) make use of the expression for the shift of the contact patch due to ψ_w. The longitudinal shift of the contact patch is given in [5].

$$\Delta_{x_i} = r_i \psi_w \tan(\delta_i \pm \phi_w) \tag{G-9}$$

The creep coefficients f_{11}, f_{12}, f_{22} and f_{33} are functions of the wheel/rail geometry, material properties, and resulting normal load. They are computed according to Kalker's linear theory [31]. Typically these calculated values are reduced by 50% to account for discrepancies between field and laboratory test data due to contaminated rail conditions in the field.

The creep coefficients are functions of the normal load, N, calculated in the following way:

$$f_{11} = \left(\frac{N}{N_N}\right)^{2/3} f_{11_N}$$

$$f_{12} = \left(\frac{N}{N_N}\right) f_{12_N}$$

$$f_{22} = \left(\frac{N}{N_N}\right)^{4/3} f_{22_N} \qquad \text{(G-10)}$$

$$f_{33} = \left(\frac{N}{N_N}\right)^{2/3} f_{33_N}$$

where f_{ij_N} are the nominal values computed for the nominal normal load N_N and f_{ij} are the values for normal load, N.

The magnitude of the resultant creep force cannot exceed the amount of available adhesion, μN, at the wheel/rail contact interface. The creep force saturation is computed according to a modified Vermeulen-Johnson model in which a saturation coefficient is determined by:

$$\varepsilon = \begin{cases} \dfrac{\mu N}{F'_R}\left[\left(\dfrac{F'_R}{\mu N}\right) - \dfrac{1}{3}\left(\dfrac{F'_R}{\mu N}\right)^2 + \dfrac{1}{27}\left(\dfrac{F'_R}{\mu N}\right)^3\right] & \text{for } F'_R < 3\mu N \\[2ex] \dfrac{\mu N}{F'_R} & \text{for } F'_R > 3\mu N \end{cases} \qquad \text{(G-11)}$$

where the unlimited resultant creep force is:

$$F'_R = + \sqrt{(F'_{CPX})^2 + (F'_{CPY})^2} \qquad \text{(G-12)}$$

The saturated creep forces and moment are then given by:

$$F_{CPX} = \varepsilon F'_{CPX}$$

$$F_{CPY} = \varepsilon F'_{CPY} \qquad \text{(G-13)}$$

$$M_{CP} = \varepsilon M'_{CP}$$

APPENDIX H

STEADY-STATE CURVING FORMULATION FOR HALF CARBODY MODEL

The nonlinear wheelset model developed in Appendix F has been coupled to the rail vehicle through suspension elements. Two wheelsets are mounted via primary suspensions to the truck frame which is then attached via the secondary suspension to the carbody. The generic truck model developed in Section 2.2.4 is attached to the nonlinear wheelset models of Appendix F to formulate the nonlinear truck model. In addition to the wheel/rail nonlinearities described in Appendices F and G the suspension models have been extended to include nonlinear effects.

H.1 Half-Carbody Model

In order to reduce the numerical computations required to solve the steady-state curving problem a single truck/half carbody model has been developed. The model is used to solve separately for the front and rear truck solution. It is shown that a completely coupled full carbody solution can be obtained by iterating on the carbody yaw angle and secondary suspension lateral force; however, in general the decoupled solution is accurate due to the typically small secondary yaw torques.

H.1.1 Degrees of Freedom

Figures H.1 and H.2 show the degrees of freedom and vehicle geometry used in the model. The degrees of freedom used in the decoupled half-carbody model are:

y_{w1} (y_{w3}) • lateral excursion of the lead wheelset of the front (rear) truck with respect to the track centerline

ψ_{w1} (ψ_{w3}) • yaw displacement of the lead wheelset of the front (rear) truck with respect to a radial line passing halfway between the lead and trailing wheelsets. [This angle is related to the lead wheelset angle of attack, $(\psi_w)_1$, of Appendices F and G, by $\psi_{w1} = (\psi_w)_1 - b/R$].

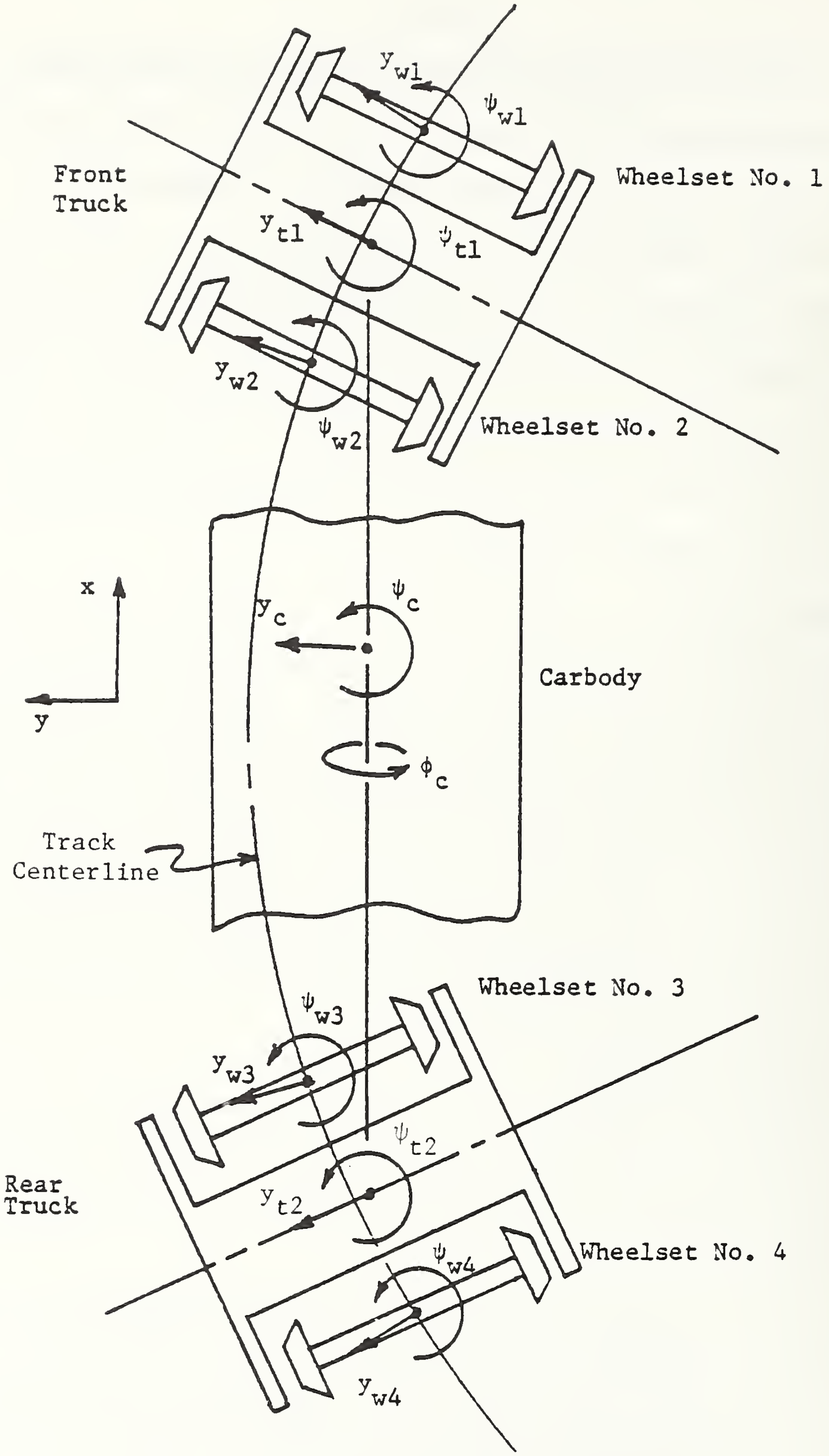

Figure H.1 Curving Model Components and Degrees of Freedom

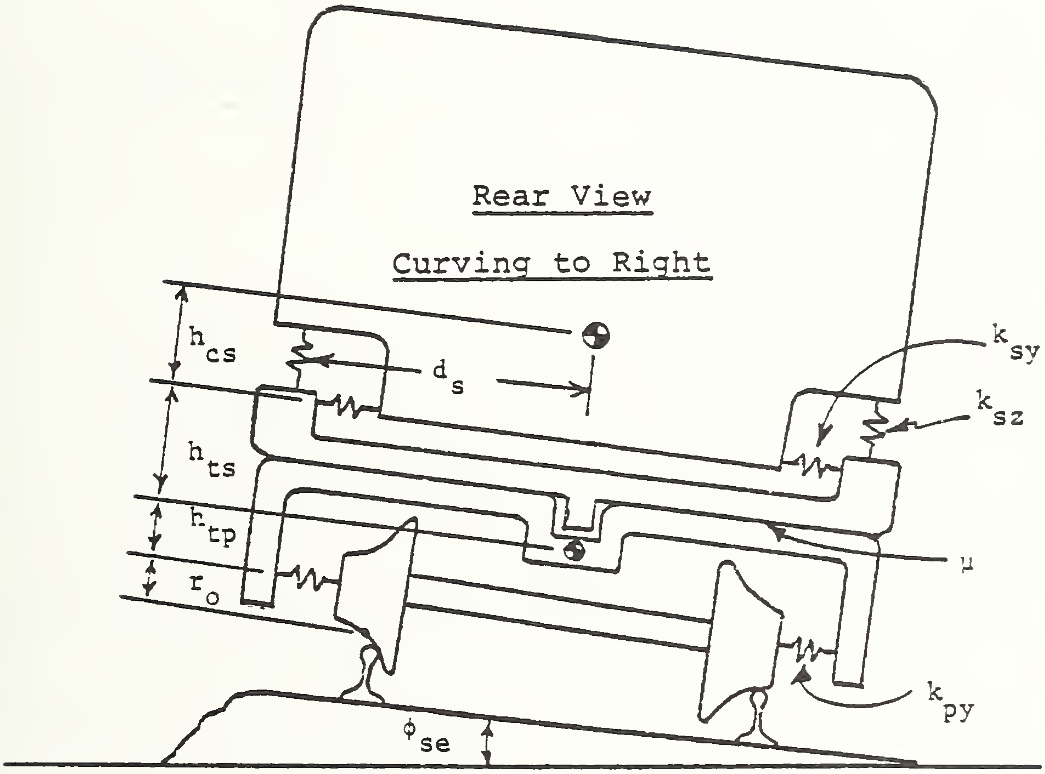

Figure H.2 Curving Model, Rear View

y_{t1} (y_{t2}) • lateral excursion of the front (rear) truck w.r.t. truck reference position (centered over track at lead and trailing wheelsets)

ψ_{t1} (ψ_{t2}) • yaw displacement of truck w.r.t. radial line passing halfway between lead and trailing wheelsets.

y_{w2} (y_{w4}) • lateral excursion of the trailing wheelset of the front (rear) truck w.r.t. track centerline

ψ_{w2} (ψ_{w4}) • yaw displacement of the trailing wheelset of the front (rear) truck w.r.t. radial line passing halfway between the lead and trailing wheelsets*

y_{cs} • lateral displacement of carbody secondary connection point relative to the truck reference position.

ϕ_c • roll displacement of the carbody w.r.t. track plane.

As shown in Figure H.1 the wheelset reference position is centered laterally on the track centerline, and square with the truck reference position in yaw. The truck reference position is centered laterally over the wheelsets at the front and rear wheelsets of the truck. The carbody reference position is centered laterally over the front and rear trucks at the secondary connection points. All degrees of freedom are in the track plane.

The model thus has eight degrees of freedom and is designed to represent a single truck with two wheelsets coupled to a half-carbody. The curving performance of either the front or the rear truck is computed separately under the assumption that coupling between the trucks is negligible for practical (typical) secondary suspensions. The assumption of decoupled trucks can then be checked as is described below.

When the torque between the front truck and the carbody is equal and opposite to the torque between the rear truck and the carbody, there is no coupling between the front and rear trucks. The assumption of decoupled trucks is then valid. However, when the secondary yaw torques between the front and

---

*This angle, ψ_{w2}, is related to the trailing wheelset angle of attack, $(\psi_w)_2$, by $\psi_{w2} = (\psi_w)_2 + b/R$.

rear trucks are not equal and opposite, the resulting coupling between the front and rear trucks can be solved iteratively. To account for coupling between the front and rear trucks in the single truck model, the following relations must be satisfied:

$$\psi_c = (y_{cs_1} - y_{cs_2}) / 2\ell_s \tag{H-1}$$

$$F_{sec_1} = (T_{car_1} + T_{car_2})/2\ell_s \tag{H-2}$$

$$F_{sec_2} = - F_{sec_1} \tag{H-3}$$

where ψ_c = carbody yaw displacement

y_{cs_i} = lateral displacement of carbody at secondary suspension connection point, ith truck

F_{sec_i} = external lateral force on carbody at secondary suspension connection point, ith truck

T_{car_i} = torque acting on carbody, ith truck

ℓ_s = half of spacing between trucks

Subscripts: 1 = front truck

2 = rear truck

The complete full vehicle (15 DOF) solution can be obtained by iterating on ψ_c and F_{sec} in successive runs of the single truck model. This is rarely necessary, though, because ψ_c and F_{sec} are usually negligibly small with regard to coupling between the two trucks.

H.1.2 Primary Suspension

The primary suspension is modelled as a system of nonlinear (piecewise linear) springs connected in parallel in the lateral and longitudinal directions, and linear springs connected in parallel in the vertical direction. The arrangement is shown in Figure H.3. The longitudinal and vertical springs yield effective yaw and roll stiffnesses, respectively. The lateral stiffness, k_{py}, is modelled as a trilinear spring, as shown in Figure H.4 representing a hardening spring. Significantly larger lateral forces are required to displace the suspension as the lateral stroke increases. Further, the effect of a "stop" at lateral clearance DY2 can be represented by making KPY3 much larger than KPY2. The longitudinal stiffness k_{px}, is modelled as a bilinear spring, as depicted in Figure H.5, and also represents a hardening spring. A "stop" can be modelled by making KPX2 much larger than KPX1.

To bypass numerical convergence difficulties which can result from a very soft primary longitudinal suspension, an auxiliary longitudinal suspension is introduced. This is shown in Figure H.6 where an auxiliary primary longitudinal suspension k_{pxaux} is placed in parallel with the existing primary longitudinal stiffness k_{px} and is connected between the wheelset and the truck frame or between the wheelset and ground. An imposed extension δ_{aux} in series with a stiff auxiliary stiffness k_{pxaux} is used to simulate a longitudinal clearance while maintaining a stiff primary suspension. A solution is obtained when an extension δ_{aux} is selected such that all the force is transmitted through the primary stiffness k_{px} and no force is transmitted through the auxiliary stiffness k_{pxaux}. When this occurs the longitudinal suspension is provided solely by the soft longitudinal stiffness k_{px}.

H.1.3 Secondary Suspension

The truck frame is connected to the carbody through the secondary suspension system in the lateral, yaw and vertical directions. Connection

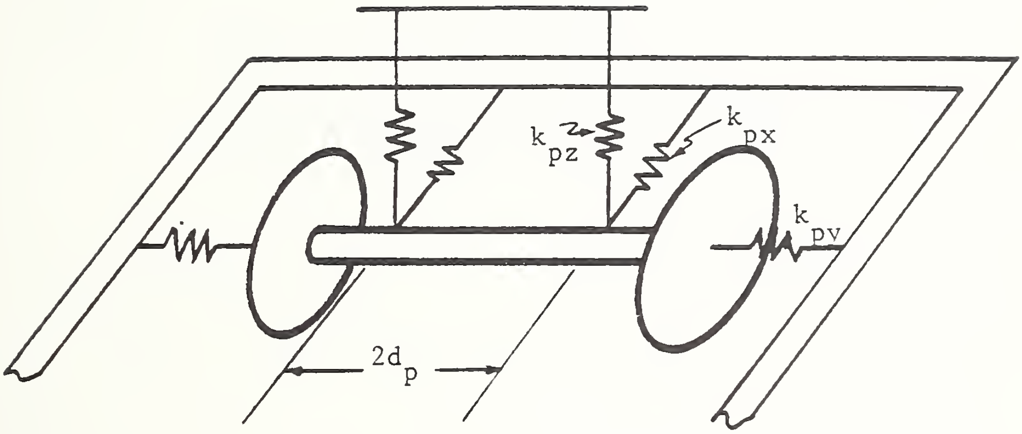

Figure H.3 Primary Suspension Stiffnesses

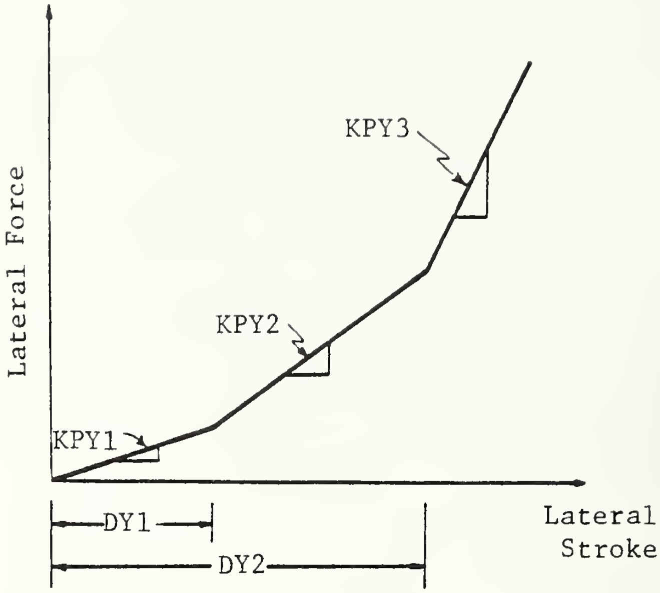

Figure H.4 Force-Displacement Characteristic For Primary Lateral Stiffness Model.

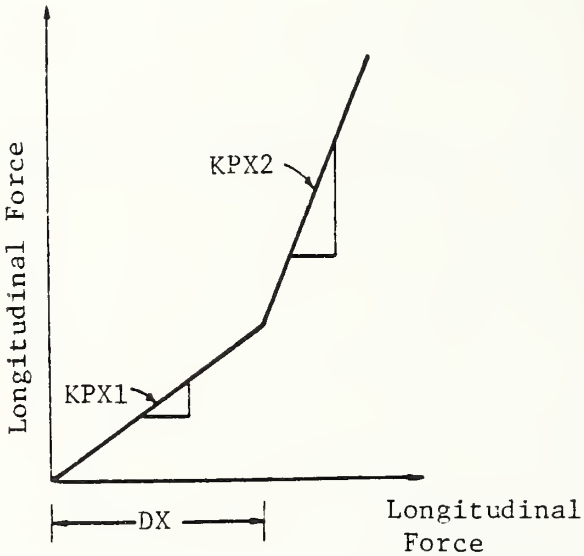

Figure H.5 Force-Displacement Characteristic for Primary Longitudinal Stiffness Model.

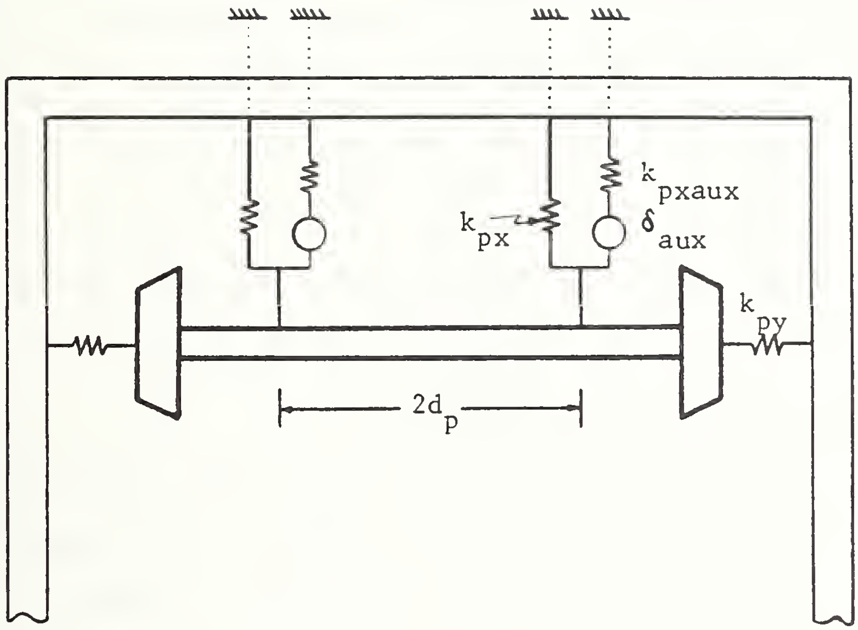

Figure H.6 Primary Suspension Arrangement with Auxiliary Suspension.

in the longitudinal direction is provided by anchor rods between the carbody and each bolster, shown in Figure C.2. Each bolster is fastened to a truck frame by a center pin so that it can rotate with respect to the truck frame. With the assumption of rigid anchor rods, each bolster follows the carbody motion in yaw and the truck motion in the lateral direction.

The secondary suspension model consists of linear springs connected in parallel in the lateral and vertical directions, two per truck for each direction. The secondary vertical stiffness k_{sz} provides roll stiffness between the truck and the carbody. Because the vertical directions are not included in the curving model as degrees of freedom, the effect of the secondary vertical stiffness k_{sz} is equivalent to a roll spring between the carbody and each truck frame:

$$k_{roll} = 2d_s^2 k_{sz} \tag{H-4}$$

In yaw, the secondary suspension consists of anchor rods between the bolster and carbody which act in series with friction pads between the bolster and truck frame, as described above. The torque vs. yaw stroke characteristic resulting from this series arrangement is shown in Figure H.7. The linear stiffness is the effective yaw stiffness of the anchor rod bushings and related components. The breakaway torque T_B results from the Coulomb sliding force between the friction pads. In the curving analysis it is assumed that the maximum torque, T_B, is established between the carbody and the truck frame. This torque is maintained regardless of any increase in the relative displacement between the two components.

H.2 Vehicle Equilibrium Conditions

The vehicle steady-state curving equations are statements of simultaneous lateral force and yaw moment equilibrium of the wheelsets, truck, and (half)

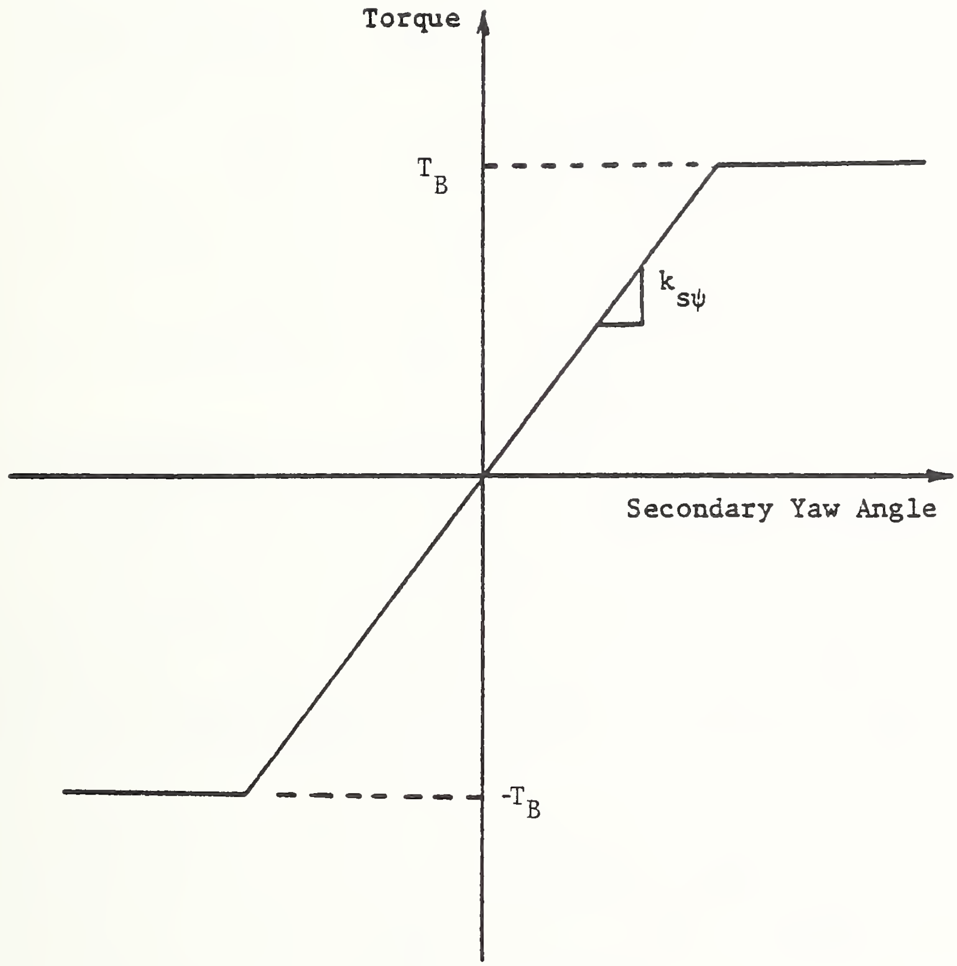

Figure H.7 Torque vs. Stroke Characteristic of the Secondary Yaw Suspension carbody. The following vehicle equilibrium conditions apply:

1.	Lateral Force Equilibrium	Lead Wheelset
2.	Yaw Moment Equilibrium	
3.	Lateral Force Equilibrium	Trailing Wheelset
4.	Yaw Moment Equilibrium	
5.	Lateral Force Equilibrium	Truck
6.	Yaw Moment Equilibrium	
7.	Lateral Force Equilibrium	Carbody
8.	Yaw Moment Equilibrium	
9.	Roll Moment Equilibrium	

Conditions (8) and (9) are decoupled conditions. Condition (8) is related to the interaction of the front and rear trucks in the analysis of a full vehicle as expressed in relations (H-1) - (H-3). Carbody roll is a decoupled degree of freedom and is discussed in Section H.3.1. Conditions (1) through (7) are coupled, and represent the set of nonlinear algebraic equations which must be solved.

The forces and moments acting upon the vehicle can be characterized as internal arising from suspension and external arising from cant deficiency, track curvature, forced-steering (from carbody yaw), and imposed wheelset yaw offsets. Thus, the equilibrium equations can be cast as follows:

$$\underline{\bar{K}}\ \underline{X} = \underline{B} \tag{H-5}$$

where the matrix produce $\underline{\bar{K}}\ \underline{X}$ represents a vector of internal suspension forces and moments and $\underline{B}$ represents the vector of all external forces and moments. The elements of the $\underline{B}$ vector due to cant deficiency and track curvature are:

$$b_1 = W_w \phi_d + F_{lat_1}$$

$$b_2 = M_{yaw_1}$$

$$b_3 = W_w \phi_d + F_{lat_2}$$

$$b_4 = M_{yaw_2} \qquad \text{(H-6)}$$

$$b_5 = W_t \phi_d$$

$$b_6 = \pm T_B$$

$$b_7 = F_{buff}$$

where F_{lat_1} and M_{yaw_1} represent the lateral force and yaw moment, respectively, acting on the leading (i = 1) and trailing (i = 2) wheelsets. For the case of a wheelset in single-point contact at both the left and right wheels, the lateral force and yaw moment are calculated as part of the analyses for the wheel/rail forces (i.e., in the wheelset subroutines). They are both functions of the track curvature. The sixth element of the $\underline{B}$ vector is the breakaway torque, T_b. The sign is positive for analysis of the leading (front) truck and negative for the trailing (rear) truck.

The matrix product $\bar{\underline{K}}\ \underline{X}$ is composed of a stiffness matrix $\bar{\underline{K}}$ due to primary and secondary suspensions, and a geometry state vector $\underline{X}$. When nonlinear suspension representations are used $\bar{\underline{K}}$ is a function of the vehicle displacement vector $\underline{X}$. The elements of $\underline{X}$ are:

$$
\begin{aligned}
X_1 &= y_{w1} \\
X_2 &= \psi_{w1} \\
X_3 &= y_{w2} \\
X_4 &= \psi_{w2} \\
X_5 &= y_T \\
X_6 &= \psi_T \\
X_7 &= y_{cs}
\end{aligned}
\tag{H-7}
$$

The seventh element represents the lateral excursion of the carbody at the secondary connection point.

For the case of the leading wheelset in two-point contact at the flanging (left) wheel, $X_1 = y_{w1}$ is fixed at the flange clearance (assuming rigid rails) and the lateral force, F_{lat_1}, becomes a state variable. The two-point contact wheelset subroutine requires F_{lat_1} as an input.

To account for initial wheelset misalignments, equation (H-5) can be modified to reflect the new "resting" (zero suspension force) state of the suspensions. The equilibrium equations can be written as

$$\underline{\bar{K}}\,(\underline{X} - \underline{X}_m) = \underline{B} \tag{H-8}$$

where $\underline{X}_m$ represents a misaligned geometry state vector. For radial and lateral misalignment of each wheelset, the elements of the $\underline{X}_m$ vector are:

$$X_{1m} = Y_{w1m}$$

$$X_{2m} = \psi_{w1m}$$

$$X_{3m} = Y_{w2m} \tag{H-9}$$

$$X_{4m} = \psi_{w2m}$$

$$X_{5m} = X_{6m} = X_{7m} = 0$$

where the first four elements are the initial lateral and yaw misalignments of the leading and trailing wheelsets, shown in Figure H.8.

H.2.1 Coupled Vehicle Equilibrium Equations

This section lists the seven coupled equilibrium equations for the half-carbody model assuming no wheelset misalignments. The following notation is used:

$$\pm = \begin{cases} + \text{ Front Truck} \\ - \text{ Rear Truck} \end{cases} \qquad \alpha = \begin{cases} 1 \text{ Truck Reference} \\ 0 \text{ Ground Reference} \end{cases}$$

$$\text{Subscript} = \begin{cases} 1 \text{ Lead Wheelset of Truck} \\ 2 \text{ Trailing Wheelset of Truck} \end{cases}$$

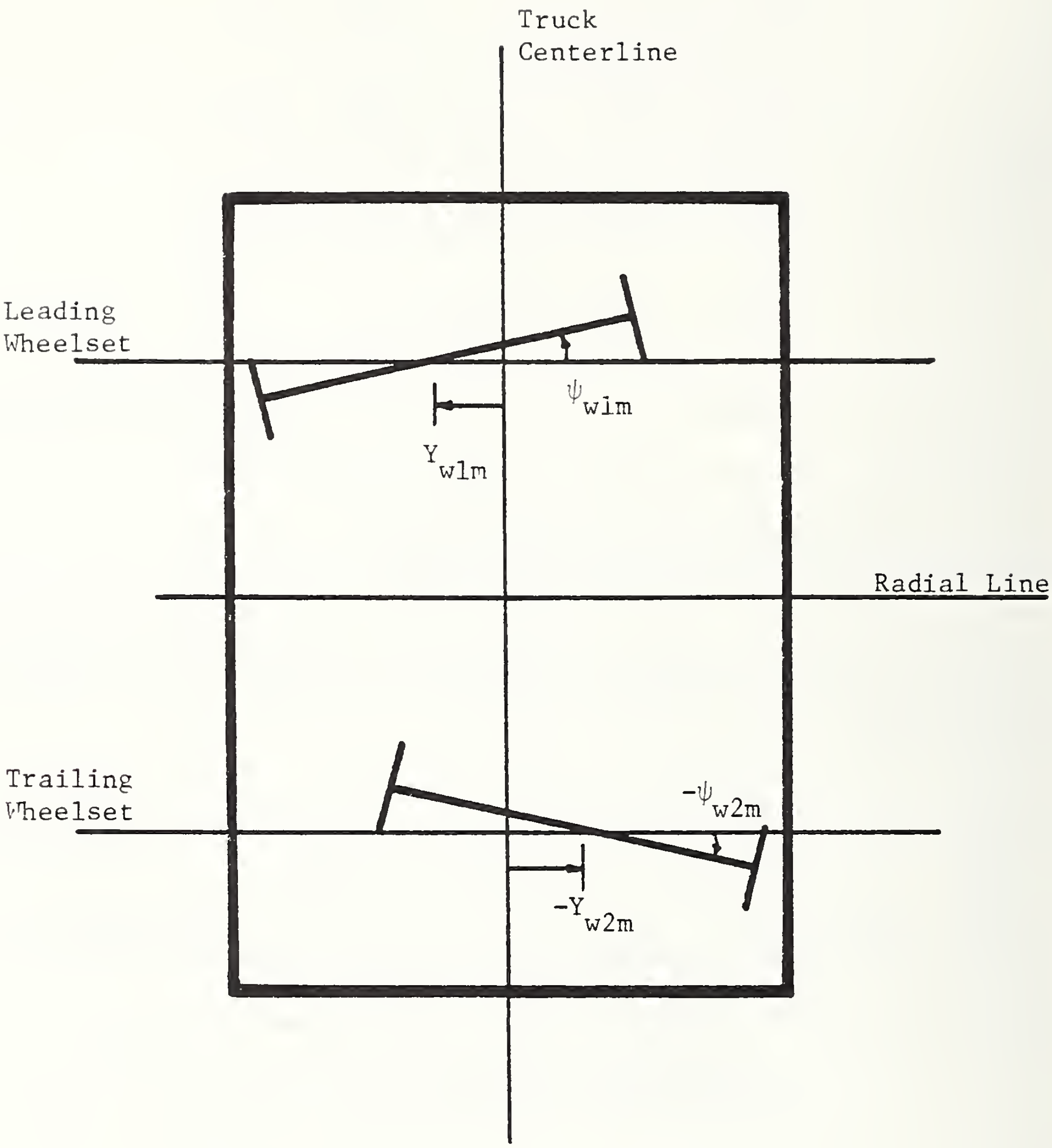

Figure H.8 Wheelset Misalignments

Leading Wheelset Lateral

$$
\begin{aligned}
& [-2k_{py_1} - \left\{ G_3 \pm \left(\frac{G_2+G_6}{b}\right)\right\}^2 (k_{b2} + k_{b3}) - (H_1 - H_3 + 1)^2 (k_{s2} + k_{s3}) - k_{s3}] y_{w1} \\
+ & [\left\{(G_3 \pm \left(\frac{G_2+G_6}{b}\right)\right\} \left\{1 \mp (G_1+G_5)\right\} (k_{b2} + k_{b3}) + b(H_1 + H_3 + 1)(k_{s2} + k_{s3}) + bk_{s3}] \psi_{w1} \\
+ & [-\left\{G_3^2 - \left(\frac{G_2+G_6}{b}\right)^2\right\} (k_{b2} + k_{b3}) - \left\{(H_1 + H_3)^2 - 1\right\} (k_{s2} + k_{s3}) - k_{s3}] y_{w2} \\
+ & [\left\{-G_3 \mp \left(\frac{G_2+G_6}{b}\right)\right\} \left\{(1 \pm (G_1 + G_5)\right\} (k_{b2} + k_{b3}) + b(H_1 + H_3 + 1)(k_{s2} + k_{s3}) - bk_{s3}] \psi_{w2} \\
+ & [2k_{py_1} + 2G_3 \left\{G_3 \pm \left(\frac{G_2+G_6}{b}\right)\right\} (k_{b2} + k_{b3}) - 2(H_2 - H_3)(H_1 + H_3 + 1)(k_{s2} + k_{s3}) + 2k_{s3}] y_T \\
+ & [2k_{py_1} b + 2(G_4 - G_5 - G_6) \left\{\mp G_3 - \left(\frac{G_2+G_6}{b}\right)\right\} (k_{b2} + k_{b3})] \psi_T \\
+ & [2(H_1 + H_2)(H_1 + H_3 + 1)(k_{s2} + k_{s3})] y_{cs} \\
+ & [2(G_1 + G_2 + G_4) \left\{\pm G_3 + \left(\frac{G_2+G_6}{b}\right)\right\} (k_{b2} + k_{b3})] \left(\Psi_c \pm \frac{\ell s}{R}\right) \\
+ & W_w \phi_d + F_{lat_1} = 0 \qquad \text{(H-10)}
\end{aligned}
$$

Leading Wheelset Yaw

$$
\begin{aligned}
& \left[\left\{ G_3 \pm \left(\frac{G_2+G_6}{b}\right) \right\} \left\{ 1 \mp (G_1 + G_5) \right\} (k_{b2} + k_{b3}) + b(H_1 + H_3 + 1)(k_{s2} + k_{s3}) + bk_{s3} \right] y_{w1} \\
& + \left[-2d_p^2 \left(k_{px_1} + k_{pxaux}\right) - (G_1 + G_5 \mp 1)^2 (k_{b2} + k_{b3}) - b^2(k_{s2} + k_{s3}) - k_{b3} - b^2 k_{s3} \right] \Psi_{w1} \\
& + \left[\left\{ G_3 \mp \left(\frac{G_2+G_6}{b}\right) \right\} \left\{ 1 \mp (G_1 + G_5) \right\} (k_{b2} + k_{b3}) + b(H_1 + H_3 - 1)(k_{s2} + k_{s3}) + bk_{s3} \right] y_{w2} \\
& + \left[\left\{ 1 - (G_1 + G_5)^2 \right\} (k_{b2} + k_{b3}) - b^2(k_{s2} + k_{s3}) - k_{b3} + b^2 k_{s3} \right] \Psi_{w2} \\
& + \left[2G_3 \left\{ -1 \pm (G_1 + G_5) \right\} (k_{b2} + k_{b3}) + 2b(H_2 - H_3)(k_{s2} + k_{s3}) - 2bk_{s3} \right] y_T \\
& + \left[2d_p^2 \left(k_{px_1} + k_{pxaux}\, \alpha\right) + 2(G_4 - G_5 - G_6) \left\{ \pm 1 - (G_1 + G_5) \right\} (k_{b2} + k_{b3}) + 2k_{b3} \right] \Psi_T \\
& + \left[-2b(H_1 + H_2)(k_{s2} + k_{s3}) \right] y_{cs} \\
& + \left[2(G_1 + G_2 + G_4)(G_1 + G_5 \mp 1)(k_{b2} + k_{b3}) \right] \left(\psi_c \pm \frac{\ell s}{R}\right) \\
& + 2\delta_{aux_1} d_p^2 k_{pxaux} + M_{yaw_1} = 0 \qquad \text{(H-11)}
\end{aligned}
$$

Trailing Wheelset Lateral

$$
\begin{aligned}
&\Big[-\Big\{G_3^2 - \Big(\frac{G_2+G_6}{b}\Big)^2\Big\}(k_{b2} + k_{b3}) - \Big\{(H_1 + H_3)^2 - 1\Big\}(k_{s2} + k_{s3}) - k_{s3}\Big]y_{w1} \\
&+ \Big[\Big\{G_3 \mp \Big(\frac{G_2+G_6}{b}\Big)\Big\}\Big\{1 \mp (G_1 + G_5)\Big\}(k_{b2} + k_{b3}) + b(H_1 + H_3 - 1)(k_{s2} + k_{s3}) + bk_{s3}\Big]\Psi_{w1} \\
&+ \Big[-2k_{py_2} - \Big\{G_3 \mp \Big(\frac{G_2+G_6}{b}\Big)\Big\}^2 (k_{b2} + k_{b3}) - (H_1 + H_3 - 1)^2 (k_{s2} + k_{s3}) - k_{s3}\Big]y_{w2} \\
&+ \Big[\Big\{-G_3 \pm \Big(\frac{G_2+G_6}{b}\Big)\Big\}\Big\{1 \pm (G_1 + G_5)\Big\}(k_{b2} + k_{b3}) + b(H_1 + H_3 - 1)(k_{s2} + k_{s3}) - bk_{s3}\Big]\Psi_{w2} \\
&+ \Big[2k_{py_2} + 2G_3\Big\{G_3 \mp \Big(\frac{G_2+G_6}{b}\Big)\Big\}(k_{b2} + k_{b3}) - 2(H_2 - H_3)(H_1 + H_3 - 1)(k_{s2} + k_{s3}) + 2k_{s3}\Big]y_T \\
&+ \Big[-2k_{py_2} b + 2(G_4 - G_5 - G_6)\Big\{\mp G_3 + \Big(\frac{G_2+G_6}{b}\Big)\Big\}(k_{b2} + k_{b3})\Big]\Psi_T \\
&+ \Big[2(H_1 + H_2)(H_1 + H_3 - 1)(k_{s2} + k_{s3})\Big]y_{cs} \\
&+ \Big[2(G_1 + G_2 + G_4)\Big\{\pm G_3 - \Big(\frac{G_2+G_6}{b}\Big)\Big\}(k_{b2} + k_{b3})\Big]\Big(\Psi_c \pm \frac{\ell s}{R}\Big) \\
&+ W_w\phi_d + F_{lat_2} = 0 \qquad \text{(H-12)}
\end{aligned}
$$

Trailing Wheelset Yaw

$$
\begin{aligned}
& [\left\{ - G_3 \mp \left(\frac{G_2+G_6}{b}\right) \right\} \left\{ 1 \pm (G_1 + G_5) \right\} (k_{b2} + k_{b3}) + b(H_1 + H_3 + 1)(k_{s2} + k_{s3}) - bk_{s3}] y_{w1} \\
+ & [\left\{ 1 - (G_1 + G_5)^2 \right\} (k_{b2} + k_{b3}) - b^2(k_{s2} + k_{s3}) - k_{b3} + b^2 k_{s3}] \Psi_{w1} \\
+ & [\left\{ -G_3 \pm \left(\frac{G_2+G_6}{b}\right) \right\} \left\{ 1 \pm (G_1 + G_5) \right\} (k_{b2} + k_{b3}) + b(H_1 + H_3 - 1)(k_{s2} + k_{s3}) - bk_{s3}] y_{w2} \\
+ & [-2d_p^2 (k_{px_2} + k_{pxaux}) - \left\{ 1 \pm (G_1 + G_5) \right\}^2 (k_{b2} + k_{b3}) - b^2(k_{s2} + k_{s3}) - k_{b3} - b^2 k_{s3}] \Psi_{w2} \\
+ & [2G_3 \left\{ 1 \pm (G_1 + G_5) \right\} (k_{b2} + k_{b3}) + 2b(H_2 - H_3)(k_{s2} + k_{s3}) + 2bk_{s3}] y_T \\
+ & [2d_p^2 (k_{px_2} + k_{pxaux}\alpha) + 2(G_4 - G_5 - G_6) \left\{ \mp 1 - (G_1 + G_5) \right\} (k_{b2} + k_{b3}) + 2k_{b3}] \Psi_T \\
+ & [-2b(H_1 + H_2)\ (k_{s2} + k_{s3})]\ y_{cs} \\
+ & [2(G_1 + G_2 + G_4)(G_1 + G_5 \pm 1)\ (k_{b2} + k_{b3})]\ \left(\Psi_c \pm \frac{\ell s}{R}\right) \\
+ & 2\delta_{aux_2}\ d_p^2\ k_{pxaux} + M_{yaw_2} \quad = \quad 0
\end{aligned}
\qquad \text{(H-13)}
$$

Truck Lateral

$$[2k_{py_1} + 2G_3 \left\{ G_3 \pm \left(\frac{G_2+G_6}{b}\right) \right\} (k_{b2} + k_{b3}) - 2(H_2 - H_3)(H_1 + H_3 + 1)(k_{s2} + k_{s3}) + 2k_{s3}]y_{w1}$$

$$+ \ [2G_3 \left\{ -1 \pm (G_1 + G_5) \right\} (k_{b2} + k_{b3}) + 2b(H_2 - H_3)(k_{s2} + k_{s3}) - 2bk_{s3}]\Psi_{w1}$$

$$+ \ [2k_{py_2} + 2G_3 \left\{ G_3 \mp \left(\frac{G_2+G_6}{b}\right) \right\} (k_{b2} + k_{b3}) - 2(H_2 - H_3)(H_1 + H_3 - 1)(k_{s2} + k_{s3}) + 2k_{s3}]y_{w2}$$

$$+ \ [2G_3 \left\{ 1 \pm (G_1 + G_5) \right\} (k_{b2} + k_{b3}) + 2b(H_2 - H_3)(k_{s2} + k_{s3}) + 2bk_{s3}]\Psi_{w2}$$

$$+ \ [-2k_{py_1} - 2k_{py_2} - 2k_{sy} - 4G_3^2 (k_{b2} + k_{b3}) - 4(H_2 - H_3)^2(k_{s2} + k_{s3}) - 4k_{s3}]y_T$$

$$+ \ [-2k_{py_1} b + 2k_{py_2} b \pm 4G_3(G_4 - G_5 - G_6)(k_{b2} + k_{b3})]\Psi_T$$

$$+ \ [2k_{sy} + 4(H_1 + H_2)(H_2 - H_3)(k_{s2} + k_{s3})]y_{cs}$$

$$+ \ [\mp 4G_3 (G_1 + G_2 + G_4)(k_{b2} + k_{b3})] \left(\Psi_c \pm \frac{\ell s}{R}\right)$$

$$+ W_T\phi_d = 0 \qquad \text{(H-14)}$$

Truck Yaw

$$
\begin{aligned}
&[2bk_{py_1} + 2\left\{\mp G_3 - \left(\frac{G_2+G_6}{b}\right)\right\}(G_4 - G_5 - G_6)(k_{b2} + k_{b3})]y_{w1} \\
&+ [2d_p^2(k_{px_1} + k_{pxaux}\alpha) + 2(G_4 - G_5 - G_6)\left\{\pm 1 - (G_1 + G_5)\right\}(k_{b2} + k_{b3}) + 2k_{b3}]\Psi_{w1} \\
&+ [-2bk_{py_2} + 2\left\{\mp G_3 + \left(\frac{G_2+G_6}{b}\right)\right\}(G_4 - G_5 - G_6)(k_{b2} + k_{b3})]y_{w2} \\
&+ [2d_p^2(k_{px_2} + k_{pxaux}\alpha) + 2(G_4 - G_5 - G_6)\left\{\mp 1 - (G_1 + G_5)\right\}(k_{b2} + k_{b3}) + 2k_{b3}]\Psi_{w2} \\
&+ [-2k_{py_1}b + 2k_{py_2}b \pm 4G_3(G_4 - G_5 - G_6)(k_{b2} + k_{b3})]y_T \\
&+ [-2d_p^2(k_{px_1} + k_{px_2} + 2k_{pxaux}\alpha) - 2b^2(k_{py_1} + k_{py_2}) - 4(G_4 - G_5 - G_6)^2(k_{b2} + k_{b3}) - 4k_{b3}]\Psi_T \\
&+ [4(G_4 - G_5 - G_6)(G_1 + G_2 + G_4)(k_{b2} + k_{b3})](\Psi_c \pm \frac{\ell s}{R}) \\
&-2(\delta_{aux_1} + \delta_{aux_2})d_p^2 k_{pxaux}\alpha \pm T_B = 0 \qquad \text{(H-15)}
\end{aligned}
$$

Carbody Lateral At Secondary

$$
\begin{aligned}
&[2(H_1 + H_2)(H_1 + H_3 + 1)\ (k_{s2} + k_{s3})]y_{w1} \\
&+ [-2b(H_1 + H_2)\ (k_{s2} + k_{s3})]\Psi_{w1} \\
&+ [2(H_1 + H_2)\ (H_1 + H_3 - 1)\ (k_{s2} + k_{s3})]y_{w2} \\
&+ [-2b(H_1 + H_2)\ (k_{s2} + k_{s3})]\Psi_{w2} \\
&+ [2k_{sy} + 4(H_1 + H_2)\ (H_2 - H_3)\ (k_{s2} + k_{s3})]y_T \\
&+ [-2k_{sy} - 4(H_1 + H_2)^2\ (k_{s2} + k_{s3})]y_{cs} \\
&+ W_c\phi_d/2 + F_{buff} + F_{sec} = 0 \qquad \text{(H-16)}
\end{aligned}
$$

H.3 Numerical Methods

The vehicle steady-state curving model is used to determine the displaced steady-state geometry and wheel/rail forces of a vehicle on a constant radius curve. The steady-state curving analysis assumes that the vehicle is dynamically stable.

H.3.1 Carbody Roll Calculation

Carbody roll is a decoupled degree of freedom. It can be calculated by considering a static moment equilibrium in the roll direction of the carbody about the secondary connection point. The calculation accounts for the following influences: (1) carbody cant deficiency forces; (2) lateral buff forces; and (3) the inverted pendulum effect of carbody weight. Figure H.9 shows the forces acting on the secondary of a truck. Expressions can be derived for: (1) the external roll moment about the secondary connection point(s) due to cant deficiency forces, $W_c\phi_d$, and buff, F_{buff} and (2) the restoring moment due to the secondary vertical stiffness, k_{sz}, and the inverted pendulum effect. Equating these moment expressions yields the relation for the carbody roll:

$$\phi_c = \frac{-\frac{W_c}{2}\phi_d h_{cs} - F_{buff} h_b}{2k_{sz} d_s^2 - \frac{W_c}{2} h_{cs}} \tag{H-17}$$

where $h_b = h_c - h_{ts} - h_{tp} - r_o$

H.3.2 Vertical Wheel Load Calculation

The net vertical loads acting on the left and right wheels, V_L and V_R, respectively, are needed to solve the wheelset equilibrium equations. These vertical wheel loads are computed by considering the static

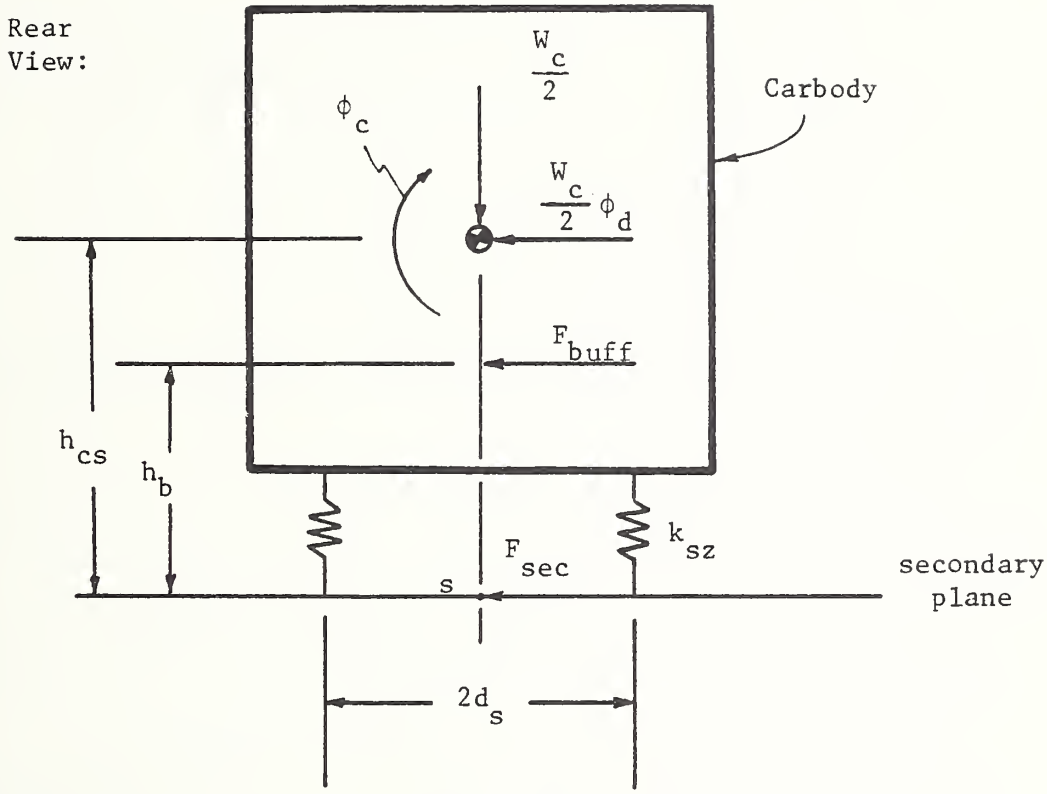

Figure H.9 Forces Acting at Secondary Suspension of a Truck

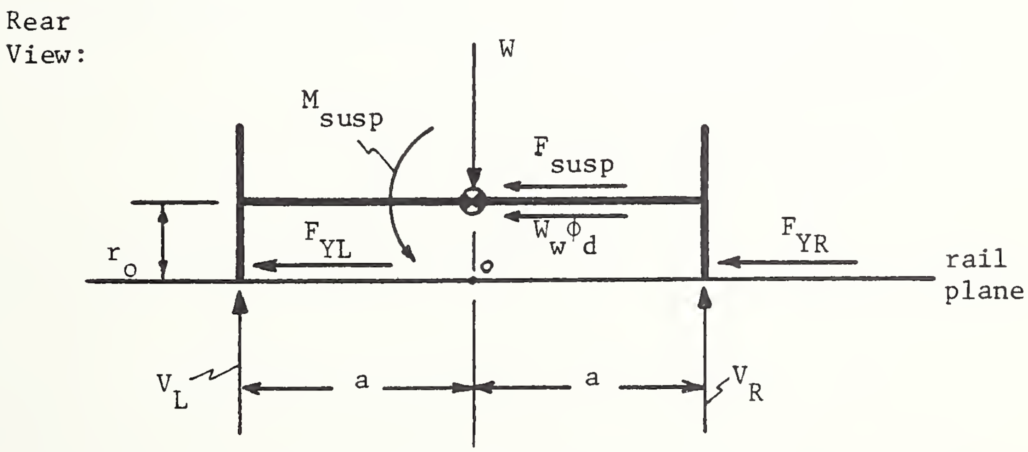

Figure H.10 Wheelset Free-Body Diagram, Rear View equilibrium of each wheelset in the roll direction. Figure H.10 shows the rear view of a wheelset free-body diagram. Expressions for the vertical wheel loads are:

$$V_L = V_{avg} + \Delta V \tag{H-18}$$

$$V_R = V_{avg} - \Delta V \tag{H-19}$$

where the average vertical wheel load, V_{avg}, is due to wheelset, truck, and carbody weight:

$$V_{avg} = \frac{W_w}{2} + \frac{W_t}{4} + \frac{W_c}{8} \tag{H-20}$$

and the vertical load shift, ΔV, arises from wheelset suspension force and moment loading. Summing moments about point 0 in Figure H.11 yields an expression for ΔV:

$$\Delta V = \frac{1}{2a} [M_{susp} + r_o (F_{susp} + W_w \phi_d)] \tag{H-21}$$

The suspension force acting on each wheelset, F_{susp} is due to primary lateral stiffness, k_{py} and to any interaxle shear stiffness, k_{s2}. Assuming no initial wheelset misalignments, it is given by

$$\begin{aligned} F_{susp} = \; & 2k_{py}(y_t + b\psi_t - y_{w1}) \\ & + k_{s2} \{ y_{w2} - y_{w1} + b(\psi_{w1} + \psi_{w2}) + \delta_{Fs} \} \end{aligned} \tag{H-22}$$

for the leading wheelset, and by

$$\begin{aligned} F_{susp} = \; & 2\, k_{py} \;(y_t + b\psi_t - y_{w2}) \\ & - k_{s2} \{ y_{w2} - y_{w1} + b(\psi_{w1} + \psi_{w2}) + \delta_{Fs} \} \end{aligned} \tag{H-23}$$

for the trailing wheelset, where δ_{Fs} represents the additional suspension stroke imposed by forced steering.

The suspension moment, M_{susp} is obtained by performing a static moment balance about the wheelset center of gravity. From Figure H.11,

$$M_{susp} = \frac{W_c}{4}\phi_d \;(h_{cs} + h_{ts} + h_{tp})$$

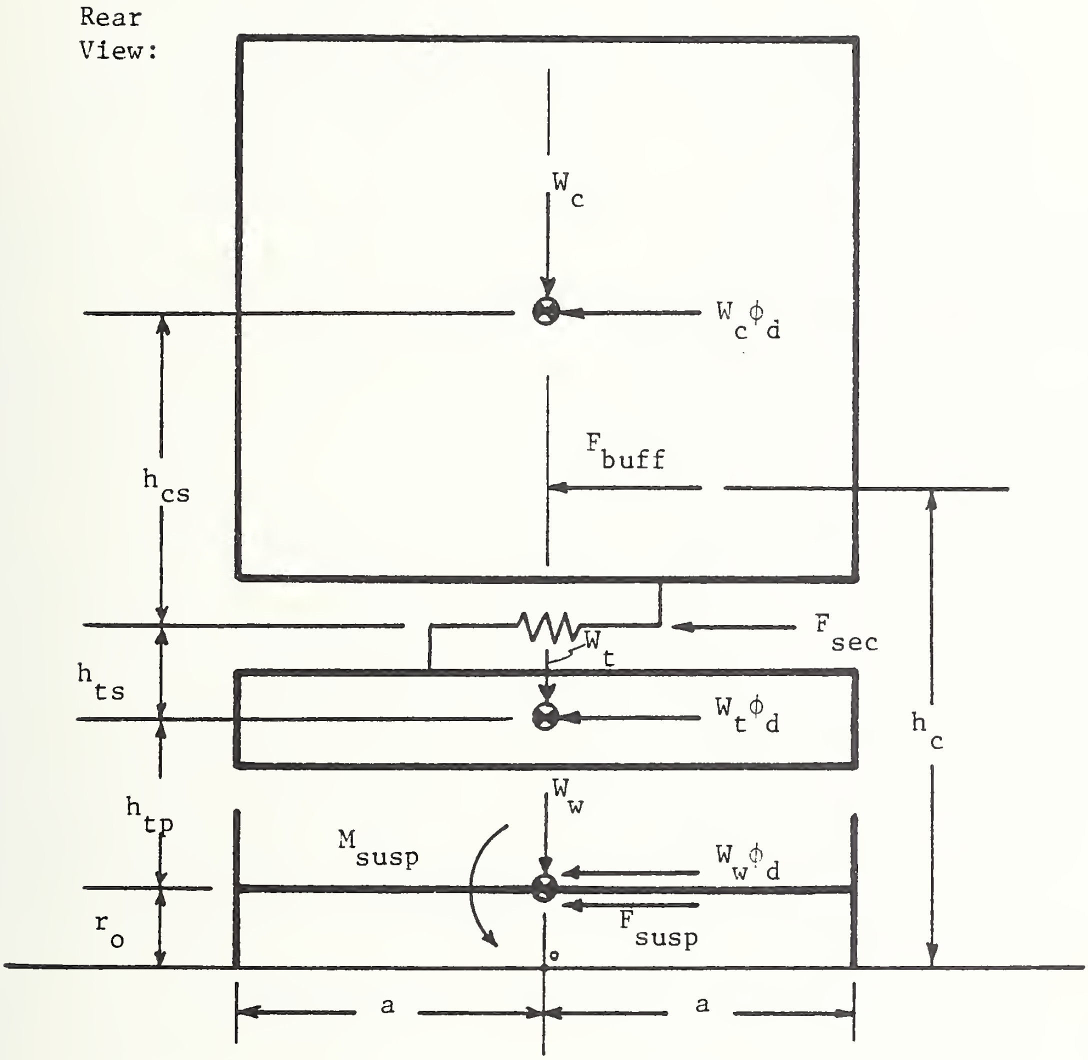

Figure H.11 Vehicle Free-Body Diagram, Rear View

$$+ \frac{W_t}{2}\phi_d h_{tp} + \frac{F_{buff}}{4}(h_c - r_o)$$

$$+ \frac{F_{sec}}{2}(h_{ts} + h_{tp}) + \frac{W_c}{4}(y_{cs} - h_{cs}\phi_c - \frac{y_1+y_2}{2})$$

$$+ \frac{W_t}{2}(y_t - \frac{y_1+y_2}{2}) \qquad \text{(H-24)}$$

H.3.3 Solution Method for Vehicle Equations

The vehicle equilibrium equations represent a set of simultaneous nonlinear algebraic equations. These equations are solved numerically by means of an iterative algorithm entitled SROOTS [32]. The major features of the method are: (1) the iterations do not include any searches along lines in the space of the variable so most situations require only one evaluation of the set of algebraic equations, and (2) the correction vector, $\hat{\delta}$, interpolates between the classical Newton-Raphson and the steepest descent corrections in a way that generally gives fast convergence. These two features make the algorithm computationally fast. A schematic of an iteration in SROOTS is shown in Figure H.12.

The standard form of the equations to be solved is:

$$F_i = 0, \qquad i = 1, 2, \ldots\ldots, N \qquad \text{(H-25)}$$

where N is the total number of equations. The method requires the following information:

(1) an initial estimate or guess of the solution vector

(2) a step length, DSTEP, to approximate the first derivatives of the functions, i.e.,

$$\frac{f_1}{X_1} \simeq \frac{f_1(X_1 + \text{DSTEP}, X_2, X_3, \ldots\ldots, X_N) - f_1(X_1, \ldots\ldots, X_N)}{\text{DSTEP}} \qquad \text{(H-26)}$$

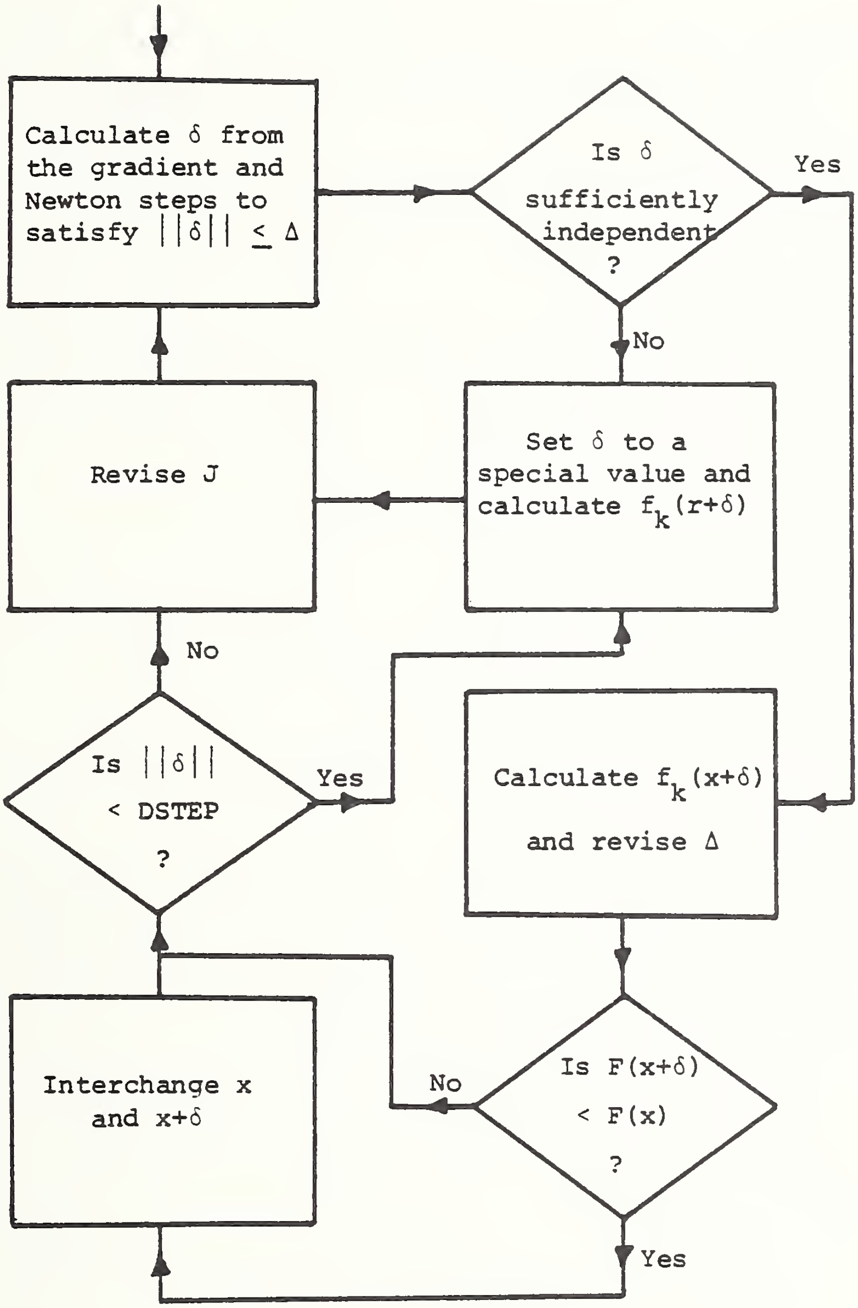

Figure H.12 Schematic of One Iteration in SROOTS, from Rabinowitz, [32]

(3) A generous estimate of the distance between the initial guess and the final solution where the distance, DMAX, is

$$\text{DMAX} = d(\underline{X},\underline{Y}) = \sum_{i=1}^{N} [(X_i - Y_i)^2]^{1/2} \qquad \text{(H-27)}$$

(4) The required accuracy of the solution, ACC, with iterations stopping when $\sum_{i=1}^{N} [f_i(\underline{X})]^2 = \text{ACC}$

(5) The maximum number of allowable iterations, MAX.

When SROOTS cannot find a solution of the equations consistent with the value of ACC, it reports one of the following errors:

(1) The number of iterations exceeds MAX.

(2) A stationary point is predicted since no solutions exist within distance DMAX of X.

(3) N + 4 calls of the residual function fail to improve X indicating that DSTEP may be too large, or that rounding errors prevent the desired accuracy from being obtained.

(4) A completely new evaluation of the partial derivatives (Jacobian) does not decrease F. This may occur for reasons indicated in (3).

SROOTS is incorporated into the steady-state curving program as shown in Figure 2.11. The main program reads the vehicle and curving input data, calls SROOTS which solves the equilibrium state equations, and appropriately formats the output. SROOTS calls CALFUN N times to set up the system Jacobian matrix (matrix of partial derivatives). In each iteration it calls MINV to invert the system matrix. CALFUN sets up the vehicle equations each time it is called. It does this by calling KMAT for the stiffness matrix and by calling WHLST1 or WHLST2 once for each wheelset to obtain the wheel forces depending whether or not two-point contact occurs at the flanging wheel. Both WHLST1 and WHLST2 call GEOM, COEFF, and CFORCE. GEOM obtains the wheel/rail geometry from the profile data table. Creep forces for each wheel are computed in CFORCE using the Kalker creep coefficients obtained from COEFF. COEFF and CFORCE are called iteratively by the wheelset routines (WHLST1, WHLST2) until the net torque on each wheelset is equal to the input value of drive/brake torque, and until wheelset roll equilibrium is satisfied.

Inputs

Wheel/Rail profile geometry data

Vehicle system inputs such as geometry, weights

Forcing Inputs:

D	degree curve
ϕ_d	cant deficiency
Buff	lateral component of buff force, per truck
T_d	wheelset drive torque (same for all wheelsets)
F_{sec}	lateral force or carbody at secondary suspension connection point
ψ_c	carbody yaw displacement

Outputs

The primary output of the steady-state curving program is the vector of static vehicle displacements which satisfies the nonlinear vehicle equations. From this solution vector, the following outputs are obtained.

- Lateral excursion of wheelsets with respect to the track centerline, y_{w_i}
- Wheelset angles of attack, ψ_{wi}
- Net axle forces and L/V ratios

- Yaw moment on each axle
- Wheel/Rail forces (creep and normal)
- Suspension strokes
- Work done at wheel/rail contact patches
- Equilibrium check

In summary, the nonlinear algebraic equilibrium equations representing steady-state curving are solved by subroutine SROOTS, which has proved to be a very robust equation solver.

APPENDIX I

PARAMETRIC CURVING DATA

In this Appendix, the results of the nonlinear steady-steady curving analysis are tabulated for a conventional, self-steered radial, and two forced-steered radial truck designs with new and Heumann wheels. The curving behavior of each truck with four suspension stiffnesses (from soft to stiff, including baseline) negotiating 2.5°,5°, 10°, and 20° curves is reported in terms of the following curving performance indices: (1) leading axle angle of attack, (2) lateral wheel/rail force at flanging wheel, (3) contact patch work at flanging wheel, and (4) total contact patch work (i.e., the sum of the contact patch work at the four wheels of the truck).

Table I.1 Curving Analysis Results for Conventional Track with Standard AAR Profile Wheels

CONVENTIONAL TRUCK WITH NEW WHEELS

		Degree Curve			
		2.5°	5°	10°	20°
k_{px} = 8.5×10^4 lb/ft	ψ_1 (°)	-0.029	0.056	0.273	0.709
	F_{Y1L} (lb)	800.	2300.	4910.	5430.
	W_{1L} (ft-lb/ft)	1	30.	86.	139.
	W_T (ft-lb/ft)	2.	33.	134.	247.
1.35×10^5 lb/ft (Baseline)	ψ_1	-0.023	0.080	0.289	0.750
	F_{Y1L}	820.	2700.	5195.	6870.
	W_{1L}	1.	39.	90.	149.
	W_T	2.	44.	118.	250.
5.0×10^5 lb/ft	ψ_1	0.080	0.237	0.600	1.173
	F_{Y1L}	2090.	4325.	6140.	6970.
	W_{1L}	33.	80.	130.	206.
	W_T	37.	99.	195.	376.
1.0×10^6 lb/ft	ψ_1	0.134	0.322	0.742	1.182
	F_{Y1L}	2680.	4785.	6250.	6955.
	W_{1L}	49.	94.	147.	207.
	W_T	56.	121.	228.	385.

ψ_1 = Leading Axle Angle of Attack (positive counterclockwise)

F_{Y1L} = Lateral Wheel/Rail Force at Flanging Wheel (positive acting in)

W_{1L} = Work at Flanging Wheel

W_T = Total Work (Sum of Work at Four Wheels)

Table I.2 Curving Analysis Results for Conventional Truck with Heumann Profile Wheels

		Degree Curve			
		2.5°	5°	10°	20°
k_{px} = 2.70 x 10^5 lb/ft	ψ_1 (°)	-0.010	-0.037	0.251	1.037
	F_{Y1L} (lb)	1580.	1700.	3310.	6120.
	W_{1L} (ft-lb/ft)	3.	7.	35.	119.
	W_T (ft-lb/ft)	8.	17.	68.	275.
4.25 x 10^5 lb/ft	ψ_1	0.010	0.118	0.436	1.115
	F_{Y1L}	1520.	1855.	4320.	6170.
	W_{1L}	5.	18.	55.	128.
	W_T	12.	33.	111.	297.
6.50 x 10^5 lb/ft (Baseline)	ψ_1	0.055	0.198	0.563	1.151
	F_{Y1L}	1470.	2290.	4790.	6180.
	W_{1L}	11.	29.	69.	131.
	W_T	20.	50.	143.	314.
1.0 x 10^6 lb/ft	ψ_1	0.097	0.261	0.660	1.170
	F_{Y1L}	1450.	2680.	5170.	6170.
	W_{1L}	16.	37.	80.	133.
	W_T	27.	63.	184.	324.

ψ_1 = Leading Axle Angle of Attack

F_{Y1L} = Lateral Wheel/Rail Force at Flanging Wheel

W_{1L} = Work at Flanging Wheel

W_T = Total Work (Sum of Work at Four Wheels)

Table I.3 Curving Analysis Results for Self-Steered Radial Truck with Standard AAR Profile Wheels

(k_{b2} = 1.0×10^3 ft-lb/rad, k_{s2} = 1.0×10^6 lb/ft)

		Degree Curve			
		2.5°	5°	10°	20°
k_{px} = 7.0×10^4 lb/ft	ψ_1 (°)	-0.011	-0.014	0.044	0.234
	F_{Y1L} (lb)	660.	1650.	4060.	6280.
	W_{1L} (ft-lb/ft)	1.	10.	50.	90.
	W_T (ft-lb/ft)	2.	14.	76.	166.
1.20×10^5 lb/ft (Baseline)	ψ_1	-0.002	0.024	0.141	0.632
	F_{Y1L}	715.	2260.	4960.	7090.
	W_{1L}	2.	24.	72.	138.
	W_T	3.	29.	103.	254.
5.0×10^5 lb/ft	ψ_1	0.083	0.231	0.598	1.042
	F_{Y1L}	2090.	4420.	6360.	7160.
	W_{1L}	34.	81.	134.	194.
	W_T	38.	101.	205.	370.
1.0×10^6 lb/ft	ψ_1	0.132	0.319	0.721	1.109
	F_{Y1L}	2700.	4910.	6570.	7140.
	W_{1L}	49.	96.	151.	203.
	W_T	57.	125.	242.	390.

ψ_1 = Leading Axle Angle of Attack

F_{Y1L} = Lateral Wheel/Rail Force at Flanging Wheel

W_{1L} = Work at Flanging Wheel

W_T = Total Work (Sum of Work at Four Wheels)

Table I.4 Curving Analysis Results for Self-Steered Radial Truck with Heumann Wheels

($k_{b2} = 1.0 \times 10^3$ ft-lb/rad, $k_{s2} = 1.0 \times 10^6$ lb/ft)

		Degree Curve			
		2.5°	5°	10°	20°
k_{px} = 2.45×10^5 lb/ft	ψ_1 (°)	0.035	0.163	0.249	0.827
	F_{Y1L} (lb)	1240.	1520.	3160.	6190.
	W_{1L} (ft-lb/ft)	6.	21.	34.	101.
	W_T (ft-lb/ft)	13.	38.	62.	256.
3.70×10^5 lb/ft	ψ_1	0.089	0.193	0.364	0.962
	F_{Y1L}	1110.	1750.	4140.	6270.
	W_{1L}	13.	25.	49.	115
	W_T	30.	44.	99.	291.
5.0×10^5 lb/ft (Baseline)	ψ_1	0.104	0.215	0.468	1.024
	F_{Y1L}	1140.	1970.	4645.	6290.
	W_{1L}	15.	29.	61.	122.
	W_T	34.	48.	127.	308.
1.0×10^6 lb/ft	ψ_1	0.123	0.269	0.634	1.109
	F_{Y1L}	1170.	2580.	5310.	6310.
	W_{1L}	17.	37.	80.	131.
	W_T	38.	62.	190.	329.

ψ_1 = Leading Axle Angle of Attack
F_{Y1L} = Lateral Wheel/Rail Force at Flanging Wheel
W_{1L} = Work at Flanging Wheel
W_T = Total Work (Sum of Work at Four Wheels)

Table I.5 Curving Analysis Results for Forced-Steered Radial Truck, FSR I, with Standard AAR Profile Wheels

($k_{px} = 7.0 \times 10^4$ lb/ft, $k_{s2} = 1.0 \times 10^6$ lb/ft)

		Degree Curve			
		2.5°	5°	10°	20°
k_{b2} = 1.68×10^5 ft-lb/rad (Baseline)	ψ_1 (°)	-0.010	-0.009	0.054	0.241
	F_{Y1L} (lb)	660.	1725.	4160.	6310
	W_{1L} (ft-lb/ft)	1.	12.	52.	91.
	W_T (ft-lb/ft)	2.	16.	79.	167.
5.0×10^5 ft-lb/rad	ψ_1	-0.007	-0.001	0.070	0.251
	F_{Y1L}	670.	1840.	4310.	6360.
	W_{1L}	1.	15.	56.	92.
	W_T	2.	18.	83.	169.
1.0×10^6 ft-lb/rad	ψ_1	-0.004	0.007	0.084	0.261
	F_{Y1L}	670.	1960.	4440.	6395.
	W_{1L}	1.	18.	60.	93.
	W_T	2.	22.	87.	171.
1.0×10^7 ft-lb/rad	ψ_1	0.016	0.035	0.124	0.281
	F_{Y1L}	975.	2370.	4760.	6475.
	W_{1L}	8.	27.	68.	96.
	W_T	10.	32.	98.	175.

ψ_1 = Leading Axle Angle of Attack

F_{Y1L} = Lateral Wheel/Rail Force at Flanging Wheel

W_{1L} = Work at Flanging Wheel

W_T = Total Work (Sum of Work at Four Wheels)

Table I.6 Curving Analysis Results for Forced-Steered Radial Truck, FSR II, with Standard AAR Profile

(k_{px} = 1.0 x 10^3 lb/ft, k_{s2} = 1.0 x 10^6 lb/ft)

		Degree Curve			
		2.5°	5°	10°	20°
k_{b2} = 1.0 x 10^5 ft-lb/rad	ψ_1 (°)	-0.021	-0.041	-0.096	-0.074
	F_{Y1L} (lb)	650.	1190.	2430.	4140.
	W_{1L} (ft-lb/ft)	0.	1.	13.	55.
	W_T (ft-lb/ft)	1.	4.	35.	137.
2.0 x 10^5 ft-lb/rad	ψ_1	-0.020	-0.040	-0.094	-0.040
	F_{Y1L}	650.	1200.	2510.	4290.
	W_{1L}	0.	1.	14.	59.
	W_T	1.	4.	37.	138.
4.1 x 10^5 ft-lb/rad (Baseline)	ψ_1	-0.018	-0.038	-0.064	0.006
	F_{Y1L}	650.	1210.	2810.	4555.
	W_{1L}	0.	1.	19.	64.
	W_T	1.	4.	45.	139.
1.0 x 10^6 ft-lb/rad	ψ_1	-0.013	-0.034	-0.015	0.076
	F_{Y1L}	650.	1250.	3330.	5070.
	W_{1L}	1.	1.	33.	72.
	W_T	1.	4.	59.	145.

ψ_1 = Leading Axle Angle of Attack

F_{Y1L} = Lateral Wheel/Rail Force at Flanging Wheel

W_{1L} = Work at Flanging Wheel

W_T = Total Work (Sum of Work at Four Wheels)

Table I.7 Curving Analysis Results for Forced-Steered Radial Truck, FSR I, with Heumann Profile Wheels

($k_{px} = 7.0 \times 10^4$ lb/ft, $k_{s2} = 1.0 \times 10^6$ lb/ft)

		Degree Curve			
		2.5°	5°	10°	20°
k_{b2} = 5.0×10^5 ft-lb/rad	ψ_1 (°)	-0.009	0.004	0.070	0.100
	F_{Y1L} (lb)	1530.	1490.	1730.	3390.
	W_{1L} (ft-lb/ft	1.	2	8	19.
	W_T (ft-lb/ft)	4.	5	13	41.
1.66×10^6 ft-lb/rad (Baseline)	ψ_1	-0.002	0.010	0.068	0.114
	F_{Y1L}	1470.	1450.	1730.	3470.
	W_{1L}	1.	2.	7	18.
	W_T	4.	6.	12.	44.
5.0×10^6 ft-lb/rad	ψ_1	0.004	0.013	0.062	0.125
	F_{Y1L}	1420.	1430.	1720.	3550.
	W_{1L}	2.	3.	6.	17.
	W_T	5.	6.	11.	47.
1.0×10^7 ft-lb/rad	ψ_1	0.006	0.014	0.060	0.129
	F_{Y1L}	1400.	1430.	1720.	3575.
	W_{1L}	2.	3.	6.	17.
	W_T	5.	6.	11.	48.

ψ_1 = Leading Axle Angle of Attack

F_{Y1L} = Lateral Wheel/Rail Force at Flanging Wheel

W_{1L} = Work at Flanging Wheel

W_T = Total Work (Sum of Work at Four Wheels)

Table I.8 Curving Analysis Results for Forced-Steered Radial Truck, FSR II, with Heumann Profile Wheels

(k_{px} = 1.0 x 10^3 lb/ft, k_{s2} = 1.0 x 10^6 lb/ft)

		Degree Curve			
		2.5°	5°	10°	20°
k_{b2} = 1.0 x 10^6 ft-lb/rad	ψ_1 (°)	-0.019	-0.026	-0.004	-0.003
	F_{Y1L} (lb)	1645.	1780.	1800.	2980.
	W_{1L} (ft-lb/ft)	1.	2	2	11.
	W_T (ft-lb/ft)	5.	6	6	30.
2.0 x 10^6 ft-lb/rad (Baseline)	ψ_1	-0.011	-0.015	0.010	0.024
	F_{Y1L}	1560.	1660.	1750.	2970.
	W_{1L}	1.	2.	2.	16.
	W_T	4.	5.	6.	31.
5.0 x 10^6 ft-lb/rad	ψ_1	-0.002	-0.004	0.024	0.056
	F_{Y1L}	1470.	1560.	1710.	3040.
	W_{1L}	1.	1	2.	17.
	W_T	4.	5.	6	33
1.0 x 10^7 ft-lb/rad	ψ_1	0.001	0.002	0.030	0.074
	F_{Y1L}	1440.	1510.	1700.	3120.
	W_{1L}	1.	1.	2.	17.
	W_T	4.	5.	7.	36.

ψ_1 = Leading Axle Angle of Attack

F_{Y1L} = Lateral Wheel/Rail Force at Flanging Wheel

W_{1L} = Work at Flanging Wheel

W_T = Total Work (Sum of Work at Four Wheels)

APPENDIX J

REPORT OF NEW TECHNOLOGY

In this report, the speed capability and curving performance of rail vehicles employing conventional and advanced truck designs are parametrically investigated using analytical and computational tools. The studies are based upon a generalized rail vehicle model which can represent conventional, self-steered, and forced-steered trucks. The curving analysis includes nonlinear wheel/rail profile geometry, wheel/rail friction force saturation, and nonlinear suspension components. A major contribution of the analysis is that it accounts for two-point wheel/rail contact, which occurs with many common wheel profiles during flanging.

The material presented in this report has been thoroughly reviewed and does not contain patentable or copyrightable material. The innovations reported in this document are described in Chapter 2 and are developed in detail in Appendices A through H.

REFERENCES

1. Boyd, P. L., Zaiko, J. P., and Jordan, W. L., "Effect of Wheel Taper and Primary Suspension Stiffness on Wheel/Rail Forces at the Washington Metropolitan Area Transit Authority," Vol. II Test Report, Interim Report, U.S. Department of Transportation, March 1980.

2. Elkins, J. A., "Analytic Studies of Curving Forces and Hunting Stability and Related Support for WMATA Phase II Truck Test Project," Interim Report, U.S. Department of Transportation, UMTA, June 1982.

3. Marcotte, P., Caldwell, W. N., and List, H. H., "Performance Analysis and Testing Conventional Three Piece Freight Car Truck Retrofitted to Provide Axle Steering," presented at the 1978 ASME Winter Annual Meeting, San Francisco, CA, 1978.

4. Sweet, L. M. and Sivak, J. A., "Nonlinear Wheelset Forces in Flange Contact, Part 1: Steady State Analysis and Numerical Results," Journal of Dynamic Systems, Measurement and Control, Vol. 101, No. 3, September 1979, pp. 238 - 246.

5. Gilchrist, A. O. and Brickle, B. V., "A Re-Examination of the Proneness to Derailment of a Railway Wheelset," Journal of Mechanical Engineering Science, Vol. 18, No. 3, 1976, pp. 131 - 141.

6. Newland, D. E., "Steering a Flexible Railway Truck on Curved Track," Journal of Engineering for Industry, A.S.M.E. Transactions, Series B, Vol. 91, No. 3, August 1969, pp. 908-918.

7. Boocock, D., "Steady-State Motion of Railway Vehicles on Curved Tracks," Journal of Mechanical Engineering Science, Vol. 11, No. 6, December 1969, pp. 556 - 566.

8. Doyle, G. R., "Conventional Versus Self-Steering Radial Truck for High-Speed Passenger Trains," ASME Report 79-RT-3, ASME/IEEE Joint Railroad Conference, 1979.

9. Elkins, J. A. and Eichoff, B. M., "Advances in Non-Linear Wheel/Rail Force Prediction Methods and Their Validation," Journal of Dynamic Systems, Measurement and Control, Vol. 104, No. 2, June 1982, pp. 133-142.

10. Bolton, P., "Wear of BS11 Rail Steels in Rolling/Sliding Contact with Class "D" Type Steel," British Railways Technical Note TNMET21, February 1980.

11. Kumar, S., Prasanna Rao, D. L., and Rajkuma, B. R., "A Wheel-Rail Wear Study for Railroad Transit Systems," I.I.T. Report IIT-TRANS-80-1, August 1980.

12. Bolton, P. J., Clayton, P. and McEwen, I. J., "Wear of Rail and Tyre Steels Under Rolling/Sliding Conditions," British Rail Research, presented at the ASME/ASNE Conference, August 1980.

13. Elkins, J. A. and Allen, R. A., "Testing a Transit Vehicle for Wheel and Rail Wear," A.S.M.E. Transactions, Paper 81-WA/DSC-19, 1981.

14. List, H. A., Caldwell, W. N, and Marcotte, P., "Proposed Solutions to the Freight Car Truck Problems of Flange Wear and Truck Hunting," ASME Paper No. 75-WA-RT-8, 1976.

15. Scheffel, H., "The Hunting Stability and Curving Ability of Railway Vehicles," Rail International, No. 2, February 1974, pp. 154-177.

16. Horak, D., Bell, C. E., and Hedrick, J. K., "A Comparison of the Stability and Curving Performance of Radial and Conventional Rail Vehicle Trucks," Journal of Dynamic Systems, Measurement and Control, Vol. 103, September 1981, pp. 191-200.

17. Wickens, A. H., "Steering and Dynamic Stability of Railway Vehicles," Vehicle System Dynamics, Vol. 5, 1975/1976, pp. 15-46.

18. Scales, B. T., "Behavior of Bogies on Curves," Railway Engineering Journal, July 1972, pp. 19-24.

19. Smith, R. E., "Steering Conversion of CTA 2400 Rapid Transit Truck, Volume I: Design Feasibility Study," Project Memorandum, U.S. Department of Transportation, Report No. DOT-TSC-UM104-PM-80-48, December 1980.

20. Bell, C. E., and Hedrick, J. K, "Forced Steering of Rail Vehicles: Stability and Curving Mechanics," Vehicle System Dynamics, Vol. 10, pp. 357-386, 1981.

21. List, H. A., "Means for Improving the Steering Behavior of Railway Vehicles," Presented to the Annual Meeting of the Transportation Research Board, January 22, 1976.

22. Cooperrider, N. K. and Law, E. H., "Data Book: Wheel/Rail Geometry for Five Wheel Profiles and Three Rail Profiles," Report No. ERC-R-75015, Department of Mechanical Engineering, Arizona State University, Tempe, Arizona 85281.

23. Cooperrider, N. K. and Law, E. H., Rail Vehicle Dynamics, January 1980.

24. Mekosh, G., "Technical Analysis for Modifying an Existing Heavy Rapid Rail Truck to a Steerable Configuration," Report for Contract No. DOT-TSC-1740, May 1980.

25. Bell, C. E., Horak, D., and Hedrick, J. K., "Stability and Curving Mechanics of Rail Vehicles," Journal of Dynamic Systems, Measurement, and Control, Vol. 103, September 1981, pp. 181-190.

26. Horak, D., "Passenger Rail Vehicle Dynamics," Ph.D. Thesis, Department of Mechanical Engineering, Massachusetts Institute of Technology, 1981.

27. Surjana, J., "Stability Analysis of Forced Steering Trucks," M.S. Thesis, Department of Mechanical Engineering, Massachusetts Institute of Technology, 1982.

28. Mekosh, G., "Design Feasibility Study for Modifying an Existing Heavy Rapid Rail Truck to a Steerable Configuration," Project Memorandum, U. S. Department of Transportation, Report No. DOT-TSC-UM104-PM-80-49, December 1980.

29. Elkins, J. A. and Weinstock, H, "The Effect of Two Point Contact on the Curving Behavior of Railroad Vehicles," A.S.M.E. Transactions, Paper 82-WA/DSC-13, 1982.

30. Bell, C. E., "Curving Mechanics of Rail Vehicles," Ph.D. Thesis, Department of Mechanical Engineering, Massachusetts Institute of Technology, 1981.

31. Kalker, J. J., "Survey of Wheel-Rail Rolling Contact Theory," Vehicle System Dynamics, No. 5, 1979, pp. 317-358.

32. Rabinowitz, P., Numerical Methods for Nonlinear Algebraic Equations, Gordon and Breach Science Publishers, London, 1970.

33. Vermeulen, P. J., Johnson, K. L., "Contact of Nonspherical Elastic Bodies Transmitting Tangential Forces," Journal of Applied Mechanics, Transactions of the ASME, pp. 338-340, June 1964.

34. Arslan, A. V., "The Application of Statistical Linearization to Nonlinear Rail Vehicle Dynamics," Ph.D. Thesis, Department of Mechanical Engineering, Massachusetts Institute of Technology, 1980.

35. Hedrick, J. K., et al., "Performance Limits of Rail Passenger Vehicles: Evaluation and Optimization," Final Report prepared by U.S. Department of Transportation, Contract DOT-OS-70052, December 1979.

36. Ahbeck, D. R., "The Effects of Track Modulus on Vehicle-Track Dynamic Interaction," IEEE/ASME Railroad Conference, Erie, PA, 1982.

37. Nagurka, M. L., "Curving Performance of Rail Passenger Vehicles," Ph.D. Thesis, Department of Mechanical Engineerng, Massachusetts Institute of Technology, 1983.

☆ U. S. GOVERNMENT PRINTING OFFICE: 1984--700-898--301

Department
ansportation
earch and
cial Programs
ninistration
all Square
ridge, Massachusetts 02142